Measurement of the Neutrino Beam with the Muon Monitor and the First Result of the T2K Long-Baseline Neutrino Oscillation Experiment

Kodai Matsuoka

March, 2011

Department of Physics, Graduate School of Science
Kyoto University

Measurement of the Neutrino Beam with the Muon Monitor and the First Result of the T2K Long-Baseline Neutrino Oscillation Experiment

A dissertation
submitted in partial fulfillment of the requirements
for the Degree of Doctor of Science
in the Graduate School of Science, Kyoto University

Kodai Matsuoka

Department of Physics, Graduate School of Science
Kyoto University
March, 2011

Dissertation Committee:

Tsuyoshi Nakaya
Atsuko K. Ichikawa
Akira Noda
Tomofumi Nagae
Takeshi Go Tsuru

Abstract

We launched the T2K accelerator-based long-baseline neutrino oscillation experiment to measure the neutrino mixing angles, θ_{23} and θ_{13}. In T2K, the ν_μ beam is generated using the J-PARC high intensity proton beam and is detected by the Super-Kamiokande detector after traveling 295 km. Stable beam operation and precise measurement of the beam are essential parts of this experiment. They are realized by precisely monitoring the proton and neutrino beams with proton beam monitors and a muon monitor.

One of the purposes of the studies presented in this thesis is to establish the well-tuned and stable beam operation and to precisely measure the beam in T2K. The study is focused on the muon monitor in particular, which monitors the neutrino beam direction by measuring the muon beam generated along with the neutrino beam from the pion decays. The muon monitor consists of two types of detector arrays: ionization chambers and silicon PIN photodiodes. We designed and constructed the muon monitor to stably measure the neutrino beam direction with a precision better than 0.25 mrad and to be tolerant of radiation. This performance of the muon monitor was confirmed in beam tests and also in the T2K beam operation. In the T2K physics data taking from January to June of 2010, the muon monitor ensured the stability of the neutrino beam: less than 0.06 mrad fluctuation of the beam direction and less than 0.8% fluctuation of the beam intensity. In this run, we achieved 72 kW of the proton beam power at the maximum and accumulated 3.28×10^{19} protons on the target.

Another purpose is to establish a method to predict the neutrino flux generated in T2K. The prediction is based on a Monte Carlo simulation, which is validated by the measurement of the beam and the external hadron production data. The neutrino flux and its systematic error arising from beam-related uncertainties were estimated, and they were used to predict the number of neutrino events at Super-Kamiokande. The expected number of ν_μ events for the θ_{23} measurement and ν_e background events for the θ_{13} measurement was estimated to be $6.35^{+1.09}_{-1.08}$ and 0.30 ± 0.08, respectively, while the observed number of ν_μ and ν_e events was eight and one, respectively. One of the dominant errors for the expected number of neutrino events is the neutrino flux error, which is dominated by the hadron production uncertainties. We confirmed that the uncertainties related to the beam operation and measurement were sufficiently small due to the stable beam operation and precise measurement of the beam.

Acknowledgements

All of my works in this thesis were supported by a lot of people. First of all, I must thank all MUMONers: Prof. Tsuyoshi Nakaya, Prof. Atsuko K. Ichikawa, Prof. Masashi Yokoyama, Prof. Takasumi Maruyama, Mr. Hajime Kubo, Mr. Akira Murakami and Mr. Kento Suzuki. Prof. Tsuyoshi Nakaya is my supervisor. He let me walk around my subjects with my own legs but he always indicates the right way which I should go. Though it was a long way to the end of this thesis, I would never have reached this successful end without his support. Prof. Atsuko K. Ichikawa is also my supervisor. She helped me a lot not only with the muon monitor work but also with the Monte Carlo simulation and the study on the neutrino flux estimation. In addition, her powerful speaking voice roused me into activity. Prof. Masashi Yokoyama was my supervisor. He greatly supported me with the design and beam tests of the muon monitor. He taught me many things on physics and experimental technique in the practical experiences. Prof. Takasumi Maruyama strongly supported me to construct the muon monitor. I spent pleasurable days with him in J-PARC, constructing the muon monitor. Mr. Hajime Kubo worked together with me on the muon monitor. We were on the same wavelength but the different phase by 180 degrees, which, I believe, resulted in the success of the muon monitor construction and operation. Mr. Akira Murakami and Mr. Kento Suzuki also worked together with me. We had many tough works, but their sincere effort as well as their jokes encouraged me in going about my business.

I would like to express my appreciation for the support by every staff of the KEK neutrino group. The strong leadership by Prof. Koichiro Nishikawa, the director of the Institute of Particle and Nuclear Studies, KEK, and Prof. Takashi Kobayashi, the T2K spokesperson, led T2K into launch in success. Dr. Takeshi Nakadaira led the commissioning of the neutrino beamline, and a lot of his advice helped me to carry my study forward. Dr. Ken Sakashita always kindly supported my work at KEK and J-PARC. The readout, DAQ and on/off-line analysis system of the neutrino beamline as well as that of the muon monitor was realized through his tremendous effort. I also appreciate the great help by Prof. Y. Fujii, Prof. Y. Yamada, Prof. T. Tsukamoto, Dr. T. Ishida, Dr. M. Tada and Dr. S.Y. Suzuki.

The muon monitor analysis on the neutrino beam cannot be done without the primary proton beam monitors, which experts are Dr. M. Shibata, Dr. H. Kakuno, Dr. N.C. Hastings, Dr. T. Ishii, Dr. M. Hartz and Dr. V. Galymov. I am thankful to them for the collaborative work.

I want to thank my collaborators of the T2K and Super-Kamiokande experiments. The data shown in this thesis is the fruits of our effort. In addition, I am grateful to the J-PARC accelerator team for their intense effort to realize the high power beam.

The beam test at ICR was supported by Prof. A. Noda, Prof. T. Shirai, Dr. H. Souda and Mr. H. Tongu. We tested the muon monitor detectors seven times at ICR, and every time they strongly supported our test from early morning to midnight. I offer profuse thanks to them. I also thank Prof. K. Yamamoto, Mr. K. Maeda, Mr K. Tashiro, Ms. T. Ozaki, Ms. C. Matsumura, Mr. M. Taguchi, Mr. M. Otani, Mr. H. Kawamuko, Mr. N. Nagai, Mr. S. Gomi, Mr. K. Ieki, Mr. S. Takahashi, Mr. T. Kikawa and Dr. Y. Igarashi for their help in the tests.

The beam test at NuMI was supported by Prof. S. Kopp, Mr. M. Proga, Dr. L. Loiacono, Dr. R. Zwaska and the staff of Fermilab. I really appreciate their cooperation. During the test, I gratefully spent precious days with the SciBooNE collaborators, in particular, Prof. M.O. Wascko, Dr. H. Tanaka, Dr. K. Hiraide, Dr. Y. Kurimoto, Dr. Y. Nakajima, Dr. H. Takei and Mr. and Mrs. Kunori.

I want to express my gratitude to also the other members of my laboratory: Prof. N. Sasao, Prof. T. Nomura, Dr. H. Nanjo, Mr. H. Yokoyama, Dr. I. Kato, Dr. K. Mizouchi, Dr. M. Hasegawa, Dr. H. Morii, Dr. T. Sumida, Dr. A. Nitta, Mr. J. Kubota, Dr. N. Taniguchi, Dr. S. Yamamoto, Dr. A. Minamino, Mr. Y. Kurosawa, Mr. K. Ezawa, Mr. T. Nobuhara, Dr. M. Ikeda, Mr. K. Shiomi, Mr. T. Usuki, Mr. N. Kawasaki, Mr. T. Masuda, Mr. D. Naito, Mr. Y. Maeda, Mr. G. Takahashi, Mr. T. Yamauchi and Mr. T. Hiraki. I wish to acknowledge the secretaries' care of my business in Kyoto University, KEK and J-PARC.

This work was supported by MEXT and JSPS with Grant-in-Aid for Scientific Research on Priority Areas 18071007, Young Scientists S 20674004, JSPS Fellows, the Global COE Program "The Next Generation of Physics, Spun from Universality and Emergence" and the Japan/U.S. Cooperation Program in the field of High Energy Physics.

My greatest gratitude goes to my family, particularly to my parents. They are, therefore I am. All my heart goes to my life partner, Sayaka Ogawa. She is, hence I am.

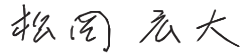

Kyoto, Japan
March, 2011

I dedicate this thesis to the peace of the world.

Contents

Acknowledgements **i**

1 Introduction **1**
1.1 History of the neutrino oscillation physics . . . 1
1.1.1 Discovery of neutrinos . . . 1
1.1.2 Solar neutrino problem . . . 1
1.1.3 Evidence of the neutrino oscillation . . . 2
1.2 Theory of the neutrino oscillation . . . 3
1.2.1 Generation mixing of neutrinos . . . 3
1.2.2 Neutrino oscillation in vacuum . . . 4
1.2.3 Matter effect on neutrino propagation . . . 6
1.2.4 CP violation in the neutrino oscillation . . . 8
1.3 Neutrino oscillation experiments . . . 9
1.3.1 Present understanding of the neutrino oscillation . . . 9
1.3.2 Outlook for the neutrino oscillation physics . . . 12
1.3.3 Approach to θ_{13} . . . 15

2 T2K Experiment **17**
2.1 Overview of T2K . . . 17
2.2 Goals of T2K . . . 18
2.3 Experimental strategy . . . 18
2.3.1 ν_e appearance search . . . 20
2.3.2 ν_μ disappearance analysis . . . 20
2.4 Features of T2K . . . 20
2.4.1 Intense neutrino beam . . . 22
2.4.2 Neutrino beam monitoring by the muon monitor . . . 22
2.4.3 Input of the hadron production cross-sections from CERN-NA61 . . . 23
2.4.4 Off-axis beam configuration . . . 23
2.5 Requirements in T2K . . . 24
2.5.1 High power beam operation . . . 25
2.5.2 Neutrino beam quality . . . 25
2.6 History of T2K . . . 26
2.7 Overview of this thesis . . . 27

3 Experimental Components **28**
3.1 J-PARC . . . 28
3.2 Neutrino beamline . . . 28
3.2.1 Primary beamline . . . 30
3.2.2 Secondary beamline . . . 33
3.2.3 Beamline online system . . . 37

3.3 Near detectors . . . 38
3.3.1 ND280 off-axis detector . . . 38
3.3.2 INGRID . . . 39
3.4 Super-Kamiokande detector (Super-K) . . . 40
3.4.1 Detector overview . . . 40
3.4.2 T2K beam data . . . 40

4 Muon Monitor Design **42**
4.1 Characteristics of the muon beam . . . 42
4.2 Requirements for the muon monitor . . . 44
4.3 Instruments of the muon monitor . . . 44
4.3.1 Ionization chamber . . . 46
4.3.2 Silicon PIN photodiode . . . 49
4.3.3 The support enclosure . . . 49
4.3.4 Electronics and cables . . . 51

5 Muon Monitor Performance **52**
5.1 Estimation of the detectors' signals . . . 52
5.2 Beam tests of the detectors . . . 53
5.2.1 Electron beam test at ICR . . . 53
5.2.2 FNAL T968 test experiment . . . 57
5.2.3 Summary of the beam tests . . . 58
5.3 Basic performance of the muon monitor . . . 59
5.3.1 Method for reconstructing the muon profile . . . 59
5.3.2 Calibration of the detectors . . . 60
5.3.3 Linearity against the beam intensity . . . 60
5.3.4 Resolutions . . . 60

6 Beam Tuning by Monitoring the Muon Beam **64**
6.1 Sensitivity to the horn focusing . . . 65
6.1.1 Dependence of the muon yield on the horn currents . . . 65
6.1.2 Dependence of the muon profile width on the horn currents . . . 65
6.2 Sensitivity to the proton beam . . . 68
6.2.1 Sensitivity of the muon beam direction to the proton beam position . . . 68
6.2.2 Sensitivity of the muon yield to the proton beam position and angle . . . 71
6.2.3 Sensitivity of the muon profile width to the proton beam position . . . 71
6.3 Stability of the muon beam . . . 71
6.3.1 Stability of the proton beam and horn currents . . . 71
6.3.2 Stability of the muon beam direction . . . 74
6.3.3 Stability of the muon yield . . . 77
6.3.4 Stability of the muon profile width . . . 78
6.3.5 Summary of the muon beam stability . . . 78
6.4 Systematic error of the muon beam direction measurement . . . 79
6.4.1 Alignment error of the muon monitor detectors . . . 79
6.4.2 Uncertainty of the relative sensor gains . . . 79
6.4.3 Non-Gaussian shape of the muon profile . . . 80
6.4.4 Non-uniformity of the thickness of the beam dump . . . 80
6.4.5 Effect of the tilted beamline against the beam dump . . . 82
6.4.6 Discrepancy of the profile center between the chamber and silicon arrays . . . 82
6.4.7 Summary of the systematic error . . . 83
6.5 Summary of the beam tuning with the muon monitor . . . 84

7 Analysis Overview **85**
7.1 Summary of the beam data . . . 85
7.1.1 Good beam spill selection . . . 85
7.1.2 Neutrino beam stability measured by INGRID . . . 87
7.1.3 Data set for the ND280 tracker . . . 88
7.1.4 Good spill selection at Super-K . . . 88
7.2 Neutrino event selection criteria at Super-K . . . 88
7.2.1 Fully-contained fiducial volume (FCFV) event selection . . . 88
7.2.2 Event classification . . . 90
7.2.3 Event selection for the ν_μ disappearance analysis . . . 90
7.2.4 Event selection for the ν_e appearance search . . . 90
7.3 Outline of the analysis . . . 91

8 Hadron Production Tuning for the Neutrino Flux Prediction **92**
8.1 Overview of JNUBEAM . . . 92
8.1.1 Hadron interactions in the target with FLUKA . . . 92
8.1.2 Particle tracking in JNUBEAM . . . 93
8.2 Hadron production in T2K . . . 95
8.2.1 Definition of the production cross-section and multiplicity . . . 95
8.2.2 Secondary particles contributing the neutrino beam . . . 97
8.2.3 Measurement of the hadron production by CERN-NA61 . . . 98
8.3 Tuning of the hadron production . . . 100
8.3.1 Overview of the tuning . . . 100
8.3.2 Secondary $\pi^\pm$ multiplicities . . . 102
8.3.3 Tertiary $\pi^\pm$ multiplicities . . . 102
8.3.4 Interaction rate . . . 104
8.4 Expected neutrino flux . . . 108
8.5 Systematic error of the neutrino flux from the hadron production uncertainties . 110
8.5.1 Uncertainty of the pion multiplicity . . . 110
8.5.2 Uncertainty of the charged kaon multiplicity . . . 110
8.5.3 Uncertainty of the K^0_L multiplicity . . . 111
8.5.4 Uncertainty of the production cross-section . . . 112
8.5.5 Systematic error of the neutrino flux . . . 113

9 Expected Number of Neutrino Events at Super-K **117**
9.1 Prediction of the number of neutrino events . . . 117
9.1.1 Normalization by the ND280 off-axis detector . . . 117
9.1.2 Expected number of neutrino events at Super-K . . . 117
9.1.3 Systematic error of the expected number of neutrino events at Super-K . 119
9.2 Systematic error of the flux normalization . . . 121
9.2.1 Uncertainty of the hadron production . . . 122
9.2.2 Uncertainties related to the neutrino beam operation . . . 123
9.3 Summary of the expected number of neutrino events . . . 128

10 Observed Number of Neutrino Events at Super-K **130**
10.1 Neutrino events at Super-K . . . 130
10.1.1 Fully-contained fiducial volume (FCFV) event . . . 130
10.1.2 ν_μ events for the ν_μ disappearance analysis . . . 132
10.1.3 Candidate for the ν_e appearance signal . . . 132
10.2 Summary of the analysis . . . 135

11 Conclusions **136**

A Near-to-Far Extrapolation **138**

B Monte Carlo Simulations for Super-K **140**
B.1 Neutrino interaction simulation (NEUT) . . . 140
B.1.1 Quasi-elastic scattering (QE) . . . 140
B.1.2 Resonant single meson production . . . 142
B.1.3 Coherent pion production . . . 142
B.1.4 Deep inelastic scattering (DIS) . . . 142
B.1.5 Nuclear effects . . . 142
B.2 Super-K detector simulation (SKDETSIM) . . . 143
B.2.1 Cherenkov photon propagation . . . 143
B.2.2 Reflection, refraction and absorption of light on materials . . . 144
B.2.3 Photoelectron production and response of the electronics . . . 144

C Neutrino Beamline Operation **145**
C.1 Detail of the good beam spill selection . . . 145
C.2 Proton beam measurement . . . 146
C.2.1 Performance of the proton beam monitors . . . 146
C.2.2 Extrapolation of the proton beam orbit and optics . . . 148

D Measurement of Neutrino Beam Events at ND280 **150**
D.1 Measurement of the neutrino beam by INGRID . . . 150
D.1.1 Neutrino event selections . . . 151
D.1.2 Neutrino beam direction measured by INGRID . . . 151
D.2 Neutrino events at the ND280 off-axis detector . . . 154
D.2.1 Neutrino event selections . . . 154

E Tuning of the Kaon Production in JNUBEAM **156**
E.1 Tuning of the kaon multiplicities and its uncertainty . . . 156
E.1.1 Kaon production data around 30 GeV . . . 156
E.1.2 Parametrization of the kaon multiplicity . . . 158
E.1.3 Reweighting of the secondary $K^{\pm}$ multiplicities . . . 161
E.1.4 Reweighting of the secondary K^0_L multiplicities . . . 164
E.1.5 Reweighting of the tertiary $K^{\pm}$ and K^0_L multiplicities . . . 164
E.1.6 Effect of the kaon multiplicity tuning on the neutrino flux . . . 164
E.2 Reevaluation of the systematic error of the neutrino flux from the hadron production uncertainty . . . 164
E.3 Simple quark parton model for the K^0_L production . . . 168

F Systematic Error of the Neutrino Flux (Supplement) **169**
F.1 Uncertainties related to the neutrino beam operation . . . 169
F.2 Uncertainties related to the alignment . . . 171

List of Tables **174**

List of Figures **176**

Bibliography **181**

Chapter 1

Introduction

The neutrino is one of the elemental particles, through which we advance our understanding of the particle physics to learn about the laws of nature. The neutrino oscillation is a phenomenon such that a neutrino changes its type (or flavor) in flight. It implies that neutrinos have masses and that leptons mix. This is the only instance experimentally verified as the physics beyond the Standard Model. By studying the neutrino oscillation, we are exploring new physics.

As an introduction to this thesis, the theories of the neutrino oscillation and current status of the knowledge obtained by experiments are described in this chapter.

1.1 History of the neutrino oscillation physics

1.1.1 Discovery of neutrinos

The neutrino was first postulated in 1930 by W. Pauli [1] to preserve the law of conservation of energy in a beta decay of an atomic nucleus:

$$n \to p + e^- + \bar{\nu}_e. \tag{1.1}$$

In 1956, the neutrino was discovered by C.L. Cowan Jr. and F. Reines [2] by detecting anti-neutrinos from a nuclear reactor with a $CdCl_2$-loaded water target ($\bar{\nu}_e + p \to n + e^+$). Then, it was showed in 1962 by L.M. Lederman, M. Schwartz and J. Steinberger [3] that there exists more than one species of neutrinos by detecting muon neutrinos from pion decays at the Brookhaven's AGS (Alternating Gradient Synchrotron). It was the first-ever use of the accelerator neutrino beam. The number of light neutrino species N_ν was determined most precisely by studying Z production in e^+e^- collisions at SLC (Stanford Linear Collider) and LEP (Large Electron Positron collider) as [4]:

$$N_\nu = \frac{\Gamma_{inv}}{\Gamma_\ell}\left(\frac{\Gamma_\ell}{\Gamma_\nu}\right)_{\mathrm{SM}} = 2.9840 \pm 0.0082, \tag{1.2}$$

where Γ_{inv}, Γ_ℓ and Γ_ν are the partial width of invisible particles, charged leptons and neutrinos, respectively. The third species of neutrinos, tau neutrino, was discovered in 2000 by the DONUT (Direct Observation of the NU Tau) experiment [5] at Tevatron.

1.1.2 Solar neutrino problem

The sun is one of the sources of neutrinos. The solar neutrinos (only ν_e) are produced by some of the fusion reactions in the pp chain or CNO (carbon-nitrogen-oxygen) cycle [6, 7].

The first experiment for the measurement of the solar neutrino started in the late 1960's by R. Davis *et al.* at Homestake [8]. They used a radiochemical method ($\nu_e + {}^{37}\mathrm{Cl} \to {}^{37}\mathrm{Al} + e^-$;

threshold 814 keV) proposed by B. Pontecorvo [9]. Their result was found to be significantly inconsistent with the standard solar model [10–12] (SSM); the measured neutrino flux (mainly from $^8\mathrm{B} \to {}^8\mathrm{B}^* e^+ \nu_e$ reactions) was one third or less of the prediction by SSM, provided nothing happens to the ν_es during their travels from the sun to the earth. This deficit of the solar neutrino flux was called "the solar neutrino problem".

The Kamiokande experiment succeeded in real time measurement of the solar neutrinos using a large water Cherenkov detector ($\nu_\ell + e^- \to \nu_\ell + e^-$, where $\ell = e$, μ or τ; threshold 7 MeV), and gave the first direct evidence in 1987 that the flux of neutrinos coming actually from the sun is significantly smaller than the SSM prediction [13]. Other experiments also observed the deficit: GALLEX [14,15] (Gallium Experiment), GNO [16] (Gallium Neutrino Observatory) and SAGE [17] (Soviet-American Gallium Experiment) utilizing another radiochemical method with Gallium ($\nu_e + {}^{71}\mathrm{Ga} \to {}^{71}\mathrm{Ge} + e^-$; threshold 233 keV); and the Super-Kamiokande experiment [18] (Super-K) with a larger water Cherenkov detector (threshold 5 MeV). At that time, people did not reach the conclusion that the deficit is caused by the neutrino oscillation.

1.1.3 Evidence of the neutrino oscillation

The cosmic ray, which interacts with nuclei in the upper atmosphere and produces pions, is another source of neutrinos, called atmospheric neutrinos. The atmospheric neutrinos are dominantly produced in decays of $\pi^+ \to \mu^+ \nu_\mu$ and subsequent $\mu^+ \to e^+ \bar{\nu}_\mu \nu_e$ (and their charge conjugates). In these decay processes, the flux ratio of $\nu_\mu + \bar{\nu}_\mu$ to $\nu_e + \bar{\nu}_e$ is expected to be two. The Kamiokande experiment reported a deficit of the atmospheric muon neutrinos [19] and mentioned that the deficit might be due to the neutrino oscillation. The evidence of the neutrino oscillation was first reported in 1998 by Super-K [20] by measuring the atmospheric neutrinos with much higher statistics. Super-K observed a zenith angle dependent deficit of the atmospheric muon neutrinos; the oscillation probability depends on the neutrino flight distance, and hence on the zenith angle of the neutrino direction for the detector near the surface of the earth. Their result is consistent with the two-flavor $\nu_\mu \leftrightarrow \nu_\tau$ oscillation.

The firmer evidence of the atmospheric neutrino oscillation was given by the Super-K L/E analysis [21] (L is the neutrino flight length and E is the neutrino energy), which ruled out other exotic explanations for the deficit such as neutrino decay [22] and quantum decoherence [23]. The K2K (KEK-to-Kamioka) experiment [24,25], which was the first accelerator-based long-baseline neutrino oscillation experiment started in 1999, confirmed the atmospheric neutrino oscillation.

The solar neutrino problem is understood as due to the neutrino oscillation. The first direct evidence for the solar neutrino oscillation came in 2001 from the initial charged current result by SNO [26] (Sudbury Neutrino Observatory) combined with the Super-K result [27]. SNO used heavy water ($\mathrm{D_2O}$) and measured $^8\mathrm{B}$ solar neutrinos via charged current (CC: $\nu_e + \mathrm{d} \to e^- + \mathrm{p} + \mathrm{p}$) and neutral current (NC: $\nu_\ell + \mathrm{d} \to \nu_\ell + \mathrm{p} + \mathrm{n}$, where $\ell = e$, μ and τ) interactions as well as $\nu_\ell e^-$ scatterings. The measurement both of the CC and NC interactions is a key feature to solve the solar neutrino problem; if the deficit of the solar neutrino flux is caused by the neutrino oscillation, the solar neutrino fluxes measured by the CC and NC interactions would be significantly different. The SNO's NC measurement further strengthened the evidence for the solar neutrino oscillation [28,29].

So far, no direct evidence of an appearance mode has been found. For example, in the $\nu_\mu \to \nu_\tau$ oscillation, a deficit of the ν_μ flux was observed, but an appearance of the ν_τ was not. OPERA [30] (Oscillation Project with Emulsion-tRacking Apparatus) is to confirm the ν_τ appearance from the $\nu_\mu \to \nu_\tau$ oscillation. It is a 730-km-baseline experiment using the CNGS [31,32] (CERN Neutrinos to Gran Sasso) neutrino beam. They observed one ν_τ appearance candidate event [33] with emulsion cloud chambers.

1.2 Theory of the neutrino oscillation

The formalism of the neutrino oscillation is given in this section. Because it is not known whether the neutrino is of the Dirac or Majorana type, the mass term of the Lagrangian is considered both for the Dirac and Majorana cases in Sec. 1.2.1. Then, the probability of the neutrino oscillation in vacuum is calculated in Sec. 1.2.2. In most experimental conditions, neutrinos propagate in matter, and the effect of the propagation in matter is discussed in Sec. 1.2.3. The CP violation in the neutrino oscillation is also mentioned in Sec. 1.2.4.

1.2.1 Generation mixing of neutrinos

Case of Dirac neutrinos

Suppose that ν is the conventional Dirac field of a neutrino, and ν_L and ν_R are the left- and right-handed fields (two-component spinors), respectively, given by

$$\nu_L = \frac{1-\gamma_5}{2}\nu, \quad \nu_R = \frac{1+\gamma_5}{2}\nu. \tag{1.3}$$

ν_L and ν_R are eigenstates of the chiral transformation $\nu \to \gamma_5\nu$ [34–36] with eigenvalues of -1 and $+1$, respectively. In the Standard Model, the charged current weak interaction via a W^+ boson takes place only with ν_L, and the Lagrangian of the interaction is expressed as

$$\mathcal{L}_{int} = \frac{g}{\sqrt{2}} W^+_\mu (\bar{\nu}_{eL}\gamma^\mu e_L + \bar{\nu}_{\mu L}\gamma^\mu \mu_L + \bar{\nu}_\tau \gamma^\mu \tau_L) + \text{h.c.}, \tag{1.4}$$

where the neutrino which produces a charged lepton ℓ is notated as ν_ℓ ($\ell = e$, μ or τ), and ν_ℓ is the eigenstate of the weak interaction, or the flavor eigenstate. If ν_R exists, the Dirac mass term can be introduced into the Lagrangian as

$$\mathcal{L}_{mass} = -\bar{\nu}^\alpha_R m_{\alpha\beta} \nu^\beta_L + \text{h.c.}, \tag{1.5}$$

where $m_{\alpha\beta}$ is the mass matrix for the flavor eigenstate $\nu^{\alpha,\beta}$, and breaks the chirality. This mass term is diagonalized as follows:*

$$\begin{aligned} \mathcal{L}_{mass} &= -\bar{\nu}'_{iR} V^{i\alpha\dagger} m_{\alpha\beta} U^{\beta j} \nu'_{jL} + \text{h.c.} \\ &= -\bar{\nu}'_{iR} m^i \nu'_{iL} + \text{h.c.}, \end{aligned} \tag{1.6}$$

where ν'_i ($i = 1$, 2 or 3) is the mass eigenstate,† and m_i represents the mass of the ith generation neutrino. $U^{\ell i}$ and $V^{\ell i}$ are the unitary matrices representing the mass generation mixing of neutrinos; i.e. the flavor eigenstate ν_ℓ is a linear combination of the mass eigenstates of three (or more) massive neutrinos ν_i:

$$\nu^\ell_L = U^{\ell i} \nu'_{iL} \tag{1.7}$$

$$\nu^\ell_R = V^{\ell i} \nu'_{iR}. \tag{1.8}$$

The matrix U is often called the Pontecorvo-Maki-Nakagawa-Sakata (PMNS) or Maki-Nakagawa-Sakata (MNS) mixing matrix [37–39].

*The phases of ν'_i are chosen so that m_i is real and semipositive definite without loss of generality.

†Neutrinos which appear in a laboratory experiment are the flavor eigenstate ν_ℓ except in a neutrino mass experiment.

Case of Majorana neutrinos

The Majorana neutrino [40] is a self-conjugate neutrino, $\nu = \bar{\nu}$ except for helicity, and the helicity flip is caused by a mass term that violates lepton number. The mass term of Majorana neutrinos is written as

$$\mathcal{L}_{mass} = -\frac{1}{2}\nu_L^{\alpha T} C^{-1} m_{\alpha\beta} \nu_L^{\beta} + \text{h.c.} \tag{1.9}$$

This is diagonalized as

$$\begin{aligned}\mathcal{L}_{mass} &= -\frac{1}{2}\nu'_{iL} C^{-1} U^{i\alpha} m_{\alpha\beta} U^{\beta j} \nu'_{jL} + \text{h.c.} \\ &= -\frac{1}{2}\nu'_{iL} C^{-1} m^{i} \nu'_{iL} + \text{h.c.}\end{aligned} \tag{1.10}$$

where C denotes the charge conjugation.

Phases of the mixing matrix

In case of n neutrino flavors and n masses neutrinos, the $n \times n$ unitary mixing matrix U in Eq. 1.7 can be parametrized by $n(n-1)/2$ Euler angles and $n(n+1)/2$ phases. Among these phases, $n-1$ phases and an overall phase can be absorbed into the charged-lepton wave function in the weak interaction Lagrangian. In addition, $n-1$ phases can be absorbed into the neutrino wave function only in case of Dirac neutrinos. In case of Majorana neutrinos, the $n-1$ phases cannot be absorbed into the neutrino wave function because the mass term is of the form $\nu'^T U^T m U \nu'$ not as $\nu'^T V^\dagger m U \nu'$ for the Dirac case. Thus, the number of remaining phases is

$$\frac{(n-1)(n-2)}{2} \quad \text{(Dirac neutrinos)}, \tag{1.11}$$

$$\frac{n(n-1)}{2} \quad \text{(Majorana neutrinos)}. \tag{1.12}$$

The only remaining phases are physical and would give rise to the CP violation.

For $n = 3$, of the many possible parametrizations, the neutrino mixing matrix can be written as

$$U = \begin{pmatrix} c_{12}c_{13} & s_{12}c_{13} & s_{13}e^{-i\delta} \\ -s_{12}c_{23} - c_{12}s_{23}s_{13}e^{i\delta} & c_{12}c_{23} - s_{12}s_{23}s_{13}e^{i\delta} & s_{23}c_{13} \\ s_{12}s_{23} - c_{12}c_{23}s_{13}e^{i\delta} & -c_{12}s_{23} - s_{12}c_{23}s_{13}e^{i\delta} & c_{23}c_{13} \end{pmatrix} \begin{pmatrix} e^{i\alpha_1/2} & & \\ & e^{i\alpha_2/2} & \\ & & 1 \end{pmatrix}, \tag{1.13}$$

where $s_{ij} = \sin\theta_{ij}$, $c_{ij} = \cos\theta_{ij}$, three θ_{ij} are referred to as the mixing angles, δ is the Dirac CP-violating phase and α_1 and α_2 are the Majorana CP-violating phases. θ_{ij} are chosen to lie in the first quadrant. Apart from the Majorana phases, the same parametrization can be taken for the CKM (Cabibbo-Kobayashi-Maskawa) quark mixing matrix [41, 42]. This neutrino mixing matrix can be written as a product of three rotations, each of which is described by one of the mixing angles, and the Majorana phases:

$$U = \begin{pmatrix} 1 & 0 & 0 \\ 0 & c_{23} & s_{23} \\ 0 & -s_{23} & c_{23} \end{pmatrix} \begin{pmatrix} c_{13} & 0 & s_{13}e^{-i\delta} \\ 0 & 1 & 0 \\ -s_{13}e^{i\delta} & 0 & c_{13} \end{pmatrix} \begin{pmatrix} c_{12} & s_{12} & 0 \\ -s_{12} & c_{12} & 0 \\ 0 & 0 & 1 \end{pmatrix} \begin{pmatrix} e^{i\alpha_1/2} & & \\ & e^{i\alpha_2/2} & \\ & & 1 \end{pmatrix}. \tag{1.14}$$

1.2.2 Neutrino oscillation in vacuum

As indicated in Eq. 1.5 and 1.9, in the presence of off-diagonal components of the neutrino mass matrix, a neutrino of a flavor eigenstate $|\nu^\alpha\rangle$ may change into another flavor eigenstate $|\nu^\beta\rangle$ in flight [38, 43]. After a time interval of t, $|\nu^\alpha\rangle_t$ is given by

$$|\nu^\alpha\rangle_t = \sum_i U^{\alpha i} e^{-iE_i t} |\nu'_i\rangle \,, \tag{1.15}$$

where E_i is the energy of the mass eigenstate $|\nu_i'\rangle$. E_i is expanded as $E_i = \sqrt{p^2 + m_i^2} \simeq p + m_i^2/2p \simeq p + m_i^2/2E$ under the condition that every mass eigenstate has the same 3-momentum $|\mathbf{p}_i| = p$ [43, 44] and $E = p \gg m_i$. Then, Eq. 1.15 is written as

$$\begin{aligned}
|\nu^\alpha\rangle_t &\simeq e^{-ipt} \sum_i U^{\alpha i} e^{-im_i^2 t/2E} |\nu_i'\rangle \\
&= e^{-ipt} U \begin{pmatrix} e^{-im_1^2 t/2E} & & \\ & e^{-im_2^2 t/2E} & \\ & & \ddots \end{pmatrix} U^\dagger |\nu^\beta\rangle \\
&= e^{-ipt} (e^{-im^\dagger m t/2E})_{\alpha\beta} |\nu^\beta\rangle \,, \qquad (1.16)
\end{aligned}$$

since $U^\dagger m^\dagger m U = m_{diag}^2$. This is a solution of the Schrödinger equation,

$$i \frac{\mathrm{d}}{\mathrm{d}t} |\nu^\alpha\rangle_t \simeq \frac{m^\dagger m}{2E} |\nu^\alpha\rangle \,, \qquad (1.17)$$

despite of the phase factor e^{-ipt}. The transition amplitude is

$$\langle \nu_\beta | \nu_\alpha \rangle_t = \left[\exp\left(i \frac{m^\dagger m}{2E} t \right) \right]_{\alpha\beta} . \qquad (1.18)$$

Because the mass term is $m^\dagger m = U m_{diag}^2 U^\dagger$, this amplitude does not differ between the Dirac and Majorana cases. Therefore, the neutrino mass type can be left out of account in neutrino oscillation experiments.[‡] The transition probability is calculated as

$$\begin{aligned}
P(\nu^\alpha \to \nu^\beta) &= |\, \langle \nu^\beta | \nu^\alpha \rangle_t \,|^2 \\
&= \left| \sum_i U^{\alpha i} e^{i m_i^2 t/2E} U^{i\beta\dagger} \right|^2 \\
&= \sum_{i,j} U_{\alpha i} U_{\beta i}^* U_{\alpha j}^* U_{\beta j} e^{i(m_i^2 - m_j^2)t/2E} \\
&= \sum_{i,j} |U_{\alpha i} U_{\beta i} U_{\alpha j} U_{\beta j}| e^{i\phi_{\alpha\beta ij}} (e^{i\Delta m_{ij}^2 t/2E} - 1) + \delta_{\alpha\beta} \\
&= 2 \sum_{j>i} |U_{\alpha i} U_{\beta i} U_{\alpha j} U_{\beta j}| \left\{ \cos\left(\frac{\Delta m_{ij}^2}{2E} t + \phi_{\alpha\beta ij} \right) - \cos \phi_{\alpha\beta ij} \right\} + \delta_{\alpha\beta}, \qquad (1.19)
\end{aligned}$$

where $\phi_{\alpha\beta ij} = -\phi_{\alpha\beta ji} = \arg(U_{\alpha i} U_{\beta i}^* U_{\alpha j}^* U_{\beta j})$ and $\Delta m_{ij}^2 = m_i^2 - m_j^2$. In this equation, the time interval t can be replaced with the neutrino travel distance L ($= ct$) since the neutrinos are relativistic. Equation 1.19 points that the neutrino oscillation occurs only when at least two neutrinos are not degenerate in mass ($m_i \neq m_j$) and the lepton mixing takes place ($U \neq I$).

Neutrino oscillation between two generations

For the mixing between two generations (two-flavor, active neutrino oscillation), the mixing matrix U can be parametrized as

$$U = \begin{pmatrix} \cos\theta & \sin\theta \\ -\sin\theta & \cos\theta \end{pmatrix} . \qquad (1.20)$$

[‡]The Majorana mass can be distinguished by detecting neutrinoless double beta decays [45, 46].

In this case, $\phi_{\alpha\beta ij} = \arg(U_{\alpha i}U^*_{\beta i}U^*_{\alpha j}U_{\beta j}) = 0$, and the transition probability in Eq. 1.19 becomes

$$P(\nu^\alpha \to \nu^\beta) = \begin{cases} 1 - \sin^2 2\theta \sin^2\left(\dfrac{\Delta m^2}{4E}L\right) & (\alpha = \beta) \\ \sin^2 2\theta \sin^2\left(\dfrac{\Delta m^2}{4E}L\right) & (\alpha \neq \beta). \end{cases} \tag{1.21}$$

The two-flavor oscillation is a good approximation of the three-flavor oscillation when one of the three mixing angles is negligibly small compared with the others.

Neutrino oscillation between three generations

For the mixing between three generations, the neutrino oscillations are parametrized by three mixing angles θ_{12}, θ_{23} and θ_{13}, two mass differences[§] Δm^2_{21} and Δm^2_{32} (since $\Delta m^2_{21} + \Delta m^2_{32} + \Delta m^2_{13} = 0$), and a CP-violating phase δ.

From the experimental data described in Sec. 1.3.1, $\Delta m^2_{21} \ll |\Delta m^2_{31}| \simeq |\Delta m^2_{32}|$. Therefore, the effect on the neutrino oscillation due to Δm^2_{21} can be disregarded for $E/L \gg \Delta m^2_{21}$. Then, the transition probability is calculated from Eq. 1.19 as

$$P(\nu_\alpha \to \nu_\beta) \simeq 4|U_{\alpha 3}|^2(|U_{\beta 3}|^2 - \delta_{\alpha\beta}) \sin^2\left(\frac{\Delta m^2_{31}}{4E}L\right) + \delta_{\alpha\beta}. \tag{1.22}$$

For the $\nu_\mu \to \nu_e$ oscillation, since $\Delta m^2_{31} \simeq \Delta m^2_{32}$,

$$P(\nu_\mu \to \nu_e) \simeq \sin^2 2\theta_{13} \sin^2\theta_{23} \sin^2\left(\frac{\Delta m^2_{32}}{4E}L\right). \tag{1.23}$$

For the $\nu_\mu \to \nu_\mu$ oscillation, if $\theta_{13} \simeq 0$, the transition probability becomes nearly equal to the two-flavor oscillation case (Eq. 1.21);

$$P(\nu_\mu \to \nu_\mu) \simeq 1 - \sin^2 2\theta_{23} \sin^2\left(\frac{\Delta m^2_{32}}{4E}L\right). \tag{1.24}$$

The $\nu_e \to \nu_e$ oscillation (with $E/L \gg \Delta m^2_{21}$) can be also considered as the two-flavor oscillation;

$$P(\nu_e \to \nu_e) \simeq 1 - \sin^2 2\theta_{13} \sin^2\left(\frac{\Delta m^2_{32}}{4E}L\right). \tag{1.25}$$

Here, the phase of the oscillation is explicitly written as

$$\frac{\Delta m^2}{4E\hbar c}L = 1.267 \cdot \frac{\Delta m^2\ [\mathrm{eV}^2]}{E\ [\mathrm{GeV}]} \cdot L\ [\mathrm{km}]. \tag{1.26}$$

1.2.3 Matter effect on neutrino propagation

When neutrinos travel through matter (e.g. in the sun, the earth or a supernova), their propagation can be significantly affected by coherent forward-scatterings between the neutrinos and matter [47]. This is essentially due to difference of potentials which ν_e, ν_μ and ν_τ feel in matter; ν_e interacts with electrons via both the neutral and charged currents, whereas ν_μ and ν_τ interact with electrons only via the neutral current. As a result, the probability for changing flavors in matter can be rather different than in vacuum, which is known as the MSW (Mikheyev-Smirnov-Wolfenstein) effect [48]. The other scatterings are not of interest and have a negligible effect:

[§]The numbering of the neutrinos with the mass m_i is arbitrary. Just for convenience, the neutrinos are numbered so that $m_1 < m_2$ to make $\Delta m^2_{21} > 0$.

such as incoherent elastic and quasi-elastic scatterings, in which the states of the initial particles change in the process (destroying the coherence between the neutrino states),[¶] and forward ν-p,n elastic scatterings, which amplitude is equal independent from neutrino flavors and does not contribute to the difference of interest.[‖]

If the effective interaction in matter $H_{\rm eff} = G_F/\sqrt{2} \cdot \bar{\nu}_\ell \gamma_\mu (1-\gamma_5) \nu_\ell \bar{e} \gamma_\mu (1-\gamma_5) e$ exists, it gives an extra potential V to the ν_ℓ energy E in Eq. 1.15, i.e. $E = \sqrt{p^2+m^2} + V$. V for a $\nu_\ell e$ interaction is given by

$$V(\nu_\ell, e) = \sqrt{2} G_F c_V n_e = \begin{cases} \pm\sqrt{2} G_F (+1/2 + 2\sin^2\theta_W) n_e & (\text{for } \nu_e) \\ \pm\sqrt{2} G_F (-1/2 + 2\sin^2\theta_W) n_e & (\text{for } \nu_\mu \text{ and } \nu_\tau), \end{cases} \tag{1.27}$$

where G_F is the Fermi coupling constant, $c_V = \rho g_V + 1$ for $\nu_e e^-$ and $c_V = \rho g_V$ for $\nu_{\mu(\tau)} e^-$, $\rho = 1$, $g_V = -1/2 + 2\sin^2\theta_W$, θ_W is the Weinberg angle, n_e is the electron number density when matter is at rest, and the $\pm$ sign in front refers to ν $(+)$ and $\bar{\nu}$ $(-)$. Hence, the potential difference is $V(\nu_e, e) - V(\nu_{\mu(\tau)}, e) = \sqrt{2} G_F n_e$. Therefore, the time evolution of the neutrino wave function is written as

$$i\frac{\rm d}{{\rm d}t}\begin{pmatrix}\nu_e \\ \nu_\mu\end{pmatrix} = \begin{pmatrix} -\dfrac{\Delta m^2}{4E}\cos 2\theta + \sqrt{2} G_F n_e & \dfrac{\Delta m^2}{4E}\sin 2\theta \\ \dfrac{\Delta m^2}{4E}\sin 2\theta & \dfrac{\Delta m^2}{4E}\cos 2\theta \end{pmatrix} \begin{pmatrix}\nu_e \\ \nu_\mu\end{pmatrix}, \tag{1.28}$$

instead of Eq. 1.17. The Hamiltonian in this equation is diagonalized by

$$\begin{pmatrix}\nu_e \\ \nu_\mu\end{pmatrix} = U \begin{pmatrix}\tilde{\nu}_1 \\ \tilde{\nu}_2\end{pmatrix} = \begin{pmatrix} \cos\tilde{\theta} & \sin\tilde{\theta} \\ -\sin\tilde{\theta} & \cos\tilde{\theta} \end{pmatrix} \begin{pmatrix}\tilde{\nu}_1 \\ \tilde{\nu}_2\end{pmatrix}, \tag{1.29}$$

$$\cos 2\tilde{\theta} = \frac{-A/\Delta m^2 + \cos 2\theta}{\sqrt{(A/\Delta m^2 - \cos 2\theta)^2 + \sin^2 2\theta}}, \tag{1.30}$$

$$\sin 2\tilde{\theta} = \frac{\sin 2\theta}{\sqrt{(A/\Delta m^2 - \cos 2\theta)^2 + \sin^2 2\theta}}, \tag{1.31}$$

$$A = 2\sqrt{2} E G_F n_e, \tag{1.32}$$

where $\tilde{\nu}$ is the energy eigenstate in matter, and the energy eigenvalue is

$$\tilde{m}^2_{1,2} = \frac{A}{2} \mp \frac{1}{2}\sqrt{(A - \Delta m^2 \cos 2\theta)^2 + (\Delta m^2)^2 \sin^2 2\theta}. \tag{1.33}$$

As Eq. 1.31 indicates, the dependence of $\sin^2 2\tilde{\theta}$ on n_e has a resonance character [48]; the resonance occurs at $A/\Delta m^2 = \cos 2\theta$, i.e.

$$n_e = n_e^{res} \equiv \frac{1}{2\sqrt{2} G_F} \frac{\Delta m^2}{E} \cos 2\theta. \tag{1.34}$$

This is called the resonance condition, and n_e^{res} is called the resonance density [48, 53]. At $n_e = n_e^{res}$, $\tilde{\theta} = \pi/4$ and two neutrinos mix maximally, independent of the value of $\sin^2 2\theta$ if $\Delta m^2 \cos 2\theta > 0$. This implies that the presence of matter can lead to a strong enhancement of the probability of flavor changing even when the $\nu_e \leftrightarrow \nu_\mu$ oscillation in vacuum is suppressed due to a small value of $\sin^2 2\theta$. In particular, in solar neutrino experiments and in long-baseline accelerator experiments to measure the $\nu_\mu \to \nu_e$ oscillation, the effect of matter (the sun and the earth,

[¶] These processes are important, however, for the supernova neutrinos [49].

[‖] The weak interaction of the flavour (anti-)neutrinos in the Standard Model is assumed (for alternatives see Ref. [47, 50–52]).

respectively) has to be taken into account. For the earth (density $\rho = 3.5$–13 g/cm^3 [54–57]), the resonance condition (Eq. 1.34) is satisfied if

$$\Delta m^2 \approx 0.8 \times 10^{-6}\ (\mathrm{eV}^2) \cdot \rho Y_e\ (\mathrm{g/cm}^3) \cdot E/10\ (\mathrm{MeV}) \cdot \sec 2\theta, \tag{1.35}$$

where $Y_e = 1/2$ is the electron yield, or the electron number per atomic number. Given $\rho \approx 3$ g/cm^3 and a ν_μ beam with 1 GeV energy, the effective mass squared difference in the earth is calculated as $\Delta m^2 \approx 2 \times 10^{-4}$ eV^2. It is not too small compared with $|\Delta m^2_{32}| \approx 2 \times 10^{-3}$ eV^2.

1.2.4 CP violation in the neutrino oscillation

If the CP invariance holds, $\nu_\alpha \leftrightarrow \nu_\beta$ and $\bar{\nu}_\alpha \leftrightarrow \bar{\nu}_\beta$ oscillations should be equal [58]:

$$P(\nu_\alpha \to \nu_\beta) = P(\bar{\nu}_\alpha \to \bar{\nu}_\beta) = P(\nu_\beta \to \nu_\alpha). \tag{1.36}$$

From Eq. 1.18, this condition is represented by

$$(m^\dagger m)^T = m^\dagger m, \tag{1.37}$$

or from Eq. 1.19,

$$\phi_{\alpha\beta ij} = 0. \tag{1.38}$$

Hence, the Dirac phase left in the mixing matrix is the source of the CP violation in the neutrino oscillation, and the Majorana phases do not contribute to the CP violation. In other words, the CP violation may occur when the number of neutrino generations $n \geq 3$ from Eq. 1.11.

In the neutrino oscillation in vacuum ($n = 3$), the CP and T violating parts are equal and are given by [59–61]

$$\begin{aligned}
\Delta P &= P(\nu_\alpha \to \nu_\beta) - P(\bar{\nu}_\alpha \to \bar{\nu}_\beta) = P(\nu_\alpha \to \nu_\beta) - P(\nu_\beta \to \nu_\alpha) \\
&= -4(\mathrm{Im}U_{\beta 1}U^*_{\beta 2}U^*_{\alpha 1}U_{\alpha 2}) \left\{ \sin\left(\frac{\Delta m^2_{21}}{2E}L\right) + \sin\left(\frac{\Delta m^2_{32}}{2E}L\right) + \sin\left(\frac{\Delta m^2_{13}}{2E}L\right) \right\} \\
&= 4 \cdot (-\mathrm{Im}U_{\beta 1}U^*_{\beta 2}U^*_{\alpha 1}U_{\alpha 2}) \cdot \left\{ -4\sin\left(\frac{\Delta m^2_{21}}{4E}L\right) \sin\left(\frac{\Delta m^2_{32}}{4E}L\right) \sin\left(\frac{\Delta m^2_{13}}{4E}L\right) \right\} \\
&= 4Jf,
\end{aligned} \tag{1.39}$$

where J and f are substituted for the second and last factors in the third line. J is defined as $J \equiv \mathrm{Im}(U_{ik}U_{jl}U^*_{il}U^*_{jk})$ [62, 63]; (i, j) and (k, l) take $(1, 2)$, $(2, 3)$ or $(3, 1)$ independently. J with any combinations of (i, j, k, l) is identical except for the sign due to unitarity of U; $J = \pm c_{12}c^2_{13}c_{23}s_{12}s_{23}s_{13}\sin\delta$. Therefore, the effect of the CP violation ΔP does not depend on the choice of α and β. Recent studies [64–67] argue that ΔP will be visible in long-baseline neutrino oscillation experiments if $|U_{e3}|$ and J are not too small.

In a practical experiment, the CP violation ($P(\nu_\mu \to \nu_e) - P(\bar{\nu}_\mu \to \bar{\nu}_e)$) differs from the T violation ($P(\nu_\mu \to \nu_e) - P(\nu_e \to \nu_\mu)$) because of the matter effect, which acts as the external field that breaks CP [68]. In particular, for a long-baseline experiment, the matter effect may compete with the intrinsic CP violation [66] since the effective Δm^2 in the earth is not too small compared with $|\Delta m^2_{32}|$ as discussed in Sec. 1.2.3. The CP-violating effect of the earth is given by [66]

$$\begin{aligned}
\Delta P^m_{\nu_\mu \to \nu_e} &= P(\nu_\mu \to \nu_e) - P(\bar{\nu}_\mu \to \bar{\nu}_e) \\
&= |U_{e3}U_{\mu 3}|^2(1 - 2|U_{e3}|^2)\frac{4AL}{E}\left\{ \frac{4E}{\Delta m^2_{31}L}\sin^2\left(\frac{\Delta m^2_{31}}{4E}L\right) - \frac{1}{2}\sin\left(\frac{\Delta m^2_{31}}{2E}L\right) \right\},
\end{aligned} \tag{1.40}$$

where A is defined in Eq. 1.32 representing the matter effect. On the other hand, the intrinsic CP-violating effect is given from Eq. 1.39 as [69]

$$\Delta P_{\nu_\mu \to \nu_e} \simeq 2 \frac{\sqrt{\sin^2 2\theta_{12}}\sqrt{\sin^2 2\theta_{23}}|U_{e3}|}{1-|U_{e3}|^2} \sin\phi \cdot \frac{\Delta m^2_{21} L}{2E} \sin^2\left(\frac{\Delta m^2_{31} L}{4E}\right), \tag{1.41}$$

where $\Delta m^2_{31} \simeq \Delta m^2_{32}$ and $\Delta m^2_{21}/2E \ll 1$ are assumed.

1.3 Neutrino oscillation experiments

1.3.1 Present understanding of the neutrino oscillation

In the case of three-neutrino mixing with $0 < \Delta m^2_{21} \ll |\Delta m^2_{31(32)}|$ and $|U_{e3}|^2 = |\sin\theta_{13}|^2 \ll 1$, the mixing angles θ_{12} and θ_{23} are associated with two decoupled two-flavor oscillations: the solar ν_e and the dominant atmospheric ν_μ (and $\bar{\nu}_\mu$) oscillations, respectively. They are often called "solar" and "atmospheric" neutrino mixing angles, and are denoted as $\theta_{12} = \theta_\odot$ and $\theta_{23} = \theta_{atm}$. Similarly, Δm^2_{21} and Δm^2_{31} are often referred to as the "solar" and "atmospheric" neutrino mass squared differences, respectively, and $\Delta m^2_{21} = \Delta m^2_\odot$ and $\Delta m^2_{31} = \Delta m^2_{atm}$.

Wide ranges of Δm^2 have been probed by various neutrino oscillation experiments as shown in Fig. 1.1. According to the neutrino energy and travel distance, sensitivities (figure of merit) of experiments to Δm^2 are different (see Table 1.1).

Measurements of $\Delta m^2_\odot$ and $\theta_\odot$

$\Delta m^2_\odot$ and $\theta_\odot$ have been measured by solar and reactor neutrino experiments. The best-fit values are $\Delta m^2_\odot = 5.89^{+2.13}_{-2.16} \times 10^{-5}$ eV^2 and $\tan^2\theta_\odot = 0.457^{+0.038}_{-0.041}$ [87] (left plot in Fig. 1.2) in a two-neutrino oscillation analysis including all the solar neutrino data (the global solar data): SNO's LETA (low-energy-threshold analysis) survival probability day/night curves [87], SNO Phase III integral rates [29], Cl [88], SAGE [17], Gallex/GNO [15, 16], Borexino [89], Super-Kamiokande Phase I (SK-I) zenith [90], and SK-II day/night spectra [85]. Combining the global solar data and the KamLAND (Kamioka Liquid scintillator Anti-Neutrino Detector; a long-baseline reactor neutrino experiment) data [77] on an assumption of the CPT invariance, the best-fit values are $\Delta m^2_\odot = 7.59^{+0.20}_{-0.21} \times 10^{-5}$ eV^2 and $\tan^2\theta_\odot = 0.457^{+0.040}_{-0.029}$ [87] (right plot in Fig. 1.2). These best-fit parameters are summarized in Table 1.2.

Measurements of $|\Delta m^2_{atm}|$ and θ_{atm}

$|\Delta m^2_{atm}|$ and θ_{atm} have been measured by atmospheric and accelerator neutrino experiments. The Super-K atmospheric neutrino data provided the best θ_{atm} measurement due to its high statistics as shown in Fig. 1.3. However, there is ambiguity in the travel distance of atmospheric neutrinos, resulting in the large systematic error of $|\Delta m^2_{atm}|$. In the zenith angle analysis [91], 15012 events were used, including fully-contained, partially-contained and up-going muon events. The 90% C.L. (confidence level) allowed region is obtained as $1.5 \times 10^{-3} < |\Delta m^2_{atm}| < 3.4 \times 10^{-3}$ eV^2 and $\sin^2 2\theta_{atm} > 0.92$, and the best-fit values are $|\Delta m^2_{atm}| = 2.1 \times 10^{-3}$ eV^2 and $\sin^2 2\theta_{atm} = 1.00$. In the L/E analysis [21], 2726 μ-like events were used. The 90% C.L. allowed region is obtained as $1.9 \times 10^{-3} < |\Delta m^2_{atm}| < 3.0 \times 10^{-3}$ eV^2 and $\sin^2 2\theta_{atm} > 0.90$, and the best-fit values are $|\Delta m^2_{atm}| = 2.4 \times 10^{-3}$ eV^2 and $\sin^2 2\theta_{atm} = 1.00$.

On the other hand, in an accelerator neutrino experiment, where the travel distance is fixed, $|\Delta m^2_{atm}|$ can be precisely measured. In the K2K experiment, a wide-band muon neutrino beam ($E_\nu \sim 1.3$ GeV) was produced by the 12 GeV KEK-PS (proton synchrotron) and was measured by Super-K. The distance from KEK to Super-K was 250 km. With 0.92×10^{20} POT (protons

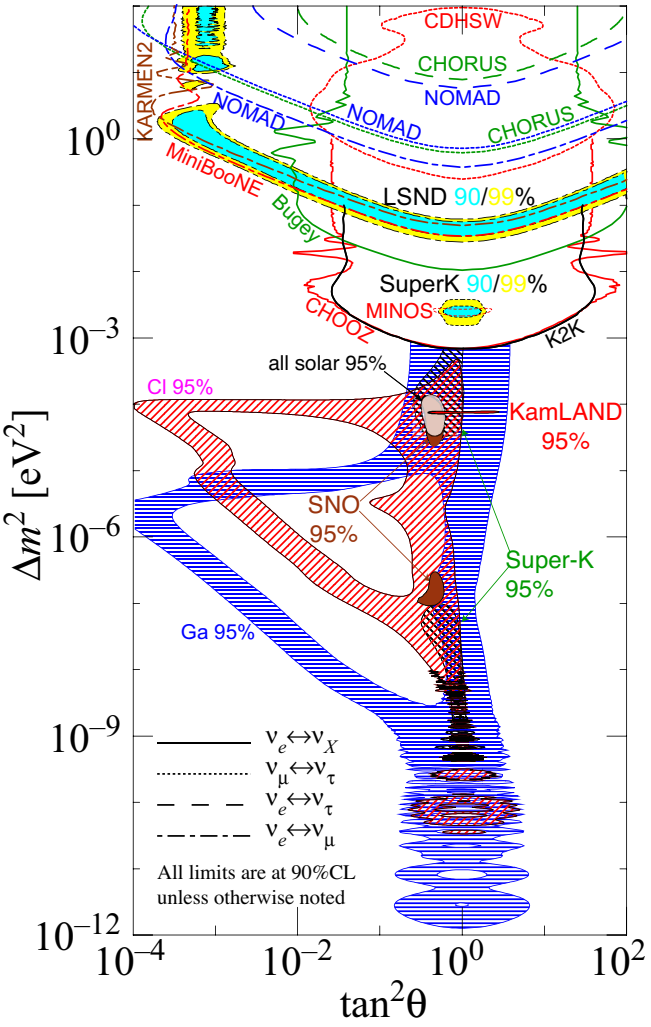

Figure 1.1: Regions of the neutrino squared-mass difference and mixing angle favored (hatched regions) or excluded (enclosed regions by lines) by various experiments: BNL E776 [70], Bugey [71], CDHSW [72], CHOOZ [73], CHORUS [74], Cl (Homestake) [75], Ga (SAGE and GALLEX) [76], KamLAND [77], KARMEN2 [78], K2K [79], LSND [80], Mini-BooNE [81], MINOS [82], NOMAD [83, 84], SNO [29], Super-K (solar neutrino) [85] and Super-K (atmospheric neutrino) [86]. CL stands for the confidence level. This figure was contributed by H. Murayama, taken from `http://hitoshi.berkeley.edu/neutrino/`.

Table 1.1: Sensitivity of different oscillation experiments to Δm^2. $\bar{E}$ is the average neutrino energy, L is the source-detector distance and $\min[\Delta m^2]$ (eV^2) $\sim 2\bar{E}/L \simeq \bar{E}(\text{GeV})/L(\text{km})$ is the sensitivity.

ν source	ν flavor from the source	$\bar{E}$ (GeV)	L (km)	$\min[\Delta m^2]$ (eV^2)
Accelerator (short baseline)	ν_μ, $\bar{\nu}_\mu$	$\sim$1	1	$\sim$1
Accelerator (long baseline)	ν_μ, $\bar{\nu}_\mu$	$\sim$1	1000	$\sim 10^{-3}$
Atmospheric ν	$\nu_{\mu,e}$, $\bar{\nu}_{\mu,e}$	$\sim$1	10^4	$\sim 10^{-4}$
Reactor (short baseline)	$\bar{\nu}_e$	$\sim 10^{-3}$	1	$\sim 10^{-3}$
Reactor (long baseline)	$\bar{\nu}_e$	$\sim 10^{-3}$	100	$\sim 10^{-5}$
Sun	ν_e	$\sim 10^{-3}$	1.5×10^8	$\sim 10^{-11}$

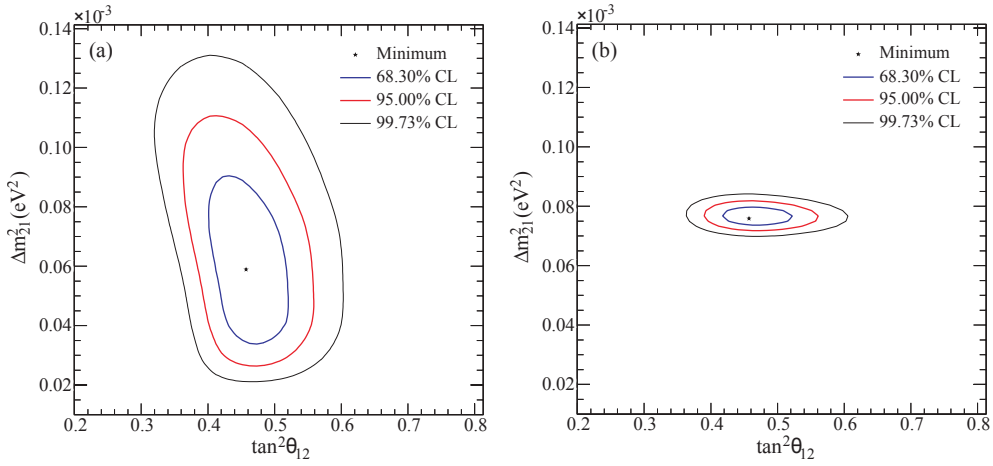

Figure 1.2: Contours of the solar neutrino oscillation parameters for (a) the global solar data and (b) the global solar + KamLAND data. This figure comes from Ref. [87].

Table 1.2: The best-fit values of $\Delta m^2_{\odot}$ and $\tan^2\theta_{\odot}$ from two-flavor oscillation analyses.

Data	$\Delta m^2_{\odot}$ (eV^2)	$\tan^2\theta_{\odot}$
Global solar [87]	$5.89^{+2.13}_{-2.16} \times 10^{-5}$	$0.457^{+0.038}_{-0.041}$
Global solar + KamLAND [87]	$7.59^{+0.20}_{-0.21} \times 10^{-5}$	$0.457^{+0.040}_{-0.029}$

on target), 112 beam-related fully-contained fiducial volume events were observed in Super-K, while the expectation without oscillation was $158.1^{+9.2}_{-8.6}$ [92]. The allowed $|\Delta m^2_{atm}|$ region at $\sin^2 2\theta_{atm} = 1$ and 90% C.L. is (1.9–3.5) $\times 10^{-3}$ eV^2 with the best-fit value of $|\Delta m^2_{atm}| = 2.8 \times 10^{-3}$ eV^2.

MINOS [93] (Main Injector Neutrino Oscillation Search) is the second accelerator-based long-baseline neutrino oscillation experiment. The muon neutrino beam is produced by the 120 GeV proton beam from the NuMI [94] (Neutrinos at the Main Injector) facility. As the far detector, MINOS uses a 5.4 kt (total mass) iron-scintillator tracking calorimeter with a toroidal magnetic field. The baseline distance is 735 km. With 3.36×10^{20} POT, 848 charged current events were observed in the far detector, while the expectation without oscillation was 1065 ± 60(sys.) [82]. They reported $|\Delta m^2_{atm}| = (2.43 \pm 0.13) \times 10^{-3}$ eV^2 at 68% C.L. and $\sin^2 2\theta_{atm} > 0.90$ at 90% C.L. The results of these experiments can be compared in Fig. 1.3 and Table 1.3.

Measurements of θ_{13}

Short-baseline reactor neutrino experiments are sensitive to the oscillation around $|\Delta m^2_{atm}|$ (see Table 1.1). Therefore, from Eq. 1.25, θ_{13} can be directly measured in the $\bar{\nu}_e \to \bar{\nu}_x$ ($x = \mu$ or τ) oscillation. CHOOZ [73,97] was the first experiment to measure θ_{13}. It measured $\bar{\nu}_e$ from nuclear reactors with a 5 ton target filled with 0.09% gadolinium loaded liquid scintillator. No evidence for $\bar{\nu}_e$ disappearance was found, and they set a 90% C.L. upper limit as $\sin^2 2\theta_{13} < 0.15$ at $|\Delta m^2_{atm}| = 2.43 \times 10^{-3}$ eV^2 [73], which is so far the most significant limit on θ_{13} directly measured. A consistent result with CHOOZ was reported by the Palo Verde reactor experiment [98].

In accelerator neutrino experiments, θ_{13} can also be measured via the $\nu_\mu \to \nu_e$ oscillation (see Eq. 1.23). K2K searched for $\nu_\mu \to \nu_e$ appearance signals, but no evidence was found. They

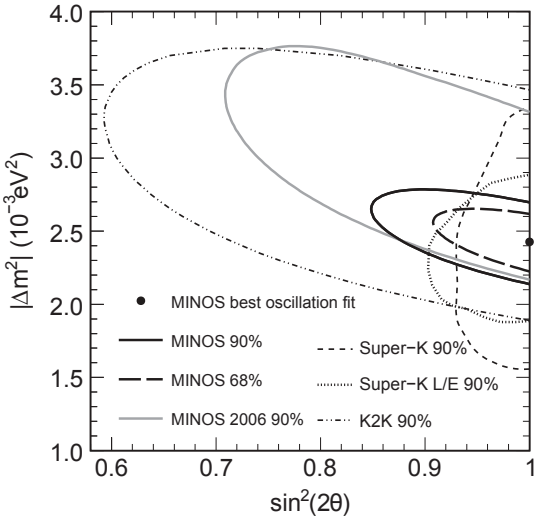

Figure 1.3: Contours of the atmospheric neutrino oscillation parameters for the MINOS [82, 95, 96], K2K [92] and Super-K atmospheric neutrino [21, 91] data. This figure comes from Ref. [82].

Table 1.3: The best-fit values of $|\Delta m^2_{atm}|$ at $\sin^2 2\theta_{atm} = 1$ and the allowed regions at 90% C.L. from two-flavor oscillation analyses. The MINOS allowed $|\Delta m^2_{atm}|$ region is at 68% C.L.

Data	$\lvert\Delta m^2_{atm}\rvert$ (eV^2)	Allowed $\lvert\Delta m^2_{atm}\rvert$ (eV^2)	Allowed $\sin^2 2\theta_{atm}$
Super-K ν_{atm} (zenith) [91]	2.1×10^{-3}	$(1.5\text{–}3.4) \times 10^{-3}$	> 0.92
Super-K ν_{atm} (L/E) [21]	2.4×10^{-3}	$(1.9\text{–}3.0) \times 10^{-3}$	> 0.90
K2K [92]	2.8×10^{-3}	$(1.9\text{–}3.5) \times 10^{-3}$	> 0.59
MINOS [82]	2.43×10^{-3}	$(2.30\text{–}2.56) \times 10^{-3}$ (68%)	> 0.85

obtained a 90% C.L. upper limit as $\sin^2 2\theta_{13} < 0.26$ at $|\Delta m^2_{atm}| = 2.8 \times 10^{-3}$ eV^2 assuming $\theta_{23} = \pi/4$ and $\delta_{\rm CP} = 0$ [79].

Recently, MINOS reported a new result on the $\nu_\mu \to \nu_e$ oscillation [99]; they observed 54 ν_e appearance candidate events while the expected number of background events was $49.1 \pm 7.0(\text{sta.}) \pm 2.7(\text{sys.})$. That results in a 90% C.L. upper limit of $2\sin^2 2\theta_{13}\sin^2\theta_{23} < 0.12$ at $\delta_{\rm CP} = 0$ for the normal hierarchy. This result represents the best constraint on θ_{13} for nearly all values of $\delta_{\rm CP}$ assuming the normal mass hierarchy and $\sin^2 2\theta_{23} = 1$.

Atmospheric and solar neutrino experiments are also sensitive to θ_{13} through sub-leading effects in the three-flavor oscillation framework. With the SK-I atmospheric neutrino data, θ_{13} and θ_{23} are constrained to $\sin^2\theta_{13} < 0.14$ and $0.37 < \sin^2\theta_{23} < 0.65$ for the normal mass hierarchy, and $\sin^2\theta_{13} < 0.27$ and $0.37 < \sin^2\theta_{23} < 0.69$ for the inverted mass hierarchy at 90% C.L [100]. With the global solar and KamLAND data, the best-fit value of $\sin^2\theta_{13} = 2.00^{+2.09}_{-1.63} \times 10^{-2}$ is obtained [87]. This implies an upper limit of $\sin^2\theta_{13} < 0.057$ at 90% C.L. [87]

As described above, the size of θ_{13} has not been determined yet. The current knowledge of θ_{13} is summarized in Table 1.4. A preference for $\theta_{13} > 0$ is implied from a global analysis of all available neutrino oscillation data as shown in Fig. 1.4: at 90% C.L., $\sin^2\theta_{13} = 0.016 \pm 0.010$ [101] as of 2008, and $\sin^2\theta_{13} = 0.02 \pm 0.01$ [102] as of 2009 including the MINOS ν_e appearance result [103].

Table 1.4: Upper limit of θ_{13} (at $|\Delta m^2_{atm}| = 2.43 \times 10^{-3}$ eV^2 for CHOOZ, at $|\Delta m^2_{atm}| = 2.8 \times 10^{-3}$ eV^2 for K2K, and at $\delta_{\rm CP} = 0$ and for the normal mass hierarchy for MINOS). The value listed in the last column is the upper limit of θ_{13} in degrees (at $\theta_{23} = 45°$ for MINOS).

Data	θ_{13} upper limit (90% C.L.)	
CHOOZ [73]	$\sin^2 2\theta_{13} < 0.15$	$\theta_{13} < 11.4°$
K2K [79]	$\sin^2 2\theta_{13} < 0.26$	$\theta_{13} < 15.4°$
MINOS [99]	$2\sin^2 2\theta_{13}\sin^2\theta_{23} < 0.12$	$\theta_{13} < 10.2°$
Super-K ν_{atm} [100]	$\sin^2\theta_{13} < 0.14$ (normal mass hierarchy)	$\theta_{13} < 22.0°$
	$\sin^2\theta_{13} < 0.27$ (inverted mass hierarchy)	$\theta_{13} < 31.3°$
Global solar + KamLAND [87]	$\sin^2\theta_{13} < 0.057$	$\theta_{13} < 13.9°$
Global data 2009 [102]	$\sin^2\theta_{13} = 0.02 \pm 0.01$	$5.7 < \theta_{13} < 10.0°$

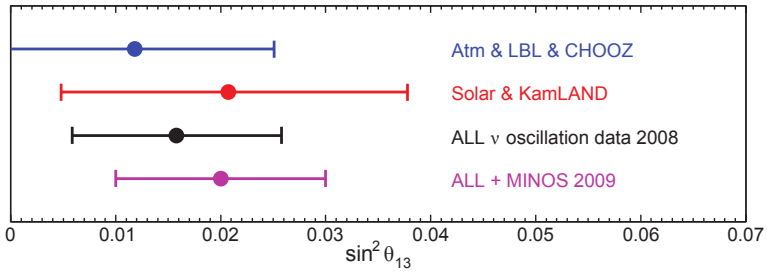

Figure 1.4: Ranges of $\sin^2\theta_{13}$ (at the 1σ level) preferred by different data sets and combinations. LBL stands for long-baseline accelerator experiments. This figure comes from Ref. [102].

1.3.2 Outlook for the neutrino oscillation physics

At present, questions on the neutrino physics to be answered are the followings:

1. Origin of the neutrino mass?
   - The absolute neutrino mass scale?
   - Why is the observed neutrino mass so small?
2. Dirac or Majorana, of massive neutrinos?
3. Existence of sterile neutrinos?
4. Neutrino mass hierarchy (sign of Δm^2_{31})?
5. Explanation for the neutrino mixing scheme?
6. The size of the CP violating phase δ?

The questions 3–5 (or 6) can be answered by neutrino oscillation experiments.

Sterile neutrinos

If the neutrino has a Majorana mass in addition to a Dirac mass, a left-handed neutrino ν_L may oscillate into an anti-neutrino ν^c_R which has the same helicity as ν_L [37]. This oscillation is an

analogy with the K^0–$\bar{K}^0$ oscillation. It takes place only if the right-handed neutrino mass m_R is as small as the left-handed one m_L and $m_R \neq m_L$. A right-handed neutrino ν_R is called the sterile neutrino since it does not interact via any of the fundamental interactions of the Standard Model except gravity.

If the $\nu_L \to \nu_R^c$ oscillation existed, neutral-current-induced reactions would also be affected [104, 105] unlike in the neutrino oscillation among different flavors. By measuring neutral current events vs. L/E, the existence of sterile neutrinos can be tested.

As shown in Fig. 1.1, LSND claimed $\bar{\nu}_\mu \to \bar{\nu}_e$ oscillations at higher Δm^2 regions [80] than the atmospheric or solar oscillation scale. If that is true, a sterile neutrino needs to be introduced into the oscillation [106–108]. MiniBooNE tested this LSND result in the $\nu_\mu \to \nu_e$ mode and excluded it at 98% C.L. [81], if the ν and $\bar{\nu}$ oscillations are the same. On the other hand, MiniBooNE reported the consistent result with LSND in the $\bar{\nu}_\mu \to \bar{\nu}_e$ mode [109]. However, there is no viable oscillation scheme consistent with the LSND and MiniBooNE results [110–112].

Neutrino mass hierarchy

In the atmospheric neutrino oscillation, the oscillation probability in the leading order (Eq. 1.24) does not distinguish the sign of Δm^2_{atm}. Therefore, there are two possible types of the neutrino mass spectrum as shown in Fig. 1.5: $\Delta m^2_{atm} = \Delta m^2_{32} > 0$ or $\Delta m^2_{atm} = \Delta m^2_{32} < 0$. In addition, there is a room to add a constant smaller than 2.5 eV (1 eV if Majorana), keeping the mass squared differences at the same values. If the additional constant is nearly equal to zero, the former case is called

- the normal mass hierarchy ($m_1 < m_2 < m_3$), in which $m_2 \simeq \sqrt{\Delta m^2_\odot}$ and $m_3 \simeq \sqrt{\Delta m^2_{atm}}$,

and the latter case is called

- the inverted mass hierarchy ($m_3 < m_1 < m_2$), in which $m_1, m_2 \simeq \sqrt{|\Delta m^2_{atm}|}$.

Another extreme case is

- the quasi-degenerate neutrinos, in which $m_1 \simeq m_2 \simeq m_3 \gg \sqrt{|\Delta m^2_{atm}|}$.

The magnitude of the matter effect in Eq. 1.29–1.32 depends on the sign of Δm^2_{31}. Therefore, in neutrino oscillation experiments, the matter effect may lead us to determine the hierarchy if $\sin^2 2\theta_{13}$ is not too small.

Explanation for the neutrino mixing scheme

It is an interesting aspect of the neutrino mixing that the MNS mixing matrix is quite different from the one for the CKM quark mixing. From the experimental results shown in Sec. 1.3.1, it is deduced that $32.7 < \theta_{12} < 36.0$ degrees (90% C.L.) [87], $36.8 < \theta_{23} < 53.2$ degrees (90% C.L.) [91] and $\theta_{13} < 11.4$ degrees (90% C.L.) [73]. Thus, the moduli of the MNS matrix elements are

$$U = \begin{pmatrix} 0.79\text{–}0.84 & 0.53\text{–}0.59 & < 0.20 \\ -(0.57\text{–}0.19) & 0.39\text{–}0.74 & 0.59\text{–}0.80 \\ 0.19\text{–}0.57 & -(0.72\text{–}0.42) & 0.59\text{–}0.80 \end{pmatrix}. \tag{1.42}$$

To explain the feature of this matrix, many models has been constructed (see e.g. Ref [113]). Among them, the so-called tri-bimaximal scenario** [115–129] is the interesting one. In this

**Originally, a very similar form of U, which is however incompatible with the recent data, has already been proposed in Ref. [114].

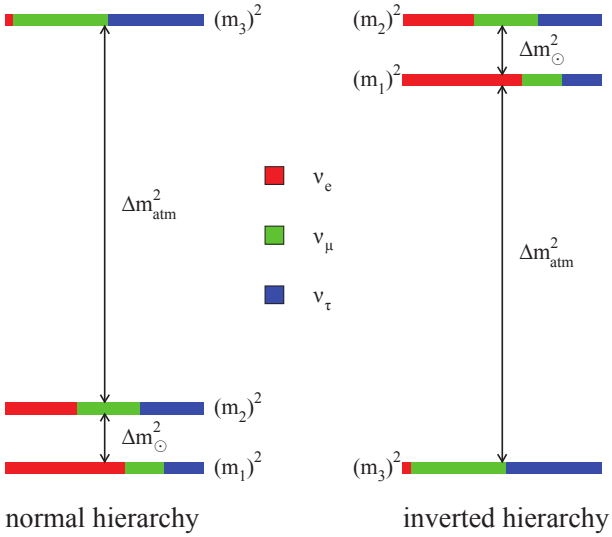

Figure 1.5: Two possible types of the neutrino mass spectrum: The normal mass hierarchy in which $\Delta m^2_{31} > 0$ and the inverted mass hierarchy in which $\Delta m^2_{31} < 0$. Here, Δm^2_{21} is positive-definite.

scenario, the MNS matrix is written as

$$U = \begin{pmatrix} \sqrt{\frac{2}{3}} & \sqrt{\frac{1}{3}} & 0 \\ -\sqrt{\frac{1}{6}} & \sqrt{\frac{1}{3}} & \sqrt{\frac{1}{2}} \\ \sqrt{\frac{1}{6}} & -\sqrt{\frac{1}{3}} & \sqrt{\frac{1}{2}} \end{pmatrix}. \tag{1.43}$$

It corresponds to $\sin^2\theta_{12} = 1/3$, $U_{e3} = 0$ and $\theta_{23} = 45$ degrees.

To proceed with further discussion on the neutrino mixing scheme, more precise measurements of the mixing angles are necessary. In particular, the measurement of θ_{13} is important since the size of θ_{13} determines whether the CP violating phase δ is measurable through neutrino oscillation or not (see Eq. 1.14). A long-baseline neutrino oscillation experiment is feasible for the δ measurement [130–134] if θ_{13} is not too small (say $|U_{e3}| = \sin\theta_{13} > 0.05$).

CP violating phase δ

Currently, the size of δ is totally unknown. The CP violation in the lepton sector might be substantially different from one in the quark sector [135]. It might answer the baryon asymmetry in the universe without resorting to grand unified theories: Decays of right-handed heavy Majorana neutrinos violate $B - L$ (B is the baryon number and L is the lepton number) at a temperature above the electroweak phase transition (so-called leptogenesis [136]), which turns into B generation through KRS mechanism [137] (see also Ref. [138]).

1.3.3 Approach to θ_{13}

There are two possible way to measure θ_{13}. One is a reactor neutrino experiment which probes θ_{13} via $\bar{\nu}_e \to \bar{\nu}_x$ disappearance. It can directly measure θ_{13} as indicated in Eq. 1.25. Many reactor experiments are planned; e.g. Double CHOOZ [139], Daya Bay [140], RENO [141], etc.

The other is an accelerator long-baseline neutrino experiment which probes θ_{13} via $\nu_\mu \to \nu_e$ appearance. Taking into account the second order in $|\Delta m^2_{21}/\Delta m^2_{31}|$ and θ_{13}, the oscillation

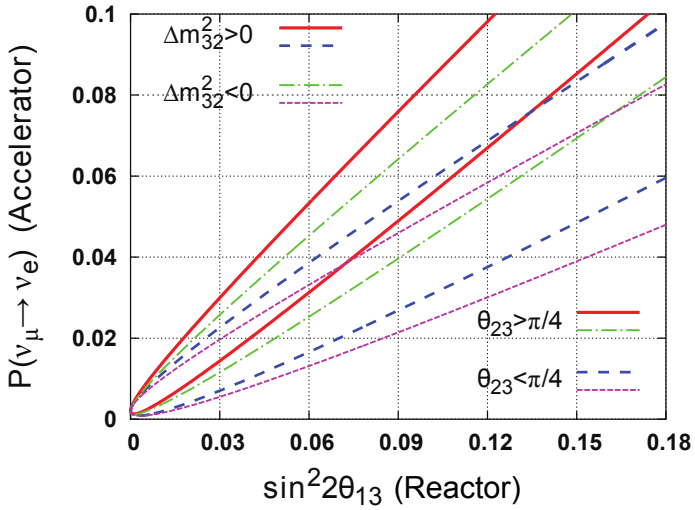

Figure 1.6: Relation between $P(\nu_\mu \rightarrow \nu_e)$ measured by long-baseline accelerator experiments and $\sin^2 2\theta_{13}$ directory measured by reactor experiments. $\sin^2 2\theta_{23} = 0.95$ is assumed. The range of $\sin^2 2\theta_{13}$ inside each radial line represents an uncertainty of $\sin^2 2\theta_{13}$ due to $\delta_{\rm CP}$, and there are four possible ranges depending on the Δm^2_{31} and θ_{23} degeneracies. For example, even if $P(\nu_\mu \rightarrow \nu_e)$ is measured to be exactly 0.03, $\sin^2 2\theta_{13}$ can have a value ranging from 0.03 to 0.12. This figure comes from Ref. [150].

probability is

$$
\begin{aligned}
P(\nu_\mu \rightarrow \nu_e) = & \frac{\sin^2[(1 \mp \hat{A})\Delta_{31}]}{(1 \mp \hat{A})^2} \sin^2 2\theta_{13} \sin^2 \theta_{23} \\
& + \frac{\Delta m^2_{21}}{\Delta m^2_{31}} \sin 2\theta_{12} \sin 2\theta_{13} \sin 2\theta_{23} (\cos\delta \cos\Delta_{31} \mp \sin\delta \sin\Delta_{31}) \\
& + \left(\frac{\Delta m^2_{21}}{\Delta m^2_{31}}\right)^2 \frac{\sin^2(\hat{A}\Delta_{31})}{\hat{A}^2} \sin^2 2\theta_{12} \cos^2 \theta_{23}, \qquad (1.44)
\end{aligned}
$$

where $\Delta_{31} \equiv \Delta m^2_{31} L/(4E)$ and $\hat{A} \equiv A/\Delta m^2_{31} = 2\sqrt{2} E G_F n_e / \Delta m^2_{31}$. The $\mp$ signs in this equation refer to the ν $(-)$ and $\bar{\nu}$ $(+)$ oscillations. There is an eight-fold degeneracy in determination of θ_{13} [142, 143] arising from three independent two-fold degeneracies: $(\delta,\ \theta_{13})$ [144], the sign of Δm^2_{31} [143] and $(\theta_{23},\ \pi/2 - \theta_{23})$ [145]. Therefore, as shown in Fig. 1.6, θ_{13} determined from $P(\nu_\mu \rightarrow \nu_e)$ by accelerator neutrino experiments includes an inherent uncertainty. However, accelerator experiments can determine θ_{13} as precisely as reactor ones, since the ν_e appearance is a clear signal and the measurement uncertainty itself is smaller than in $\bar{\nu}_e$ disappearance measurements. Both accelerator and reactor experiments are complementary; by combining measurements of these experiments, the precision of θ_{13} can be improved [146] and the degeneracies may be solved [147].

There are two new accelerator experiments to explore θ_{13}: NOνA [148] (NuMI Off-axis ν_e Appearance experiment) and T2K [149] (Tokai-to-Kamioka). The former is under construction and will begin taking data in 2013. The latter is the experiment described in this thesis. We are going to measure θ_{13} and elucidate the neutrino oscillation with T2K.

Chapter 2

T2K Experiment

T2K is an accelerator-based neutrino experiment, which has just started the beam data taking. In this chapter, an introduction to T2K is described; the physics goals, strategy and requirements are explained, and an overview of this thesis is given at the end of this chapter.

2.1 Overview of T2K

T2K is a long-baseline accelerator neutrino experiment between Tokai and Kamioka. The overview of T2K is illustrated in Fig. 2.1. An intense muon neutrino beam (∼0.6 GeV) is produced from pion two-body decays ($\pi \to \mu\nu_\mu$) at J-PARC [151] (Japan Proton Accelerator Research Complex) in Tokai. The neutrinos are measured by the near detector at the J-PARC site before oscillation, and are measured after traveling 295 km by the Super-Kamiokande water Cherenkov detector [152] (Super-K) in Kamioka. T2K is the first experiment that adopts the off-axis beam configuration [153]; the neutrino beam is aimed off the Super-K direction by 2.5 degrees. The neutrino beam direction is controlled by monitoring the muon beam direction by the muon monitor. The neutrino and muon beam directions should be the same because the neutrinos and muons originate from the same parent pions.

The muon neutrinos produced at J-PARC oscillate in flight mostly into tau neutrinos at the Super-K position. Most of the tau neutrinos in the T2K beam are not detected in Super-K because tau leptons cannot be produced in the charged current ν_τ interactions.* Therefore, the observed number of neutrino events by the charged current ν_μ interactions in Super-K is expected to decrease due to the $\nu_\mu \to \nu_\tau$ oscillation (ν_μ disappearance). On the other hand, the $\nu_\mu \to \nu_e$ oscillation can be clearly identified in Super-K as more ν_e events than the expected background events (ν_e appearance). The neutrino mixing angles θ_{23} and θ_{13} are measured in the ν_μ disappearance and ν_e appearance, respectively.

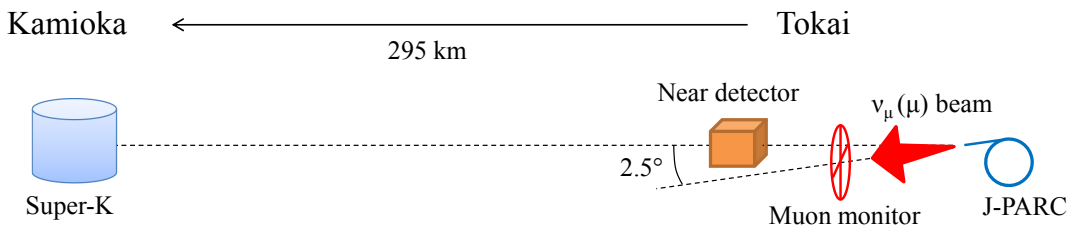

Figure 2.1: Overview of the T2K experiment.

*The energy threshold for tau lepton production is approximately 3.5 GeV while the T2K neutrino beam energy is around 0.6 GeV.

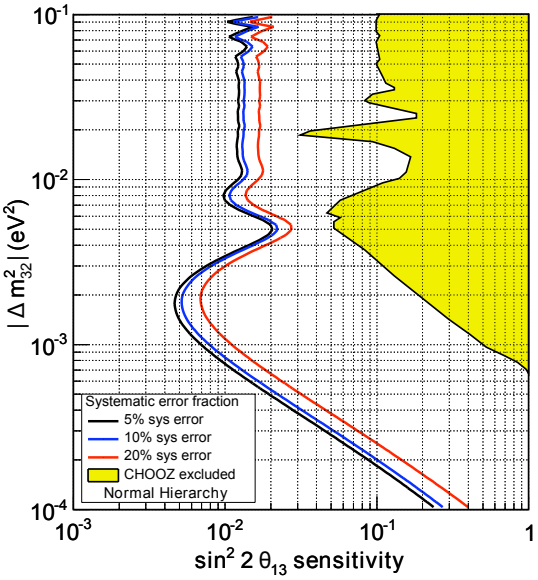

Figure 2.2: T2K sensitivity (limit) to θ_{13} at 90% C.L. as a function of $|\Delta m^2_{32}|$ with 8.33×10^{21} POT on the assumption of the normal mass hierarchy. Three contours are drawn for the different systematic errors on the background estimation. The painted region has been excluded to 90% C.L. by the CHOOZ experiment [73].

2.2 Goals of T2K

The main goals of T2K are

- to measure θ_{13}, or to probe $\sin^2 2\theta_{13}$ with sensitivity down to 0.006 at 90% C.L.;
- to measure $\sin^2 2\theta_{23}$ and $|\Delta m^2_{32}|$ with a precision of $\delta(\sin^2 2\theta_{23}) \approx 0.01$ and $\delta(|\Delta m^2_{32}|) < 10^{-4}$ eV^2;

with $\sim 8 \times 10^{21}$ POT (protons on target). For the sensitivity to θ_{13}, $|\Delta m^2_{32}| = 2.4 \times 10^{-3}$ eV^2, $\delta = 0$ and normal mass hierarchy are assumed.

The sensitivity to θ_{13} at 90% C.L. as a function of $|\Delta m^2_{32}|$ is shown in Fig. 2.2. T2K is to probe θ_{13} with higher sensitivity by more than one order of magnitude than the current CHOOZ limit at $\sin^2 2\theta_{13} \approx 0.15$. The precise measurement of $\sin^2 2\theta_{23}$ and $|\Delta m^2_{32}|$ is important for the measurement of θ_{13} (see Eq. 2.1). In addition, with this $\sin^2 2\theta_{23}$ sensitivity, the question whether θ_{23} is 45° or not is expected to be answered.

2.3 Experimental strategy

The neutrino transition and survival probabilities are approximately expressed as

$$P(\nu_\mu \to \nu_e) \approx \sin^2 2\theta_{13} \sin^2 \theta_{23} \sin^2 \left(\frac{\Delta m^2_{32} L}{4E_\nu} \right), \tag{2.1}$$

$$P(\nu_\mu \to \nu_\mu) \approx 1 - \sin^2 2\theta_{23} \sin^2 \left(\frac{\Delta m^2_{32} L}{4E_\nu} \right), \tag{2.2}$$

where L is the neutrino travel length and E_ν is the neutrino energy. In T2K, L is fixed at 295 km, which is the distance between J-PARC and Super-K. E_ν is adjusted around 0.6 GeV as shown

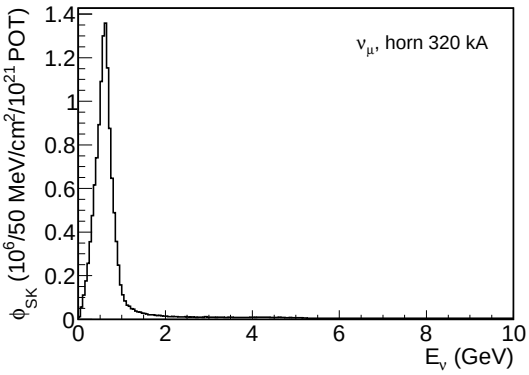

Figure 2.3: ν_μ energy spectrum at Super-K estimated with a Monte Carlo simulation (JNUBEAM).

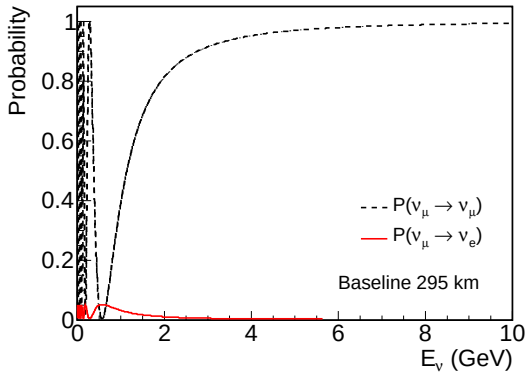

Figure 2.4: Neutrino oscillation probability P as a function of the neutrino energy E_ν, assuming $\sin^2 2\theta_{13} = 0.1$, $\sin^2 2\theta_{23} = 1$ and $|\Delta m^2_{32}| = 2.4 \times 10^{-3}$ eV^2. The neutrino travel length L is fixed at 295 km.

in Fig. 2.3 to get the maximal $P(\nu_\mu \to \nu_e)$ and the minimal $P(\nu_\mu \to \nu_\mu)$. In Fig. 2.4, $P(\nu_\mu \to \nu_e)$ and $P(\nu_\mu \to \nu_\mu)$ are plotted assuming $\sin^2 2\theta_{13} = 0.1$, $\sin^2 2\theta_{23} = 1$ and $|\Delta m^2_{32}| = 2.4 \times 10^{-3}$ eV^2 in accordance with Eq. 2.1 and 2.2. These equations tell that $N^{obs}_{\rm SK}/N^{null}_{\rm SK}$ oscillates as a function of E_ν, where $N^{obs}_{\rm SK}$ and $N^{null}_{\rm SK}$ are the number of neutrino events observed at Super-K and the one expected in case of null oscillation, respectively. Therefore, the parameters θ_{13}, θ_{23} and $|\Delta m^2_{32}|$ can be derived from measurements of $N^{obs}_{\rm SK}$ as a function of E_ν. Hence, $N^{obs}_{\rm SK}(E_\nu)$ and the flavor (identification of ν_e or ν_μ) are what we are going to measure in T2K.

The neutrino energy E_ν can be reconstructed as E^{rec}_ν in charged current quasi-elastic (CCQE) interactions ($\nu_\ell + n \to \ell + p$) by measuring the lepton momentum p_ℓ and angle θ_ℓ with respect to the beam direction:

$$E^{rec}_\nu = \frac{(m_n - V)E_\ell + (m_p^2 - m_\ell^2)/2 - (m_n - V)^2/2}{(m_n - V) - E_\ell + p_\ell \cos\theta_\ell}, \tag{2.3}$$

where m_n, m_p and m_ℓ are the mass of the neutron, proton and lepton, respectively, E_ℓ is the lepton energy and V is the nuclear potential of oxygen (set to be 27 MeV). In the CCQE interaction, only one Cherenkov ring by the charged lepton is detected in most cases. In the other (non-CCQE) interactions, the hadrons or gammas can also emit Cherenkov light, and typically multi-rings are detected. Therefore, the CCQE interaction can be distinguished by counting the number of Cherenkov rings. The neutrino flavor can be identified in Super-K[†] by analyzing the sharpness of the Cherenkov ring edge; a muon makes a sharp edge ring (identified as a μ-like event) and an electron makes a fuzzy one due to electromagnetic showers (identified as an e-like event).

The number of neutrino events observed in Super-K $N^{obs}_{\rm SK}(E^{rec}_\nu)$ is compared with the expectation for given oscillation parameters given as

$$N^{exp}_{\rm SK}(E^{rec}_\nu; \Delta m^2, \theta) = \int {\rm d}E_\nu \; M_{\rm SK}(E^{rec}_\nu, E_\nu) \times P(E_\nu; \Delta m^2, \theta) \cdot \phi_{\rm SK}(E_\nu) \cdot \sigma(E_\nu) \cdot \epsilon_{\rm SK}(E_\nu), \tag{2.4}$$

where σ is the neutrino cross-section, ϵ is the neutrino detection efficiency and M is the detector response function representing the probability to observe E_ν as E^{rec}_ν. Therefore, in addition to

[†]Only in charged current interactions, the neutrino flavor can be deduced from the induced charged lepton species. In neutral current interactions, since no charged lepton is produced, one cannot tell the neutrino flavor and cannot see the neutrino oscillation effect.

the measurement of $N_{\rm SK}^{obs}(E_\nu^{rec})$ and the flavor identification, the estimation of $\phi_{\rm SK}$, σ, ϵ and M is necessary. The $\phi_{\rm SK}$ is estimated using a Monte Carlo (MC) simulation, called JNUBEAM.

2.3.1 ν_e appearance search

The signals of the ν_e appearance are single-ring e-like events in CCQE samples.

One of the dominant backgrounds is the ν_e contamination in the ν_μ beam. The ν_e contamination originates mainly from the following decay chains, $\pi^+ \to \mu^+\nu_\mu$ and $\mu^+ \to e^+\bar{\nu}_\mu\nu_e$. It also comes from K_{e3} decays. These intrinsic beam ν_e backgrounds are not avoidable in T2K. However, the fraction of the ν_e contamination in the beam is estimated to be small: approximately 0.5% at the ν_μ spectrum peak and 1% in the total flux before oscillation. The amount of the ν_e contamination is measured by the near detector and is extrapolated to Super-K to precisely estimate the number of the intrinsic beam ν_e backgrounds.

The other dominant background is caused by neutral current single π^0 production interactions (NC1π^0: $\nu_\ell + N \to \nu_\ell + N' + \pi^0$, where N and N' are nucleons); if Cherenkov rings by two gammas from the π^0 decay overlap or one of them is missed, this event looks like a single-ring e-like event. The T2K sub-GeV neutrino beam is suitable to reduce this NC1π^0 background since the NC1π^0 cross-section decreases as the neutrino energy decreases.

With the T2K full statistics of 8×10^{21} POT, the expected number of ν_e appearance signals at Super-K ($0.35 \leq E_\nu \leq 0.85$ GeV) is 143 (or 14) if $\sin^2 2\theta_{13} = 0.1$ (or 0.01). The expected number of background events is 26, of which 16 are the intrinsic beam ν_e backgrounds, and the others are the NC1π^0 backgrounds. The expected $N_{\rm SK}^{obs}(E_\nu^{rec})$ histogram is shown in Fig. 2.5.

2.3.2 ν_μ disappearance analysis

The signals for the ν_μ disappearance analysis are single-ring μ-like events in CCQE samples. The dominant background comes from charged current single π production interactions (CC1π: $\nu_\mu + N \to \mu + N' + \pi$). If the pion is not detected due to its low momentum or absorption by the nucleus, this event looks like a single-ring μ-like event.

The expected spectra of single-ring μ-like events in CCQE samples, $N_{\rm SK}^{null}(E_\nu^{rec})$ and $N_{\rm SK}^{obs}(E_\nu^{rec})$, are shown in Fig. 2.6 (upper plots) for the null oscillation case and for $\sin^2 2\theta_{23} = 1$ and $|\Delta m^2_{32}| = 2.4 \times 10^{-3}$ eV^2, respectively. One can clearly see that $N_{\rm SK}^{obs}$ dramatically decreases due to the neutrino oscillation ($\int N_{\rm SK}^{obs}/N_{\rm SK}^{null} \approx 0.27$ in this figure) and that there is a dip around 0.6 GeV in $N_{\rm SK}^{obs}(E_\nu^{rec})$ due to the local minimum of the oscillation probability $P(\nu_\mu \to \nu_\mu)$. By taking a ratio of $N_{\rm SK}^{obs}(E_\nu^{rec})$ to $N_{\rm SK}^{null}(E_\nu^{rec})$, the lower plot in Fig. 2.6 is obtained. It represents $P(\nu_\mu \to \nu_\mu)$ in Fig. 2.4 smeared mainly with the non-CCQE backgrounds and the E_ν^{rec} uncertainty.[‡] Naively, the depth of the dip and the energy at the dip correspond to $\sin^2 2\theta_{23}$ and $|\Delta m^2_{32}|$, respectively.

2.4 Features of T2K

T2K is designed to accumulate neutrino events with high statistics, to precisely reconstruct neutrino events, to precisely predict the neutrino flux $\phi_{\rm SK}$, etc. as indicated in Fig. 2.7. To measure θ_{13}, the statistics is a crucial issue since $P(\nu_\mu \to \nu_e)$ is small. High statistics is realized using intense neutrino beam (see Sec. 2.4.1) and the large volume Super-K detector. Super-K has a good capability of measuring E_ν and identifying neutrino flavors. The probability of misidentification, where a muon is identified as an electron, and vice versa, is about 1% for the T2K neutrino energy. In addition, Super-K has been well calibrated, and ϵ and M in Eq. 2.4 can be estimated precisely. The precise estimation of $\phi_{\rm SK}$ is realized by precisely monitoring the

[‡]The E_ν^{rec} uncertainty mainly comes from the Fermi motion.

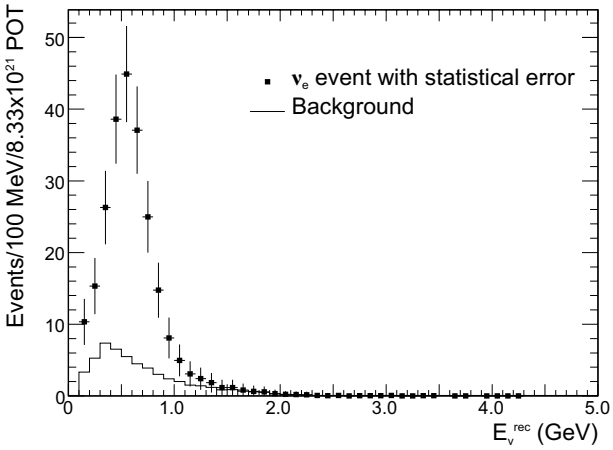

Figure 2.5: Expected number of ν_e events as a function of the reconstructed neutrino energy E_ν^{rec} for given neutrino oscillation parameters, $\sin^2 2\theta_{13} = 0.1$, $\sin^2 2\theta_{23} = 1$ and $|\Delta m^2_{32}| = 2.4 \times 10^{-3}$ eV^2. The sum of ν_e appearance signals and backgrounds is given by the point. The solid line shows the background estimation.

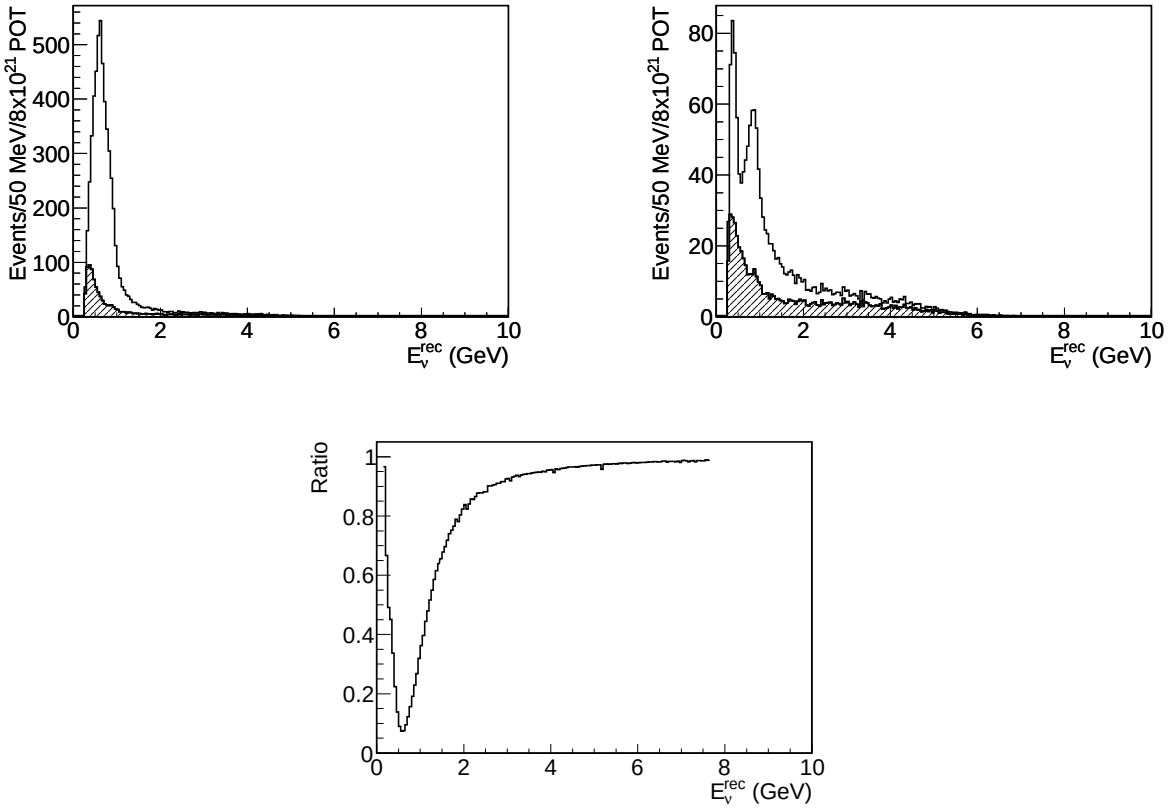

Figure 2.6: Expected energy spectrum of single-ring μ-like events in CCQE samples at Super-K for the null oscillation case (upper left) and for $\sin^2 2\theta_{23} = 1$ and $|\Delta m^2_{32}| = 2.4 \times 10^{-3}$ eV^2 (upper right). The hatched histogram shows the contribution of non-CCQE backgrounds. The lower plot is the ratio of the upper two histograms. The depth of the dip and the energy at the dip correspond to $\sin^2 2\theta_{23}$ and $|\Delta m^2_{32}|$, respectively.

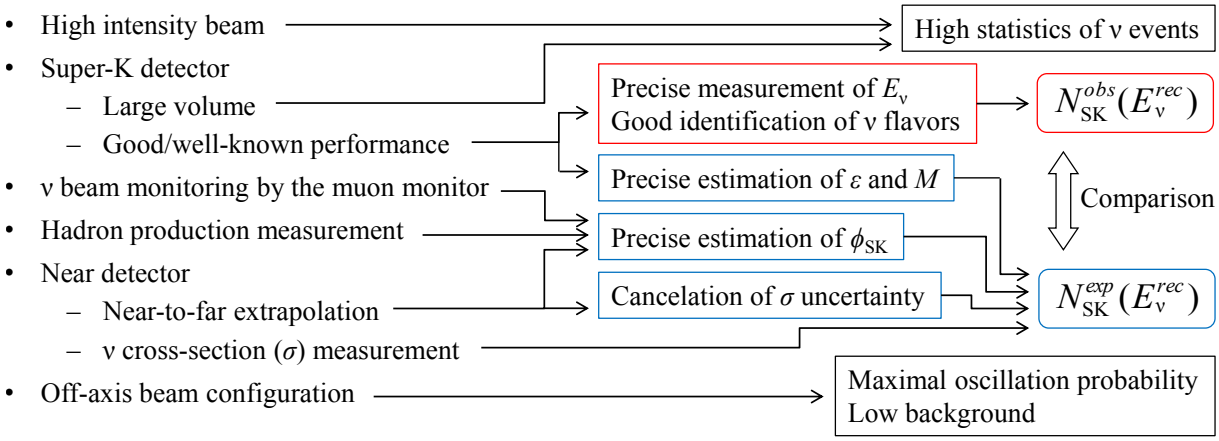

Figure 2.7: Features of T2K. The experimental features listed in the left-hand side give us the advantages pointed by arrows.

neutrino beam with the muon monitor (see Sec. 2.4.2), by utilizing measured hadron production cross-sections for JNUBEAM (see Sec. 2.4.3) and by extrapolating the neutrino flux measured by the near detector to the Super-K position (called the near-to-far extrapolation). The near-to-far extrapolation is a powerful tool to cancel out some uncertainties related to the neutrino flux and cross-sections between the near and far detectors. The off-axis beam configuration maximizes the oscillation probability and reduces background events (see Sec. 2.4.4), resulting in the high sensitivity to θ_{13}.

2.4.1 Intense neutrino beam

To generate an intense muon neutrino beam, T2K utilizes the J-PARC 30 GeV and 750 kW[§] proton beam, which is designed to be the most powerful beam in the world. As shown in Fig. 2.8, the proton beam is hit on a graphite target to produce pions, and three magnetic horns focus the pions and parallel their directions with an electromagnetic force. The pions decay in flight into pairs of a muon and a muon neutrino. As a result, a bunch of neutrinos heading for nearly the same direction, or the neutrino beam, is produced.

In addition to the high power proton beam, the key component in T2K for the the intense neutrino beam is a series of the three magnetic horns. The horns are excited with 320 kA[¶] pulsed current. They increase the neutrino flux by approximately 16 times at 0.6 GeV (by approximately five times in total).

In combination with the intense neutrino beam and the huge Super-K detector 50 kt in weight (22.5 kt for the fiducial volume), a few ν_μ events per day are expected at Super-K.

2.4.2 Neutrino beam monitoring by the muon monitor

The neutrino beam flux, energy, profile, direction, etc. depend on the proton beam parameters at the target, kinematics of the pions at the production and the horn focusing effect. They can be monitored with the muon monitor by measuring the muon beam generated along with the neutrino beam. Because the muon beam can be measured for every shot, the muon monitor gives real-time information of the neutrino beam, which can be used for feedback of the neutrino

[§]Design value. The operational beam power is different in this thesis.
[¶]Design value. The operational current was lowered to 250 kA in this thesis.

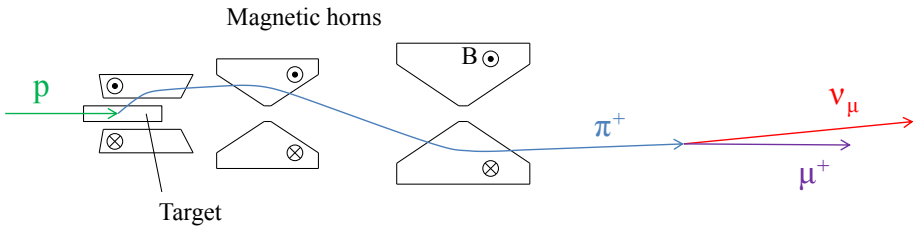

Figure 2.8: Illustration (cross section view) of an example of the pion decay chain producing a muon neutrino. The pion produced in the proton and graphite target interaction is focused by the three magnetic horns, and decays into a muon and a muon neutrino in flight. Inside the horn, there is a toroidal magnetic field.

beam control. This neutrino beam monitoring by the muon monitor is one of the most important features in T2K. Only with the quality-controlled neutrino beam, ϕ_{SK} can be estimated reliably.

The neutrino beam monitoring is also important for the near-to-far extrapolation. Because the near detector does not measure the exactly same neutrino spectrum as Super-K due to the acceptance difference, an uncertainty of the neutrino beam direction causes an uncertainty of the extrapolation (see Appendix A for detail). Hence, without the precise measurement of the neutrino beam direction, the near-to-far extrapolation does not avail to estimate ϕ_{SK} precisely.

2.4.3 Input of the hadron production cross-sections from CERN-NA61

The T2K neutrino beam originates mainly from charged pion decays (for $E_\nu < 3$ GeV) and charged kaon decays (for $E_\nu > 3$ GeV), and ϕ_{SK} depends on the pion and kaon kinematics at the production. Therefore, the pion and kaon production cross-sections in 30 GeV proton and carbon interactions are necessary to estimate ϕ_{SK}. The NA61/SHINE (SHINE – SPS Heavy Ion and Neutrino Experiment) experiment at CERN [154,155] measured these cross-sections for T2K [156,157], to which JNUBEAM was tuned.

2.4.4 Off-axis beam configuration

The peaked energy spectrum of the neutrino beam (Fig. 2.3) is realized by virtue of the off-axis beam configuration. In the pion two-body decay ($\pi \to \mu\nu_\mu$), E_ν in the laboratory system is written as

$$E_\nu = \frac{m_\pi^2 - m_\mu^2}{2(E_\pi - p_\pi \cos\theta_\nu)} = \frac{m_\pi^2 - m_\mu^2}{2(1/\beta_\pi - \cos\theta_\nu)p_\pi}, \tag{2.5}$$

and as shown in Fig. 2.9, cannot exceed the energy

$$E_\nu^{max} = \frac{m_\pi^2 - m_\mu^2}{2m_\pi \sin\theta_\nu}, \tag{2.6}$$

where m_π and m_μ are the pion and muon mass, respectively, E_π is the pion energy, p_π is the pion momentum and θ_ν is the angle between the pion and neutrino directions. For neutrinos going to Super-K, θ_ν is close to the angle between the neutrino beam and Super-K directions (called the off-axis angle) since the horns focus the pions to the beam axis direction. Thus, the energy spectrum at Super-K peaks at lower energy in the off-axis beam configuration than in a conventional on-axis beam configuration as shown in Fig. 2.10. The spectrum peak energy is adjustable by changing the off-axis angle. In T2K, the off-axis angle is set at 2.5 degrees to adjust the spectrum peak energy around 0.6 GeV, at which we believe the oscillation probability reaches its maximum.

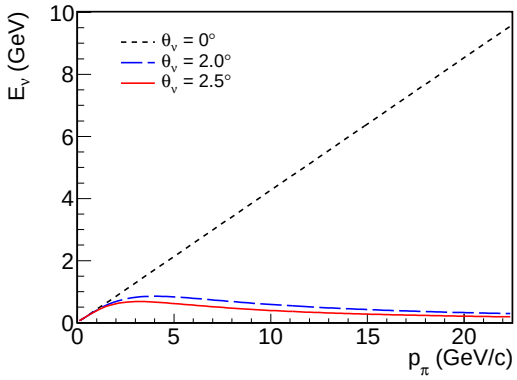

Figure 2.9: Neutrino energy as a function of the pion momentum when the neutrino is produced in a certain direction in accordance with Eq. 2.5.

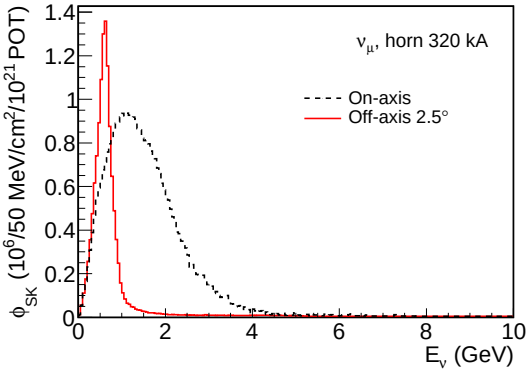

Figure 2.10: ν_μ energy spectra at Super-K in the off- and on-axis beam configurations. They are estimated with JNUBEAM.

2.5 Requirements in T2K

The followings are required to achieve the T2K goals:

- the high power beam operation,
- the neutrino beam of high quality,
- the accurate reconstruction of neutrino events at Super-K and the understanding of its performance,
- the precise measurement of the neutrino flux at the near detector, and
- the understanding of the neutrino cross-sections.

Because the sensitivity to θ_{13} is limited by the statistics at the early stage as shown in Fig. 2.11, it is essential to accumulate the integrated beam power as much as possible. To realize the 750 kW beam power operation, the loss of the proton beam must be small; otherwise the beamline is radioactivated. Therefore, it is required for us to precisely tune and measure the proton beam in the T2K beamline. The measurement of the proton beam is also necessary to guarantee the neutrino beam quality, which enables precise estimation of the neutrino flux at Super-K. In addition, monitoring of the horn currents and monitoring of the neutrino beam by the muon monitor are important to produce the neutrino beam with high quality. Namely, understanding of the beam and beamline is the most important thing at the early stage of T2K. The necessity to precisely tune and measure the beam is discussed in the following sections.

The uncertainty of the Super-K measurement can be disregarded at the early stage because Super-K has run since 1996 and its detector response has been well understood. On the other hand, the performance of the near detector, which started in operation in 2010, has to be well understood to utilize the near-to-far extrapolation. Studies on the near detector measurement are written in elsewhere [158]. The uncertainties on the neutrino cross-sections are large and should be reduced. The neutrino cross-sections are measured by the near detector, which will reduce the uncertainties in future. Those issues on Super-K, the near detector and the neutrino cross-sections are beyond the aim of this thesis, and should be discussed in the future analysis.

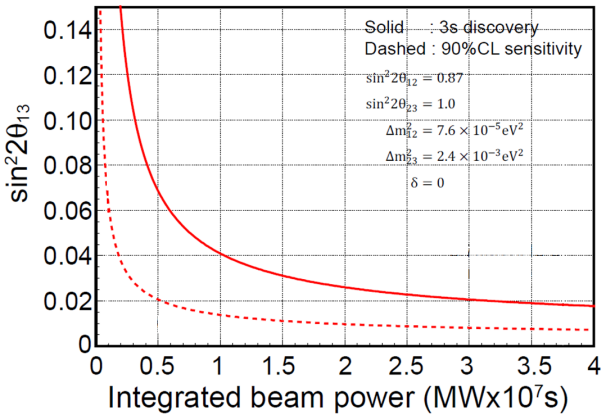

Figure 2.11: T2K sensitivity to θ_{13} as a function of the integrated beam power. The oscillation parameters written in this figure and 10% systematic error on the background estimation are assumed.

2.5.1 High power beam operation

To accept the high power proton beam into the T2K beamline, it is important to precisely tune not only the proton beam orbit but also the proton beam position and size on the target. If the beam hits off the target center or the beam size on the target is too small, a localized thermal shock in the target due to the beam heating could break the target. On the contrary, if the beam size is too large, the rim of the beam misses hitting the target and the generated neutrino flux decreases. To prevent those risks, the proton beam (Gaussian profile) center should hit within $\pm$1 mm of the target center, and the beam size should be $\sim$6.0 mm in RMS (Root Mean Square) for the 750 kW operation, while the target size is 26 mm in diameter. The well-tuned proton beam on the target results also in producing the high quality neutrino beam.

The radiation level around the target and horns is exorbitantly high. Therefore, the target, horns and components around them must be robust against the radiation to accept the high power beam. The muon monitor also must be tolerant of radiation because it suffers the muon beam of high intensity. The muon monitor is also required to work stably in order to guarantee the neutrino beam quality for every shot. Therefore, the robustness of the muon monitor is important to maximize the integrated proton beam power.

2.5.2 Neutrino beam quality

In order to achieve the target sensitivity to θ_{13}, the systematic error on the background estimation has to be less than 10% (see Fig. 2.2). In other words, the total uncertainty of the neutrino flux at Super-K (ϕ_{SK}), the neutrino cross-section (σ) and the Super-K efficiency (ϵ_{SK}) has to be less than 10%. Assuming the uncertainty of each of the three terms is equal, the required precision of ϕ_{SK} is 6%.

For the ν_μ disappearance measurement, the minimum value of the ratio $N^{obs}_{\mathrm{SK}}/N^{null}_{\mathrm{SK}}$ (see the lower plot in Fig. 2.6) has to be measured with an approximately 10% precision to determine $\sin^2 2\theta_{23}$ (or the depth of the dip in that plot) with a 1% precision. Therefore, the total uncertainty of the above three terms ϕ_{SK}, σ and ϵ_{SK} should be 10% or less in total, and ϕ_{SK} has to be estimated with a roughly 6% precision or better. To achieve a 4% precision of $|\Delta m^2_{32}|$, the uncertainty of the neutrino energy scale has to be less than 4% since $|\Delta m^2_{32}|$ corresponds to the neutrino energy at the minimum of the ratio.

In summary, it is required to estimate ϕ_{SK} with a precision better than 6% and the neutrino energy scale with a precision better than 4%. To achieve these precisions, the precise measurement of the beam and stable beam operation are necessary as described below. The requirements discussed below are more stringent so that those precisions are achieved even when ϕ_{SK} and the neutrino energy scale are estimated without the near-to-far extrapolation.

Requirements for the beamline operation

The uncertainty of ϕ_{SK} originates from the uncertainties related to the beamline: the proton beam parameters on the target, pion and kaon kinematics at the production in the target, horn magnetic fields, alignment of the target and horns, etc. Therefore, understanding of the beam and beamline is required to make the ϕ_{SK} uncertainty small. The precise measurements of the proton beam and horn currents are also essential for the beam tuning and stable beam operation. During the operation, the proton beam center and size on the target and the horn currents are required to be monitored with a precision better than 500 μm, 700 μm and 2%, respectively. In addition, the proton beam intensity is required to be monitored with a few percent precision, which turns into the uncertainty of the ϕ_{SK} absolute scale as it is.

Requirement for the neutrino beam direction

The most important signpost in the beam tuning is the neutrino beam direction. This is because the energy spectrum of the neutrino beam depends on the neutrino beam direction, or the off-axis angle, as shown in Eq. 2.5. Hence, a shift of the neutrino beam direction causes a shift of the spectrum peak energy and a variation of the neutrino flux, resulting in the ϕ_{SK} uncertainty. The neutrino beam direction is defined as the direction from the target to the center of the neutrino beam profile. It is required to be tuned within 1 mrad, which comes from the following estimation.

In T2K, neutrinos constituting the spectrum peak (around 0.6 GeV) mainly come from a-few-GeV pions. According to Fig. 2.9, these pions produce neutrinos of nearly the maximum energy. Therefore, Eq. 2.6 can be considered as a relation between the spectrum peak energy (E_ν^{max}) and the off-axis angle (θ_ν). According to this equation, when θ_ν changes by 1 mrad from 2.5°, E_ν^{max} changes by approximately 16 MeV, or 2–3% around the spectrum peak energy.[‖] Hence, a 1 mrad uncertainty of the off-axis angle causes a 2–3% uncertainty of the neutrino energy scale around the spectrum peak energy, resulting in a 2–3% uncertainty of $|\Delta m^2_{32}|$.

In T2K, the neutrino beam direction is monitored by the muon monitor as well as by the INGRID (Interactive Neutrino GRID) detector. INGRID monitors the mean neutrino beam direction for tens of thousands of spills by reconstructing the neutrino beam profile. The INGRID measurement is used for a confirmation that the neutrino beam direction measured with the muon monitor is surely consistent with the direction of the neutrino beam itself. Because the T2K shot-by-shot neutrino beam direction is monitored only by the muon monitor, the muon monitor is one of the most important detectors in T2K. Therefore, this thesis is devoted to the muon monitor design, performance and results achieved in the T2K beam operation.

2.6 History of T2K

T2K was proposed in 2000 [149]. To realize the experiment, the construction of J-PARC and the T2K neutrino beamline started in 2001 and 2004, respectively. All the constructions finished in March, 2009.

[‖] This change of the spectrum peak energy was confirmed in the MC simulation by changing the beamline tilt by 1 mrad.

T2K started the beam operation on April 23, 2009. In April and May, intermittent beam time was assigned for T2K, for eight days in total. The neutrino beamline was cautiously commissioned with a quite low intensity beam (∼0.5 kW); many operational checks were done for every component in the beamline, and the proton beam orbit and size were tuned. At that time, only the first horn out of three was installed and operated at 273 kA. In November of 2009, the beam commissioning resumed with the full beamline setup, and INGRID started in operation. Operation of the three horns at 320 kA was tested, but due to a problem of the horn power supply, the operational current during the following physics run was limited to 250 kA. In 2009, most of the commissioning tasks were completed in success and our beamline got ready for continuous operation to study neutrino oscillations (physics run).

The first series of the physics runs started in the end of January of 2010, and continued till the end of June, 2010. The near detector started in measurement with the almost full setup in February, 2010.

After the horn power supply was replaced with new one during the summer shutdown of the accelerator in 2010, the physic run restarted in November. The beam power was 145 kW as of March, 2011.

2.7 Overview of this thesis

The aim of this thesis is to present that we succeeded in launching the T2K experiment in operation with satisfaction of the above requirements.

As discussed above, we rely on several beam monitors to stably produce the neutrino beam of high quality. Among them, the muon monitor is one of the most essential monitors. Therefore, construction of the muon monitor which stably and precisely monitor the neutrino beam was one of the key points which were necessary to make a success of the T2K launch. It is one of two main subjects of this thesis. We show results obtained with the muon monitor in the beam operation during the first physics runs from January to June in 2010.

The other subject of this thesis is the estimation of the neutrino flux with uncertainties related to the beam to present how much we understand the beam.

The experimental setup in T2K is explained in Chap. 3, and the muon monitor design is given in Chap. 4 in detail. The performance of the muon monitor was tested in beam tests and in the T2K beamline. The results of these tests are presented in Chap. 5. What we achieved with the muon monitor during the physics run are presented in Chap. 6. From Chap. 7, the subject is changed to the estimation of the neutrino events at Super-K, focusing on the neutrino flux estimation. The overview of this analysis is given in Chap. 7. The neutrino flux is estimated in Chap. 8 and the expected number of neutrino events is presented in Chap. 9. The expected number is compared with the observed number of neutrino events in Chap. 10. Finally, our conclusion is given in Chap. 11.

Chapter 3

Experimental Components

The T2K experimental setup consists of J-PARC (Sec. 3.1), the neutrino beamline and beam monitors (Sec. 3.2), the near detector (Sec. 3.3) and Super-K (Sec. 3.4). These hardware descriptions are given in this chapter.

3.1 J-PARC

J-PARC, the Japan Proton Accelerator Research Complex, is a complex of accelerator facilities which produce various kinds of particle beams such as neutron, muon, neutrino and kaon beams with high intensity. These beams are used to research into mysteries of the creation and structure of our universe by investigating matter at all levels, from quarks to organisms.

J-PARC consists of three accelerators [151] as shown in Fig. 3.1:

- a linear accelerator (LINAC), which accelerates an H^- beam up to 400 MeV* (181 MeV at present);
- a Rapid-Cycling Synchrotron (RCS), which accelerates a proton beam to 3 GeV;
- a 30 GeV synchrotron (Main Ring; MR).

An H^- beam produced with a negative ion source is accelerated up to 400 MeV (181 MeV at present) by the LINAC, and is converted to an H^+ beam by charge stripping foils at the RCS injection. Then, the beam is accelerated up to 3 GeV by the RCS with a 25 Hz cycle. The RCS has two buckets, and both buckets are filled with the beam, i.e. there are two bunches in a cycle. About 4–5% of the RCS beam are supplied to the MR.† The two bunches in the RCS are injected to the MR at once, and the injection is repeated four times to fill eight of nine buckets in the MR as shown in Fig. 3.2. The last bucket is reserved for the rise-time of the extraction kicker magnet. After the injection, the eight (six until June 2010) bunches of the proton beam are accelerated to 30 GeV. Then all the bunches in the MR are extracted to the neutrino beamline at once (fast extraction). The MR cycle is $\sim$0.3 Hz.‡ The design beam power is 1.0 MW for the RCS and 0.75 MW for the MR. The parameters of each accelerator are summarized in Tab. 3.1.

3.2 Neutrino beamline

A train of bunches of protons in one cycle from the MR is extracted as a spill to the T2K neutrino beamline to produce the neutrino beam. The parameters of the extracted proton beam are listed in Tab. 3.2.

*The beam energy at the LINAC will be upgraded to 600 MeV with superconducting magnets.

†In most of the RCS cycles, the 3 GeV beam is extracted to MLF.

‡There is a plan to increase the MR cycle in order to achieve 0.75 MW beam power.

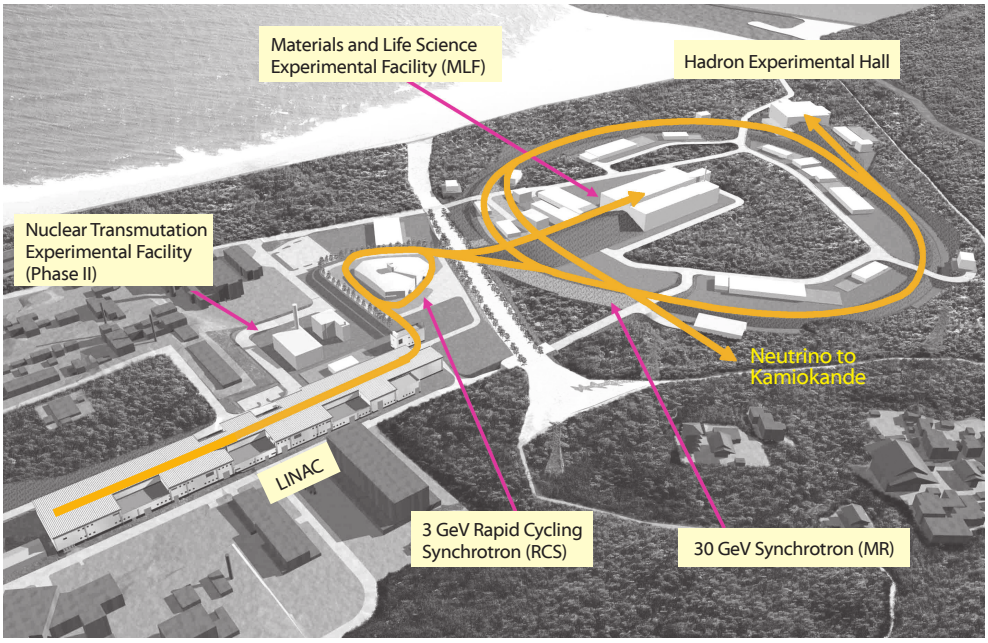

Figure 3.1: Bird eye's view of the J-PARC site. J-PARC consists of the LINAC, RCS and MR. There are three experimental facilities: a material and life science experimental facility (MLF), in which pulsed neutron and muon beams produced from the RCS proton beam are utilized to promote material and life science; a hadron experimental facility in which hadron beams produced from the MR slow-extracted proton beam are utilized to research nuclear and particle physics; and a neutrino experimental facility for T2K.

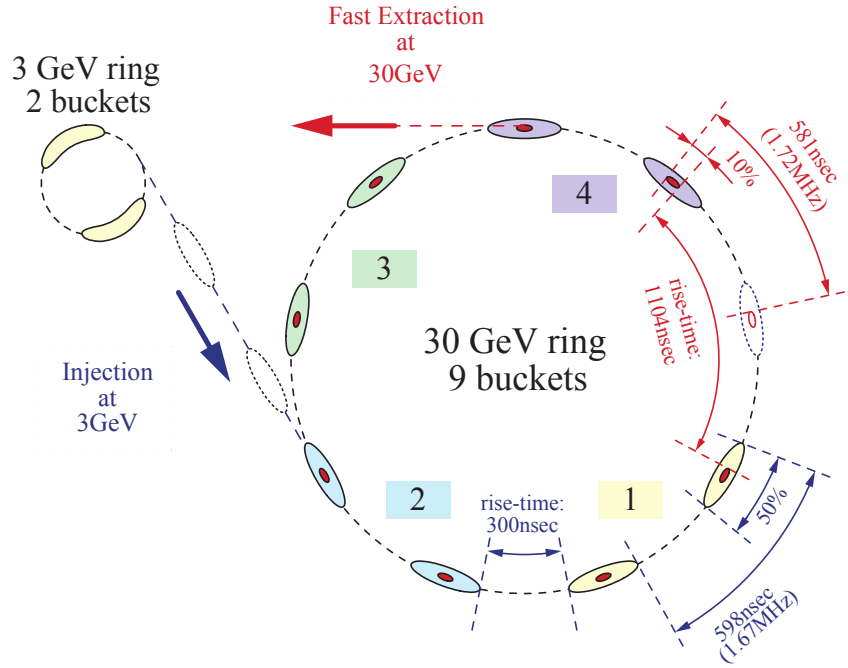

Figure 3.2: Injection scheme from the RCS to the MR.

Table 3.1: Design parameters of the LINAC, RCS and MR in J-PARC.

	LINAC	RCS	MR
Particle	H^-	p	p
Kinetic energy	400 MeV	3 GeV	30 GeV
Beam power		1.0 MW	0.75 MW
Repetition	25 Hz	25 Hz	∼0.3 Hz
Number of buckets		2	9
Total length	249 m		
Circumference		348.333 m	1567.5 m

Table 3.2: Design parameters of the fast extracted proton beam.

Beam kinetic energy	30 GeV
Beam intensity	3.3×10^{14} p/spill
Spill cycle	∼0.3 Hz
Number of bunches	8 /spill
Bunch interval	581 nsec
Bunch width	58 nsec

The neutrino beamline is composed of two sections: the primary and secondary beamlines. In the primary beamline, the extracted proton beam is transported to point toward Super-K. In the secondary beamline, the proton beam impinges on a target to produce secondary pions, which are focused by magnetic horns and decay into neutrinos. An overview of the neutrino beamline is drawn in Fig. 3.3. Each component in the beamline is described in this section.

3.2.1 Primary beamline

The primary beamline consists of the preparation (∼50 m long), arc (∼150 m) and final focusing (∼40 m) sections. In the preparation section, the extracted proton beam is tuned with a series of 11 normal conducting magnets (four steering, two dipole and five quadrupole magnets) so that the beam can be accepted by the arc section. In the arc section, the beam is bent toward the direction of Super-K by 80.7 degrees, with 104 m radius of curvature, using 14 doublets of superconducting combined function magnets [159–161] (SCFMs). At intervals of SCFMs, three pairs of horizontal and vertical superconducting steering magnets are installed to correct the beam orbit. In the final focusing section, ten normal conducting magnets (four steering, two dipole and four quadrupole magnets) guide and focus the beam onto the target, while directing the beam downward by 3.637 degrees. The beam duct, inside of the primary beamline, is kept at high vacuum.

The well-tuned proton beam is essential for the stable neutrino beam production and for the less beam loss which is necessary to realize the high power beam operation. Therefore, the intensity, position, profile and loss of the proton beam along the primary beamline are precisely monitored by five current transformers (CT), 21 electro-static monitors (ESM), 19 segmented secondary emission monitors (SSEM) and 50 beam loss monitors (BLM), respectively. The performance of these monitors described below was evaluated in the beam operation (see Appendix C.2.1 for detail). Figure 3.4 shows photographs of these monitors. For the radiation tolerance, polyimide cables and ceramic feedthroughs are used for the beam monitors. The

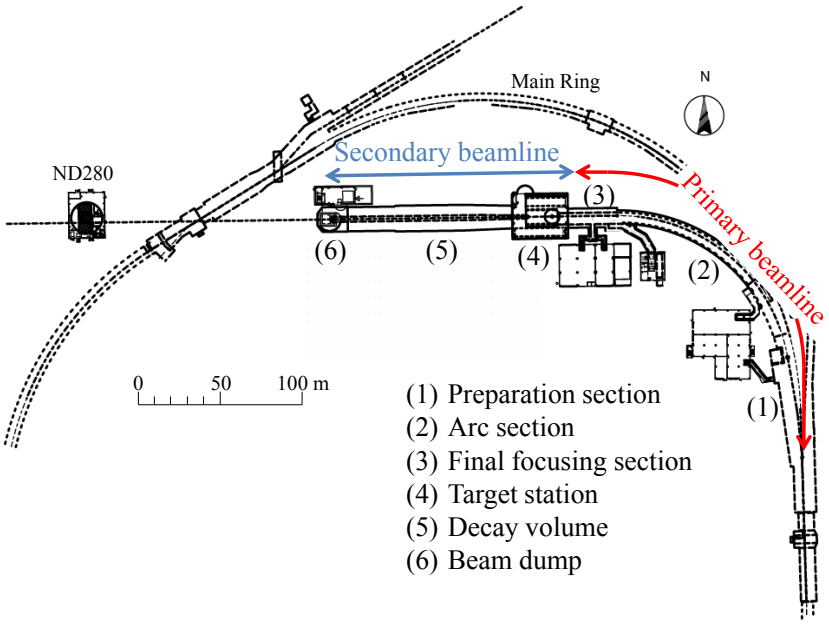

Figure 3.3: Overview of the T2K neutrino beamline.

monitor locations are shown in Fig. 3.5. The most downstream ESM and SSEM are installed in the "monitor stack" located in the 70 cm thick wall at the end of the primary beamline. Because of the high radiation level, the monitor stack is equipped with a remote-handling system for the monitors.

Beam intensity monitor (CT)

The CT is a toroidal coil: 50 coils of a copper wire around a ferromagnetic core. To realize a wide dynamic range of the response linearity for the short pulsed bunches, the CT uses FINEMET® (nanocrystalline Fe-based soft magnetic material) core, which has a high saturation flux density, high relative permeability and low core loss over a wide frequency range. The core is 260 mm in inner diameter and it weights 7 kg. It is impregnated with epoxy resin. Between the core and the copper wire, radiation tolerant insulators are used: polyimide and alumina fibar tapes. Each CT is covered by an iron shield against electromagnetic noise.

The CT signal is read by a 160 MHz FADC. The CT is calibrated by using another coil around the core, to which a beam-like pulse current from a pulse generator is applied. The precision of the calibration is 2% in the absolute scale. The shot-by-shot fluctuation of the intensity measurement is 0.5%. The CT also measures the beam timing. The shot-by-shot fluctuation of the timing measurement is 5 nsec in RMS.

Beam position monitor (ESM)

The ESM has four round-rectangular electrodes surrounding the proton beam orbit (80-degree coverage per electrode). By measuring top-bottom and left-right asymmetry of the beam-induced current on the electrodes, it monitors the proton beam center position nondestructively (without direct interaction with the beam). The longitudinal length of the ESM is 125 mm for the 15 ESMs in the preparation and final focusing sections, 210 mm for the five ESMs in the arc section and 160 mm for the ESM in the monitor stack.

The ESM signal is read by a 160 MHz FADC. The systematic error of the beam center

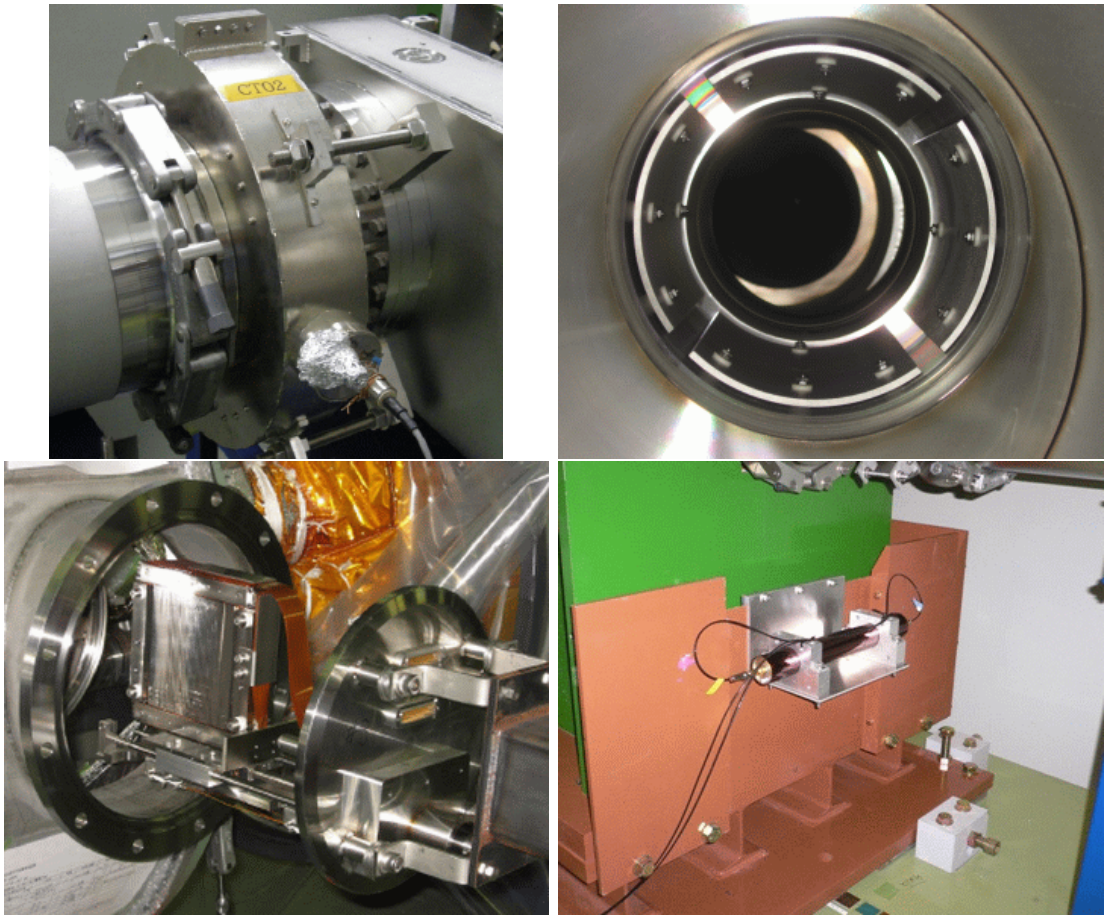

Figure 3.4: Photographs of the primary beamline monitors. Upper left: CT (outside view). Upper right: ESM (inside view showing four electrodes). Lower left: SSEM (being installed in the arc section). Lower right: BLM (installed beside a normal conducting magnet).

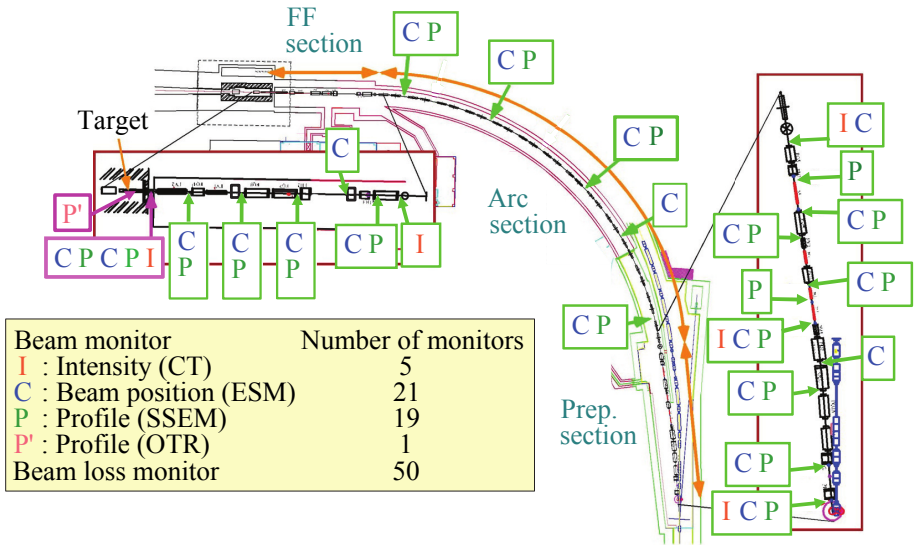

Figure 3.5: Location of the primary beamline monitors.

position measurement is estimated to be less than 0.45 mm, while the required precision is 0.50 mm.

Beam profile monitor (SSEM)

The SSEM has two thin (5 μm, 10^{-5} interaction length) titanium foils stripped horizontally and vertically, and an anode HV foil between them. The strips are hit by the proton beam and emit secondary electrons in proportion to the beam intensity. The electrons drift along the electric field and induce currents on the strips. The induced signals are transmitted to 65 MHz FADCs through twisted pair cables. The signal distribution is reconstructed as the proton beam profile. The systematic error of the beam center position and width measurements is estimated to be less than 0.45 mm and 0.20 mm, respectively, while the required precision is 0.50 mm and 0.70 mm, respectively.

Optics parameters of the proton beam (Twiss parameters and emittance) are reconstructed from the profiles measured by the SSEMs, and are used to estimate the profile center, width and divergence at the target.

Since the SSEM causes a beam loss (0.005% loss), it is remotely inserted into the beamline only when the beam profile needs to be measured. The position in the beamline can be reproduced with a 10 μm precision.

Beam loss monitor (BLM)

To monitor the beam loss, 19 and 10 BLMs are installed near the beam duct in the preparation and the final focusing sections, respectively, and 21 BLMs are near the SCFMs in the arc section. The BLM is a wire proportional chamber filled with Ar-CO_2 mixture. The signal is integrated during each spill, and if it exceeds a threshold, a beam abort signal is fired. The raw signal before integration is read by a FADC with 30 MHz sampling for software monitoring.

3.2.2 Secondary beamline

The secondary beamline consists of three sections: the target station, decay volume and beam dump. The secondary beamline is filled with helium gas (1 atm) to reduce the pion absorption and to suppress tritium and NO_x production by the beam. The target station contains the followings from the upstream; a titanium-alloy beam window to separate the primary beamline vacuum and the target station helium; a baffle which is a collimator to protect the magnetic horns; an optical transition radiation (OTR) monitor to monitor the proton beam profile just upstream of the target; the target to generate secondary pions; and three magnetic horns excited by 320 kA (250 kA until June 2010) current pulses to focus the pions. The pions enter the $\sim$96 m long decay volume to mostly decay into muons and muon neutrinos. All the remnants of the undecayed pions and other hadrons are stopped by the beam dump.

Target station

The target station is a 15 m long, 4 m wide and 11 m high helium vessel made of 10 cm thick steel. Including the decay volume, the volume of the vessel is 1500 m^3. Water cooling channels, called plate coils, are welded to the surface of the vessel, and 30°C water cools the vessel to prevent its thermal deformation. Tons of concrete and iron shieldings are put in and around the target station.

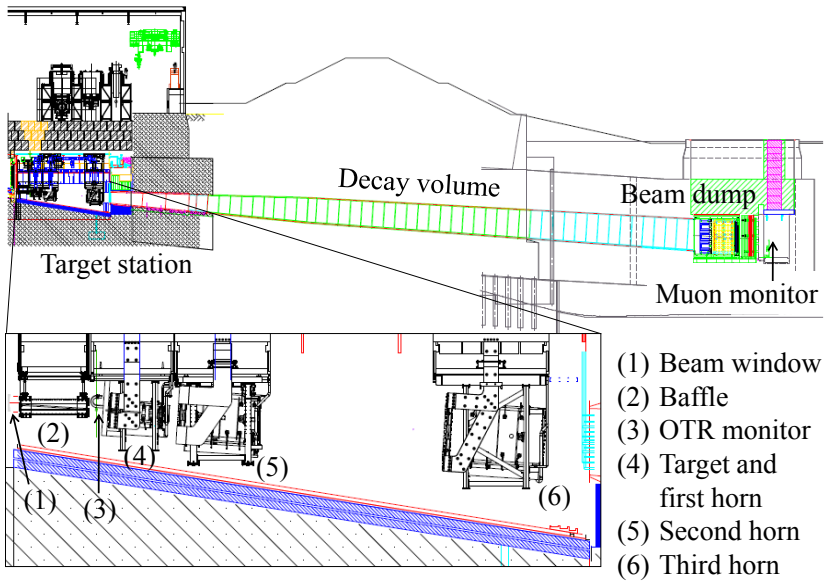

Figure 3.6: Side view of the secondary beamline.

Baffle

The baffle is located between the beam window and the OTR monitor. It is a 1.7 m long, 0.3 m wide and 0.4 m high graphite block, with a beam hole 30 mm in diameter. The primary proton beam passes through this hole.

OTR monitor

The OTR monitor has a thin titanium-alloy foil, which is placed at 45 degrees to the incident proton beam. As the beam passes through the foil, visible light (transition radiation) is produced. Some amounts of light reflected backward at 90 degrees to the beam are directed away from the target area; the light is transported in a dogleg path through the iron and concrete shieldings by four aluminum 90-degree off-axis parabolic mirrors to a less-radiation location. It is then collected by a CCD camera to produce an image of the proton beam profile.

The OTR monitor has an eight-position carousel holding four titanium-alloy foils, an aluminum foil, a fluorescent ceramic foil, a calibration foil and an empty disk (Fig. 3.7). A stepping motor is used to rotate the carousel from one foil to the next. The aluminum and ceramic foils are used for the middle and low intensity beam, respectively, because they reflect more intense light than the titanium foil. The calibration foil has precisely machined fiducial holes, of which image can be taken using back-lighting from lasers and filament lights. It is used for monitoring the alignment of the OTR system. The empty disk is used for back-lighting the mirror system.

The systematic error of the beam center position and width measurements is estimated to be 0.4 mm and 0.3 mm, respectively.

Target

The target core is a 2.6 cm diametral, 91.4 cm long and 1.8 g/cm^3 graphite rod, which corresponds to 1.9 radiation length. The core is surrounded by a graphite tube, and they are contained in a titanium case as shown in Fig. 3.8. The target is inserted in the first horn as shown in Fig. 3.9.

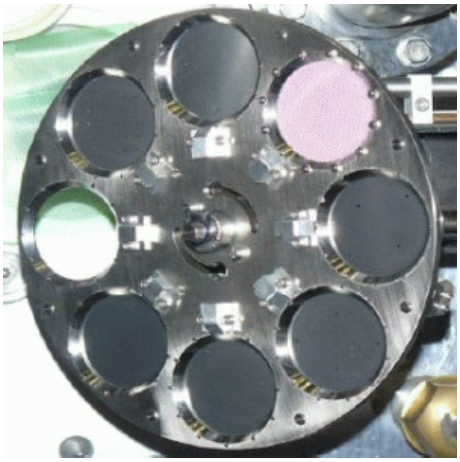

Figure 3.7: Photograph of the OTR monitor carousel.

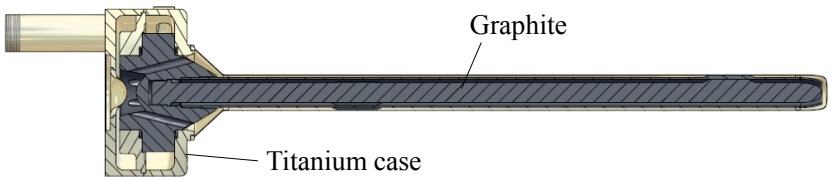

Figure 3.8: Cross section view of the target. The proton beam enters from the left side. The vertical and horizontal scales are different (4 : 1) in this figure.

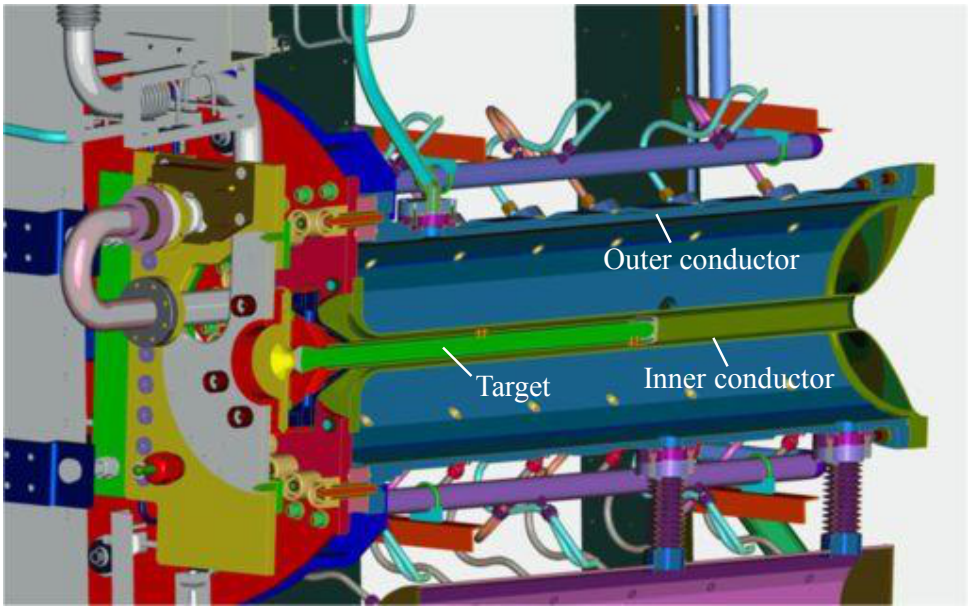

Figure 3.9: Cross section view of the first horn.

Table 3.3: Systematic error on the horn magnetic field.

Systematic error of the horn current measurement	
Calibration of the Rogowski coil	1%
Calibration of the readout electronics	$< 1\%$
Setting of the Rogowski coil	$< 1\%$
Total	$< 1.8\%$
Discrepancy between the measured and expected magnetic fields	$< 2\%$

Magnetic horn

The magnetic horn consists of two coaxial (inner and outer) conductors which encompass a closed volume [162, 163]. The conductors are loaded with a pulsed current, and a toroidal magnetic field is generated in that volume. The field varies as $1/r$, where r is a distance from the horn axis. The maximum field is 2.1 T for the current at 320 kA.

T2K adopts the three-horn configuration. The first horn collects the pions, and the second and third horns focus them. The horn conductor is made of aluminum-alloy (6061-T6). The dimensions (the minimum inside diameter, inner conductor thickness, outside diameter and length) are 54 mm, 3 mm, 400 mm and 1.5 m for the first horn, 80 mm, 3 mm, 1000 mm and 2 m for the second horn, and 140 mm, 3 mm 1400 mm and 2.5 m for the third horn, respectively. They are optimized to maximize the neutrino flux; the inside diameter is as small as possible to gain the maximal magnetic field, and the conductor is as thin as possible to minimize the pion absorption, while it is tolerant of the Lorentz force by the 320 kA current and the thermal shock by the beam.

Horn current monitor

The horns are connected in series by four pairs of aluminum bus-bars, through which the pulsed current (a few msec width) is loaded. The currents on the bus-bars are monitored by four Rogowski coils per horn with 200 kHz FADCs. The systematic errors of the current measurement are summarized in Table 3.3. The Rogowski coil and the readout electronics were calibrated to a precision of 1% and less than 1%, respectively. The signal of the Rogowski coil can be changed by the shape of the coil, and the maximum change is estimated at 1%. In total, the systematic error of the horn current measurement is less than 1.8%.

The magnetic field in each horn was measured by using a three-axis hall probe calibrated to a precision of $\pm 1\%$. The measured magnetic field agreed with the expectation from the load current within 1–2%. Therefore, it is concluded that the uncertainty of the horn magnetic field expected from the measured current is 2%.

Decay volume

The decay volume is a 96 m long steel tunnel. The cross section is 1.4 m wide and 1.7 m high at the entrance, and 3.0 m wide and 5.0 m high at the end. The decay volume is surrounded by 6 m thick reinforced concrete shieldings. Along the beam axis, 40 plate coils are welded on the steel wall to cool the wall and concrete with water.

Beam dump

The beam dump sits at the end of the decay volume. Its core is made of 75 ton graphite (1.7 g/cm^3), and is 3.174 m long, 1.94 m wide and 4.69 m high. It is contained in the helium

vessel. Two and fifteen iron plates in and outside the vessel, respectively, are placed at the downstream of the graphite core. The total iron thickness is 2.40 m. Only muons above 5 GeV can go through the beam dump to reach the downstream muon pit.

Muon monitor

The muon monitor [164,165] is located just behind the beam dump, where the distance from the target is 118 m. It sits on the beam axis and measures the bunch-by-bunch intensity and profile of the muon beam. The neutrino beam direction is measured as a direction from the target to the center of the muon profile. Detailed descriptions of the muon monitor are given in Chap. 4.

3.2.3 Beamline online system

For the stable and safe operation of the beamline, the online system collects information on the beamline equipments and the beam measured by the beam monitors, and feeds it back to the operation. It also provides the spill information to Super-K for the event synchronization by means of the GPS (Global Positioning System).

Event synchronization

Both at J-PARC and Super-K sites, the event timing is measured by using one pps (pulse per second) from two GPS receivers (for redundancy) and a 100 MHz clock from a rubidium clock with a precision of approximately 10 nsec. When the timing signal synchronized with the MR extraction is received, the time is recorded to a LTC (Local Time Clock) module at J-PARC. The LTC module counts the accumulated number of the received signals as the spill number. This time information and the spill number are sent to Super-K through L2-VPN, and are returned from Super-K to check consistency. The LTC module also provides the beam trigger for the beam monitors.

Data acquisition (DAQ) system of the beam monitors

The signals of the beam monitors are gathered into five nearby locations and are read by each readout system on a spill by spill basis. For the SSEM, BLM, horn current monitor and the muon monitor, the COPPER/FINESSE readout system [166] is utilized. At each location, the signals are built into a sub-event. The sub-events from all the locations are sent to MIDAS [167], which controls the overall DAQ system, and are built into an event. The data size an event is approximately 1.8 MB including the GPS data. The data processed by MIDAS is sent to an event-distributor, which then distributes the data to online monitoring programs so that every spill is monitored in real time. The data is also recorded in a disk in a ROOT [168] format.

Beamline control system

The online monitoring programs analyze the beam monitor data and output physics quantities such as the proton beam center, width, etc. These beam monitor outputs as well as the spill number, status of the beamline equipments, etc. are recorded by EPICS [169]. EPICS also controls the beamline equipments by PLCs (Programmable Logic Controllers).

Based on the data from EPICS, the beam orbit and optics are simulated by SAD [170], and the magnet currents to be adjusted are also calculated.

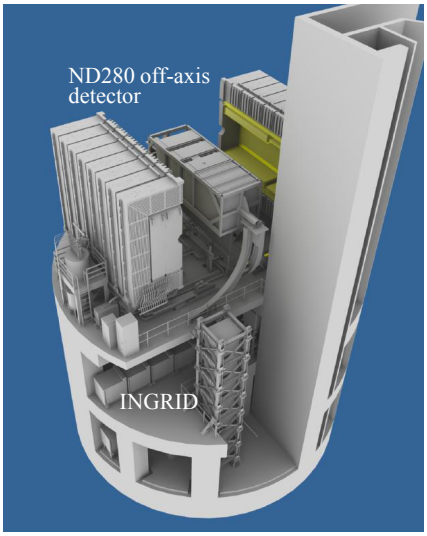

Figure 3.10: ND280 detectors. The ND280 off-axis detector and the magnet are located at the upper level, and the vertical and horizontal INGRID modules are located at the bottom levels. The magnet is opened in this figure. The neutrino beam enters from the right side.

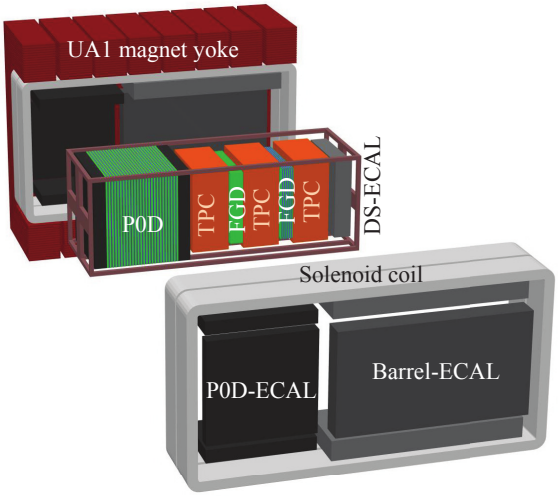

Figure 3.11: Exploded view of the ND280 off-axis detector. The neutrino beam enters from the left side.

Interlock

The interlock system is working to protect persons (PPS: Person Protection System) and the machines (MPS: Machine Protection System). PPS is fired by an emergency stop button, door interlock, radiation monitor and so on. MPS is fired by a quenching of the SCFMs, error from the normal conducting magnet or horn system, excess of the loss monitor signal and so on.

3.3 Near detectors

The neutrino energy spectrum, flavor content, and interaction rates of the unoscillated beam are measured by a set of detectors at the near (J-PARC) site. They are called the ND280 detectors because they are located approximately 280 m from the target (Near Detector at 280 m). There are two detectors at the ND280 site. One is a magnetized tracking detector located in the same direction to Super-K, called the ND280 off-axis detector. It is used to predict the neutrino flux at Super-K. Another is the INGRID (Interactive Neutrino GRID) detector located on the beam axis. It measures the on-axis neutrino beam profile to monitor the neutrino beam direction. These detectors are housed in a pit inside the ND280 hall as shown in Fig. 3.10.

3.3.1 ND280 off-axis detector

An exploded view of the ND280 off-axis detector is shown in Fig. 3.11. The ND280 off-axis detector elements are contained inside the magnet recycled from the UA1 experiment at CERN [171]. The magnet generates a horizontal uniform magnetic field of 0.2 T with a 2900 A current.

Inside the upstream end of this magnet sits a Pi-Zero Detector [172] (P0D) consisting of tracking planes of scintillating bars alternating with lead foils and water. The objective of the P0D is to measure the neutral current π^0 production rate ($\nu_\mu + N \rightarrow \nu_\mu + \pi^0 + X$) for the estimation of the background against the ν_e appearance signal at Super-K.

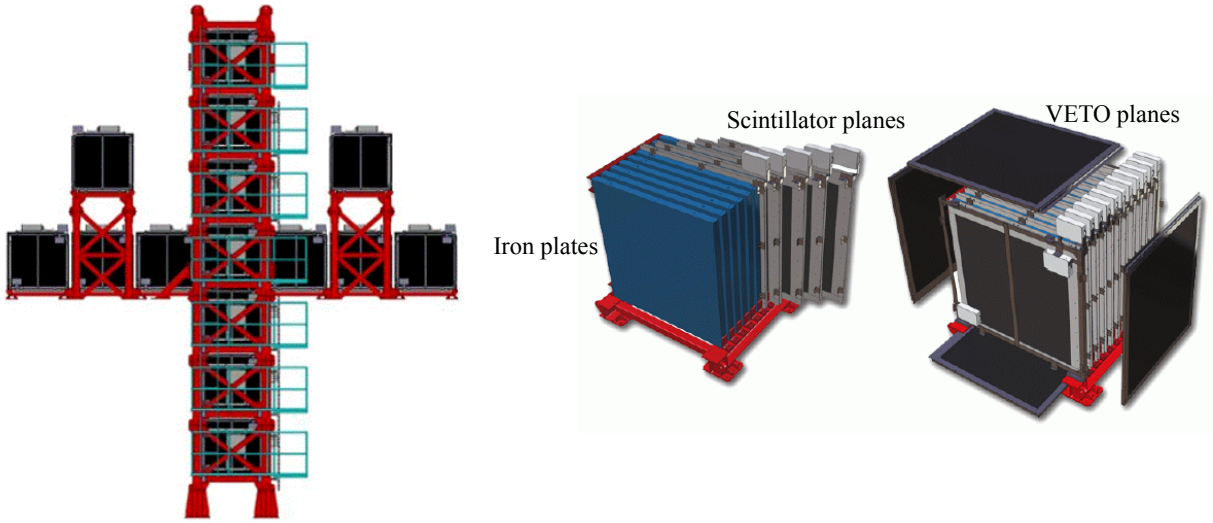

Figure 3.12: INGRID detector. Left: Front view. INGRID consists of seven horizontal and seven vertical modules. There are extra two modules on the diagonal, which were installed during the summer shutdown in 2010. Right: Exploded view of an INGRID module.

Downstream of the P0D, three Time Projection Chambers [173] (TPCs), together with two Fine Grained Detectors [174] (FGDs) are placed to measure charged current interactions. The TPCs use a gas mixture Ar:CF_4:iC_4H_{10} (95:3:2) and MicroMegas detectors [175]. They measure the three-momenta of charged particles produced in neutrino interactions to reconstruct the neutrino energy spectrum, and measure the ionization rate to determine the particle type. The FGDs consist of layers of finely segmented scintillating bars. They provide target mass for neutrino interactions as well as tracking of charged particles coming from the interaction vertex. The downstream FGD also provides water target.

The P0D, TPCs, and FGDs are all surrounded by an sampling electromagnetic calorimeter (ECAL). Each ECAL module consists of layers of plastic scintillator bars and Pb absorber sheets between the layers. The role of the ECAL is to detect γ-rays which do not convert in the inner detectors and to detect charged particles for their identification (electron-muon-pion separation).

All sides of the magnet are instrumented with the Side Muon Range Detector [176] (SMRD). Scintillator plates are inserted between gaps of the magnet yokes to measure the ranges of muons which exit any side of the inner detectors.

3.3.2 INGRID

INGRID consists of seven horizontal and seven vertical modules (and two extra modules on the diagonal, which are not used in this thesis). Each module is made of alternate layers of an iron plate and scintillator bars as shown in Fig. 3.12. INGRID counts the number of neutrino events in each module and reconstructs the neutrino profile. To measure the neutrino beam direction with a precision much better than 1 mard, neutrino events are accumulated for approximately one day in the 750 kW operation. INGRID complements the measurement of the neutrino beam direction with the muon monitor, since it monitors the neutrino beam itself while the muon monitor monitors the neutrino beam by measuring the muon beam spill-by-spill.

3.4 Super-Kamiokande detector (Super-K)

Super-K [152] serves as the far detector in T2K. It is in operation also to study the atmospheric [20, 21] and solar [27, 177] neutrinos, to watch cosmic neutrinos from supernova explosions [178], to search for baryon-number-violated proton decay signals [179, 180], and more.

3.4.1 Detector overview

Super-K is located 295 km west of J-PARC in the Kamioka mine, 1 km deep inside a mountain (see Fig. 3.13). It is a cylindrical cavern, 39 m in diameter and 42 m in height, filled with 50 kton of pure water and has a 22.5 kton fiducial volume. It is mainly comprised of two segments: the inner and outer detectors. The inner detector holds 11129 inward-facing 20 inch diameter photomultiplier tubes (PMTs) on its cylindrical wall. Neutrinos are detectable with these PMTs by measuring Cherenkov lights emitted by charged particles from neutrino interactions in water. The Cherenkov lights are fitted to rings, from which the particles' vertex, energies, directions and species are reconstructed. Neutrino interactions are distinguished from the other activities like cosmic muons by selecting events in which the vertex exists inside the Super-K fiducial volume. The outer detector contains 1885 outward-facing 8 inch PMTs on the inner wall. It is used to veto cosmic muons and other backgrounds and to discriminate charged particles which exit the inner detector.

Two MC simulation programs are utilized to estimate the number of neutrino events in Super-K. These simulation programs are described in Appendix B.

3.4.2 T2K beam data

Super-K records the charge (the amount of Cherenkov light) and timing of each PMT signal as a "hit". Every hit is continuously collected, and is built as an event by an online software-trigger program.

The T2K beam data is acquired by recording all hits in a 1 msec time window synchronized with the beam arrival timing as illustrated in Fig. 3.14. The beam arrival time is determined by utilizing the GPS time synchronized between J-PARC and Super-K; the T2K beam neutrinos are expected to arrive at Super-K approximately 1 msec after the proton beam hits on the target, where 1 msec is the neutrino TOF (Time of Flight) for 295 km. The beam timing information is a powerful tool to distinguish the T2K beam neutrino events from the other atmospheric neutrino events, low energy backgrounds, etc. Further reduction of the T2K beam data is described in Sec. 7.1.4 and 10.1.

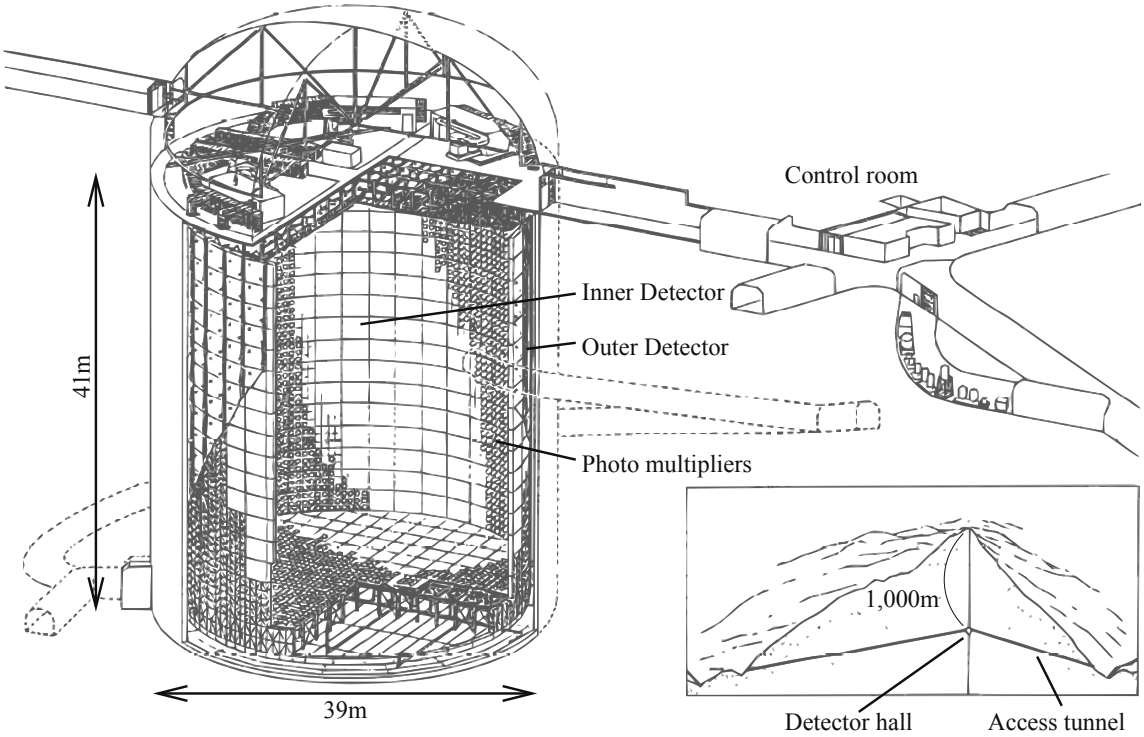

Figure 3.13: Schematic overview of Super-K. This figure comes from Ref. [149].

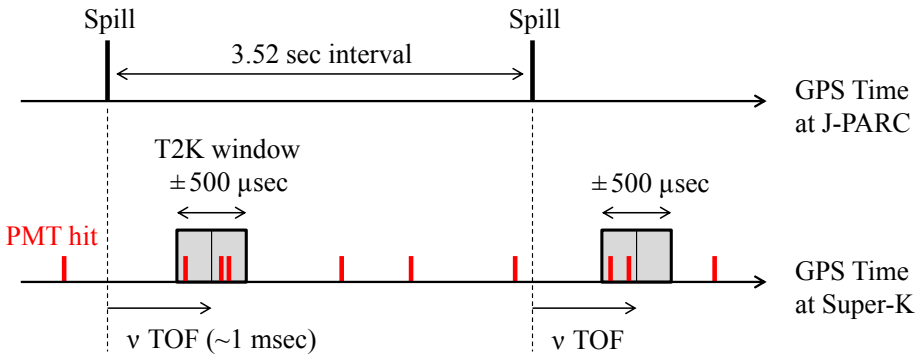

Figure 3.14: Illustration of the T2K beam data acquisition at Super-K. The T2K time window for ± 500 μsec is set at the beam arrival time which is approximately 1 msec of the neutrino TOF (Time Of Flight) after each spill.

Chapter 4

Muon Monitor Design

The neutrino beam can be monitored by measuring the muon beam. The measurement of the muon beam in T2K is a challenging task because the intensity of the muon beam is extremely high and the radiation damage and radioactivation must be taken care of (Sec. 4.1). Therefore, the requirements for the muon monitor is stringent (Sec. 4.2). We designed and built the muon monitor to conquer these difficulties and to measure the muon beam stably and precisely (Sec. 4.3).

4.1 Characteristics of the muon beam

The characteristics of the muon beam at the muon monitor position is studied with the Monte Carlo simulation (JNUBEAM, pre-tuned version; see Sec. 8.1 for detail).

The expected profile of charged particles is shown in Fig. 4.1. It is close to a Gaussian distribution with a sigma of approximately 1 m around the beam center. The number of charged particles at the profile center is estimated at $\sim 8 \times 10^7$ /cm^2/spill for 3.3×10^{14} protons/spill. The expected ratio of the muons to all the charged particles is 87% and the remaining percentage is predominantly due to δ-rays knocked out by the muons. Only muons with energy above 5 GeV can go through the beam dump and reach the muon monitor. This muon energy threshold for the beam dump is chosen to minimize the hadron flux at the muon monitor while keeping the sensitivity to the neutrino beam direction. The momentum distribution of the muons at the muon monitor is shown in Fig. 4.2. The mean momentum is approximately 3 GeV/c. An absorbed dose at the muon monitor is estimated at about 100 kGy for a 100-day operation with the 750 kW proton beam power. Therefore, ordinary plastics, Fe, etc. cannot be used due to radiation damage or radioactivation. The muon beam structure is the same as the proton beam one: eight bunches/spill, 581 nsec bunch interval and 58 nsec bunch width. These characteristics of the muon beam are summarized in Table 4.1.

Figure 4.3 shows the momentum-angle (p-θ) distribution of secondary pions whose descendant muons reach the muon monitor (also see Fig. 8.5 for comparison with the distribution for neutrinos). There are two islands; the upper one is constituted by pions focused by the horns and disappears when the horns are off, and the lower one is constituted by pions not affected by the horns and remains when the horns are off. The upper island is the dominant constitution of the muon beam. Therefore, the muon beam is sensitive to the horn focusing effect.

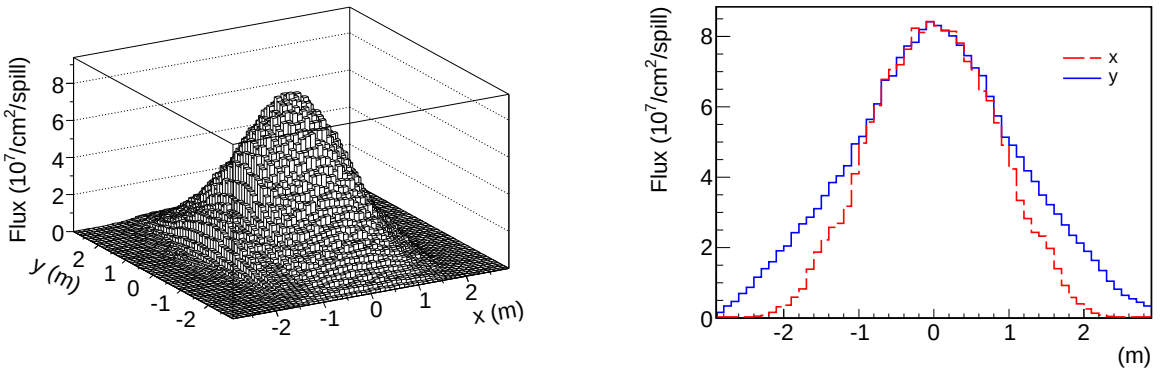

Figure 4.1: Profile of charged particles at the muon monitor: a two-dimensional histogram (left) and slice histograms at $y = 0$ and $x = 0$. These are estimated by JNUBEAM with the horn currents at 320 kA, and are scaled to 3.3×10^{14} protons/spill. The horizontal and vertical axes are denominated x and y, respectively. The difference between the x and y profiles comes from the difference of the horizontal and vertical sizes of the decay volume.

Table 4.1: Characteristics of the muon beam at the muon monitor for the beam intensity at 3.3×10^{14} protons/spill and the horn currents at 320 kA. These are estimated by JNUBEAM.

Number of charged particles	$\sim 8 \times 10^7$ /cm^2/spill around the beam center
Beam composition	muons (87%) and δ-rays (13%)
Profile shape	nearly Gaussian distribution ($\sigma \approx 1$ m)
Mean muon momentum	$\sim$3 GeV/c
Spill cycle	$\sim$0.3 Hz
Number of bunches	8 bunches/spill
Bunch interval	518 nsec
Bunch width	58 nsec
Absorbed dose	$\sim$1 kGy/day

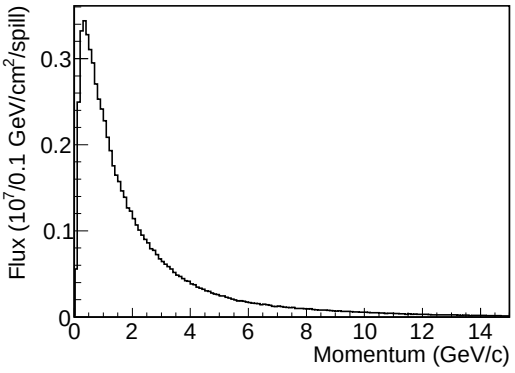

Figure 4.2: Momentum distribution of muons at the muon monitor for the beam intensity at 3.3×10^{14} protons/spill and the horn currents at 320 kA.

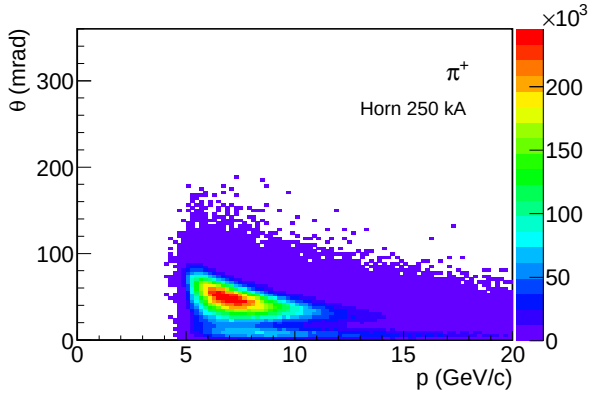

Figure 4.3: p-θ distribution of secondary pions whose descendant muons reach the muon monitor.

4.2 Requirements for the muon monitor

The requirements for the muon monitor are:

1. to monitor the stability of the neutrino beam intensity with a precision better than 3% by measuring the muon beam intensity;
2. to measure the neutrino beam directions in x and y with a precision better than 0.25 mrad each, which corresponds to a 3 cm precision of the muon profile center, in order to tune the neutrino beam direction within 1 mrad;
3. to measure the beam intensity and direction on a bunch-by-bunch basis;
4. to measure the intense muon beam of 10^5–10^7 μ/cm^2/bunch, which corresponds to the proton beam intensity of $4 \times (10^{11}$–$10^{13})$ protons/bunch;
5. to be tolerant of radiation and resistant to activation;
6. to run stably to minimize deadtime due to repair.

To reconstruct the muon profile, the muon monitor is equipped with 49 sensors in a 150×150 cm^2 plane. The muon intensity is monitored by measuring a sum of the 49 sensor signals. The error on the intensity monitoring comes from the deviation from the detector's linearity against the muon intensity and the detector's stability, which have to be kept within 3% in total. The muon profile is measured by using the relative signal of each sensor. Therefore, the error on the beam direction measurement comes from relative gain differences among the sensors in addition to the linearity and stability. To achieve the requirement (2), each sensor should measure the muon intensity within 4% precision.

The muon monitor must satisfy the requirements (1), (2) and (3) for the intense muon beam of $\sim 10^7$ μ/cm^2/bunch, when the proton beam intensity is 3.3×10^{14} protons/(8 bunches). It is the same with the low intensity beam of $\sim 10^5$ μ/cm^2/bunch at the beginning of the beam tuning, when the proton beam intensity is 4.1×10^{11} protons/bunch (only one bunch per spill). Therefore, the linearity over the wide range of the intensities (wide dynamic range) is required. It is one of the most stringent requirements.

A muon monitor is a commonly used instrument in accelerator neutrino experiments [92, 181–184]. However, the muon monitor in T2K is a challenging detector; it has difficulty in precisely measuring the most intense muon beam ever and in stably working in such a severe radiation environment. Compared to the currently operating muon monitors in the CNGS [185] and NuMI [186] beamlines, where the maximum muon beam intensities are 4.8×10^4 μ/cm^2/bunch(2 nsec) and 6.2×10^4 μ/cm^2/bunch(3–8 nsec),* respectively, the T2K muon beam intensity, 1×10^7 μ/cm^2/bunch(58 nsec), is much higher.

4.3 Instruments of the muon monitor

A schematic view of the muon monitor is shown in Fig. 4.4 and the photograph is in Fig. 4.5. The muon monitor consists of two independent detector systems: an array of ionization chambers and another array of silicon PIN photodiodes. In each array, there are 7×7 sensors at 25-cm intervals. The 7×7 is the minimum number of sensors with which the muon profile center can be surely reconstructed with a precision better than 3 cm even if the measurement error of each sensor is 4%.

*At the most upstream muon monitor. CNGS and NuMI have two and three muon monitors in different alcoves, respectively.

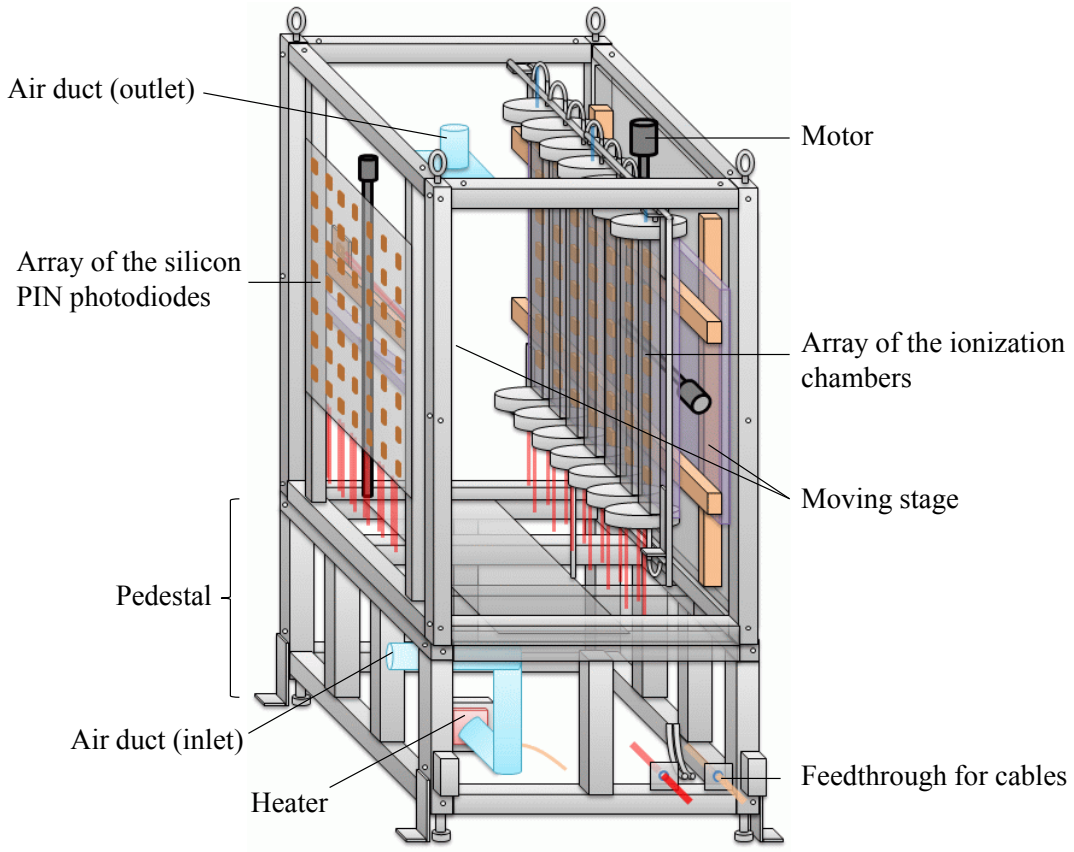

Figure 4.4: Schematic view of the muon monitor. The beam enters from the left side. On the upstream side, 49 silicon PIN photodiodes are placed on the support enclosure. On the downstream side, the large moving stage holds seven ionization chambers, each of which contains seven sensors. The whole structure is covered with aluminum insulation panels, which are not drawn in this figure.

The ionization chamber is suitable for the T2K muon monitor because its structure and operation are simple and robust and because it can be made out of radiation tolerant material. However, to get stable response, fine control of the gas quality is necessary. On the other hand, the silicon PIN photodiode is easy to handle, and its response is expected to be stable unless radiation damage. Only radiation damage is the disadvantage of the photodiode. Because the signal of the photodiode is larger than the one of the ionization chamber, the photodiode is useful at the early stage of T2K in particular when the beam intensity is low and the signal of the ionization chamber is small. Hence, these different types of detectors provide redundant and complementary measurements.

The signals of the detectors are read by 65 MHz FADCs. The signal of the silicon PIN photodiode needs to be attenuated by 30 dB at the maximum. An attenuator which has linearity within $\pm 0.9\%$ up to 30 V of an input pulse and cross-talk of less than 0.02% between adjacent channels is used for the photodiode.

The detectors are put inside an aluminum support enclosure. The support enclosure has three roles: to align the detectors, to keep the temperature inside the enclosure for the ionization chamber gas, and to be equipped with a moving stage for each detector array. The sensors are relatively calibrated using the muon beam by moving the stage.

Almost all components of the muon monitor in the muon pit are made out of radiation

Figure 4.5: Photograph of the silicon PIN photodiodes (right) and the ionization chambers (left) in the support enclosure. The beam enters from the right side.

tolerant and low-activation materials such as polyimide, PEEK^{TM}, ceramic, aluminum and so on. EPDM has the lowest radiation dose limit of 10^6 Gy [187] among the materials in the muon pit except the silicon PIN photodiodes. The radiation tolerance of the photodiode is discussed in Sec. 4.3.2 and 5.2.1. Other instruments, like the readout electronics and high voltage (HV) units, are put in an electronics hut on the ground level.

4.3.1 Ionization chamber

A parallel plate ionization chamber[†] is used. The sensitive volume is $75 \times 75 \times 3$ mm^3.

To get wide dynamic range, two kinds of gases are used for the ionization chamber: Ar with 2% N_2 for a low intensity beam and He with 1% N_2 for a high intensity beam. By switching the gas from Ar to He, the signal is reduced by one order of magnitude because the ionization yields for a minimum ionization particle (MIP) in Ar and He gases at the standard condition[‡] (STP) are 95.6 cm^{-1} and 7.80 cm^{-1} [188], respectively. As a result, depletion of the signal due to recombination of electrons and ions can be avoided and the linearity of the signal to the beam intensity is guaranteed. To get a faster response, only the charge induced by electrons' drift is used as a signal, and one by ions' drift (10^3 times slower) is disregarded. In addition, N_2 is added as a quencher, which makes the response faster. The N_2 plays another important role by making the Jesse effect [189] saturated,[§] where the signal is insensitive to the amount of impurities in

[†]The ionization chamber for the NuMI muon monitor [186] was referred to on our ionization chamber mechanical design. They use pure He gas.

[‡]The temperature is 20°C and the pressure is 101.325 kPa (absolute).

[§]If there is only a few impurities in the gas, there is a big increase in ionization due to Penning ionization.

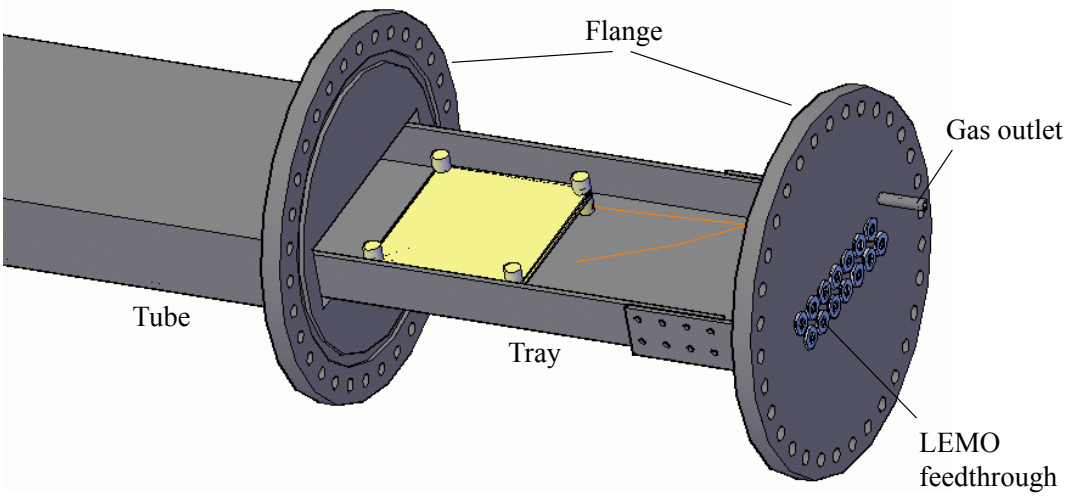

Figure 4.6: Drawing of the bottom end of the ionization chamber. In this figure, the tray is pulled out of the tube and one of the seven sensors appears.

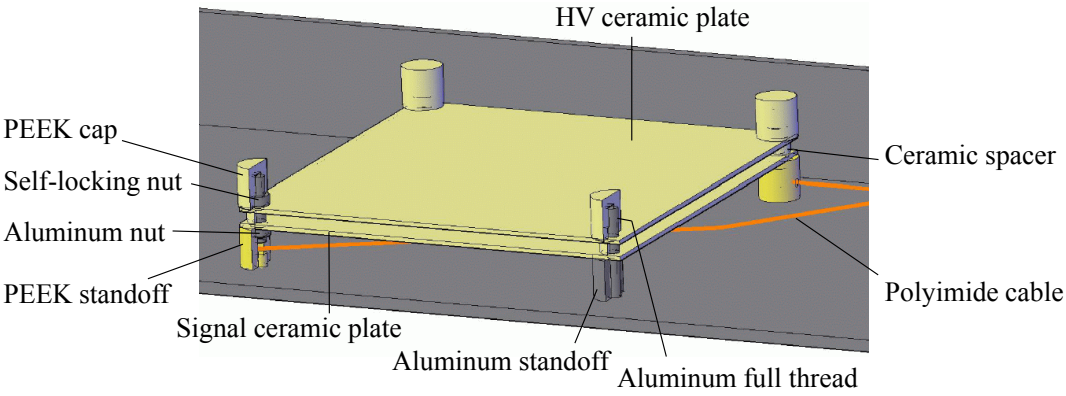

Figure 4.7: Drawing of a sensor of the ionization chamber. The two sets of standoffs, ceramic spacers and PEEK caps are shown in section.

the gas.

Keeping the gas temperature, pressure and purity is necessary to guarantee the stable response of the ionization chamber. Variance of the temperature and pressure leads to variance in gas density, which varies the signal size. Each parameter should be kept within 1.7% to keep the signal variance within 3%. The O_2 contamination is the most important index of the gas purity since oxygen captures carrier electrons and decreases the signal. It should be kept below 100 ppm in order to keep the signal depression by the electron attachment less than 1% [190]. The gas system is designed to keep variation of the gas temperature, pressure and purity much less than those requirements.

Therefore, the signal increases as a function of the density of impurities.

Design of the ionization chamber

The ionization chamber array consists of seven ionization chambers. A drawing of the ionization chamber is shown in Fig. 4.6. Each ionization chamber contains seven sensors. The sensors sit on a 1929-mm-long aluminum tray at an interval of 250 mm. The tray is inserted into a $150 \times 50 \times 1956$ mm^3 aluminum tube. At each end of the tube, an aluminum flange 235 mm in diameter is welded. Other aluminum flanges are attached to them and seal the tube with O-rings (U-TIGHT SEAL® JIS G-180) made of Inconel® and aluminum. Gas flows through 1/4-inch tubes welded to the flanges. On the bottom side flange, fourteen feedthrough connectors (LEMO® SWH.0S) for both signal and HV cables are mounted. The LEMO feedthrough is sealed with an O-ring made of EPDM. At the top in three out of the seven ionization chambers, a Pt100 resistance thermometer (PRT) in the four-wire configuration is installed to measure the temperature in the tube. For these PRTs, four-twisted polyimide-insulated wires and D-sub feedthrough connectors are used. The insulators of those LEMO and D-sub feedthrough connectors are made of PEEK.

Each sensor of the ionization chamber consists of two parallel $100 \times 100 \times 1$ mm^3 alumina-ceramic plates, which are separated by 3 mm by ceramic spacers with a tolerance of 100 μm. A drawing of the sensor is shown in Fig. 4.7. Signal (75×75 mm^2) and HV (93×93 mm^2) electrodes made of Ag-Pt are printed on the ceramic plates. The tolerance of the electrode size is 100 μm. The signal electrode is surrounded by a grounded electrode, which ensures a uniform electric field over the signal electrode. Thus, ionization pairs generated only in the $75 \times 75 \times 3$ mm^3 volume contribute to the signal. Conductive parts except the signal/HV electrodes are insulated from the gas with the PEEK caps, ceramic spacers and PEEK standoffs in order to prevent stray ionization from collecting on the conductors [191].

Gas system

A diagram of the gas system is drawn in Fig. 4.8. There are two feeds of the gas for the ionization chambers. Each feed consists of a manifold of five 7-m^3 gas cylinders. The gas pressure in each manifold is monitored by a pressure transducer (IBS® HSV-020MP). At the outlet of the manifold, the gas is decompressed to 0.2 MPa by a regulator (Swagelok® KCM). This regulator has a mechanism which automatically switches the gas feed from a depleted supply to the other and that ensures continuous flow of the gas. At the downstream of the regulator, the flow rate is set at approximately 100 cc/min to minimize the O_2 contamination. Two rotameters for Ar and He gases are built into the line and they are exchangeable with ball valves at their inlets and outlets. Proportional relief valves (Swagelok SS-RL3S4) in the line release the gas to protect the gas system if the pressure accidentally reaches 200 kPa (absolute). Tee-type filters (Swagelok TF) protect the gas system from particulate contaminants. Stainless tubes (1/4 inch) are used for the gas line to minimize outgassing from the tubes.

The gas temperatures in the ionization chambers are monitored by the three PRTs. Temperatures in all of the ionization chambers are kept within 1.5°C gradient and ± 0.2°C variance at around 34°C. The absolute gas pressure is monitored by five pressure transducers (IBS HBV-300KP), which are kept separate from the muon pit to avoid radiation. Two of them monitor the pressures in the feed and exhaust lines in the facility building, and two others monitor ones near the muon pit. The fifth pressure transducer at the most downstream point is used for the PID control of a solenoid control valve (burkert® Type2822), which keeps the gas pressure in the entire gas line at 130 ± 0.2 kPa (absolute). The O_2 contamination is monitored by an oxygen analyzer (TORAY® LC-750L) in the exhaust line. It is kept below 2 ppm at a gas flow rate of 100 cc/min. The flow rate is monitored by a mass flow meter (HORIBASTEC® SEF-E40) just downstream of the control valve.

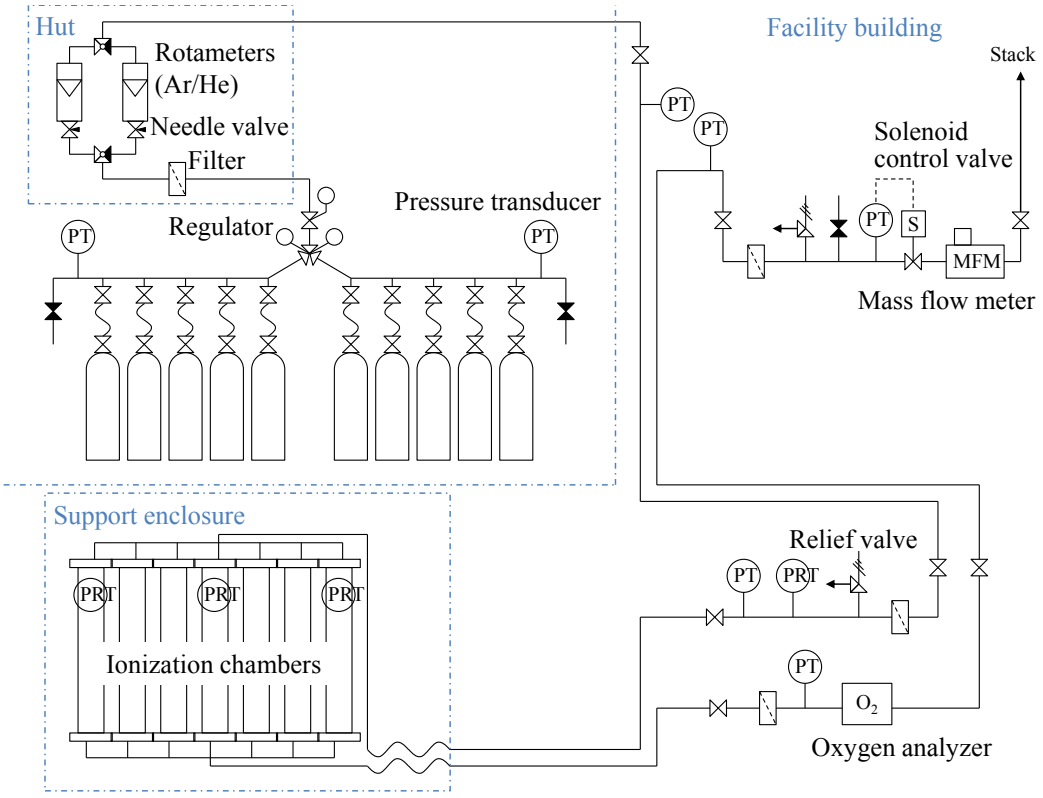

Figure 4.8: Diagram of the gas system for the ionization chambers. PT stands for a pressure transducer and PRT stands for a Pt100 resistance thermometer. The dash-dotted lines shows boundaries of the electronics hut, the facility building, and the support enclosure.

4.3.2 Silicon PIN photodiode

The silicon PIN photodiode (HAMAMATSU® S3590-08) has an active area of 10×10 mm^2 and a depletion layer thickness of 300 μm. The silicon layer is mounted on a ceramic base. To fully deplete the layer, a bias voltage of 80 V is applied.

The silicon PIN photodiode is not tolerant of the severe radiation in the muon pit. The depletion voltage or the collected charge varies as a function of fluence. There is a report [192] that as the 647-MeV proton fluence increases, the depletion voltage of their 200-μm thick silicon PIN detectors decreases. The depletion voltage falls 50% at about 0.7×10^{13} protons/cm^2 and reaches a minimum at 1.25×10^{13} protons/cm^2, where type inversion occurs. A 647-MeV proton causes approximately the same amount of radiation damage as the 1-MeV equivalent neutron fluence [193]. For the T2K muon beam, the fluence is estimated at about 10^7 1-MeV neutrons/cm^2/spill at the beam center at 0.75 MW. Therefore, the depletion voltage is expected to fall 50% in a month (about 0.7×10^6 spills).

Packages of the photodiodes were designed so that installation or replacement of the photodiodes can be quickly done in situ. The photodiode is put on a PEEK base fixed on the support enclosure and is covered by an aluminum base. In the PEEK base, two sockets soldered with co-axial polyimide cables are fixed.

4.3.3 The support enclosure

The dimensions of the support enclosure normal to and along the beam axis are 2.51 m and 1.71 m, respectively, and the height is 4.36 m. The height of the beam axis at the silicon array

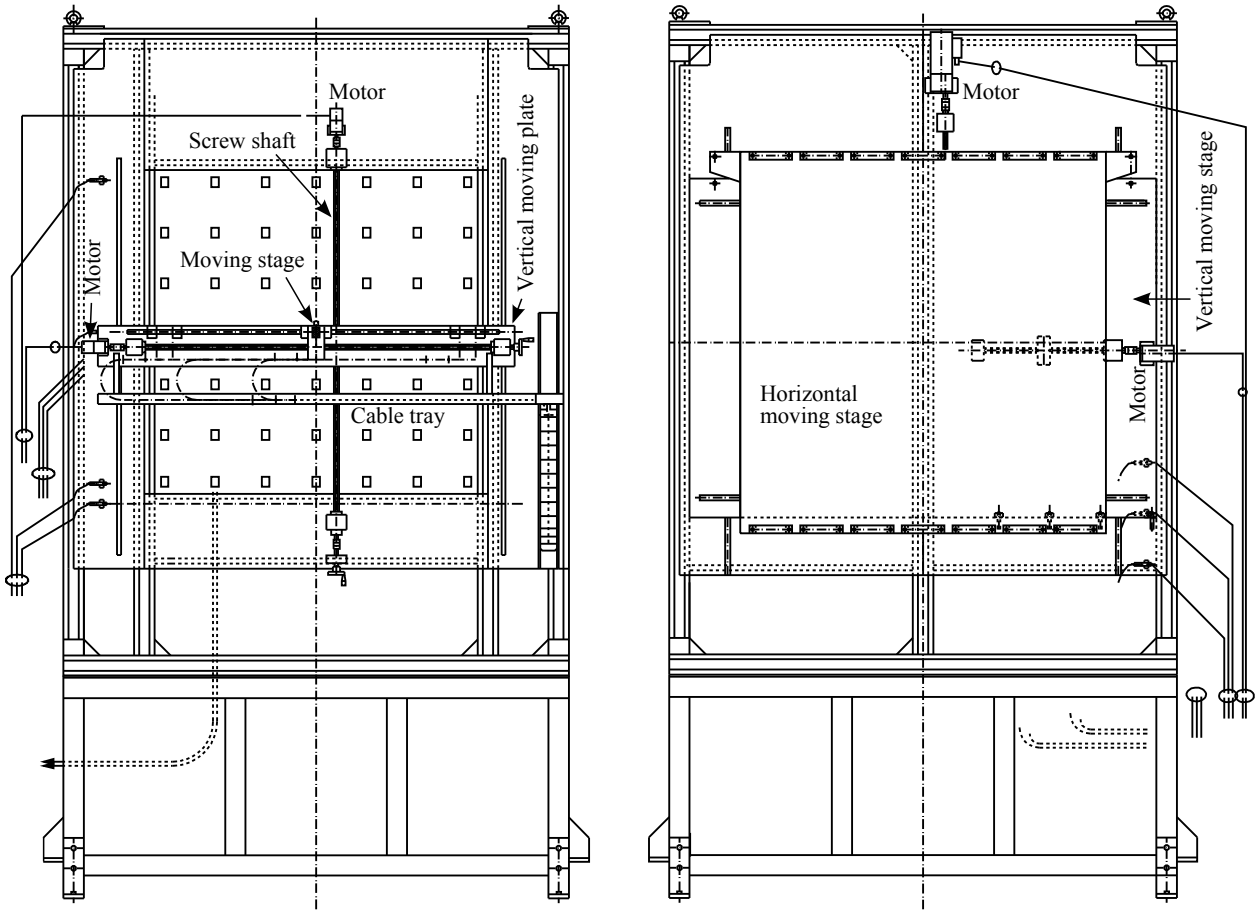

Figure 4.9: Moving stage for the silicon PIN photodiode (left) and for the ionization chamber (right). The left figure is a view from the downstream. The right figure is a view from the upstream. The ionization chambers are held on the horizontal moving stage in the right figure.

is 2.87 m from the floor. The secondary beamline was surveyed from the target station to the muon pit and the beam axis in the muon pit was defined with a precision better than 1 cm. The detectors are set with a precision better than 1 mm relative to the beam axis.

The support enclosure has two moving stages for relative calibration of the detectors: a small one which moves an extra silicon PIN photodiode just behind the silicon array (Fig. 4.9 left) and a large one which moves the ionization chambers (Fig. 4.9 right). The small moving stage is driven horizontally and vertically along linear guides by two stepping motors (ORIENTAL MOTOR RK569AMC). On the linear guides, radiation-hard lubricant (MORESCO-HIRAD® RG-42-1) is used as grease. The beam axis position, that is the origin of the stage, is detected by limit sensors of sliding touch type (Metrol® BP) assembled with polyimide-insulated wires. The large stage for the ionization chambers moves horizontally and vertically along linear guides by two induction motors (ORIENTAL MOTOR BHI62SMT and 4IK25GN). The position of the stage is detected by six limit sensors aligned horizontally and vertically at 25-cm intervals. Every limit sensor is aligned with a precision better than 1 mm.

The muon monitor is thermally insulated from the muon pit because the temperature in the muon pit could vary up to 33°C.[¶] Therefore, the support enclosure is covered by double aluminum panels filled with glass wool. The temperature around the ionization chambers is kept at around 34°C by a sheathed heater and the variance of the temperature is within ±0.7°C.

[¶]The variation of the temperature is due to a heat transfer from cooling water pipes for the beam dump.

4.3.4 Electronics and cables

The 65-MHz FADCs are employed in the COPPER/FINESSE readout system. The FADC gate opens for 7 μsec to contain all of the eight bunches. The FADC has an input impedance of 50 Ω and an amplifier of gain-5 or gain-1 with a shaping time of 50 nsec. The gain-5 FADCs are used for the ionization chambers and the gain-1 for the silicon PIN photodiodes. The full scale of the FADC is ± 1 V after the amplifier and the dynamic range is 12 bits. Because the signal of the silicon PIN photodiode is above the FADC full scale, it is attenuated with the π-type attenuator by 0, 15 or 30 dB according to the beam intensity. A protection circuit is implemented for each channel and prevents surge voltage going to the FADC. It consists of two zener diodes (RENESAS® HZ3A2) whose zener voltage is 2.6–2.8 V. A series of the diodes in a reverse and forward bias order is connected parallel to the FADC input. Thus a voltage loaded on the FADC is restricted within ± 4 V.

HV units (REPIC® RPH-32010) are used to apply bias voltages to the detectors individually. Low-pass filters follow the HV units to protect the electronics against surge voltage from the HV units and to ensure stable HV supply.

In the muon pit, polyimide cables are used except for the power cables of the heater and the motors. In the other area, non-halogen cables are used. For example, co-axial non-halogen cables with 50-Ω impedance (NH-5D-FB-E for the signal and RG-174/U$\times$10C NH-MCX for the HV) are laid for about 60 m from the electronics hut to a patch panel at the entrance of the muon pit. From the patch panel to the detectors, co-axial polyimide cables with 50-Ω impedance are laid for about 10 m both for the signal and the HV.

The FADCs and the signal cables were calibrated with a CAMAC charge/time generator (Phillips 7120) with a 1% precision.

Chapter 5

Muon Monitor Performance

The performance of the muon monitor detectors is presented in this chapter. Before installing the detectors in the T2K beamline, the ionization chambers and the silicon PIN photodiodes were tested with the 100 MeV electron beam at the Institute for Chemical Research (ICR) in Kyoto University and with the muon beam in the NuMI beamline (FNAL T968 test experiment) to check if they met the requirement for the muon monitor. The results of these tests are described in Sec. 5.2. After the installation in the T2K beamline, the integrated performance of the detectors as the muon monitor was checked with the T2K muon beam. The results are described in Sec. 5.3.

5.1 Estimation of the detectors' signals

The detector's collected charge Q can be estimated by using the following equation:

$$Q = \begin{cases} Ne_0(\Delta_{ave}/\Delta_{mip})Y_{mip}V/2 & \text{for the ionization chamber,} \\ Ne_0(\Delta_{ave}/\Delta_{mip})Y_{mip}V & \text{for the silicon PIN photodiode,} \end{cases} \quad (5.1)$$

where N is the number of charged particles passing through the detector, e_0 is the electron charge, Δ_{ave} and Δ_{mip} are the ionization energy losses by a muon of average energy in the T2K muon beam and by a MIP, respectively, Y_{mip} is the ionization yield for a MIP, and V is the active volume of the detector. For the ionization chamber, the right side of Eq. 5.1 is divided by two since only the charge induced by electrons is used. The average energy of the muons at the muon pit is estimated at approximately 3 GeV (see Fig. 4.2).

The values in Eq. 5.1 for He, Ar and silicon are listed in Table 5.1. Y_{mip} for the He-N_2 mixture (expressed as Y'_{mip}) is larger than one for pure He gas by about 50% [189] due to the

Table 5.1: Estimated collected charge Q for the T2K muon beam at the intensity of 1×10^7 /cm^2/bunch with parameters in Eq. 5.1 (Δ_{ave}, Δ_{mip} and Y_{mip} for pure He and Ar gases; Y'_{mip} and Q for the He-N_2 and Ar-N_2 mixtures; Y_{mip} and Y'_{mip} at 34°C and 130 kPa [absolute]).

	Helium	Argon	Silicon
Δ_{ave} (MeV g^{-1}cm^2) [194]	2.427	1.980	1.991
Δ_{mip} (MeV g^{-1}cm^2) [194]	1.937	1.519	1.664
Y_{mip} (pairs/cm)	9.55 [188]	117 [188]	9×10^5
Y'_{mip} (pairs/cm)	14.3 (with N_2)	117 (with N_2)	
Q (nC/bunch)	0.242 (with N_2)	2.06 (with N_2)	52

Jesse effect, while Y_{mip} for the Ar-N_2 mixture is almost same as one for pure Ar gas. Q of the He-N_2 and Ar-N_2 ionization chambers and the silicon PIN photodiode are estimated at 0.242, 2.06 and 52 nC/bunch, respectively, for the muon beam intensity of 1×10^7 /cm^2/bunch.

The collected charge for the electron beam is not the same as one for the T2K muon beam discussed above. In Eq. 5.1, Δ_{ave} can be replaced with the ionization energy loss Δ_e by a 100 MeV electron in He, Ar and silicon: 2.609, 2.105 and 1.919 MeV g^{-1}cm^2 [195], respectively. Therefore, the difference of the collected charge is given as Δ_e/Δ_{ave}: 1.075 for He, 1.063 for Ar and 0.964 for silicon.

5.2 Beam tests of the detectors

The electron beam tests at ICR were conducted* to measure the detector's charge collection time, dependence of the collected charge on the applied voltage and linearity of the collected charge to the beam intensity. In addition, the radiation tolerance of the photodiode was examined by measuring the collected charge as a function of the electron beam fluence. The results of these tests are described in Sec. 5.2.1. Because each beam time at ICR was limited to a week, the detectors were also tested in the NuMI beamline to check the long-term stability of their response, which is indispensable for the beam monitor. The result is described in Sec. 5.2.2. The characteristics of the ICR electron beam and the NuMI muon beam are listed in Table 5.2.

5.2.1 Electron beam test at ICR

Test configuration at the electron beamline

The linear accelerator produced the 100 MeV electron beam with a repetition rate of 15 Hz. The beam intensity was 10^7 to 10^9 electrons/pulse and the width was 60 nsec. They were adjusted to those of the expected T2K muon beam. Because the profile of the electron beam was close to a Gaussian distribution with a sigma of 0.6 cm, the signal electrode of the ionization chamber received the whole beam. The fraction of the electrons passing through the silicon PIN photodiode was estimated from the profile.

Detectors were placed in the beamline in the following order from the upstream: current transformers (CTs) for intensity monitors, an array of nine silicon PIN photodiodes for a profile

Table 5.2: Characteristics of the ICR electron beam and the NuMI muon beam at the muon alcove 2 [186]. Those for the expected T2K muon beam are also listed for comparison. The intensity of the electron beam is adjustable and the maximum used value averaged over the active area of the ionization chamber is listed. The intensity of the NuMI muon beam is the nominal value for the test. The intensity of the T2K muon beam is the Monte Carlo expectation at the beam center.

	ICR electron	NuMI muon	T2K muon
Intensity [10^7/cm^2/bunch(batch)]	< 2.3	0.03	1
No. of bunches (batches) in a spill	1	5 or 6	8
Bunch (batch) width [sec]	60 n	1.6 μ	58 n
Spill repetition [Hz]	15	0.53	0.285
Beam size (σ) [m]	0.006	0.8	1

*We had the tests seven times in October of 2005, December of 2006, July of 2006, June of 2007, July of 2008, September of 2008 and July of 2009.

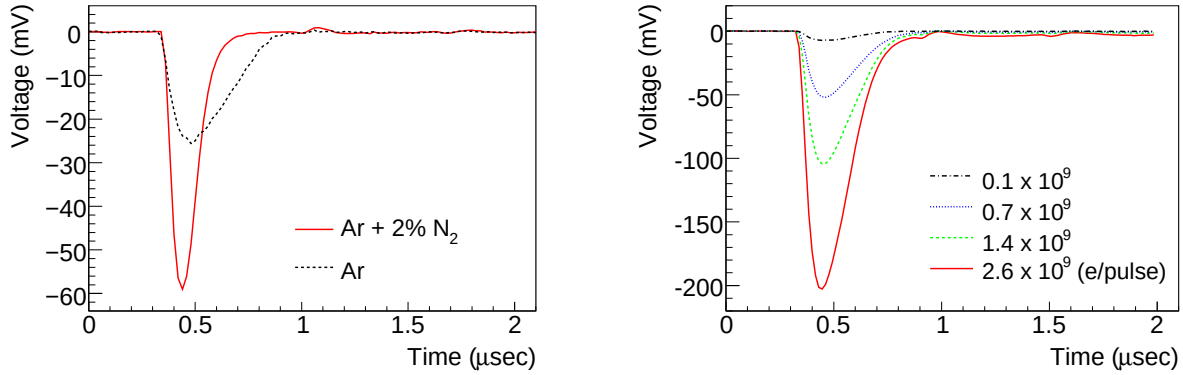

Figure 5.1: Left: pulse shapes of the ionization chamber with the Ar-N_2 mixture and with pure Ar gas at the same applied voltage of 200 V and at the same beam intensity of 8×10^7 electrons/pulse. They were read by the FADC. Right: pulse shapes of the ionization chamber with the He-N_2 mixture at 200 V and at several beam intensities.

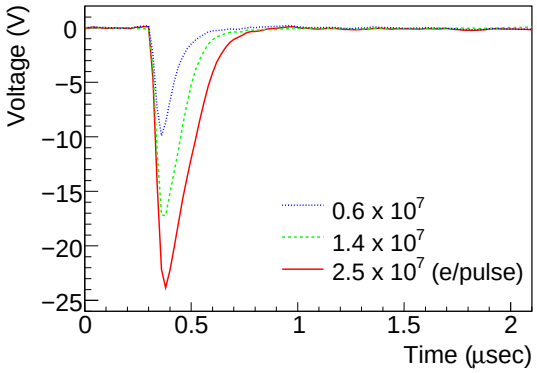

Figure 5.2: Pulse shapes of the silicon PIN photodiode at several beam intensities. They were read by the FADC. The applied voltage was 80 V. Intensities passing through the full active area of the photodiode are written in this figure.

monitor and a sensor of the ionization chamber. Both the Ar with 2% N_2 and He with 1% N_2 were tested at room temperature, atmospheric pressure and a flow rate of approximately 100 cc/min. Variation of the temperature and the pressure during the measurement was negligible. The O_2 contamination in the gas was less than 100 ppm.

Signals of the detectors were read by the COPPER/FINESSE FADCs. Signals of the photodiodes were attenuated by 16 to 46 dB with variable attenuators.

Result: charge collection time

The full widths of the detectors' pulses were measured. They have to be shorter than 581 nsec (the T2K bunch interval) for the bunch-by-bunch measurement of the T2K muon beam.

The left graph in Fig. 5.1 shows pulse shapes of the ionization chamber with the Ar-N_2 mixture and with pure Ar gas at the same applied voltage of 200 V and at the same beam intensity of 8×10^7 electrons/pulse. Adding 2% N_2 makes the response twice as fast as that of pure Ar. The full pulse width of the Ar-N_2 chamber is 400 nsec. The right graph in Fig. 5.1 shows pulse shapes of the ionization chamber with the He-N_2 mixture at 200 V and at several beam intensities. The full pulse width is 700 nsec, but the fraction of the pulse which piles up

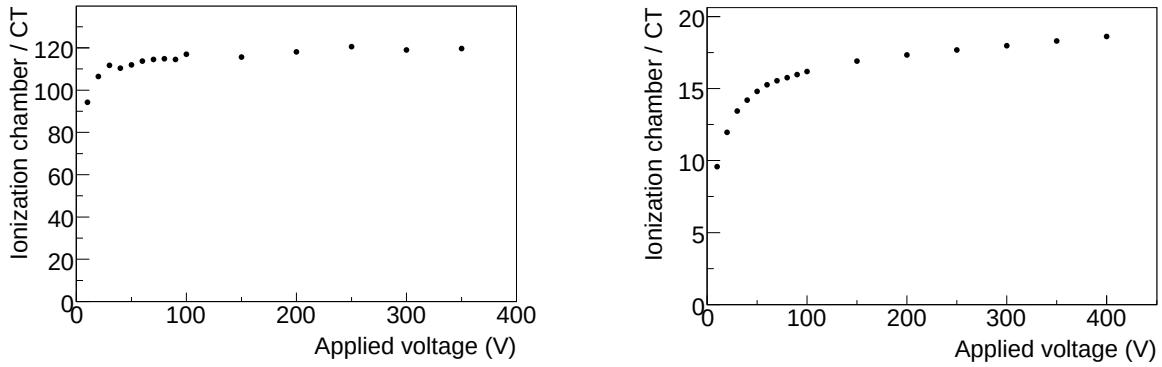

Figure 5.3: Collected charge as a function of the applied voltage for the ionization chamber with the Ar-N_2 (left) and with the He-N_2 mixtures (right). The collected charge of the ionization chamber is normalized by the one of the CT.

on the following bunch is less than 1%.

Figure 5.2 shows pulse shapes of the silicon PIN photodiode at the applied voltage of 80 V and at several beam intensities. Both the pulse height and width depend on the beam intensity. That is because the drift velocity decreases with the depletion of the electric potential between the electrodes when there is a large charge induced by the drift of the ionization electrons. The full pulse width is 500 nsec at 1.4×10^7 electrons/cm^2/pulse.

Result: dependence of the collected charge on the applied voltage

Figure 5.3 shows the collected charge of the ionization chamber normalized by the CT signal as a function of the applied voltage. The beam intensity was kept at 3×10^7 electrons/pulse for the Ar-N_2 mixture and 6×10^8 electrons/pulse for the He-N_2 mixture. The signal of the Ar-N_2 ionization chamber in the left graph gets closer to a constant value as the applied voltage increases. On the other hand, the signal of the He-N_2 ionization chamber in the right graph does not, although the increase is negligibly as small as 0.04%/V at 200 V. This increase is due to the contribution by ions;[†] about 10% of ions from ionization pairs contribute to the signal at 200 V and the contribution increases as the applied voltage increases, while the electrons are fully collected.

Result: linearity

Figure 5.4 shows the collected charge of the ionization chamber versus the beam intensity at several applied voltages. For the Ar-N_2 mixture, the beam intensity was measured by the nine silicon PIN photodiodes of the profile monitor instead of the CT because the CT signal was too small to be measured. The response is linear to the beam intensity at voltages above 100 V for the Ar-N_2 and at 200 V for the He-N_2 ionization chamber. For the He-N_2 ionization chamber at the lower applied voltages, the recombination of electrons and ions can be clearly seen at the high intensities. The residual to a linear fit is less than $\pm 2.4\%$ up to 1.4×10^6 electrons/cm^2[‡] for the Ar-N_2 and $\pm 1.7\%$ up to 2.3×10^7 electrons/cm^2 for the He-N_2 ionization chamber at 200 V.

The electron beam concentrates around the center of the signal electrode of the ionization chamber, while the T2K muon beam uniformly passes over the electrode. Because the probability of the recombination is proportional to the density of ions and electrons, the number of

[†]For a 3-mm gap and at 200 V, the drift time of He_2^+, He^+ ions and an electron in 0°C 1-atm He gas is 23 μsec [196], 40 μsec [196] and 380 nsec [197], respectively, while the drift time of Ar_2^+, Ar^+ ions and an electron in Ar gas is 0.17 msec [196], 0.27 msec [196] and 750 nsec [198], respectively.

[‡]The average beam intensity over the signal electrode.

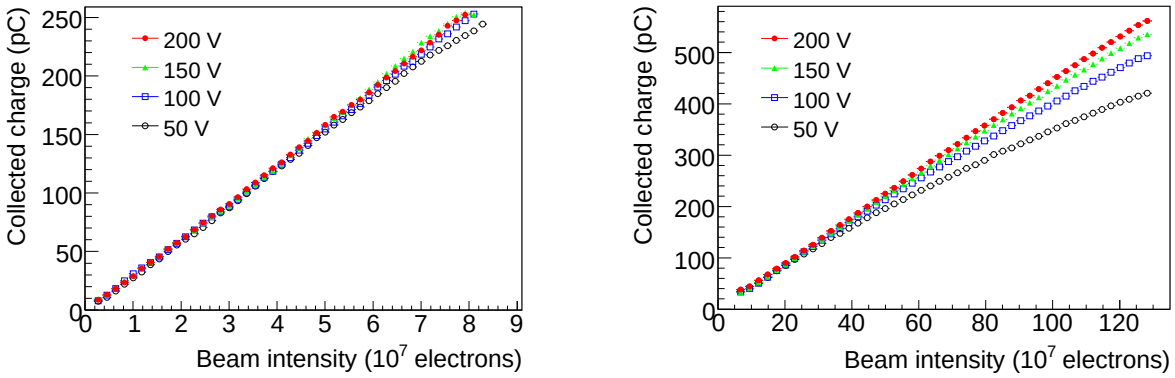

Figure 5.4: Collected charge versus the beam intensity for the ionization chamber with the Ar-N_2 mixture (left) and with the He-N_2 one (right) at several applied voltages.

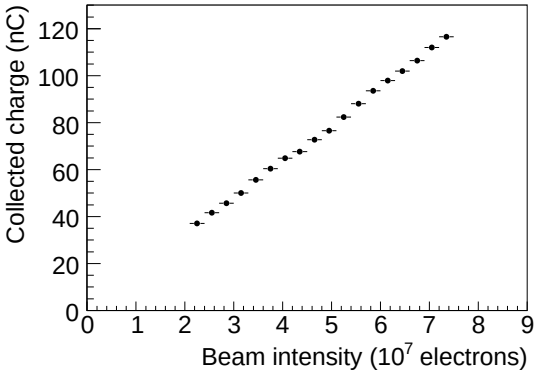

Figure 5.5: Collected charge versus the beam intensity for the silicon PIN photodiode. Approximately 30% of the beam enters the active area.

recombinations is proportional to $\int_S f(x,y)^2 \mathrm{d}x\mathrm{d}y$, where $f(x,y)$ is the beam density and S is the active area. The number of recombinations is approximately 12 times larger for the electron beam than for the first bunch of the T2K muon beam: $\int_S f_e(x,y)^2 \mathrm{d}x\mathrm{d}y \approx 12 \int_S f_\mu(x,y)^2 \mathrm{d}x\mathrm{d}y$. In the case of the T2K multi-bunch beam, the number of recombinations increases in proportion to the number of bunches (n) because ions produced by the preceding bunches stay between the electrodes due to their long drift time; i.e. $\int_S n f_\mu(x,y) \cdot f_\mu(x,y)\, \mathrm{d}x\mathrm{d}y \approx n/12 \int_S f_e(x,y)^2 \mathrm{d}x\mathrm{d}y$. Therefore, the number of recombinations in this test is equivalent to one at the twelfth bunch. Thus, the linearity at 200 V is guaranteed for all eight bunches in T2K as a result of this test.

Figure 5.5 shows the collected charge of the silicon PIN photodiode at the center of the profile monitor versus the beam intensity. The fraction of the beam electrons passing through its active area is estimated at approximately 30%. The response is linear to the beam intensity. The residual to a linear fit is less than $\pm 1.9\%$ up to 2.2×10^7 electrons/cm^2.

The collected charge of the ionization chamber at 200 V is approximately 250 pC at 7.9×10^7 electrons/pulse for the Ar-N_2 mixture, while the rough estimation at STP with the correction of energy loss by the electron/muon beam was 250 pC as discussed in Sec. 5.1. For the He-N_2 mixture, the collected charge is approximately 250 pC at 5.6×10^8 electrons/pulse and the estimated one was 234 pC (including the ions' contribution by 10%). For the silicon PIN photodiode, the collected charge is approximately 53 nC at 3.3×10^7 electrons/pulse and the estimated one was 50 nC. The measured and estimated charges agree well, which ensures that

the detectors work as designed.

Result: radiation tolerance of the silicon PIN photodiode

Three silicon PIN photodiodes were continuously irradiated with the electron beam for four hours. The beam intensity was around 1×10^9 electrons/cm^2/pulse, and the total fluence was 2.1×10^{14} electrons/cm^2.

After the irradiation of 2.1×10^{14} electrons/cm^2, the collected charge of the silicon PIN photodiodes decreased by approximately 4%. However, up to 1×10^{14} electrons/cm^2, no deficit of the collected charge was observed. Because a 100 MeV electron is equivalent to 0.0787 1-MeV neutrons in terms of the radiation damage [193], 1×10^{14} electrons/cm^2 corresponds to the irradiation to the T2K muon beam at 0.75 MW for a month. This result tells that this silicon PIN photodiode is more tolerant of radiation than the expectation discussed in Sec. 4.3.2.

5.2.2 FNAL T968 test experiment

Test configuration at the NuMI beamline (FNAL T968)

The NuMI beamline is operated for the MINOS long-baseline accelerator neutrino experiment. The typical beam intensity during our measurement was 2×10^{13} protons-per-pulse (ppp) with a repetition rate of 0.53 Hz. A spill contains 5 or 6 batches in 8.14 or 9.78 μsec, respectively, and a batch contains 84 bunches. The width of the bunch is 3 to 8 nsec. We installed a miniature ionization chamber and two silicon PIN photodiodes just behind the NuMI muon monitor [186] in the muon alcove 2. They estimated the intensity of charged particles there at 1.7×10^6 /cm^2/spill at the beam profile center for 2×10^{13} ppp [186].

The miniature chamber has the same design as the ionization chamber of the T2K muon monitor, but only three sensors. It was hung vertically and the top sensor was near the center of the muon beam. The exhaust pure He gas from the NuMI muon monitor 2 was supplied to the miniature chamber. The gas pressure, temperature and flow rate were at atmospheric pressure, room temperature and approximately 500 cc/min, respectively. The O_2 contamination at the outlet of the miniature chamber was measured once after the installation and was 52.0 ppm. The silicon PIN photodiodes were put on the rear of the miniature chamber. Their centers were aligned with those of the top two sensors of the miniature chamber.

The signal was read by a CAMAC charge ADC (LeCroy® 2249W). The signal of the photodiode was attenuated by 20 dB with a co-axial type attenuator.

Result: long-term stability of the response

In order to measure long-term stabilities of the detectors, the irradiation of the NuMI muon beam to the T2K prototype detectors was continued for half a year. For the miniature chamber, 200 V was applied. The results are plotted in Fig. 5.6, where the collected charges are normalized to the proton beam intensity. The linearity of the collected charge to the proton beam intensity is within 1% (Fig. 5.7).

The gas pressure varied in a range 1.01–1.07 atm. Therefore, the collected charge of the miniature ionization chamber is divided by the gas pressure to be normalized to an equivalent signal at 1 atm. Because variation of the gas temperature was ± 0.5°C around 27.6°C, no correction of the temperature is applied. Two periods, around January 14th and May 28th, had reduced the gas purity,[§] and the efficiency, or the collected charge, jumped up above 1.5 pC/10^{12} ppp due to the Jesse effect. Except for these periods, the ionization chamber worked stably with no trouble. The stability is 1.5% for half a year.

[§]This was due to an accident during an exchange of the gas cylinders.

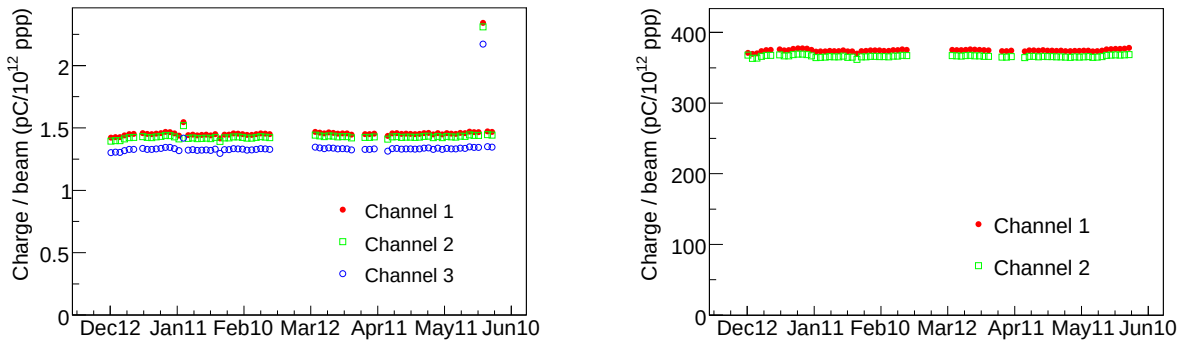

Figure 5.6: Stability of the signal of the miniature ionization chamber with the pure He gas (left) and the silicon PIN photodiodes (right) measured in the NuMI beamline. The collected charge of the detectors is normalized by the proton intensity. The two spikes in the ionization chamber charges in January and May are due to deterioration of the gas purity.

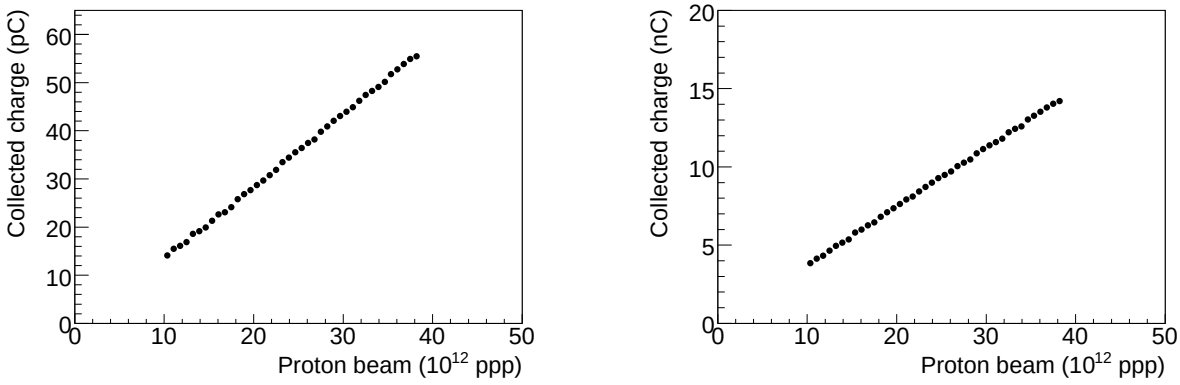

Figure 5.7: Collected charge versus the proton beam intensity for the miniature ionization chamber with the pure He gas (left) and the silicon PIN photodiode (right) measured in the NuMI beamline.

The silicon PIN photodiodes show the stable response from beginning to end. The stability is less than 1% for half a year.

5.2.3 Summary of the beam tests

The performances of the detectors measured in the beam tests are summarized in Table 5.3. The applied voltage to the ionization chamber is selected at 200 V so that the response is linear to the beam intensity within 3%. The Ar-N_2 mixture can be used up to 1.4×10^6 charged particles/cm^2/bunch. Based on the linearity and stability measured in the tests, the error on the muon intensity monitoring is expected to be less than 2.9%. If the relative gains of the sensors are calibrated with a precision better than 2%, the error on the relative intensity measurement of each sensor is expected to be 4% (sum of 2.9% and 2%), which satisfies the requirement for the beam direction measurement. Consequently, the beam tests proved that both the ionization chamber and silicon PIN photodiode have sufficient performance to be used for the muon monitor.

Putting the experience in the beam tests, the sophisticated gas system is fabricated in the T2K experiment; the gas temperature and pressure are kept within 1% variance; the O_2 con-

Table 5.3: Specification of the muon monitor detectors and their performances measured in the beam tests.

	Ionization chamber		Silicon PIN
	Ar with 2% N_2	He with 1% N_2	photodiode
Active volume (mm)	$75 \times 75 \times 3$		$10 \times 10 \times 0.3$
Num. of sensors	49		49
Intensity (particles/cm^2/bunch)	(0.05-1.4)$\times 10^6$	(0.1-2.3)$\times 10^7$	$\leq 2.2 \times 10^7$
Applied voltage (V)	200		80
Pulse full width (nsec)	400	700	< 500
Linearity (%)	2.4	1.7	1.9
Long-term stability (%)	1.5 (pure He)		< 1
Gas temperature (°C)	$\sim 34 \pm 0.2$		
Gas pressure (kPa [absolute])	130 ± 0.2		

tamination is reduced down to 2 ppm; adding N_2 gas makes the gas response independent of impurities amount; and the two-manifold configuration with the automatic switching regulator reduces the risk of gas impurification during an exchange of the gas cylinders. This system ensures a more stable response in T2K run periods than in the beam tests.

The silicon PIN photodiode can be used for a month at 0.75 MW without signal depletion due to the radiation damage.

5.3 Basic performance of the muon monitor

The ionization chambers and silicon PIN photodiodes were integrated into the muon monitor and were installed in the T2K neutrino beamline. Before starting the continuous beam operation, the detectors were relatively calibrated and the performance as the muon monitor was checked with the T2K muon beam. The results are presented in this section.

5.3.1 Method for reconstructing the muon profile

A typical wave form of the signal from the ionization chamber and silicon PIN photodiode is shown in Fig. 5.8. Each of the six bunches[¶] can be clearly seen without overlap thanks to the fast response of the detectors.[‖] Each bunch signal is integrated to obtain the charge, and the charge is used to reconstruct the muon profile for each bunch. Figure 5.9 shows the charge distribution of the 49 sensors. The distribution is fitted with a 2D Gaussian. The center and 1σ of the Gaussian are defined as the center position (x_0, y_0) and width (σ_x, σ_y) of the muon profile, respectively (x = horizontal, y = vertical). The sum of the charges of 49 sensors is defined as the total charge, and the total charge normalized by the proton beam intensity is defined as the muon yield.

In Fig. 5.9, (x_0, y_0) and (σ_x, σ_y) are (0.18, 1.73) cm and (108.7, 127.5) cm for the chamber array, and (-0.68, 0.06) cm and (103.5, 116.8) cm for the silicon array, respectively. The muon profile width σ_y is larger than σ_x. This difference originates from the oblong shape (cross section)

[¶]The number of bunches in the operation discussed in this thesis is six, while the nominal one is eight.

[‖]The small positive pulse after the last bunch was caused by reflection at the HV low-pass filter, where a small impedance mismatching existed. The low-pass filter was improved to suppress the reflection pulse during the summer shutdown in 2010.

of the decay volume. In addition, the profile width at the chamber array is larger than one at the silicon array. This difference comes from a divergence of the muon beam.

5.3.2 Calibration of the detectors

Calibration of the ionization chamber

The ionization chamber is calibrated by moving the entire chamber array by ±25 cm and measuring the muon profile at nine different configurations. The 25 cm is equal to the interval of the sensors. These nine measured profiles should be the same on the assumption that the muon beam profile itself does not change.

During the calibration, the proton beam intensity was 4.5×10^{12} protons/spill (1 bunch in a spill), and the horn currents were 320 kA each. Ten spills were used for each configuration. The stability of the muon beam was measured by the silicon array. The fluctuation of the collected charge measured by each silicon sensor was less than 0.6%.

The nine profiles were fitted with 48 parameters of the relative sensor gains to minimize the differences among the configurations. The difference of the relative gains was 2.6% at the maximum. This difference is consistent with the 3.3% tolerance of the active volume of the ionization chamber. The error of the relative gain obtained in this method was 0.4%. Hence, the 49 sensors were calibrated with a precision of 0.4%, while the requirement for the precision is 2% at most as discussed in Sec. 5.2.3.

Calibration of the silicon PIN photodiode

The silicon PIN photodiode is calibrated one by one sensor by measuring the muon beam with the extra sensor on the small moving stage behind the silicon array.

During the calibration, the proton beam intensity was 1.3×10^{13} protons/spill (6 bunches in a spill), and the horn currents were 250 kA each. Ten and several spills were used for each sensor.

The charge ratio of each sensor to the moving one was within 1.02–1.05. The mean of the ratios was 1.035. The ratio is apart from 1 since the muon beam has a divergence. The obtained error of the ratio or the relative gain was 0.1%, which satisfies the requirement.

5.3.3 Linearity against the beam intensity

Figure 5.10 shows the total charge of the muon monitor as a function of the proton beam intensity. Data in the same condition of the proton beam (beam center at the target: $x_0 = 0.4 \pm 0.4$ mm, $y_0 = 0.8 \pm 0.4$ mm) and the horn currents (250 kA) are plotted. The data are fitted with a linear function, and the residual of the data from the fit line is less than 1.2% for the chamber array and less than 0.4% for the silicon array up to 7.3×10^{13} protons/spill (corresponding to 100 kW beam power). This result is consistent with the one obtained in the beam test described in Sec. 5.2.1.

5.3.4 Resolutions

The intrinsic resolution of the muon monitor can be deduced by comparing the independent measurements of the chamber and silicon arrays. It depends on the signal-to-noise ratio of each sensor and the resolution of the FADC.

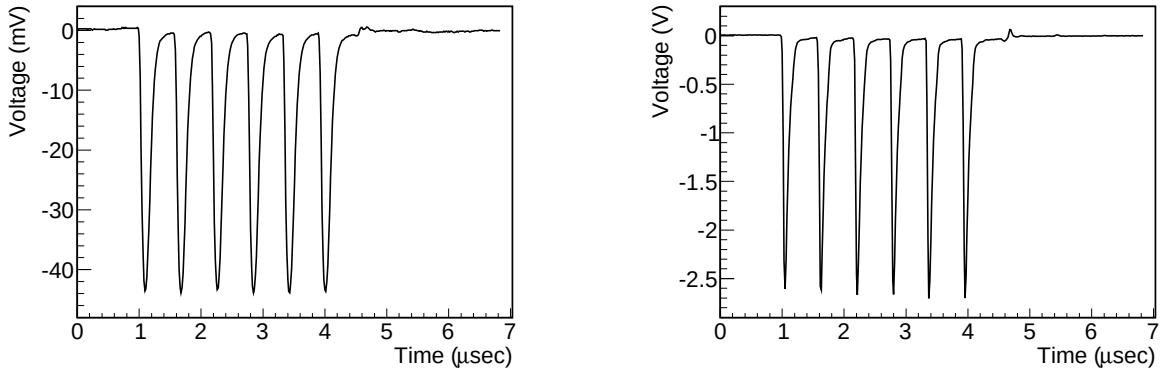

Figure 5.8: Typical waveform of the signal from the ionization chamber (left) and silicon PIN photodiode (right) at the center of each array when the proton beam intensity is 3.83×10^{13} protons/spill (or 52 kW beam power) and the horn currents are 250 kA each. These were obtained by using the FADC.

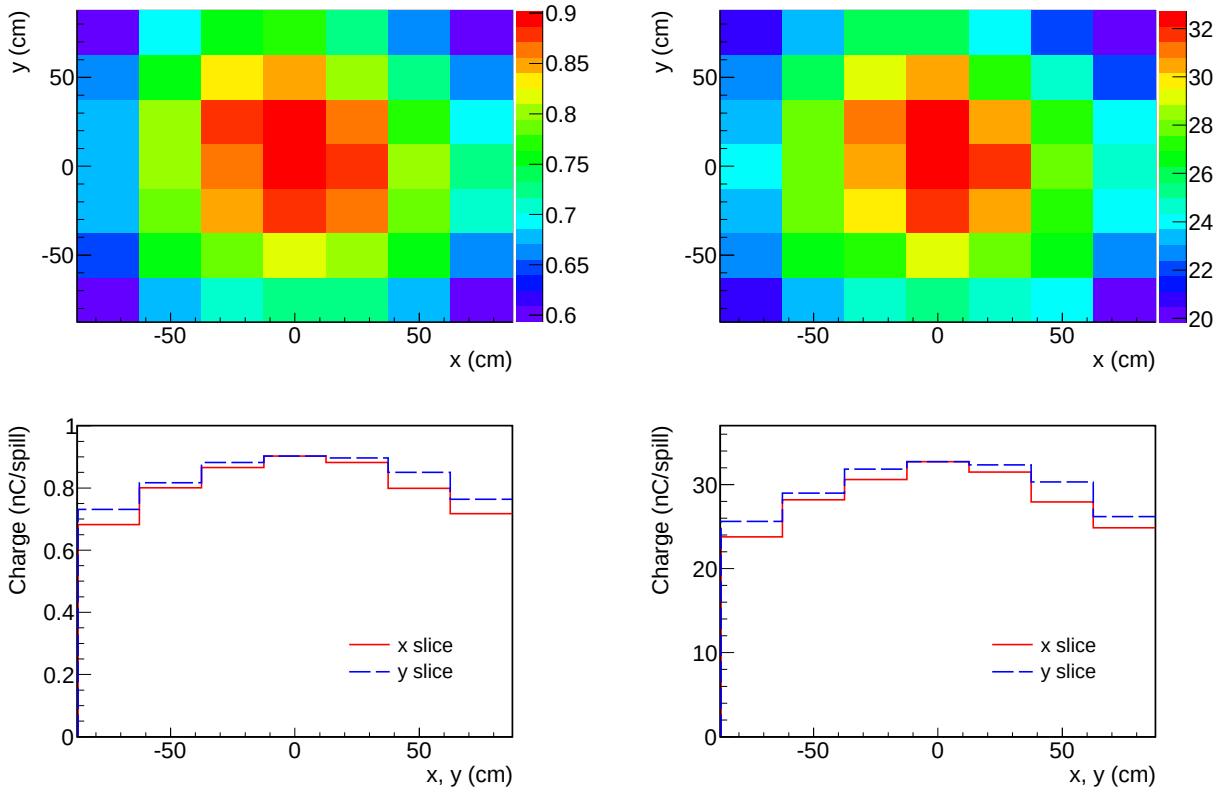

Figure 5.9: Charge distributions of the the chamber (left) and silicon (right) arrays for the same spill when the proton beam intensity is 3.83×10^{13} protons/spill (or 52 kW beam power) and the horn currents are 250 kA each. The upper plots are the 2D distributions, and the lower plots are the slice distributions at $y = 0$ (solid line: x slice) and at $x = 0$ (dashed line: y slice).

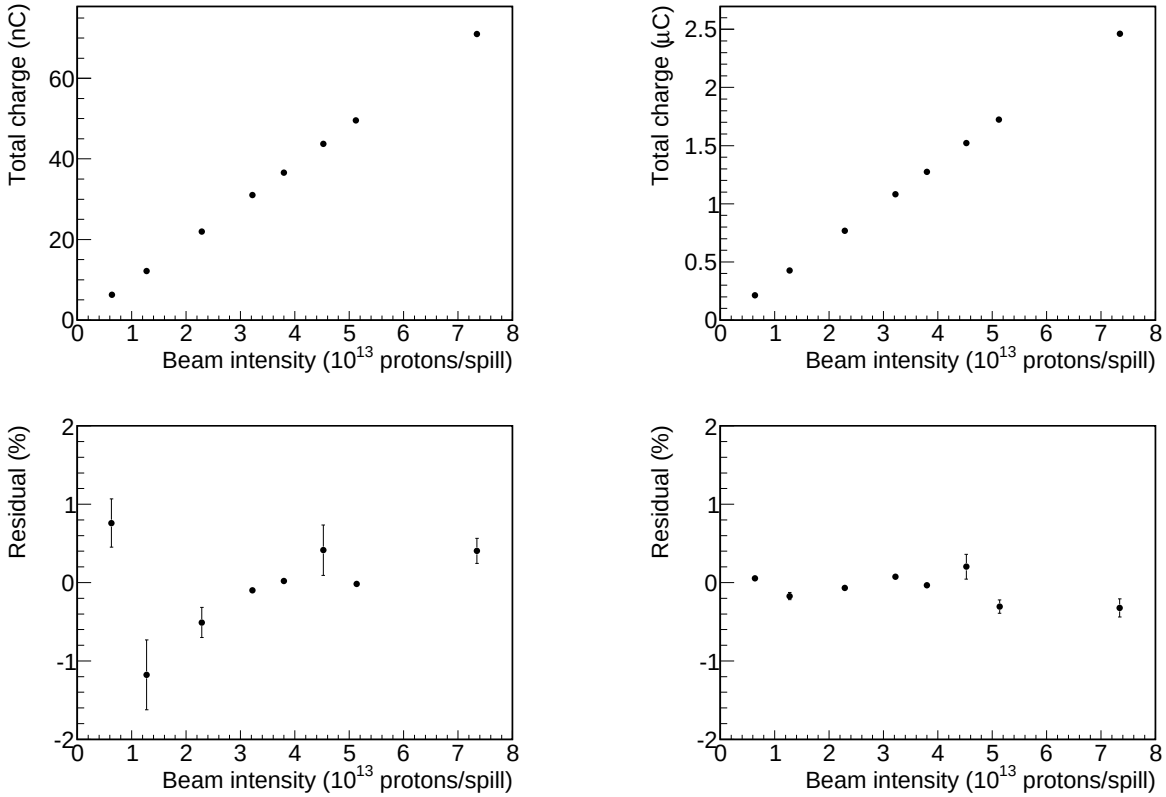

Figure 5.10: Total charge of the chamber (upper left) and silicon (upper right) arrays as a function of the proton beam intensity. The beam intensity 7.3×10^{13} protons/spill corresponds to 100 kW beam power. The residual of the chamber (lower left) and silicon (lower right) data from the linear fit is also shown.

Total charge resolution

The intrinsic resolution for the total charge measurement is estimated by taking the total charge ratio of the chamber and silicon arrays for each spill. This is because the fluctuation of the muon beam intensity itself cancels out in this ratio. The total charge ratio was measured spill-by-spill as a function of the beam intensity. Figure 5.11 shows the RMS/mean of the ratio, or the resolution. The resolution in this figure is a convoluted resolution of the chamber and silicon arrays. It gets better as the beam intensity increases since the signal-to-noise ratio increases with the beam intensity. The obvious noise was only the electrical one in the readout system (less than 1 mV in RMS). Since the pulse height of the silicon PIN photodiode signal is larger by approximately 60 times than the one of the ionization chamber signal (see Fig. 5.8), the resolution at the lower intensities in this figure is considered to be the resolution of the ionization chamber itself. Therefore, this 0.3% resolution at 1×10^{13} protons/spill corresponds to the resolution of the silicon PIN photodiode at 1.7×10^{11} protons/bunch, assuming the resolution depends only on the signal-to-noise ratio. Thus, it can be concluded that the silicon array measures the muon beam intensity with a precision much better than the requirement at any proton beam intensity from 4.1×10^{11} protons/bunch to 3.3×10^{14} protons/spill. Above 3×10^{13} protons/spill, the resolution of each detector is estimated to be less than 0.1%, where only the resolution of the FADC affects the total charge resolution.

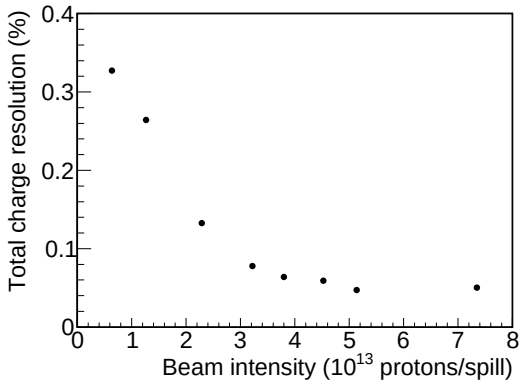

Figure 5.11: Intrinsic resolution for the total charge measurement as a function of the proton beam intensity. This is a convoluted resolution of the chamber and silicon arrays. The beam intensity 7.3×10^{13} protons/spill corresponds to 100 kW beam power.

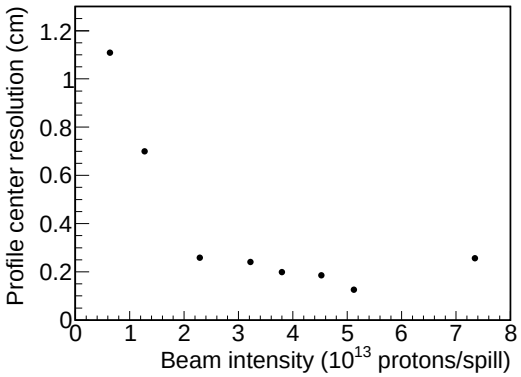

Figure 5.12: Intrinsic resolution for the profile center measurement as a function of the proton beam intensity. This is a convoluted resolution of the chamber and silicon arrays. The beam intensity 7.3×10^{13} protons/spill corresponds to 100 kW beam power.

Profile center resolution

The intrinsic resolution for the profile center measurement is obtained by subtracting the profile center of the chamber array from one of the silicon array for each spill. This is because the fluctuation of the muon beam center itself cancels out by taking the difference. Figure 5.12 shows the fluctuation of the center difference in RMS, or the resolution, as a function of the proton beam intensity. The resolution in this figure is a convoluted resolution of the chamber and silicon arrays. In the same manner as discussed above, it can be concluded that the silicon array measures the muon profile center, or the neutrino beam direction, with a precision much better than the requirement at any proton beam intensity from 4.1×10^{11} protons/bunch to 3.3×10^{14} protons/spill. Above 2×10^{13} protons/spill, the resolution of each detector is estimated to be less than 0.3 cm.

Chapter 6

Beam Tuning by Monitoring the Muon Beam

The first shot of the T2K neutrino beam* was on April 23 of 2009. Figure 6.1 shows the signal of the muon monitor for the first shot, indicating the generation of the neutrino beam. Since then, the neutrino beam has been well tuned using the muon monitor. The commissioning of the T2K neutrino beamline successfully finished in 2009. That pushed the experiment to start the continuous beam data taking called the physics run.

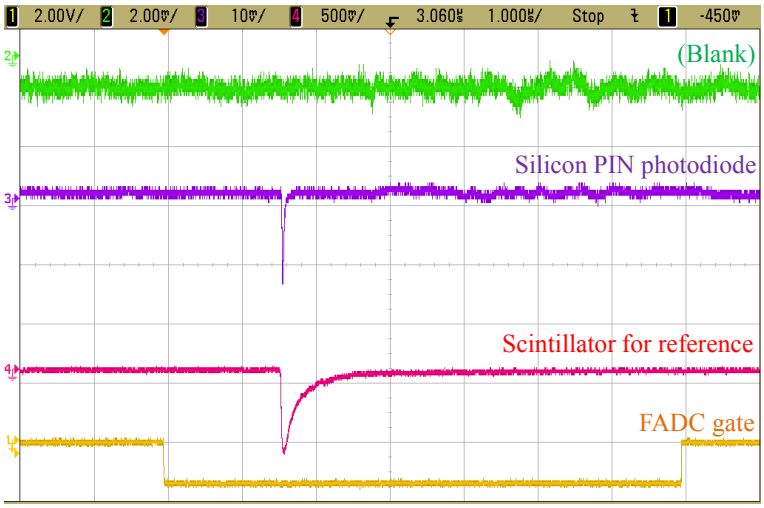

Figure 6.1: First neutrino beam signal taken by the muon monitor. This is an snapshot of an oscilloscope for the beam, showing the signals from the silicon PIN photodiode and a plastic scintillator and the FADC gate synchronized with the beam timing. The scintillator was put behind the muon monitor as a reference at that time.

*At that time, the proton beam hit the baffle.

As described in Sec. 2.5.2, the stable beam operation and precise measurement of the neutrino beam are essential for the precise estimation of the neutrino flux, and they are realized by monitoring the muon beam with the muon monitor. This chapter describes how we tuned the neutrino beam with the muon monitor. In Sec. 6.1 and 6.2, the sensitivities of the muon monitor to the horn currents and proton beam are presented. The horn currents and proton beam parameters are important since their variations cause a variation of the neutrino/muon beam. On the contrary, by monitoring the muon beam, variations of the horn currents and proton beam can be evaluated. In Sec. 6.3, the stability of the neutrino beam monitored by the muon monitor is presented for the physics run from January to June of 2010. The systematic error of the muon monitor measurement is discussed in Sec. 6.4.

6.1 Sensitivity to the horn focusing

The horn status is monitored by two kinds of monitors: the Rogowski coils, which measure the horn currents; and the muon monitor, which measures the muons from the horn-focused pions or the horn focusing effect. To show the ability of the muon monitor to monitor the horn focusing, the dependence of the muon yield and profile width on the horn currents was measured. During the measurement, the proton beam was stable, and the variation of the muon beam due to the proton beam fluctuation can be disregarded. In this section, only the results measured by the silicon array are shown.

6.1.1 Dependence of the muon yield on the horn currents

The muon monitor confirmed that the horns focus the neutrino parent pions; the muon yield increases and the profile sharpens as the horn currents increase as shown in Fig. 6.2. The dependence of the muon yield on the horn currents is shown in Fig. 6.3 and 6.4. Compared to the muon yield without the horn focusing, the muon yield increases by 2.5 times only with the first horn at 320 kA and by 6 times with the all horns at 320 kA.

The dependence on the first horn current around 250 kA is shown in Fig. 6.5, where the second and third horn current is fixed at 251.8 kA with $\pm$0.1 kA fluctuation. The variation of the total charge is 0.40%/kA. The dependence on the second and third horn current around 250 kA is shown in Fig. 6.6, where the first horn current is fixed at 248.0 kA with $\pm$0.1 kA fluctuation. The variation of the total charge is 0.33%/kA. Since the total charge resolution of the muon monitor is less than 0.1% above 3×10^{13} protons/spill, the muon monitor is sensitive to the $\sim$0.3 kA variation of the horn currents. This sensitivity is sufficient to monitor the horn currents.

The dependence on the horn current around 320 kA was also measured. It is 0.18%/kA for the first horn, where the second and third horn current is fixed at 317.6 ± 0.2 kA, and 0.33%/kA for the second and third horn, where the first horn current is fixed at 321.2 ± 0.2 kA. Those horn current dependences are summarized in Table 6.1.

6.1.2 Dependence of the muon profile width on the horn currents

The focusing of the neutrino parent pions by the horns can also be confirmed by examining the dependence of the muon profile width (σ) on the horn currents. The dependence is shown in Fig. 6.7 and 6.8. Without the horn focusing, the width (in x) is 132 cm. By increasing the horn currents, the width increases at first, and then decreases down to 84 cm with all the horns at 320 kA.

The reason of this increase is the following: As discussed in Sec. 4.1, the muon profile can be divided into two components; one composed of muons whose parent pions are produced forward

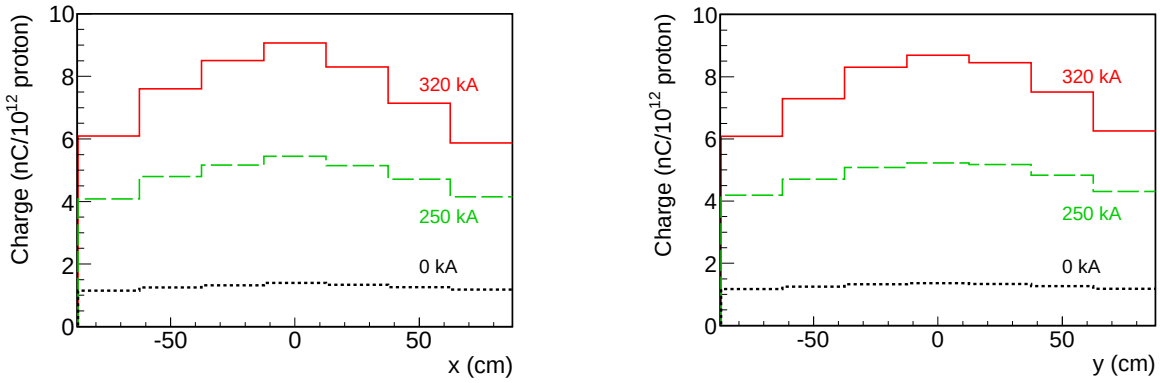

Figure 6.2: Projection distributions of the silicon array for different horn currents: 320 kA (solid line), 250 kA (dashed line) and 0 kA (dotted line).

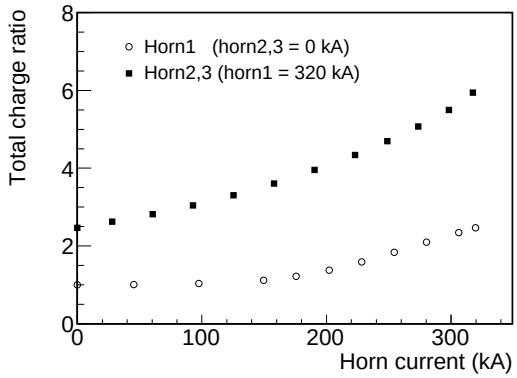

Figure 6.3: Total charge of the silicon array normalized to one at 0 kA as a function of the first horn current (circle) and the second and third horn current (rectangle). The second and third horn current is fixed at 0 kA for the circle points, and the first horn current is fixed at 320 kA for the rectangle points.

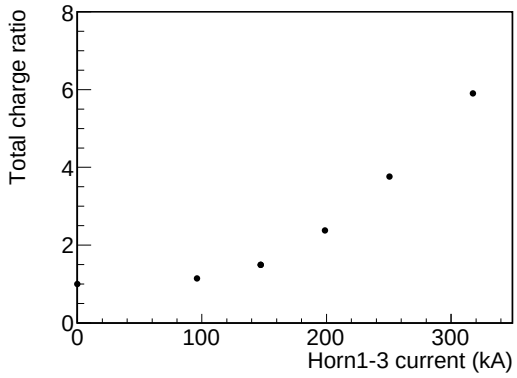

Figure 6.4: Total charge of the silicon array as a function of the all horn currents. Every horn current is set to be the same value.

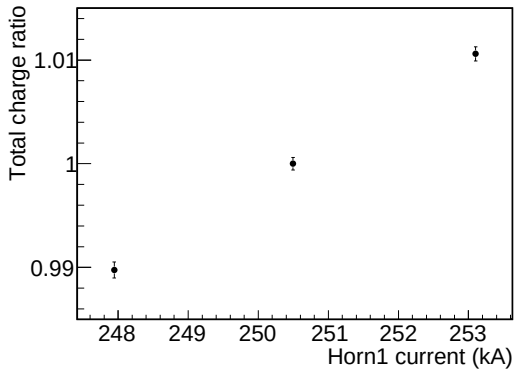

Figure 6.5: Total charge of the silicon array as a function of the first horn current around 250 kA. The second and third horn current is fixed at 251.8 ± 0.1 kA.

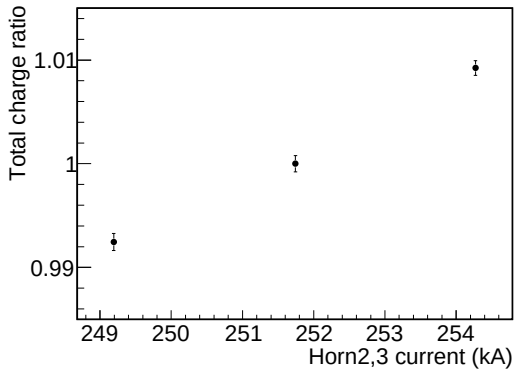

Figure 6.6: Total charge of the silicon array as a function of the second and third horn current around 250 kA. The first horn current is fixed at 248.0 ± 0.1 kA.

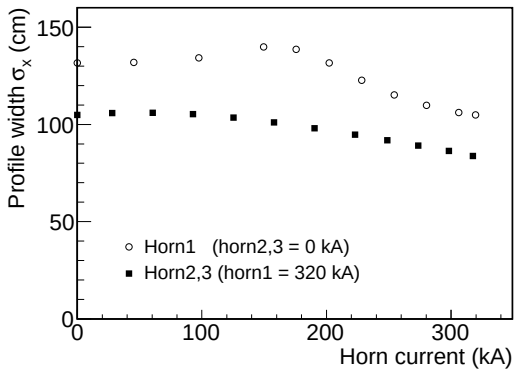

Figure 6.7: Muon profile width (σ_x) as a function of the first horn current (circle) and the second and third horn current (rectangle). The second and third horn current is fixed at 0 kA for the circle points, and the first horn current is fixed at 320 kA for the rectangle points.

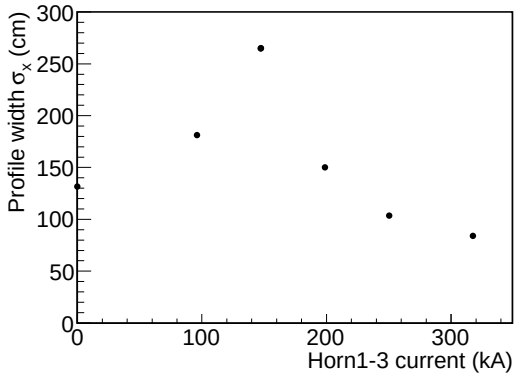

Figure 6.8: Muon profile width (σ_x) as a function of the all horn currents. Every horn current is set to be the same.

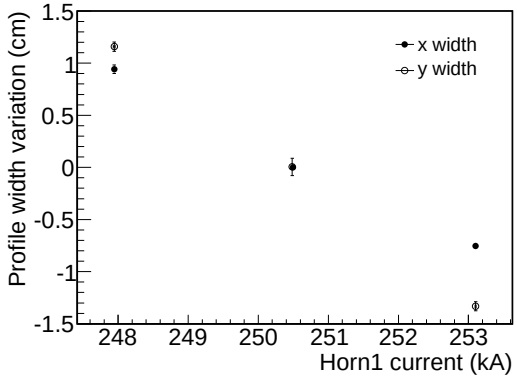

Figure 6.9: Variation of the muon profile width (σ_x with disc and σ_y with circle points) as a function of the first horn current around 250 kA. The second and third horn current is fixed at 251.8 ± 0.1 kA.

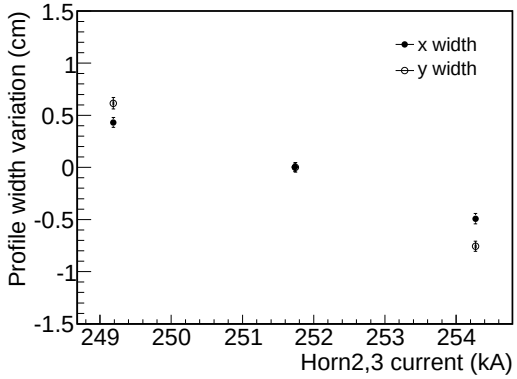

Figure 6.10: Variation of the muon profile width (σ_x with disc and σ_y with circle points) as a function of the second and third horn current around 250 kA. The first horn current is fixed at 248.0 ± 0.1 kA.

Table 6.1: Dependence of the muon beam on the horn currents.

		First horn		Second and third horn	
		∼250 kA	∼320 kA	∼250 kA	∼320 kA
Total charge	(%/kA)	0.40	0.18	0.33	0.33
Profile width σ_x	(cm/kA)	−0.33	−0.05	−0.18	−0.11
σ_y	(cm/kA)	−0.48	−0.06	−0.27	−0.13

and are not focused by the horns (direct muons), and the other composed of muons whose parent pions are focused by the horns (focused muons). At 0 kA, the muon profile is composed of only the direct muons. By increasing the horn currents, the focused muons increase and the profile width of these muons decreases, while the profile of the direct muons does not change. Since the profile width of the focused muons is wider than that of the direct muons at the low horn currents, the total profile width increases as the fraction of the focused muons increases.

The dependence on the first horn current around 250 kA is -0.33 cm/kA for σ_x and -0.48 cm/kA for σ_y (Fig. 6.9), where the second and third horn current is fixed at 251.8 ± 0.1 kA. For the second and third horn current, it is -0.18 cm/kA for σ_x and -0.27 cm/kA for σ_y (Fig. 6.10), where the first horn current is fixed at 248.0 ± 0.1 kA.

The dependence on the horn current around 320 kA was also measured. It is -0.05 cm/kA (σ_x) and -0.06 cm/kA (σ_y) for the first horn, where the second and third horn current is fixed at 317.6 ± 0.2 kA, and -0.11 cm/kA (σ_x) and -0.13 cm/kA (σ_y) for the second and third horn, where the first horn current is fixed at 321.2 ± 0.2 kA. Those horn current dependences are also summarized in Table 6.1. It was confirmed that the horn currents are also monitored with the muon profile width.

6.2 Sensitivity to the proton beam

In the beam operation, the proton beam is tuned so that the muon profile center is on the muon monitor center. In other words, the muon monitor determines the neutrino beam direction. To tune the proton beam with the muon monitor, the relation between the proton and muon beams has to be known. Therefore, the dependences of the muon profile center and width on the proton beam position were measured. These dependences are also important to check the alignment of the proton beam monitors, target, horns and muon monitor. During the measurement, the horn currents were stable (250.2 ± 0.2 kA for the first, 250.9 ± 0.1 kA for the second and 250.2 ± 0.1 kA for the third horn), and the variation of the muon beam due to the horn current fluctuations can be disregarded. In this section, only the results measured by the silicon array are shown.

6.2.1 Sensitivity of the muon beam direction to the proton beam position

With the horn focusing (250 kA)

The targeting position of the proton beam was scanned in the horizontal direction (x), while the angle of the proton beam direction relative to the beam axis s ($\mathrm{d}x/\mathrm{d}s$) was kept within -0.01–0.01 mrad. Figure 6.11 shows examples of the charge distribution of the silicon array projected onto the x and y axes for different targeting positions. A shift of the proton beam center makes the muon profile asymmetric, and hence a shift of the muon profile center. As shown in Fig. 6.12, the shift of the proton beam from the target center is almost linearly magnified in the inverse direction at the muon monitor. The data around the target center ($-2.5 < x < 2.5$ mm) is fitted with a linear function, and the result is listed in Table 6.2. The slope, or the magnification factor, is approximately -21. Since the muon profile center resolution is less than 0.3 cm, the muon monitor is sensitive to the x-shift of the proton beam with a resolution better than 0.3 cm / 21 = 0.15 mm. The fit result shows that the intercept is not zero. That indicates a misalignment of the proton beam monitors, target, horns or muon monitor. However, this misalignment is less than the alignment precisions (less than 0.4 mm for the proton beam monitors, 0.1 mm for the target, 0.3 mm for the horns and 6.3 mm for the muon monitor) and is sufficiently small to be disregarded as compared to the required precision.

The muon profile center can also shift by a shift of the proton beam angle. In order to check if the magnification factor depends on the proton beam angle, another target scan was done with a different beam angle by about 0.1 mrad ($\mathrm{d}x/\mathrm{d}s = -0.12$–$-0.09$ mrad). The result is shown in

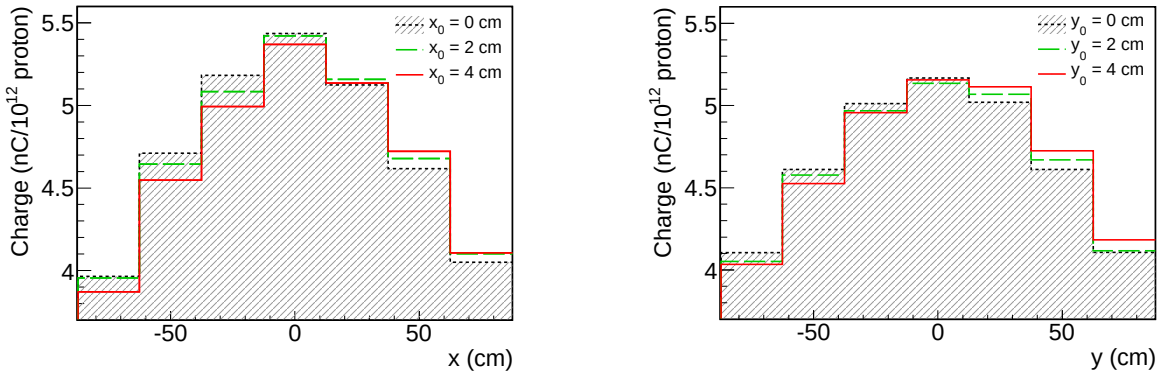

Figure 6.11: Projection distributions of the silicon array for shifted proton beams in x (left) and y (right) directions. Muon profiles which centers (x or y) are reconstructed at 0 cm (dotted line), 2 cm (dashed line) and 4 cm (solid line) are superimposed to show the variation of the profile. The vertical scale is normalized by the number of protons.

Fig. 6.13 and Table 6.2. The magnification factor does not depend on the proton beam angle. Instead, the intercept shifts by -0.27 cm. It means that when the proton beam angle shifts, the muon profile center also shifts by approximately 2.7 cm/mrad.

The correlation in the vertical direction (y) is shown in Fig. 6.14. The proton beam angle $\mathrm{d}y/\mathrm{d}s$ was kept within -0.13–0 mrad. The data around the target center ($-2.0 < y < 2.0$ mm) is fitted (Table 6.2); the magnification factor is approximately -30,[†] and the sensitivity to the y-shift of the proton beam is better than 0.1 mm.

Without the horn focusing (0 kA)

Without the horn focusing, there is a positive correlation between the muon profile and proton beam centers as shown in Fig. 6.15. During the scan, the proton beam angle $\mathrm{d}x/\mathrm{d}s$ was kept within -0.01–0.01 mrad. The data around the target center ($-2.5 < x < 2.5$ mm) is fitted, and the result is listed in Table 6.2.

The reason of the negative (horn on) and positive (horn off) correlation is explained as follows: The proton beam shift, for example in $+x$ direction, makes an asymmetric profile of the pions off the target because pions generated toward the $+x$ directions are less absorbed in the target than those generated toward the $-x$ directions. Therefore, there are more pions on the $+x$ side, resulting in a $+x$ shift of the muon profile center without the horn focusing. With the horn focusing, which functions like a conical reflecting surface, the pion asymmetry is reversed, resulting in a $-x$ shift of the muon profile center.

The intercept without the horn focusing is 2.47 cm, which indicates a misalignment of the proton beam monitors, target or muon monitor.[‡] It is larger than the alignment precisions. In addition, the fact that the intercepts with and without the horn focusing are not the same indicates a misalignment of the proton beam monitors, target or horns; if all of them were perfectly aligned, the intercepts with and without the horn focusing would be the same. Though this issue has not been settled completely, the difference of the intercepts with and without the horn focusing is probably caused by the target tilt relative to the first horn axis. The effect of the target tilt on the neutrino flux is evaluated in Appendix F.2.

[†]The magnification factor in y is larger than one in x. This may be due to the x-y difference of the decay volume geometry.

[‡]The effect of the horns' alignment does not appear in this case.

Table 6.2: Result of the fitting to the correlation between the muon profile center x_μ (mm) and the proton beam center x_p (mm), where M is the slope (x_μ/x_p) and C is the x_μ-intercept.

	M	C (cm)	χ^2/ndf
x scan (250 kA, $-0.01 < \mathrm{d}x/\mathrm{d}s < 0.01$ mrad)	-20.9 ± 0.3	0.23 ± 0.04	8.75/5
x scan (250 kA, $-0.12 < \mathrm{d}x/\mathrm{d}s < -0.09$ mrad)	-20.7 ± 0.3	-0.04 ± 0.05	3.29/4
y scan (250 kA, $-0.13 < \mathrm{d}y/\mathrm{d}s < 0$ mrad)	-30.3 ± 0.3	-0.34 ± 0.03	28.7/6
x scan (0 kA, $-0.01 < \mathrm{d}x/\mathrm{d}s < 0.01$ mrad)	8.2 ± 0.6	2.47 ± 0.08	11.8/5

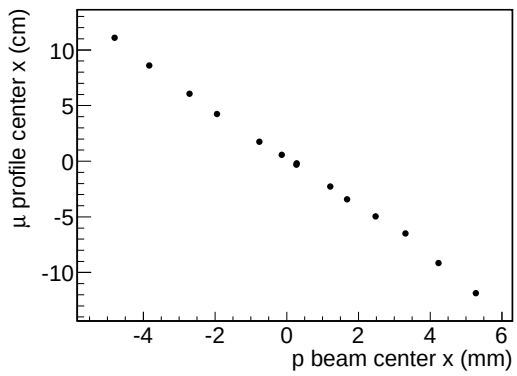

Figure 6.12: Correlation between the muon profile and proton beam centers in the horizontal direction. The horn currents are 250 kA each.

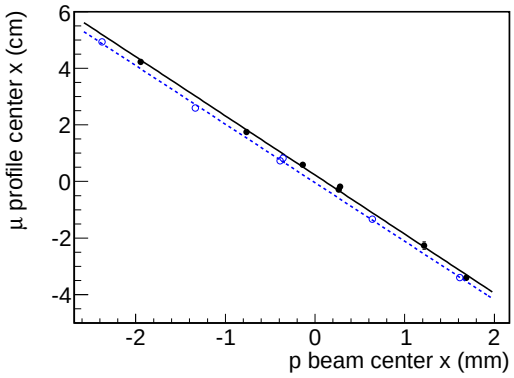

Figure 6.13: Correlation between the muon profile and proton beam centers with different proton beam angles: (disc) $-0.01 < \mathrm{d}x/\mathrm{d}s < 0.01$ mrad and (circle) $-0.12 < \mathrm{d}x/\mathrm{d}s < -0.09$ mrad. Fitted lines are also drawn (solid and dotted lines for disc and circle points, respectively). The horn currents are 250 kA each.

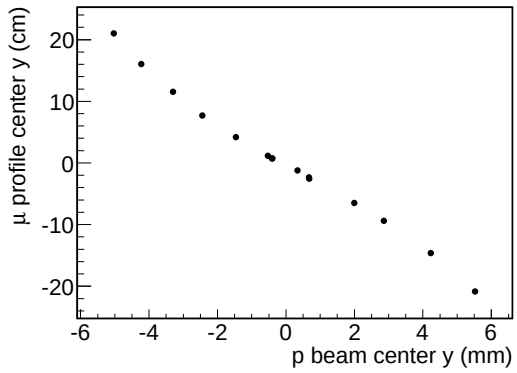

Figure 6.14: Correlation between the muon profile and proton beam centers in the vertical direction. The horn currents are 250 kA each.

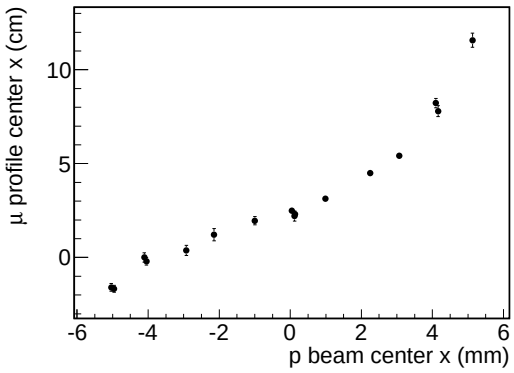

Figure 6.15: Correlation between the muon profile and proton beam centers in the horizontal direction. All the horns are off.

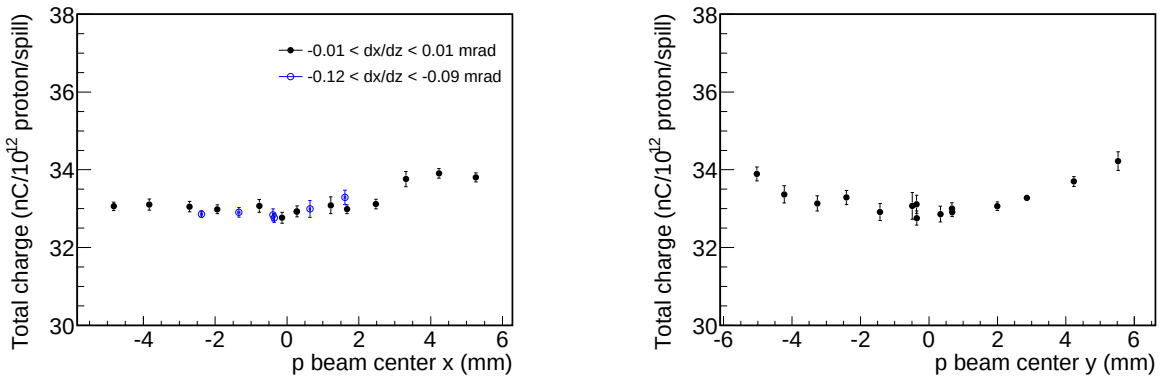

Figure 6.16: Correlation between the muon yield and the shift of the proton beam center in the horizontal (left) and vertical (right) directions. In the left plot, two data sets with different beam angles are plotted: (disc) $-0.01 < \mathrm{d}x/\mathrm{d}s < 0.01$ mrad and (circle) $-0.12 < \mathrm{d}x/\mathrm{d}s < -0.09$ mrad. The horn currents are 250 kA each.

6.2.2 Sensitivity of the muon yield to the proton beam position and angle

There is less correlation between the muon yield and the proton beam center as shown in Fig. 6.16 (at 250 kA). The distribution is flat within the error around the target center ($-2 < x$ or $y < 2$ mm). The left plot of this figure shows two data sets with different beam angles: $\mathrm{d}x/\mathrm{d}s \sim 0$ and -0.1 mrad. It tells that the muon yield is not sensitive to the beam angle ($\sim$0.1 mrad), either. Therefore, for the muon yield stability discussed in Sec. 6.3.3, the fluctuation of the proton beam position and angle can be disregarded.

6.2.3 Sensitivity of the muon profile width to the proton beam position

With the horn focusing, the muon profile width increases as the proton beam shifts from the target center as shown in Fig. 6.17. A quadratic function $a(x-b)^2 + c$ is fitted to the data, and the result is listed in Table 6.3. The non-zero constant b indicates a misalignment of the proton beam monitors, target or horns. The misalignment effect of the target and horns on the neutrino flux is evaluated in Appendix F.2.

The left plot of Fig. 6.17 shows two data sets with different beam angles: $\mathrm{d}x/\mathrm{d}s \sim 0$ and -0.1 mrad. The best fit value of b is the same between the two; b does not depend on the beam angle ($\sim$0.1 mrad).

6.3 Stability of the muon beam

The muon monitor monitored the muon beam over the entire run. This section focuses on the muon beam stability during the physics run. Before that, the stability of the proton beam and horn currents is mentioned since it relates to the stability of the muon beam. Only the data after the good spill selection (see Sec. 7.1.1) is shown in this section.

6.3.1 Stability of the proton beam and horn currents

Stability of the proton beam at the target

Figure 6.18 shows the history of the extrapolated proton beam center on the target upstream surface (see Appendix C.2.2 for the extrapolation). The proton beam was stably transported to

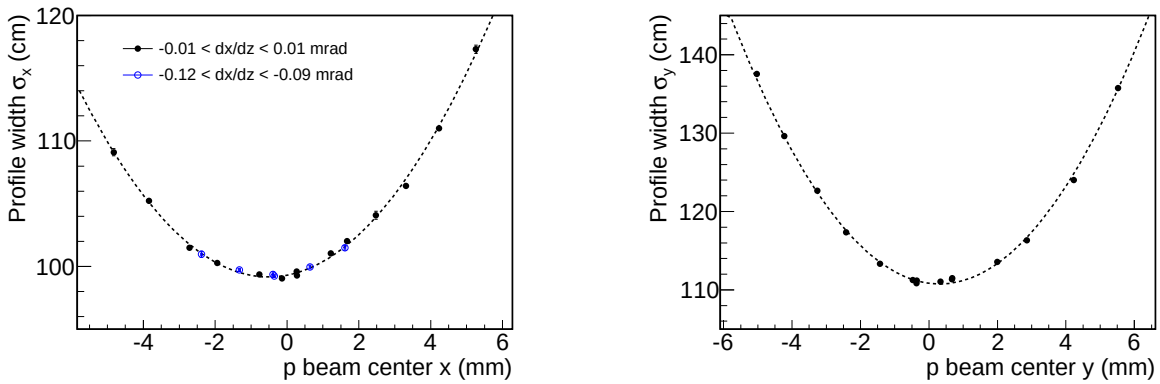

Figure 6.17: Correlation between the muon profile width and the shift of the proton beam center in the horizontal (left) and vertical (right) directions. The dotted line is a quadratic function fitted to the data. In the left plot, two data sets with different beam angles are plotted: (disc) $-0.01 < \mathrm{d}x/\mathrm{d}s < 0.01$ mrad and (circle) $-0.12 < \mathrm{d}x/\mathrm{d}s < -0.09$ mrad. The horn currents are 250 kA each.

Table 6.3: Result of the fitting with $a(x-b)^2+c$ to the correlation between the muon profile width and the proton beam center. The horn currents are 250 kA each.

	a	b (mm)	c (cm)	χ^2/ndf
x scan ($-0.01 < \mathrm{d}x/\mathrm{d}s < 0.01$ mrad)	0.54 ± 0.01	-0.51 ± 0.03	99.3 ± 0.1	15.5/11
x scan ($-0.12 < \mathrm{d}x/\mathrm{d}s < -0.09$ mrad)	0.50 ± 0.05	-0.49 ± 0.08	99.4 ± 0.1	1.04/3
y scan ($-0.13 < \mathrm{d}y/\mathrm{d}s < 0$ mrad)	0.92 ± 0.01	0.31 ± 0.02	110.8 ± 0.1	62.8/12

the target center; the mean of the beam center and the spill-by-spill fluctuation in RMS were 0.3 ± 0.3 mm in x and 0.9 ± 0.2 mm[§] in y, while the target radius is 13 mm.

Figure 6.19 shows the history of the extrapolated proton beam angle at the target. The proton beam was delivered almost parallel to the target; the mean of the beam angle and the spill-by-spill fluctuation in RMS were -0.04 ± 0.04 mrad in x and 0.00 ± 0.05 mrad in y.

Figure 6.20 shows the history of the extrapolated proton beam width at the target. Just before each continuous run, 50 or 100 spills were measured by the six downstream SSEMs (SSEM14–19) and the OTR monitor. After that, SSEM14–17 were extracted from the beamline, and the relative change of the beam width was monitored only with SSEM18, SSEM19 and the OTR monitor. The beam width was well tuned at 4.1 ± 0.3 mm in x and 4.2 ± 0.1 mm in y.

Those stabilities of the proton beam center, angle and width are summarized in Table 6.4.

Accumulated proton beam profile

For each spill, the position-angle profile of the proton beam at the entrance of the baffle is reconstructed by measuring the beam envelope with the SSEMs and the OTR monitor (see Appendix C.2.2 for detail). The profile is accumulated for every spill which passes the good beam spill selection. The accumulated profile is shown in Fig. 6.21, and its parameters are listed

[§]The proton beam was intentionally aimed off the target center in y to adjust the muon beam y center on the muon monitor center which was misaligned by -2.5 cm in y. This misalignment was not noticed till the end of May, 2010.

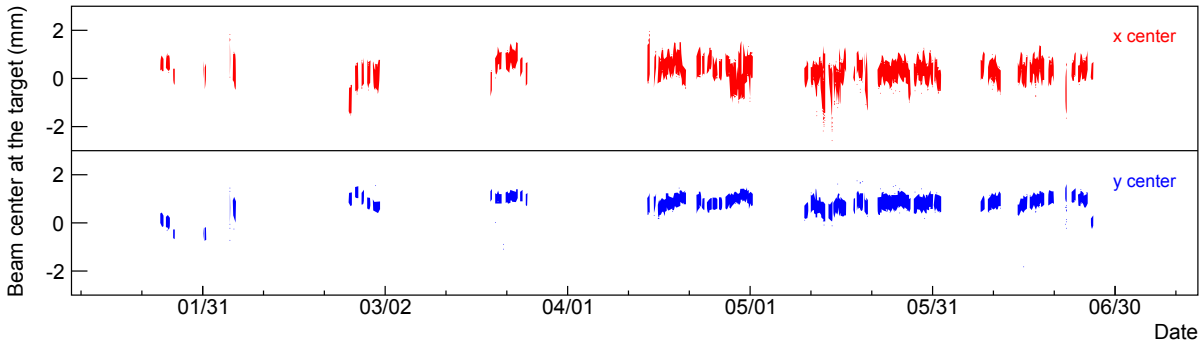

Figure 6.18: Proton beam center x (upper) and y (lower) at the target during the physics run.

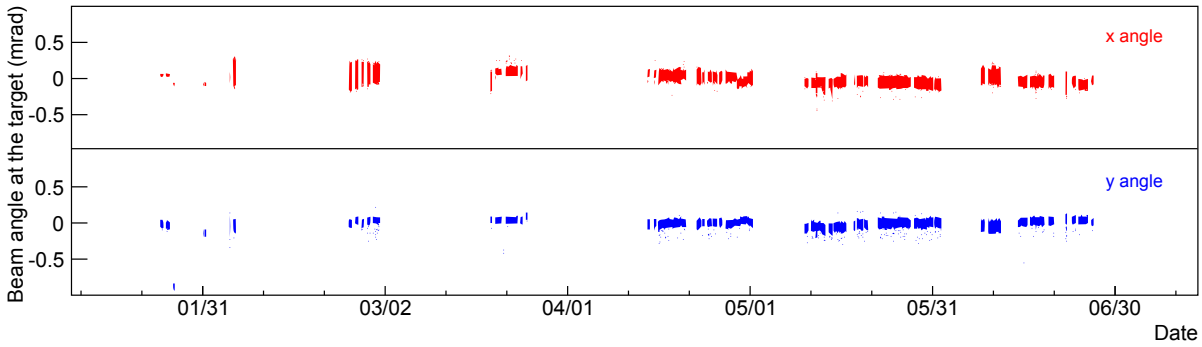

Figure 6.19: Proton beam angle $\mathrm{d}x/\mathrm{d}s$ (upper) and $\mathrm{d}y/\mathrm{d}s$ (lower) at the target during the physics run.

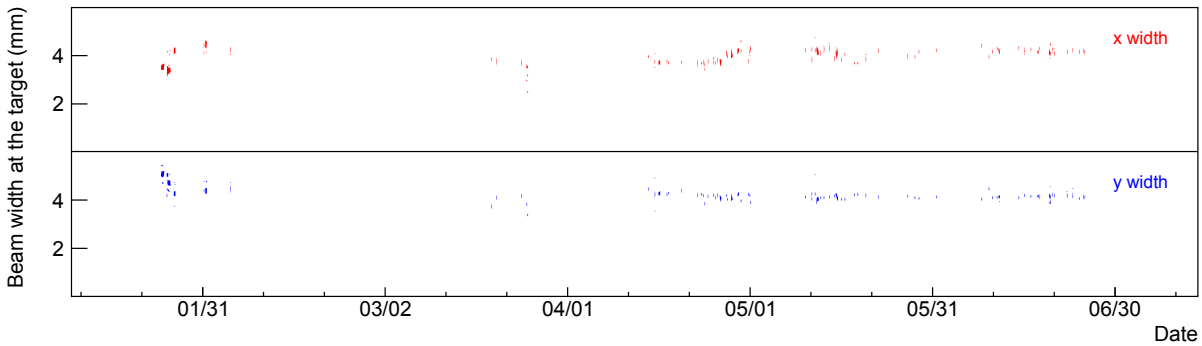

Figure 6.20: Proton beam width σ_x (upper) and σ_y (lower) at the target during the physics run. Only data measured by using SSEM14–19 and the OTR monitor are plotted.

Table 6.4: Stability of the proton beam on the target surface during the physics run.

			Mean	RMS
Proton beam center	x_0	(mm)	0.3	0.3
	y_0	(mm)	0.9	0.2
Proton beam angle	$\mathrm{d}x/\mathrm{d}s$	(mrad)	-0.04	0.04
	$\mathrm{d}y/\mathrm{d}s$	(mrad)	0.00	0.05
Proton beam width	σ_x	(mm)	4.1	0.3
	σ_y	(mm)	4.2	0.1

in Table 6.5. This profile is used as the input to JNUBEAM to estimate the neutrino flux at Super-K.

The geometrical targeting efficiency is calculated from the accumulated profile on the target surface. It is defined as a geometrical overlap between the 2D Gaussian beam and the upstream surface of the target (disc with a radius of 13 mm). The center and width of the accumulated profile at the target are (0.27, 0.85) mm and (4.133, 4.192) mm, respectively, and the geometrical targeting efficiency is estimated to be 99.1%.

Systematic errors of the proton beam parameters

The systematic errors of the proton beam parameters are summarized in Table 6.5.

The uncertainty of the beam center and angle originates mainly from the alignment error of the SSEMs, ESMs and OTR monitor; the alignment error between the primary and secondary beamlines; and the systematic error of the SSEMs, ESMs and OTR monitor measurements.

The uncertainty of the beam width, Twiss parameter α and emittance originates mainly from the systematic error of the SSEMs, ESMs and OTR monitor measurements; an effect of the momentum dispersion ($\Delta p/p = 0.3\%$); and an uncertainty on the magnitude of the focusing and defocusing by the quadrupole magnets, which arises from uncertainties of the effective magnetic field length and the magnetic field strength (7%).

The uncertainty of the number of protons comes from the absolute scale uncertainty of the CT measurement.

Stability of the horn currents

Figure 6.22 shows the history of the horn currents measured by the Rogowski coils. The mean of the currents and the spill-by-spill fluctuation are summarized in Table 6.6. For every spill except one, the horn currents were stable within 250 ± 5 kA.

6.3.2 Stability of the muon beam direction

The muon profile center is plotted for every spill in Fig. 6.23. One can clearly see that the muon profile center was tuned well within ± 11.8 cm (± 1 mrad for the beam direction). However, the profile center x was not stable when the proton beam power was above 50 kW. This is because the magnet core of the extraction kicker saturated due to the beam induction heating,[¶] the extraction force of the kicker magnets dropped, and the horizontal proton beam drifted in $-x$ direction at the target. Thus, the muon profile center drifted in $+x$ direction, while no drift was

[¶]During the summer shutdown in 2010, the kicker magnets were replaced with new ones which were equiped with improved cooling systems. The replacement was planned for a faster rise of the magnetic field, which was necessary for the eight-bunch operation.

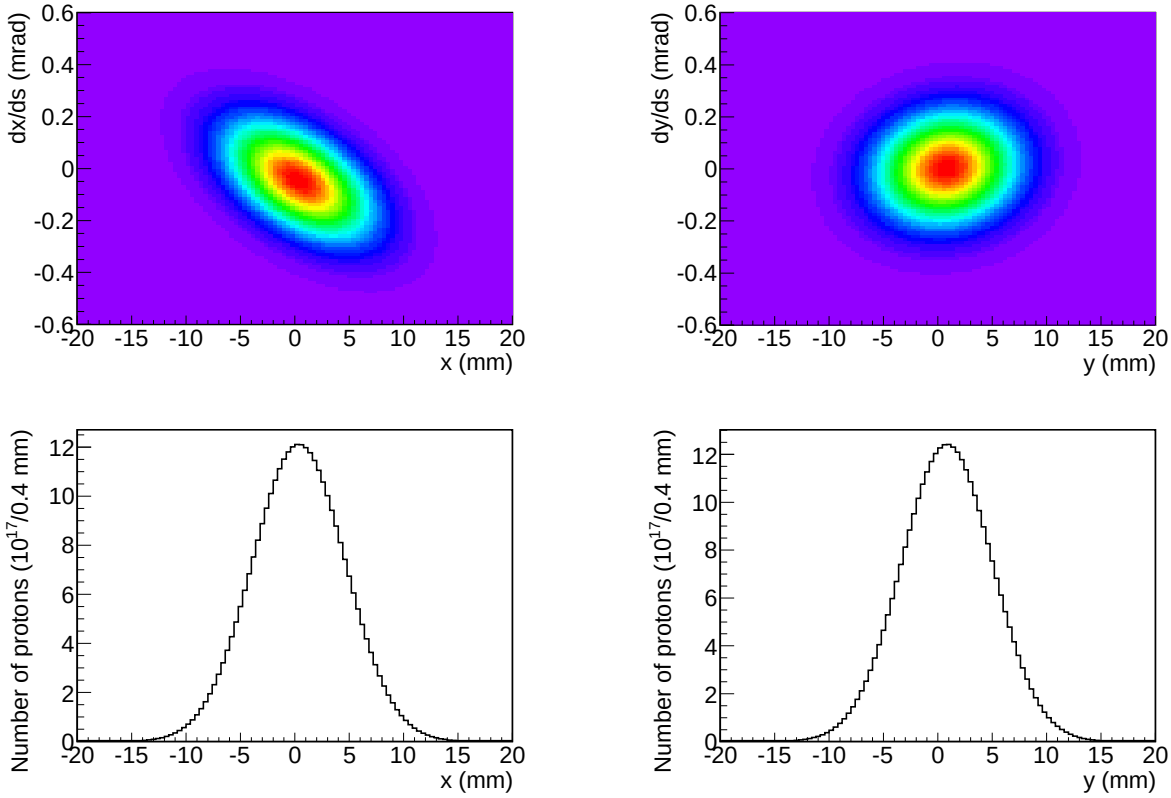

Figure 6.21: Accumulated proton beam profile at the entrance of the baffle in x (left) and y (right) over the physics run. Upper: profile in the position-angle phase space of the beam. Lower: position profile of the beam.

Table 6.5: Parameters of the accumulated proton beam profile at the entrance of the baffle and their systematic errors. The center values are used as inputs to JNUBEAM.

			Center value	Systematic error
Center	x_0	(mm)	0.37	0.38
	y_0	(mm)	0.84	0.58
Angle	$\mathrm{d}x/\mathrm{d}s$	(mrad)	-0.044	0.056
	$\mathrm{d}y/\mathrm{d}s$	(mrad)	0.004	0.286
Width	σ_x	(mm)	4.273	0.11
	σ_y	(mm)	4.167	0.97
Twiss parameter	α_x		0.60	0.32
	α_y		-0.09	1.68
Emittance	ϵ_x	(π mm mrad)	2.13	0.77
	ϵ_y	(π mm mrad)	2.29	0.54
Number of protons			3.28×10^{19}	2%

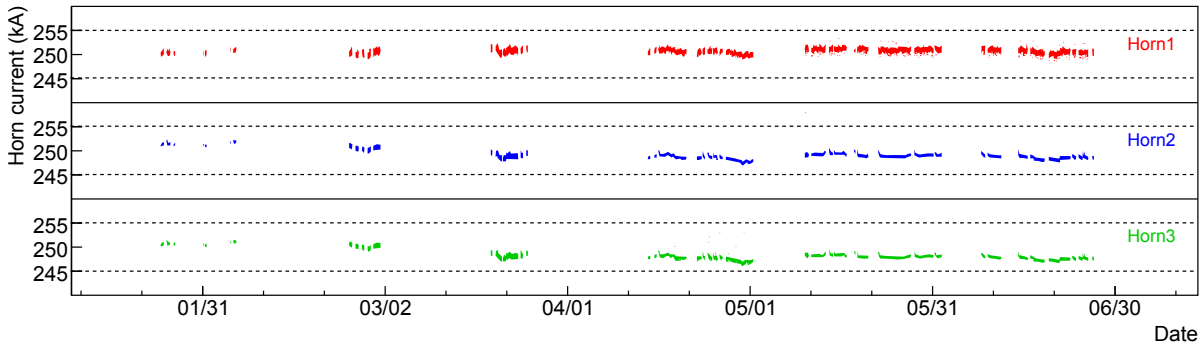

Figure 6.22: First (upper), second (middle) and third (lower) horn currents during the physics run. The threshold of the horn current cut is drawn with dotted lines. It is set at ±5 kA from the nominal value of each horn current (250 kA). The data after the normal beam condition selection is shown in this figure.

Table 6.6: Stability of the horn currents during the physics run.

		Mean	RMS
First horn	(kA)	250.71	0.43
Second horn	(kA)	248.96	0.73
Third horn	(kA)	248.09	0.80

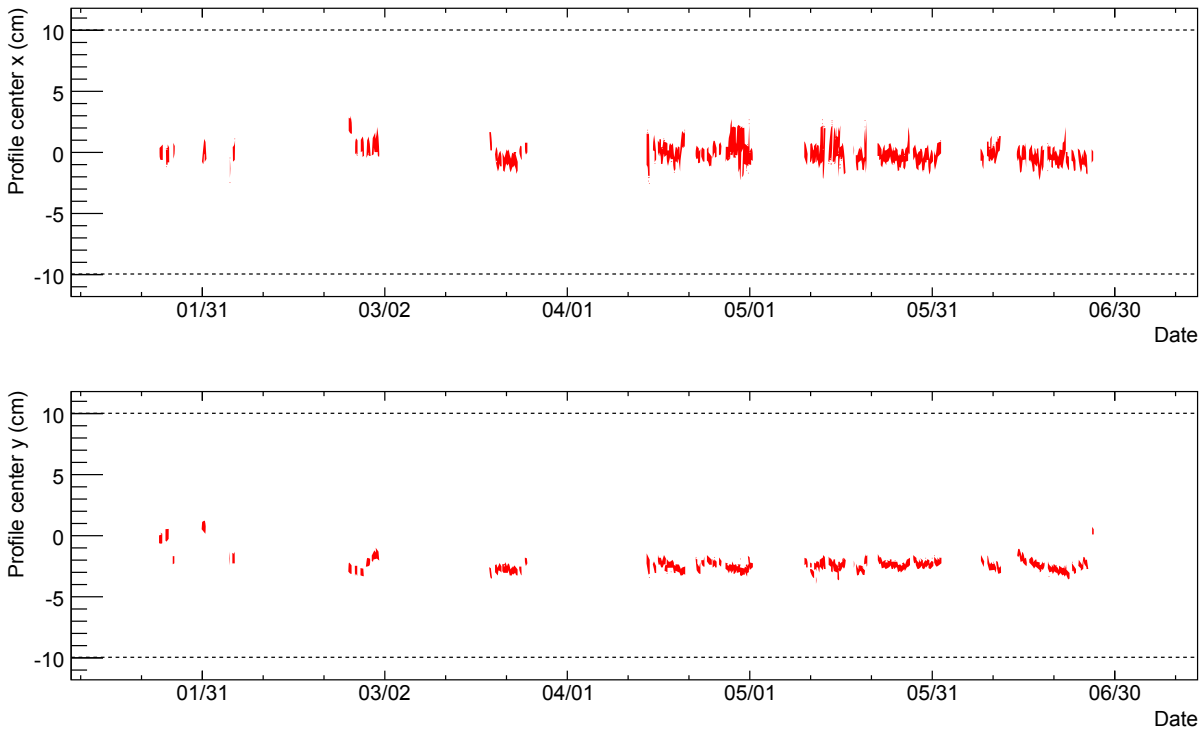

Figure 6.23: Muon profile center x (upper) and y (lower) measured by the silicon array during the physics run. The threshold of the muon profile center cut for the good beam spill selection is drawn with dotted lines.

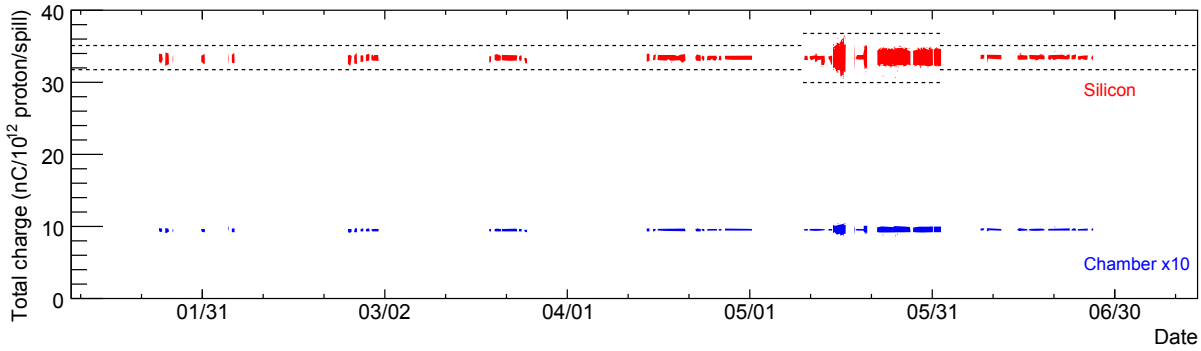

Figure 6.24: Muon yield during the physics run. The threshold of the muon yield cut is drawn with dotted lines. The muon yield measured by the chamber array is scaled up by 10 times.

found in y. When the shift of the muon profile center x exceeded 2 cm, the beam was stopped and the proton beam orbit was adjusted. Thus, over the physics run periods, the variation of the x center was kept in 0.62 cm in RMS for the silicon array, while one of the y center was 0.53 cm.[‖] The RMS of the muon profile center is nearly consistent with the expectation from the fluctuation of the proton beam center. As shown in Table. 6.4, the RMS of the proton beam center is 0.3 mm in x and 0.2 mm in y. It corresponds to 0.63 cm in x and 0.60 cm in y of the muon profile center since a shift of the proton beam center is magnified by approximately 21 and 30 times in x and y, respectively, as discussed in Sec. 6.2.1. The RMS of the proton beam angle is 0.04 mrad in x and 0.05 mrad in y, and the variation of the muon profile center due to the one of the proton beam angle is estimated to be less than the muon profile center resolution. Therefore, it is considered that the variation of the muon profile center during the physics run was almost due to the variation of the proton beam center.

The mean of the profile center measured by the silicon array was $(-0.10, -2.46)$ cm. The y center mean was not zero because the beam had been aimed at $y = -2.5$ cm by mistake; the muon monitor was misaligned 2.5 cm below.

6.3.3 Stability of the muon yield

The muon yield is plotted for every spill in Fig. 6.24. The muon yield was stable over the physics run periods. An RMS/mean of the yield was 0.8% for the chamber array and 0.7% for the silicon array. Sometimes in May, the fluctuation of the muon yield was larger by about 50% than in the other period, but it was due to the CT measurement of the proton beam intensity; the attenuator level of the CT readout system was changed from -46 to -60 or -66 dB and the CT signal-to-noise ratio became worse.

The fluctuation of the muon yield is expected from the fluctuations of the CT measurement (0.5%; see Table C.1), the first horn and the second and third horn currents (0.43 and 0.76 kA, respectively; see Table 6.6) and the muon monitor measurement ($\sim$0.1%; see Fig. 5.11). The fluctuations of the horn currents correspond to 0.18 and 0.25% fluctuation of the muon yield, respectively. Thus, the expected total fluctuation of the muon yield is 0.6%, which is nearly consistent with the RMS/mean of the measured yield above.

[‖] At the beginning and the end of the physics run, the proton beam was intentionally shifted for study. When those spills are excluded, the variation of the y center is 0.36 cm in RMS.

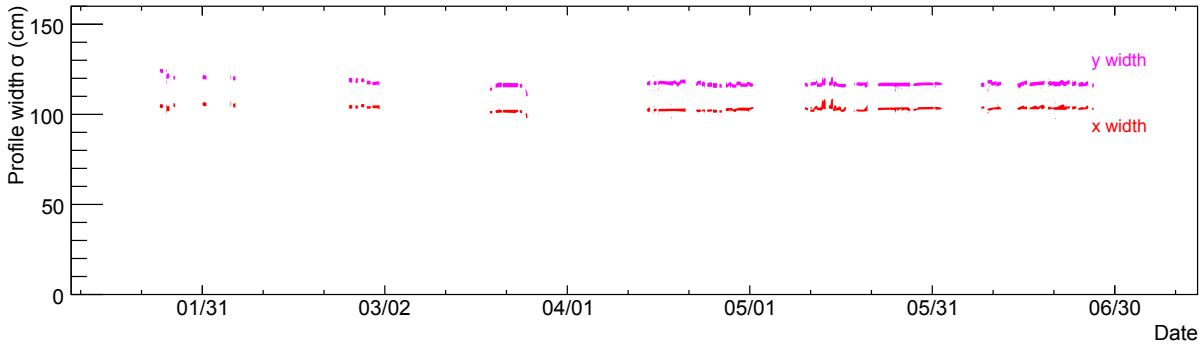

Figure 6.25: Muon profile width measured by the silicon array during the physics run. The lower and upper points show σ_x and σ_y, respectively.

Table 6.7: Stability of the muon beam during the physics run after the good spill selection.

			Silicon array		Chamber array	
			Mean	RMS	Mean	RMS
Muon profile center	x_0	(cm)	−0.10	0.62	0.45	0.47
	y_0	(cm)	−2.46	0.53	−0.69	0.48
Muon beam direction	θ_x	(mrad)	−0.01	0.06	0.04	0.04
	θ_y	(mrad)	−0.21	0.05	0.06	0.04
Muon profile width	σ_x	(cm)	103.0	0.9	108.0	1.2
	σ_y	(cm)	117.0	1.1	127.8	1.1
Muon yield		(nC/10^{12}p/spill)	33.53	0.7%	0.9616	0.8%

6.3.4 Stability of the muon profile width

The muon profile width is plotted for every spill in Fig. 6.25. Over the physics run periods, an RMS of σ_x is 0.9 cm and one of σ_y is 1.1 cm for the silicon array.

6.3.5 Summary of the muon beam stability

The stability of the muon profile center, width and muon yield during the physics run is summarized in Table 6.7. This table includes the muon beam direction calculated from the profile center. Both the silicon and chamber arrays monitored the muon beam stably, and they confirmed that the neutrino beam was delivered to Super-K with less fluctuation than required; the fluctuation of the beam direction and intensity was less than 0.25 mrad and less than 3%, respectively.

There is a discrepancy between the muon profile centers measured by the silicon and chamber arrays. This discrepancy relates to the systematic uncertainty of the muon monitor, which is discussed in Sec. 6.4.

6.4 Systematic error of the muon beam direction measurement

The systematic error of the muon beam direction measurement is evaluated in this section to determine the absolute neutrino beam direction. The beam direction error results in the uncertainty of the neutrino flux at Super-K and is required to be less than 0.25 mrad each in x and y. The following error sources are taken into account: the alignment error of the muon monitor sensors, the uncertainty of the relative gain difference among the sensors, a non-Gaussian shape of the muon profile, non-uniformity of the thickness of the beam dump, the effect of the tilted beamline against the beam dump, and the discrepancy of the profile center between the chamber and silicon arrays.

6.4.1 Alignment error of the muon monitor detectors

Reference marks for the muon monitor and the target were set in the muon pit and the target station, respectively, during the construction of the beamline. The relative positions among these reference points were measured through the decay volume. After the construction, the relative positions need to be traced, but they cannot be measured through the decay volume since the decay volume end is closed. Therefore, the horizontal positions of the reference marks in the muon pit and the target station were transferred to the ground level through vertical holes, and then they were traversed. For the relative height, the amount of the sink of the muon pit and the target station was measured through the holes.

The alignment error in the horizontal position comes from the traverses (6.1 mm) and the ground-to-underground transfer (1.2 mm). The alignment error in height comes from consecutive level measurements through the decay volume (2.8 mm), the measurement of the sink (4.4 mm) and the deflection of the vertical due to the Japan trench nearby (3.5 mm). In addition, the alignment error comes from the setting of the muon monitor (1 mm) and the target (< 1 mm). Those errors are summarized in Table 6.8. The total alignment error of the muon monitor relative to the target is 6.3 mm in horizontal and 6.5 mm in height. Thus, the systematic error of the muon beam direction is 0.054 mrad in horizontal and 0.055 mrad in vertical.

6.4.2 Uncertainty of the relative sensor gains

As discussed in Sec. 5.3.2, the sensors of the muon monitor were calibrated to a precision of 0.1% for the silicon PIN photodiode and 0.4% for the ionization chamber. With a Toy Monte Carlo simulation, the systematic error on the muon profile center with the 0.1% (0.4%) relative gain difference is estimated at 0.08 cm (0.30 cm). Thus, the systematic error of the muon beam direction is 0.007 mrad (0.026 mrad).

Table 6.8: Alignment error of the muon monitor detectors relative to the target.

	Horizontal position	Height
Target setting error	< 1 mm	< 1 mm
Reference point error	6.1 mm	6.3 mm
Muon monitor setting error	1 mm	1 mm
Total error	6.3 mm	6.5 mm

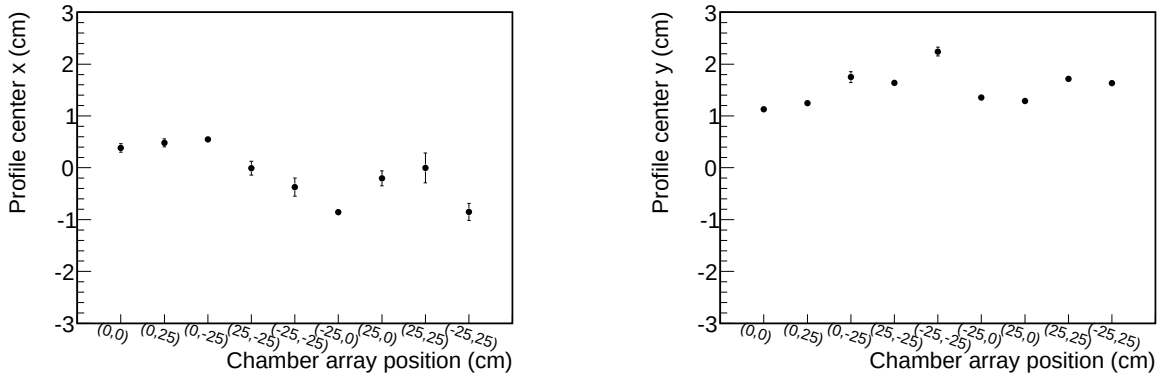

Figure 6.26: Variation of the muon profile center measured by the chamber array at different positions during the calibration of the ionization chamber. The ordinate is the profile center difference between the chamber and silicon arrays to cancel the beam shift itself.

6.4.3 Non-Gaussian shape of the muon profile

To get the muon profile center, the measured profile is fitted to a Gaussian distribution. If the profile is asymmetric or not a Gaussian shape, the fitted profile center can be different from the actual center. In addition, secondary particles (δ-ray and γ) from nearby materials can distort the muon profile in case they are not symmetric nor uniform.

The uncertainty of the fitting of the muon profile to a Gaussian distribution can be estimated by fitting different portions of the same profile. If the muon profile is in perfect accord with a Gaussian distribution, the fitting results should be the same. For this study, the chamber calibration data is used, in which the same muon profile was measured at different positions by moving the chamber array by ± 25 cm. Figure 6.26 shows the variation of the muon profile center measured by the chamber array during the calibration. The profile center x shifts in the $-x$ direction when the chamber array moves both by 25 cm and -25 cm in x, and the profile center y shifts in the $+y$ direction when the chamber array moves both by 25 cm and -25 cm in y. These shifts indicate that the muon profile is asymmetric. On the other hand, the shift of the profile center in x (or y) is small when the chamber array moves only in y (or x). The maximum difference of the x (y) center, 1.25 cm (1.12 cm), is regarded as the systematic error of the muon monitor due to the non-Gaussian shape of the muon profile. It corresponds to 0.106 mrad (0.095 mrad) error of the muon beam direction.

6.4.4 Non-uniformity of the thickness of the beam dump

The beam dump consists of the graphite cores, Fe plates and concrete wall (see Table 6.9 and Fig. 6.27). If the thickness of the beam dump is not uniform along the x or y direction, the muon profile at the muon monitor is distorted. To estimate the amount of the distortion, JNUBEAM is used to simulate the muon profile in the following cases:

1. nominal;
2. the thickness only on the $+x$ side of one of the Fe plates "D" is changed by +0.24 cm (or +1.88 g/cm^2 of the effective thickness d_{eff} = thickness $\times$ density), +1.0 cm (+7.83 g/cm^2), -0.12 cm (-0.94 g/cm^2) or -1.0 cm (-7.83 g/cm^2);
3. the density only on the $+x$ side of the concrete wall "G" is increased by 1% (+2.3 g/cm^2).

The pre-tuned version of JNUBEAM and the default proton beam parameters (0.6 cm width in RMS) are used in this study. As shown in Fig. 6.28, when the thickness of the $+x$ side increases,

Table 6.9: Density (ρ) and thickness (d) of the dump graphite core, Fe plates and concrete wall (see Fig. 6.27). The error marked with * is referred to JIS G 3193, and is counted as 3σ error. The other errors are based on measurements. $\Delta d_{\rm eff}$ is $+1\sigma$ error of the effective thickness ($\rho \cdot \Delta d$). Qt. stands for the number of blocks of each dump material. The estimated profile center shift caused by the asymmetric $d_{\rm eff}$ ($\Delta d_{\rm eff} \cdot \sqrt{\rm Qt.}$) is summarized in the last column.

	Material	ρ (g/cm^3)	d (cm)	$\Delta d_{\rm eff}$ (g/cm^2)	Qt.	Profile shift (cm)
A	Graphite	1.707 ± 0.009	45.001 ± 0.003	0.005	7	Negligible
B	Fe	7.83 ± 0.03	$20.00^{+0.24}_{-0.12}$*	0.627	2	-0.107
C	Fe	7.85 ± 0.02*	$8.00^{+0.17}_{-0.09}$*	0.448	1	-0.054
D	Fe	7.83 ± 0.03	$20.00^{+0.24}_{-0.12}$*	0.627	5	-0.169
E	Fe	7.8435 ± 0.0083	10.083 ± 0.033	0.259	7	-0.083
F	Fe	7.85 ± 0.02*	$10.00^{+0.23}_{-0.11}$*	0.605	3	-0.126
G	Concrete	2.30 ± 0.023	100	2.3	1	-0.276
					Total	-0.38

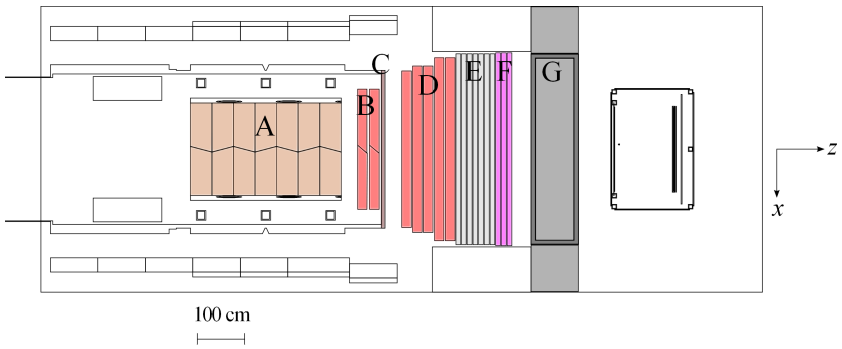

Figure 6.27: Top view of the beam dump. A: graphite core. B–F: Fe plates. G: concrete wall. The beam enters from the left side.

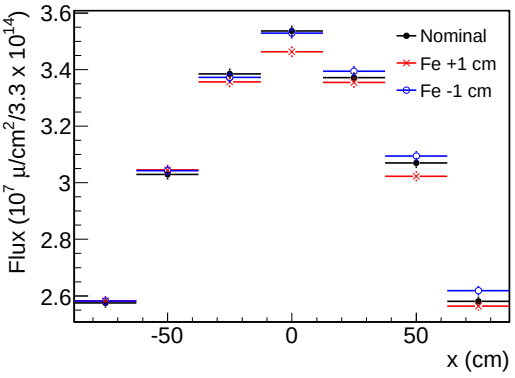

Figure 6.28: Muon profile at the silicon array when the beam dump Fe on the $+x$ side is thicker by ± 1 cm. The error bar is the MC statistical error.

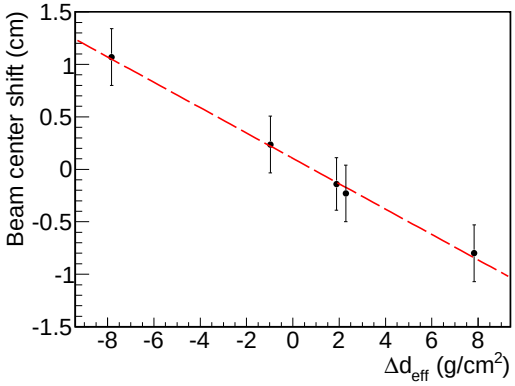

Figure 6.29: Shift of the muon profile center as a function of the asymmetric effective thickness $\Delta d_{\rm eff}$ of the dump. The linear fit is overlaid.

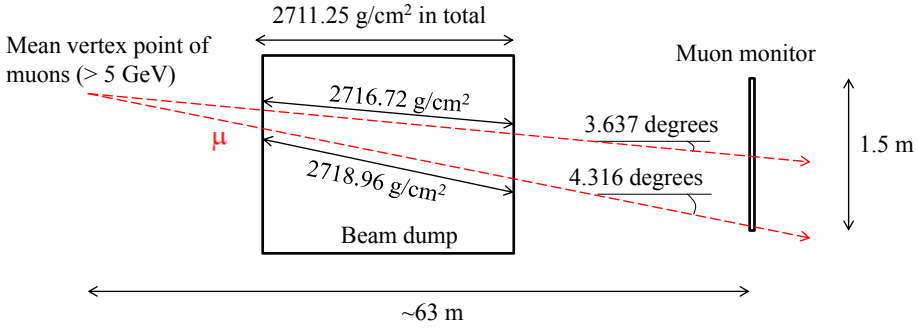

Figure 6.30: Illustration of muon paths to the muon monitor across the beam dump (side view). The dashed arrows show the paths from the mean vertex point of muons to the center and bottom edge of the muon monitor.

the muon flux on the $+x$ side decreases. That results in a shift of the muon profile center in the $-x$ direction. The profile center shifts almost linearly as a function of the d_{eff} asymmetry: -0.12 cm shift/(g/cm^2) obtained by fitting the shifts in case 2 and 3 as shown in Fig. 6.29. Thus, a shift proportion to $+1\sigma$ error of the effective thickness Δd_{eff} for each dump component is assigned as the systematic error of the muon profile center as listed in Table 6.9. In total, the systematic error is 0.38 cm for the profile center and 0.032 mrad for the beam direction.

6.4.5 Effect of the tilted beamline against the beam dump

The beamline is tilted by 3.637 degrees relative to the horizontal, but the beam dump sits level. That makes a difference of the effective thickness of the beam dump for muons with different angles. Figure 6.30 shows examples of muon paths from the mean vertex point to the muon monitor. For muons above 5 GeV which can reach the muon monitor, the mean vertex point is approximately 63 m away from the muon monitor. For a muon which is produced at the mean vertex point and goes to the muon monitor center along the beamline axis, the effective thickness of the beam dump is 2716.72 g/cm^2. For another muon which goes to the muon monitor bottom edge from the mean vertex point, the effective thickness is 2718.96 g/cm^2. There is a 2.24 g/cm^2 difference between these two muons. This difference of the effective thickness of the beam dump makes the muon profile asymmetric at the muon monitor and causes a muon profile center shift as discussed in Sec. 6.4.4. For muons produced at the more downstream part of the decay volume, the difference of the effective thickness becomes larger, and the profile asymmetry is emphasized. In JNUBEAM with the default proton beam parameters (0.6 cm width in RMS and no proton beam center shift), the muon profile y center shifts by $+1.35 \pm 0.22$ cm, where 0.22 cm is the MC statistical error. The same result is obtained with the different hadron production model (GCALOR instead of FLUKA for the hadron production in the target). Thus, it is concluded that the muon profile center at the muon monitor is shifted by 1.35 cm in the $+y$ direction due to the tilted beamline. The measured profile y center should be corrected by -1.35 cm. (This correction has not been applied in this chapter.) The MC statistical error of 0.22 cm is assigned to the systematic error of this correction.

6.4.6 Discrepancy of the profile center between the chamber and silicon arrays

There is a discrepancy of the profile center between the chamber and silicon arrays (0.55 cm in x and 1.77 cm in y). This discrepancy may be considered to be due to the difference of the nearby structure between the chamber and silicon arrays, which distorts the muon profile differently at

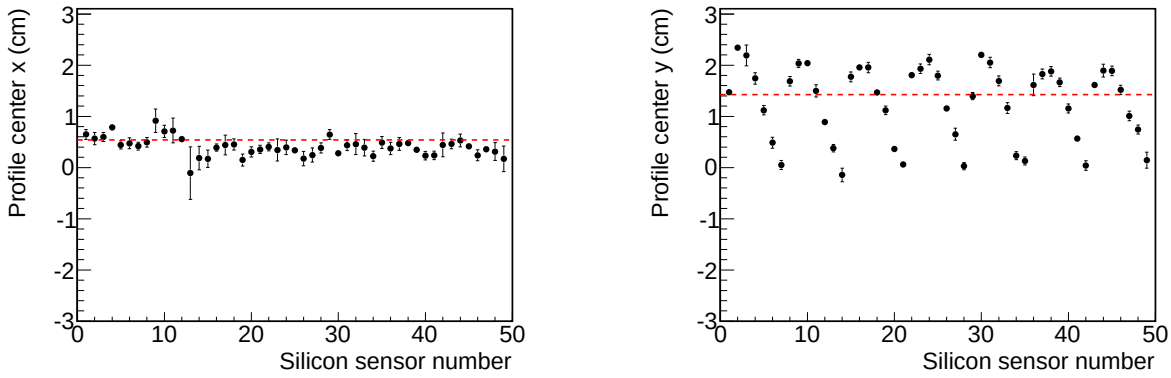

Figure 6.31: Variation of the muon profile center measured by the chamber array during the calibration of the silicon PIN photodiode. The ordinate is the profile center difference between the chamber and silicon arrays to cancel the beam shift itself. The abscissa corresponds to the position of the silicon moving stage. The dashed line shows the profile center for the same beam condition when the silicon moving stage is lowered at the bottom (nominal position).

the chamber and silicon arrays. The most possible structure that could make the discrepancy is the silicon moving stage just behind the silicon array. The stage moves horizontally along a 7.5 mm thick plate which holds a horizontal linear guide and screw shaft. The plate moves vertically along a vertical screw shaft standing 10-cm aside the muon monitor y center (see Fig. 4.9). During the physics run, the plate is lowered at the bottom (50 cm below the bottom silicon sensors) not to obstruct the muon beam against the chamber array. Actually, it did affect the profile at the chamber array during the calibration of the silicon PIN photodiode as shown in Fig. 6.31. When the silicon moving stage is on the top sensors, the profile center y measured by the chamber array shifts by approximately -1.4 cm from one in the nominal case in which the stage is lowered at the bottom. On the other hand, when the stage is just behind the bottom sensors, the shift of the profile center is little. Therefore, the effect of the stage on the profile at the chamber array can be disregarded when the stage is lowered at the bottom. For the vertical screw shaft, its effect on the profile center at the chamber array is estimated using JNUBEAM, which can reproduce the profile center shift during the silicon calibration shown in Fig. 6.31. The profile center at the chamber array does not change whether the vertical screw shaft exists or not.

Another possible source which causes the discrepancy of the profile center between the chamber and silicon arrays is the difference of the sensor gains. However, the error of the profile center from this source is too small to explain the discrepancy as described in Sec. 6.4.2, and the discrepancy has not been understood. Therefore, the discrepancy is accounted as the systematic error on the muon profile center. It corresponds to 0.047 mrad in x and 0.150 mrad in y of the muon beam direction error.

6.4.7 Summary of the systematic error

The systematic error of the muon monitor on the muon profile center or the beam direction measurement is summarized in Table 6.10. The total error on the beam direction is 0.132 mrad in x and 0.192 mrad in y, which is smaller than the requirement of 0.25 mrad. Thus, it is concluded that the muon monitor successfully measured and monitored the beam direction.

Table 6.10: Summary of the systematic error of the muon monitor.

Error source	Profile center		Beam direction	
	Δx (cm)	Δy (cm)	$\Delta\theta_x$ (mrad)	$\Delta\theta_y$ (mrad)
Alignment	0.63	0.65	0.054	0.055
Sensor gain uncertainty	0.08	0.30	0.007	0.026
Profile asymmetry	1.25	1.12	0.106	0.095
Beam dump non-uniformity	0.38	0.38	0.032	0.032
Tilted beamline effect	–	0.22	–	0.019
Chamber/silicon discrepancy	0.55	1.77	0.047	0.150
Total	1.56	2.26	0.132	0.192

6.5 Summary of the beam tuning with the muon monitor

The muon monitor worked over the entire runs from the commissioning periods to the physics data taking. Due to some electronics troubles of the muon monitor, 513 spills (0.05% of the total) are discarded as bad spills which cannot be used for the ND280 and Super-K analyses. Except for these bad spills, the muon monitor ensured the stability of the neutrino beam: less than 0.06 mrad fluctuation of the beam direction and less than 0.8% fluctuation of the beam intensity. The systematic error on the beam direction is evaluated to be 0.2 mrad. Thus, it is concluded that we succeeded in the construction and operation of the muon monitor which stably monitors the neutrino beam with a precision better than the requirement and in the neutrino beam operation with the muon monitor.

Chapter 7

Analysis Overview

From this chapter, the subject is changed from the beam operation to the analysis for the estimation of the neutrino flux and events at Super-K, which is the second subject of this thesis. In the first place, the beam data used for this analysis is summarized in Sec. 7.1. The criteria to select the neutrino events at Super-K are described in Sec. 7.2. Then, the outline for the estimation of the neutrino events is given in Sec. 7.3.

7.1 Summary of the beam data

The data taken from January to June of 2010 is used for this analysis. There are six physics run periods according to the MR run number: run 29 to 34 (Table 7.1). The total time for the physics run was 3.7×10^6 seconds or 42.5 days. The history of the number of protons delivered to the neutrino beamline is shown in Fig. 7.1. In total, 1169162 spills and 3.35×10^{19} protons were delivered, and 1026385 spills and 3.28×10^{19} protons were used for the physics run.

7.1.1 Good beam spill selection

As shown in the previous chapter, the neutrino beam of good quality was provided over the entire physics run. For the ND280 and Super-K analyses, the following "good beam spill" selections are applied offline to the beam data to further guarantee the neutrino beam quality:

Table 7.1: Summary of the physics run in the first half of 2010.

Run	Period	Beam power (kW)		Number of protons delivered
		Average	maximum	in the physics run
29	Jan. 23 – Feb. 5	16	19	0.04×10^{19}
30	Feb. 24 – Feb. 28	26	33	0.11×10^{19}
31	Mar. 19 – Mar. 25	31	41	0.22×10^{19}
32	Apr. 13 – May. 1	44	66	0.76×10^{19}
33	May. 9 – Jun. 1	48	72	1.22×10^{19}
34	Jun. 7 – Jun. 26	51	70	0.93×10^{19}
Total	3.7×10^6 seconds (42.5 days)			3.28×10^{19}

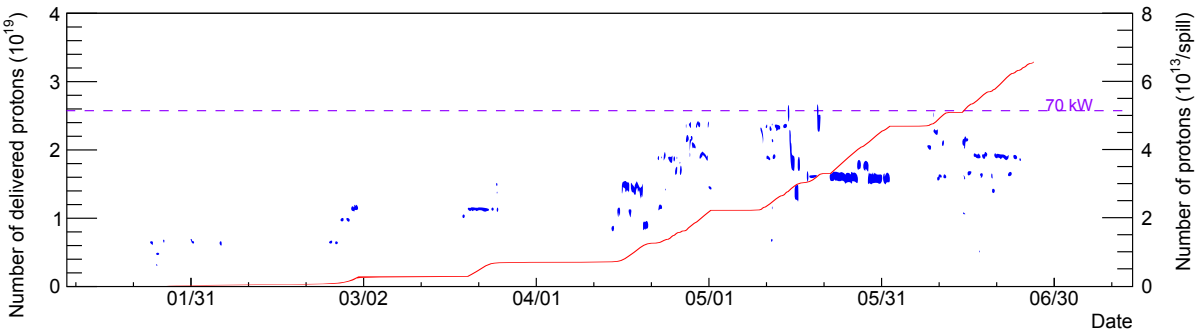

Figure 7.1: Number of protons delivered to the neutrino beamline during the physics run. (Solid line: Accumulated number of protons. Dots: Number of protons per spill.) The dashed line indicates 70 kW of the beam power.

1. "Physics run": Spills during the physics run are selected. The physics run selection excludes spills for the beam tuning or monitor studies such as calibrations, beam based alignment studies and so on.

2. "Beam trigger": Spills with the beam trigger are selected. The beam trigger is synchronized with the MR extraction. This selection excludes spills with test dummy triggers.

3. "Good GPS status": The time difference between the two GPSs (GPS1 and GPS2) at the J-PARC site has to be less than 200 nsec to guarantee the good status of the GPS system.

4. "Spill flag": The number of protons is required to be more than 1×10^{11} protons/spill at the most downstream CT. The spill flag excludes spills which do not contain the beam due to a machine interlock etc.

5. "Normal beam condition": Every component in the beamline has to be under the normal condition.

6. "Horn current cut": Variation of every horn current has to be within ± 5 kA from a nominal value (250 kA in this thesis).

7. "Muon profile center cut": The muon profile center (at the silicon array) has to be within ± 10 cm both in x and y.

8. "Muon yield cut": Variation of the muon yield (total collected charge of the silicon array) normalized by the number of protons per spill has to be within $\pm 5\%$ from a nominal value.

There is no selection based on the proton beam orbit; the neutrino beam direction within 1 mrad shift is guaranteed by the muon profile center cut. The detail of these selections are described in Appendix C.1.

The number of spills after each selection is listed in Table 7.2. In total, 1006982 spills and 3.26×10^{19} protons are used for the ND280 and Super-K analyses. The fraction of the spill loss due to troubles with the beamline components was 0.7%. The neutrino beam was well tuned and was stably produced.

Table 7.2: Number of spills after each good beam spill selection. The percentage after the spill flag indicates the quality of the neutrino beamline operation.

Selection	Number of spills	
All delivered spills	1169162	
1. Physics run	1026385	
2. Beam trigger	1015465	
3. Good GPS status	1015465	
4. Spill flag	1013762	100%
5. Normal beam condition	1007377	99.4%
6. Horn current cut	1007376	99.4%
7. Muon profile center cut	1007376	99.4%
8. Muon yield cut	1006982	99.3%
Number of protons after the selections	3.26×10^{19}	

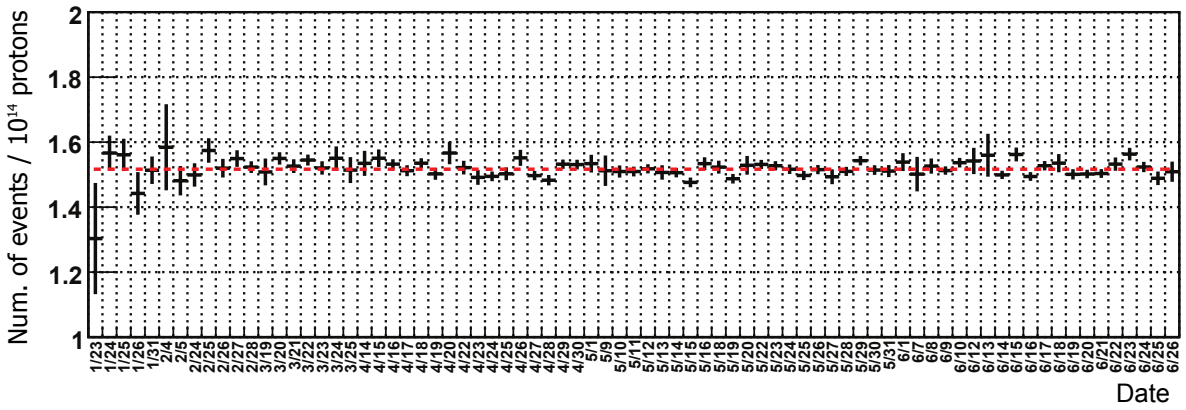

Figure 7.2: Daily number of neutrino events observed by INGRID (all modules). It is normalized to the number of protons. The data is fitted to a constant (dotted line). This figure comes from Ref. [199].

7.1.2 Neutrino beam stability measured by INGRID

Among the good beam spills, the number of spills which can be used for the INGRID analysis is 1005887. It corresponds to 3.255×10^{19} protons. The efficiency of the INGRID DAQ was 99.9%.

Neutrino events are selected according to the criteria described in Appendix D.1.1. Figure 7.2 shows the neutrino event rate observed by INGRID. The event rate was stable within the statistical error of approximately 1.7%.

The mean neutrino profile center during the physics run was $0.2 \pm 1.4(\text{sta.}) \pm 9.2(\text{sys.})$ cm in x and $-6.6 \pm 1.5(\text{sta.}) \pm 10.4(\text{sys.})$ cm in y [199], which corresponded to the neutrino beam direction:

$$0.01 \pm 0.05(\text{sta.}) \pm 0.33(\text{sys.}) \text{ mrad in } x, \tag{7.1}$$

$$-0.24 \pm 0.05(\text{sta.}) \pm 0.37(\text{sys.}) \text{ mrad in } y, \tag{7.2}$$

in the INGRID coordinate system. The INGRID coordinate system is different from the beamline one in x, i.e. $x_{\text{INGRID}} = -x_{beam}$. INGRID confirmed that the neutrino beam was produced in the direction between ± 1 mrad from the design beam axis.

7.1.3 Data set for the ND280 tracker

In this thesis, only the trackers (TPCs and FGDs) in the ND280 off-axis detector are used for the ND280 analysis. They started in operation on March of 2010 (Run 31–34). Among the good beam spills, the number of protons which can be used for the ND280 tracker analysis is 2.88×10^{19}.

7.1.4 Good spill selection at Super-K

To select spills which can be used for the Super-K analysis, the following cuts are applied to the good beam spills on the basis of the Super-K DAQ (data acquisition) status and acquired data quality:

1. Super-K DAQ alive: the Super-K DAQ program must be running to collect the beam data. The dead-time in this physics run was due to Super-K DAQ crashes.

2. Bad subrun cut: bad subruns caused by flashing PMTs, DAQ troubles, blasting in the mine, etc. are discarded. A subrun is a unit of the Super-K data corresponding to approximately one-minute observation.

3. DAQ/GPS error cut: the number of the inner and outer detector PMT hits in the T2K 1 msec beam-time window is required to be above 48000 and 6000, respectively. Because the most of the hits are due to the PMTs' continuous dark noise, this number indicates the DAQ goodness and should be constant. The threshold of this number was determined by checking data in dummy spills. In addition, if both of the two GPSs at Super-K flag an error, this spill is cut.

4. Special data block cut: PMT hit signals are recorded in units of a 17 μsec data block, but there are two special data blocks which cannot be used for the analysis: "pedestal block" to take pedestal data and "TDC reset block" to reset TDCs. The pedestal and TDC reset blocks are generated once per 65536 ($\sim$1.1 sec) and once per 4096 ($\sim$70 msec) data blocks, respectively. These special data blocks are discarded.

5. Pre-activity cut: when there is an activity in 100 μsec before the event timing or before the leading edge of the spill in case of no event, this spill is cut to reject decay electrons from cosmic muons stopped inside the detector.

The number of spills after each cut is listed in Table 7.3. The number of the selected good spills for the Super-K analysis is 999070, which corresponds to 3.23×10^{19} protons. The total inefficiency of the Super-K DAQ by these cuts is 0.8%. Histories of the accumulated number of protons for the good spills and the DAQ inefficiency are plotted in Fig. 7.3.

7.2 Neutrino event selection criteria at Super-K

Among the Super-K good spills, neutrino events are selected according to the criteria described in the following sections.

7.2.1 Fully-contained fiducial volume (FCFV) event selection

A fully-contained (FC) event is defined as an event in which a neutrino interacts in the Super-K inner detector (ID) and the neutrino-induced charged particle(s) deposits all the energy in ID not in the outer detector (OD). Only FC events are selected to reconstruct the particle energy. The selection criteria to extract FC events from the T2K beam events in the 1 msec beam-time window are the followings:

Table 7.3: Number of spills after each good spill selection at Super-K. Inefficiency of the Super-K DAQ for each cut is also listed.

Selection	Number of spills	Inefficiency (%)
Beam good spills	1006982	
1. Super-K DAQ alive	1006129	0.08
2. Bad subrun cut	1003093	0.3
3. DAQ/GPS error cut	1003093	0
4. Special data block cut	1002281	0.08
5. Pre-activity cut	999070	0.3
After the selections	3.23×10^{19} protons	0.8%

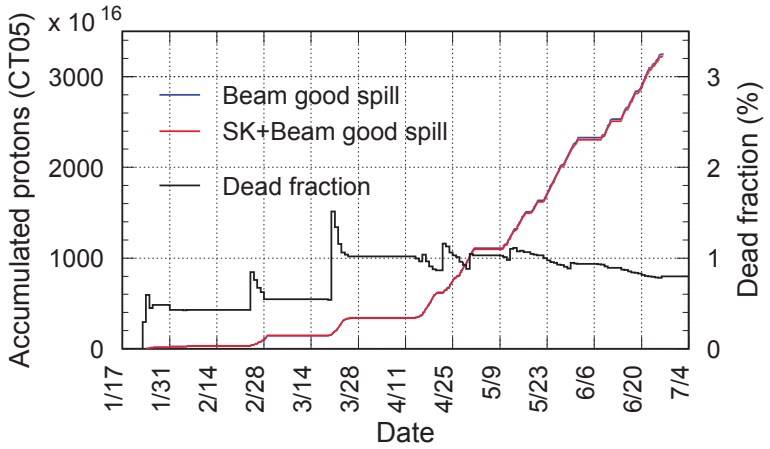

Figure 7.3: History of the accumulated number of protons for the good beam spills with the Super-K good spill selections. The history of the Super-K dead fraction is also drawn. This figure comes from Ref. [200].

1. No calibration flag: it is checked that the event is not flagged as a detector calibration event, though the Super-K auto-calibration scheduler is set to avoid accidental coincidence of the calibration and T2K beam event.

2. NHITAC $<$ 16: the number of OD-PMT hits in the largest hit cluster (NHITAC) is required to be less than 16 to reject incoming particles such as cosmic muons and to select FC events.

3. PE300 $\geq$ 200 p.e. and PEMAX/PE300 $\leq$ 0.5: events in which the total charge of the ID-PMT hits in a 300 nsec time window (PE300) is less than 200 p.e. are cut as low energy backgrounds. The charge of 200 p.e. corresponds to a $\sim$20 MeV electron. In addition, events in which the maximum charge (p.e.) in a single ID-PMT hit (PEMAX) per PE300 is more than a half of the total charge are cut. Such events are caused most likely by radioactivity near the PMT.

4. Flasher cut: a "flasher event" is caused by a PMT which emits light due to arch discharge on dynodes. Flasher events are cut by discriminating its characteristics: typical flasher events have a broader PMT hit timing distribution than neutrino events; they have a tendency to be repeated with a similar spatial hit distribution.

Additional cuts are applied to the FC events to extract fully-contained fiducial volume (FCFV) events:

1. $D_{\mathrm{wall}} > 200$ cm: the distance from the reconstructed vertex to the nearest ID wall (D_{wall}) is required to be larger than 200 cm. The cylindrical volume with $D_{\mathrm{wall}} > 200$ cm is the Super-K fiducial volume of 22.5 kt in weight.

2. $E_{\mathrm{vis}} > 30$ MeV: the sum of the visible energy (E_{vis}) calculated on an assumption that all rings are produced by electrons is required to be larger than 30 MeV, which corresponds to 200 MeV/c for a muon. This cut further reduces low energy backgrounds.

7.2.2 Event classification

The FCFV events are further classified as single-ring μ-like, single-ring e-like and multi-ring events. Details of the classification can be found elsewhere [201]. The number of rings in an event (N_{ring}) is determined by a likelihood method applied to each N_{ring} hypothesis. The particle identification (μ-like or e-like) is done for the most energetic ring found in the event based on the ring pattern; a diffused ring arising from an electromagnetic shower is classified as the e-like event, while a ring with a sharp edge arising from an unscattered particle is classified as the μ-like event.

7.2.3 Event selection for the ν_μ disappearance analysis

For the ν_μ disappearance analysis, the following cuts are applied to the single-ring μ-like events:

1. $p_\mu > 200$ MeV/c: events with the reconstructed muon momentum of 200 MeV/c or less are cut to keep the performance of the particle identification and to reduce contamination of decay electrons from invisible muons.

2. One decay electron or less: the number of decay electrons is required to be one or less. This cut enhances CCQE events, in which the stopped muon in ID decays into an electron.

7.2.4 Event selection for the ν_e appearance search

Signals of the ν_e appearance are searched in the FCFV events based on the cut criteria below. These criteria were predefined [202] using a MC sample to avoid any artificial bias to the analysis.

1. $E_{\mathrm{vis}} > 100$ MeV: events with the visible energy of 100 MeV or less are cut to reduce backgrounds from NC interactions and Michel electrons produced by invisible muons.

2. Single-ring: CCQE events are selected by selecting single-ring events.

3. e-like ring: events with an e-like ring are selected.

4. No decay electrons: it is required that there is no subsequent event which indicates a Michel electron from a muon decay. This cut reduces ν_μ backgrounds misidentified as ν_e.

5. POLfit mass < 105 MeV/c^2: invariant π^0 mass reconstructed by the POLfit (Pattern Of Light fit) algorithm [203, 204] is required to be less than 105 MeV/c^2. POLfit is a π^0 fitter used for e/π^0 separation at Super-K to reduce π^0 backgrounds in electron signal candidates. It assumes the second gamma ring in a single-ring e-like event and tries to find it. If the e-like ring originates from one of the gammas from a π^0 decay, POLfit reconstructs the invariant mass of the e-like and second gamma rings around the π^0 mass (135 MeV/c^2).

6. $E_\nu^{\mathrm{rec}} < 1250$ MeV: only events in which the reconstructed neutrino energy (E_ν^{rec}) according to Eq. 2.3 is less than 1250 MeV are selected. The higher energy neutrinos are considered to be mostly the beam ν_e contamination since the T2K ν_μ beam spectrum peaks around 0.6 GeV, where the oscillation probability $P(\nu_\mu \to \nu_e)$ is expected to be maximal.

7.3 Outline of the analysis

The goal of this analysis is to obtain the expected number of neutrino events at Super-K and its systematic error related to the beam and beamline, and to show that the quality of our neutrino beam meets the T2K requirement. In this analysis, the expected number of neutrino events at Super-K ($N_{\rm SK}^{exp}$) is estimated from the MC prediction at Super-K ($N_{\rm SK}^{\rm MC}$) normalized by the ratio of the observation to the expectation at the ND280 off-axis detector ($N_{\rm ND}/N_{\rm ND}^{\rm MC}$):

$$\begin{aligned} N_{\rm SK}^{exp}(\Delta m^2,\theta) &= \frac{N_{\rm ND}}{N_{\rm ND}^{\rm MC}} \cdot N_{\rm SK}^{\rm MC}(\Delta m^2,\theta) \\ &= N_{\rm ND} \cdot \frac{\sum_{\nu_\ell}\sum_{I}\sum_{E_\nu^{rec}} M^{I,\nu_\ell}(E_\nu^{rec},E_\nu) \times P_{osc}^{\nu_\ell}(E_\nu;\Delta m^2,\theta) \cdot N_{\rm SK}^{I,\nu_\ell}(E_\nu)}{\sum_{\nu_\ell}\sum_{I}\sum_{E_\nu} N_{\rm ND}^{I,\nu_\ell}(E_\nu)}, \end{aligned} \tag{7.3}$$

where ν_ℓ denotes the neutrino flavor (ν_μ, $\bar{\nu}_\mu$ or ν_e; $\bar{\nu}_e$ is disregarded because its fraction is small); I denotes the neutrino interaction mode (CCQE, CC1π, etc.); E_ν and E_ν^{rec} denote bins of the true and reconstructed neutrino energies, respectively; $M^{I,\nu_x}(E_\nu^{rec},E_\nu)$ is a matrix representing a probability to observe E_ν as E_ν^{rec}, and is different from neutrino interaction mode to mode and from neutrino flavor to flavor; Δm^2 and θ are the neutrino oscillation parameters; and $P_{osc}^{\nu_\ell}$ is the neutrino oscillation probability, and is different from flavor to flavor. Only the integrated numbers of neutrino events are evaluated since the neutrino energy spectrum at the ND280 off-axis detector is not available at this moment. $N_{\rm SK(ND)}^{I,\nu_\ell}(E_\nu)$ is estimated from

$$N^{I,\nu_\ell}(E_\nu) = \phi^{\nu_\ell}(E_\nu) \cdot \sigma^{I,\nu_\ell}(E_\nu) \cdot \epsilon^{I,\nu_\ell}(E_\nu), \tag{7.4}$$

where ϕ is the neutrino flux, σ is the neutrino cross-section and ϵ is the detector efficiency. The neutrino flux has to be estimated for each neutrino flavor and both for the ND280 off-axis detector and Super-K. The way to estimate the neutrino flux is discussed in this thesis.

Prediction of the neutrino flux

The neutrino flux is determined by the proton beam parameters at the target, horn focusing effect and hadron production cross-sections. Therefore, precise measurements of (1) the proton beam, (2) the horn currents and (3) the hadron production cross-sections are necessary to precisely estimate the neutrino flux. The measurements of the first two items were described in Sec. 6.3.1, and the one of the last item is described in Sec. 8.2.3. With these items, the neutrino flux is estimated by the MC simulation program, JNUBEAM. The first two items are used just as inputs to JNUBEAM. The last item is used to tune the hadron production in JNUBEAM. Because the systematic error of the neutrino flux arising from the uncertainties of the hadron production of interest in T2K is known to be large, the hadron production cross-sections have to be measured in the other experiment and the hadron production in JNUBEAM has to be tuned. The way of the tuning is described in Chap. 8. Then, the number of neutrino events at Super-K is estimated in Chap. 9, and is compared to the observation in Chap. 10.

The systematic error of the neutrino flux is evaluated from the uncertainties of the hadron production in Chap. 8 and from the uncertainties related to the beam and beamline in Chap. 9. Since Super-K and the ND280 off-axis detector measure neutrinos from almost the same parent particles, the neutrino flux errors at Super-K and the ND280 off-axis detector are expected to correlate with each other. Therefore, it is expected that these flux errors cancel out in terms of the near-to-far extrapolation as described in Fig. 2.7.

Chapter 8

Hadron Production Tuning for the Neutrino Flux Prediction

To estimate the neutrino flux precisely, the hadron production in the MC simulation program (JNUBEAM) is tuned to the external experimental data in this chapter. An overview of JNUBEAM is firstly given in Sec. 8.1, and the hadron production of interest in T2K is explained in Sec. 8.2. Then, in Sec. 8.3, the detail of the hadron production tuning is described. The expected neutrino flux after the tuning is shown in Sec. 8.4. The systematic error of the neutrino flux from the hadron production uncertainties is evaluated in Sec. 8.5.

8.1 Overview of JNUBEAM

JNUBEAM is based on the GEANT3 [205] simulation tool. The geometry of the secondary beamline is replicated in JNUBEAM including the horn magnetic fields.

The method to estimate the neutrino flux is as follows: Firstly, the 30 GeV proton interaction in the target (and the baffle) and its hadronic chains are simulated by FLUKA 2008* [206, 207]. Information on the position and momentum of exiting particles from the target and on those of their ancestors in the interaction and decay chains is transferred to JNUBEAM. Secondary, the particles are transported in JNUBEAM. Hadron interactions in JNUBEAM are simulated by GCALOR [208]. In order to save CPU time, whenever a particle decays into neutrino(s), the flavor and energy of the neutrino(s) as well as the ancestor's information are stored with the probability that the neutrino is produced in the direction of ND280 or Super-K. Lastly, the neutrino flux is obtained from these pieces of information.

FLUKA is used as a base simulation for the hadron interactions in the target because it shows better agreement with the measurement by the NA61/SHINE experiment at CERN [157, 209] than the GEANT3 implemented hadron interaction models. However, there is still a discrepancy between FLUKA and NA61. Therefore, the hadron interactions in the target need to be tuned so that they reproduce the NA61 and some other available hadron production data.

8.1.1 Hadron interactions in the target with FLUKA

The geometry used in FLUKA is illustrated in Fig. 8.1. Protons with 30.9328 GeV/c are generated at the entrance of the baffle in accordance with the measured proton beam parameters shown in Sec. 6.3.1 (see Table 6.5). The baffle is modeled as a $29 \times 40 \times 171.145$ cm^3 graphite rectangular block. The proton beam goes through the cylindrical hole of 3.0 cm in diameter

*A stand-alone FLUKA based simulation is used because there is no built-in interface between FLUKA 2008 and GEANT3.

in the baffle. For the target, only its graphite core is modeled as a simple cylinder of 2.6 cm in diameter and 90 cm in length. Other complicated structure of the target is replicated in JNUBEAM. The baffle hole and the volume between the baffle and target are filled with He gas.

When particles exit the baffle and the target regions, their information is stored to be input to JNUBEAM. Electrons and photons above 1 GeV are not stored to reduce the file size. For the other particles, no energy cut is applied other than the tracking threshold of 10 MeV.

8.1.2 Particle tracking in JNUBEAM

The particles from the FLUKA output are tracked in JNUBEAM, where almost all the components in the secondary beamline are replicated as shown in Fig. 8.2. The geometry of each component and the alignment are based on measurements and survey.

The energy threshold for the tracking is set at 0.1 GeV for hadrons and muons and at 1.0 GeV for gammas and electrons. Downstream of the beam dump, an additional threshold at 1.0 GeV is applied for neutral hadrons and muons to save running time. For the muon monitor study, the energy threshold for particles other than charged hadrons downstream of the beam dump is lowered to 10 keV.

Horn magnetic field

The magnetic field between the horn inner and outer conductors is implemented in JNUBEAM according to Ampère's law. The measured current is used as the input (see Table 6.6).

The magnetic field in the inner conductor is also implemented. The horn conductor is made of aluminum, and the thickness of the inner conductor is 3 mm. Since the low frequency pulsed current (3.6 msec full width) is loaded into the horn, the skin effect is small (the estimated skin depth is approximately 5 mm). Therefore, it can be assumed that the current flows in the conductor uniformly. On this assumption, the magnetic field at radius r in the inner conductor is calculated with Ampère's law as:

$$B(r) = \frac{\mu_0 I}{2\pi r}\frac{r^2 - a^2}{b^2 - a^2}, \tag{8.1}$$

where μ_0 is the magnetic permeability, I is the current and a and b are the inner and outer radii of the inner conductor, respectively.

Neutrino-producing decay modes

In JNUBEAM, $\pi^{\pm}$, $K^{\pm}$, K^0_L and $\mu^{\pm}$ decays listed in Table 8.1 are considered as neutrino sources. Current best knowledge of the branching ratios and $K^{\pm}_{\ell 3}$ decay form factors is used. The polarization effect in muon decays is also taken into account.

When a neutrino-producing decay occurs, the probability that the neutrino is produced in a direction of the detector (Super-K or the ND280 off-axis detector), $\mathcal{N}$, is calculated according to the following equations (except for the muon decay):

$$\mathcal{N} = N_{\mathrm{POT}} \cdot \mathcal{B} \cdot \Delta\Omega \cdot S, \tag{8.2}$$

$$\Delta\Omega = \begin{cases} \gamma(1 - \beta\cos\theta)\left(\dfrac{\sin\theta^{cm}}{\sin\theta}\right)^3 & (\theta \neq 0), \\ \dfrac{1}{\gamma^2(1-\beta)^2} & (\theta = 0), \end{cases} \tag{8.3}$$

$$S = \frac{A \cdot n_z}{4\pi L(z)^2}, \tag{8.4}$$

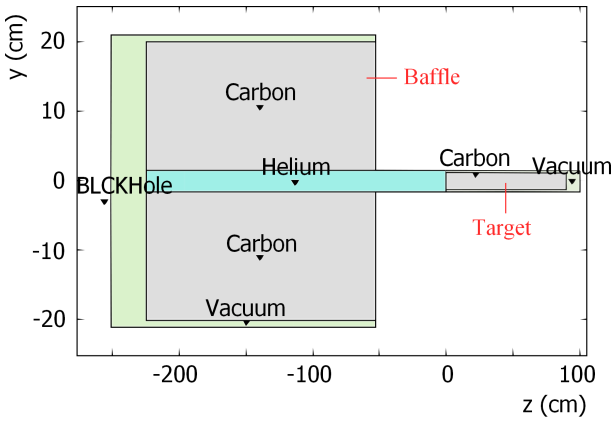

Figure 8.1: Geometrical setup in the FLUKA simulation (y-z cross section view).

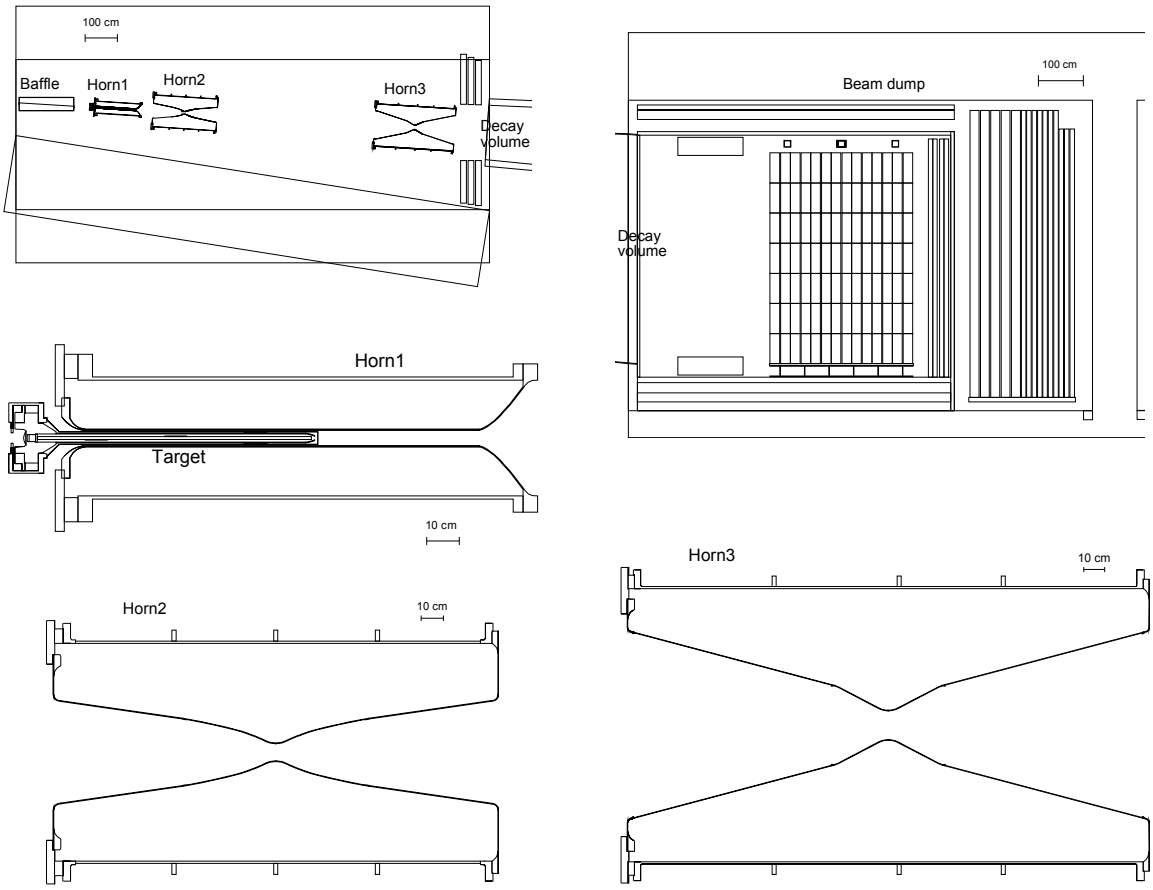

Figure 8.2: Geometrical setup in JNUBEAM. Upper left: target station (side view). Upper right: beam dump (side veiw). Lower: horns (top view).

Table 8.1: Neutrino-producing decay modes considered in JNUBEAM. In this table, decay modes for $\bar{\nu}_\mu$ and $\bar{\nu}_e$ are omitted. The π^- and K^- modes are charge conjugates of the π^+ and K^+ modes, respectively. The branching ratio (%) [194] is written below each mode.

	Parent particle				
	π^+	K^+	K^0_L	μ^+	μ^-
ν_μ	$\mu^+\nu_\mu$	$\mu^+\nu_\mu$, $\pi^0\mu^+\nu_\mu$	$\pi^-\mu^+\nu_\mu$		$e^-\nu_\mu\bar{\nu}_e$
	99.9877	63.55, 3.353	27.04		≈100
ν_e	$e^+\nu_e$	$\pi^0 e^+\nu_e$	$\pi^- e^+\nu_e$	$e^+\bar{\nu}_\mu\nu_e$	
	1.23×10^{-4}	5.07	40.55	≈100	

where N_{POT} is a normalization factor for POT, $\mathcal{B}$ is the branching ratio, γ and β are the Lorentz factors of the parent particle, θ is the angle between the directions of the parent particle momentum p and a given position on the detector surface in the lab system, θ^{cm} is the same angle in the center-of-mass system, S is the detector acceptance, $L(z)$ is the distance from the decay position (z) to the position on the detector surface (L = const. for Super-K), A is the surface area of the detector, and $n_z = p_z/p$. Super-K is treated as a point-like detector; i.e. $A \cdot n_z = 1$. The neutrino energy is calculated as:

$$E_\nu = p_\nu^{cm} \cdot \frac{\sin\theta^{cm}}{\sin\theta}, \tag{8.5}$$

where p_ν^{cm} is the neutrino momentum in the center-of-mass system.

Figure 8.3 shows the neutrino flux at Super-K and each neutrino-parent particle contribution, and Table 8.2 shows the proportion of each parent particle. (This flux is estimated with JNUBEAM before the hadron tuning, called pre-tuned JNUBEAM.) The main contributor to the flux is π^+ (for ν_μ), π^- (for $\bar{\nu}_\mu$), K^+ (for ν_e) and K^0_L (for $\bar{\nu}_e$). For the ν_μ and ν_e flux, the contribution of K^+ becomes dominant at higher neutrino energies.

8.2 Hadron production in T2K

8.2.1 Definition of the production cross-section and multiplicity

In T2K, the proton beam of 30 GeV kinetic energy interacts with the graphite target. The hadronic interactions in the target are categorized into:

- elastic interaction, in which the proton is scattered by the carbon nucleus coherently without producing any particles;
- quasi-elastic interaction, in which the proton is scattered by the nucleus incoherently;
- inelastic interaction, in which hadrons are produced.

In this thesis, the firstly-occurrent inelastic interaction inside the target is defined as the primary interaction, and the hadrons produced at the primary interaction including the scattered nucleons are called secondary particles. The secondary particle also interacts or is absorbed in the target or other materials such as the horn aluminum conductor. This interaction is called the secondary interaction, which can produce tertiary particles.

The cross-sections for the elastic and quasi-elastic interactions are called the elastic (σ_{el}) and quasi-elastic (σ_{quel}) cross-sections, respectively. The cross-section for the inelastic interaction is

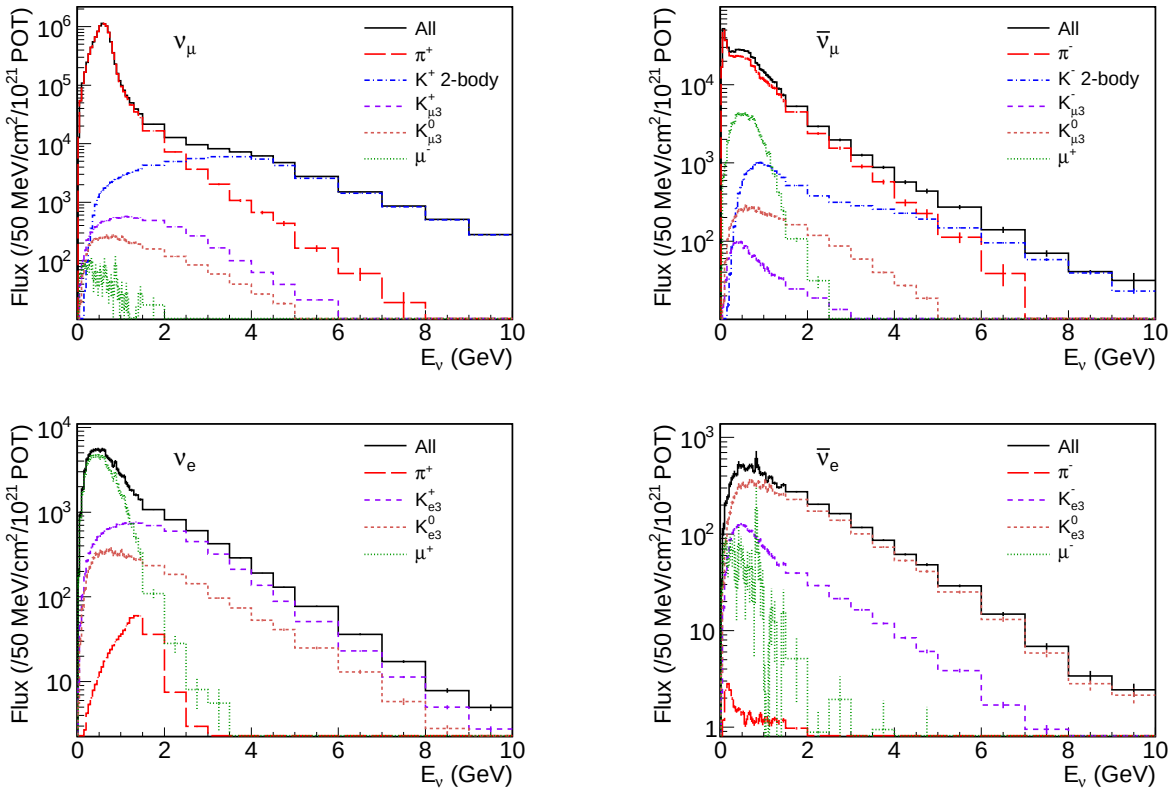

Figure 8.3: Contribution of each parent particle to the neutrino flux at Super-K for ν_μ (upper left), $\bar{\nu}_\mu$ (upper right), ν_e (lower left) and $\bar{\nu}_e$ (lower right). The error bars are the MC statistical errors. It is estimated with the pre-tuned JNUBEAM.

Table 8.2: Proportion of particles which are parents of neutrinos at Super-K. Only particles whose daughter neutrinos have energies below 10 GeV are counted. It is estimated with the pre-tuned MC.

Parent particle	ν_μ	$\bar{\nu}_\mu$	ν_e	$\bar{\nu}_e$
π^+	94.91%		0.97%	
π^-		83.22%		0.36%
K^+ (2-body decay)	4.73%			
K^- (2-body decay)		6.09%		
K^+ (3-body decay)	0.25%		31.71%	
K^- (3-body decay)		0.33%		17.31%
K^0_L	0.10%	1.49%	12.73%	76.32%
μ^+		8.87%	54.59%	
μ^-	0.01%			6.01%

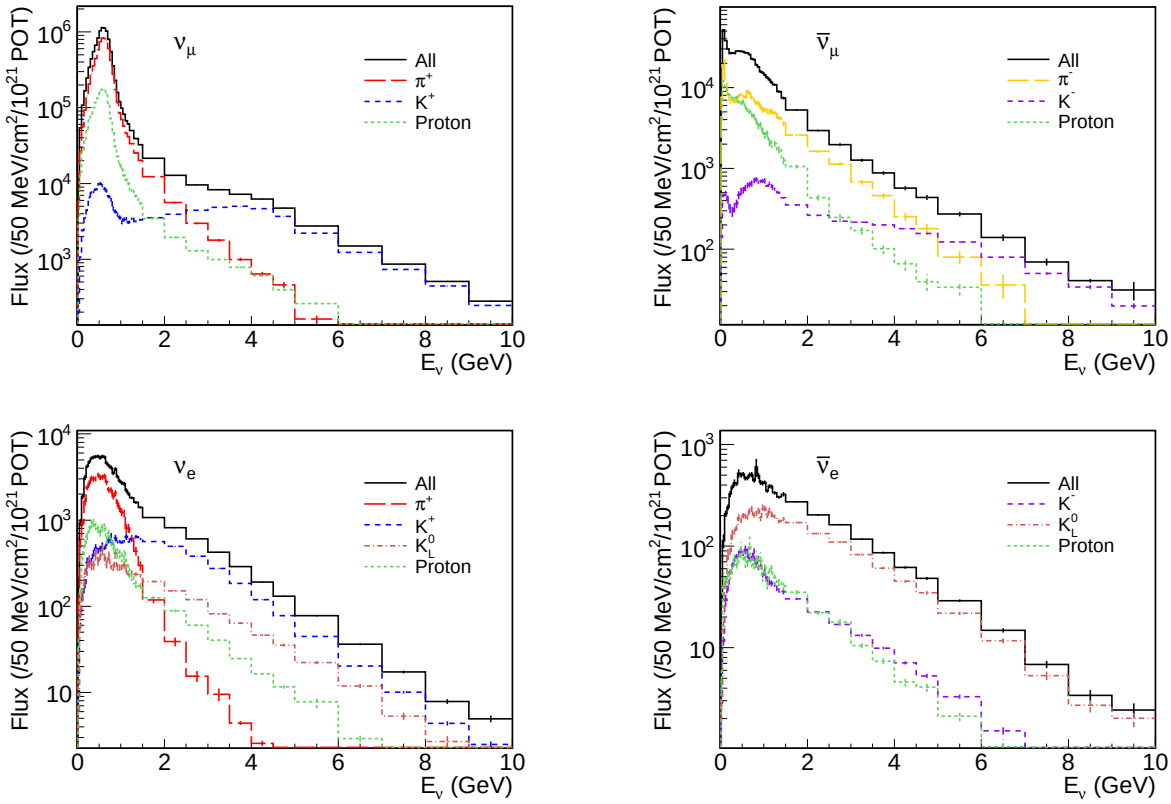

Figure 8.4: Contribution of each secondary particle to the neutrino flux at Super-K for ν_μ (upper left), $\bar{\nu}_\mu$ (upper right), ν_e (lower left) and $\bar{\nu}_e$ (lower right). Only the flux from the mainly contributing secondary particles is plotted. The error bars are the MC statistical errors. It is estimated with the pre-tuned JNUBEAM.

called the production cross-section (σ_{prod}) defined as $\sigma_{prod} = \sigma_{toal} - \sigma_{el} - \sigma_{quel} = \sigma_{inel} - \sigma_{quel}$, where σ_{total} is the total cross-section and σ_{inel} is the inelastic cross-section defined as $\sigma_{inel} = \sigma_{toal} - \sigma_{el}$. In this thesis, σ_{quel} is estimated by using a model constructed by G. Bellettini *et al* [210] to deduce σ_{prod}.

The number of secondary particles produced in an inelastic interaction is called the multiplicity, which is the differential inclusive production cross-section normalized by σ_{prod}:

$$\frac{\mathrm{d}^2 n}{\mathrm{d}p\,\mathrm{d}\theta} = \frac{1}{\sigma_{prod}} \frac{\mathrm{d}^2 \sigma}{\mathrm{d}p\,\mathrm{d}\theta}, \tag{8.6}$$

where p is the momentum and θ is the polar angle relative to the beam direction.

8.2.2 Secondary particles contributing the neutrino beam

The contribution of each secondary particle species to the neutrino flux at Super-K is shown in Fig. 8.4, and the proportion of the secondary particle species to the neutrino flux is listed in Table 8.3. The pions are the main contributor to the neutrino flux at the lower energies, and the kaons are the one at the higher energies.[†] The secondary protons also have a large contribution since they produce pions as listed in Table 8.4. The beam ν_e background at Super-K mainly

[†]In the two-body decay, the heavier kaon mainly produces a higher energy neutrino than the lighter pion (see Eq. 2.5).

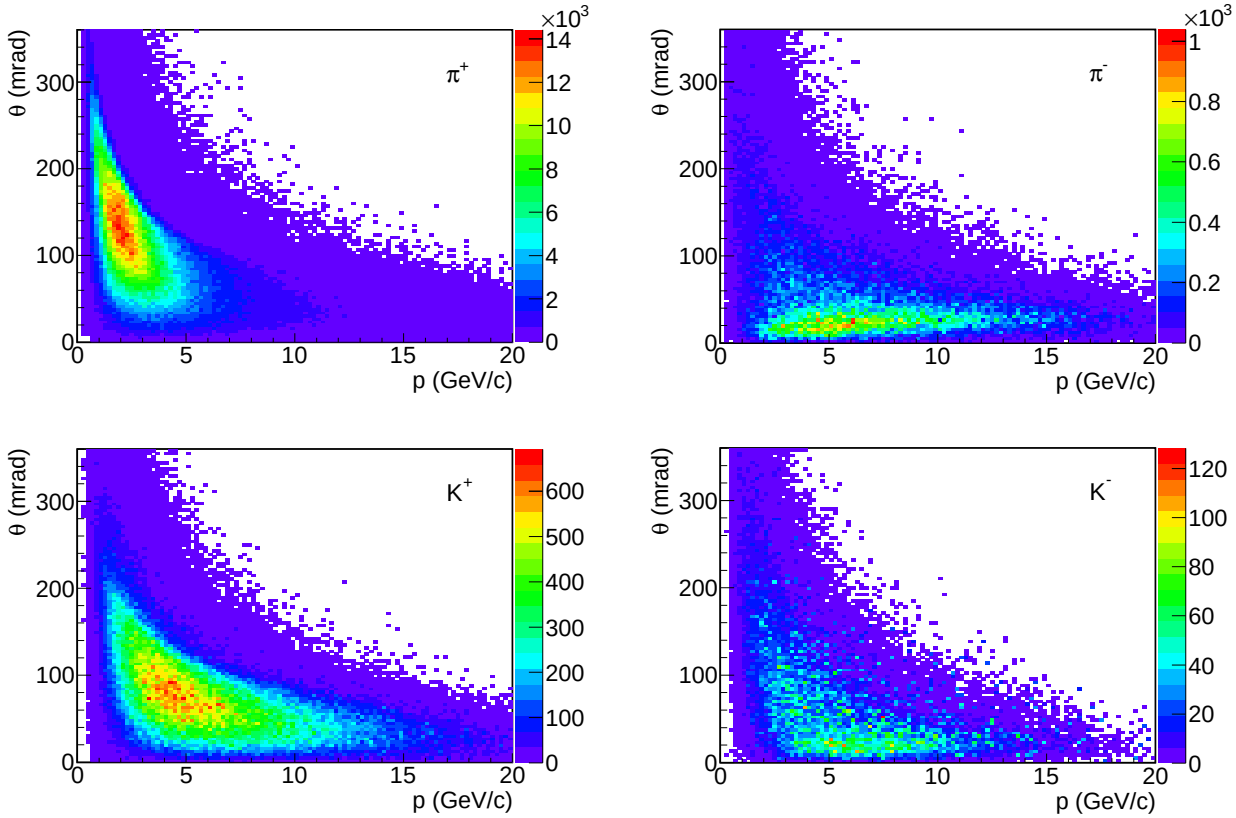

Figure 8.5: p-θ distribution of secondary pions and kaons whose descendant neutrinos go to Super-K. It is estimated with the pre-tuned JNUBEAM.

comes from the π^+ via the following decay chains: $\pi^+ \to \mu^+\nu_\mu$, $\mu^+ \to e^+\bar{\nu}_\mu\nu_e$. The K^+ and K^0_L (decaying via the K_{e3} modes) are also important for the estimation of the beam ν_e background. Most of the secondary particles contribute to the neutrino flux via their decays. Some of them contribute to it after undergoing reinteractions (secondary interactions), but its fraction is as small as 10% or less as listed in Table 8.5.

In T2K, the pions and kaons produced with $p \approx$ a few GeV and $\theta < 300$ mrad are important (see Fig. 8.5, in which only pions and kaons whose descendant neutrinos go to Super-K are plotted). The π^+ produced with $p \approx 2$ GeV/c and $\theta = 100$–200 mrad is predominantly focused by the horns to point the on-axis direction and constitutes the peak around 0.6 GeV of the ν_μ flux at Super-K. The π^- produced forward and less defocused by the horns[‡] constitutes the similar peak of the $\bar{\nu}_\mu$ flux to ν_μ around 0.6 GeV. Another peak of $\bar{\nu}_\mu$ around 0 GeV originates from π^- defocused by the horns and straying far away from the Super-K direction.

8.2.3 Measurement of the hadron production by CERN-NA61

The multiplicities and production cross-sections needed for T2K are measured by the CERN-NA61/SHINE experiment [154, 155]. During 2007 run [156, 157], data was taken for interactions of 30 GeV protons on two graphite targets with different geometry:

- a thin target to study the primary interaction,
- a T2K replica target to predict the T2K neutrino flux and to study the secondary interaction.

[‡]The forward π^- goes through the inside of the horn inner conductor, where the magnetic field is zero.

Table 8.3: Proportion of secondary particles which contribute to the neutrino flux of each flavor (below 10 GeV) at Super-K. It is estimated with the pre-tuned JNUBEAM.

Secondary particle	ν_μ	$\bar{\nu}_\mu$	ν_e	$\bar{\nu}_e$
π^+	67.5%	11.7%	38.8%	3.4%
π^-	2.0%	36.6%	1.7%	4.0%
K^+	4.8%	2.2%	26.9%	3.0%
K^-	0.1%	4.9%	0.4%	13.0%
K^0_L	2.8%	4.4%	11.9%	55.8%
Proton	15.8%	21.4%	13.6%	13.0%
Neutron	5.2%	13.6%	5.2%	5.4%
Others (Λ, Σ, $\bar{n}$, etc.)	1.8%	5.2%	1.5%	2.4%
Total	100%	100%	100%	100%

Table 8.4: Proportion of tertiary particles produced by the secondary protons to the total neutrino flux of each flavor (below 10 GeV) at Super-K. It is estimated with the pre-tuned JNUBEAM. The last line (total) is equal to the proportion of the secondary protons in Table 8.3.

Tertiary particle	ν_μ	$\bar{\nu}_\mu$	ν_e	$\bar{\nu}_e$
π^+	12.3%	2.1%	6.6%	0.4%
π^-	0.2%	11.5%	0.2%	0.9%
K^+	0.6%	0.3%	3.4%	0.4%
K^-	0.0%	0.7%	0.0%	1.6%
K^0_L	0.3%	0.5%	1.4%	7.5%
Proton	1.7%	3.3%	1.4%	1.4%
Neutron	0.5%	2.1%	0.4%	0.4%
Others (Λ, Σ, $\bar{n}$, etc.)	0.2%	0.9%	0.2%	0.4%
Total	15.8%	21.4%	13.6%	13.0%

Table 8.5: Proportion of secondary particles which contribute to neutrinos at Super-K after undergoing reinteractions (secondary interactions). It is estimated with the pre-tuned MC. The value listed in this table is the fraction of these secondary particles to the total neutrino flux of each flavor. Only π and K are listed in this table. For protons, neutrons, etc., see Table 8.3.

Secondary particle	ν_μ	$\bar{\nu}_\mu$	ν_e	$\bar{\nu}_e$
π^+	10.5%	6.6%	7.2%	3.4%
π^-	2.0%	7.8%	1.7%	2.3%
K^+	0.8%	0.8%	2.7%	2.8%
K^-	0.1%	0.8%	0.4%	2.1%
K^0_L	0.6%	1.1%	1.9%	4.9%

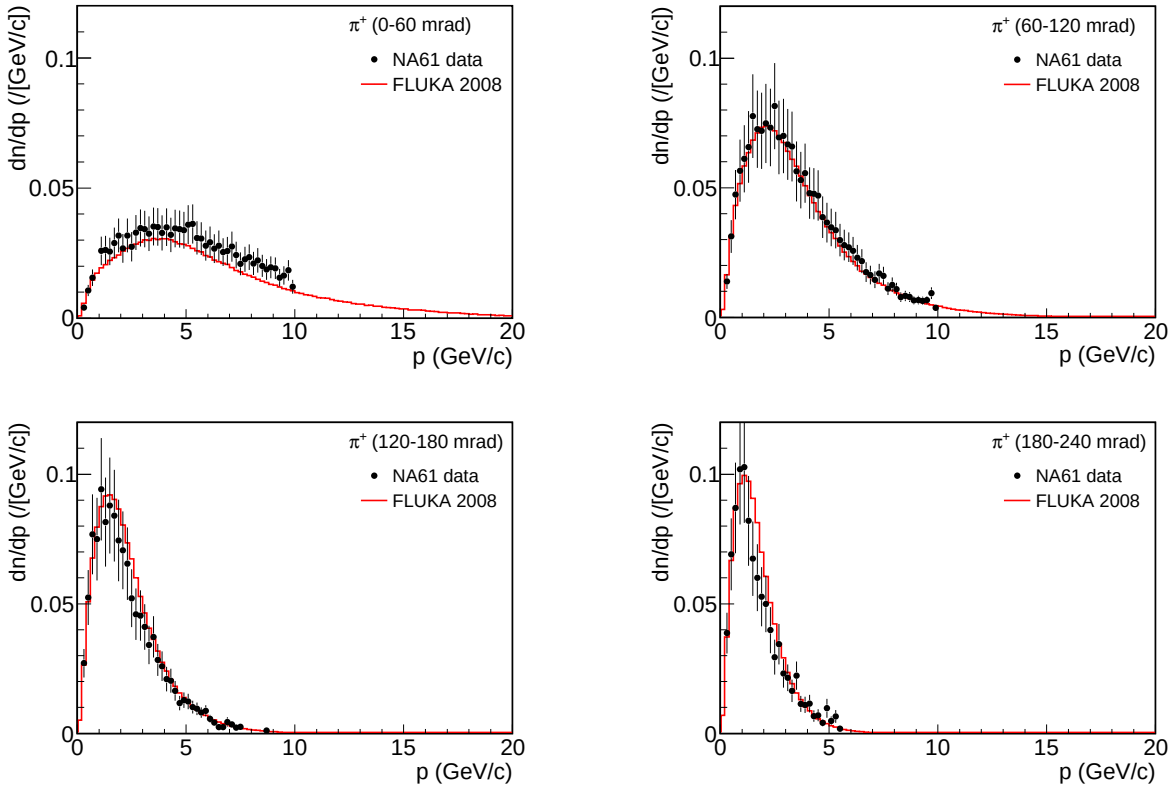

Figure 8.6: $\mathrm{d}n/\mathrm{d}p(p)$ distribution of π^+ in different θ angle intervals in 30 GeV proton and C interactions measured by NA61 [209]. The FLUKA prediction (solid line) is also drawn. The error bar shows the 20% overall error.

The thin target is a 2.5×2.5 cm^2 and 2 cm thick rectangle with a density of 1.84 g/cm^3, which corresponds to approximately 4% of the nuclear interaction length. The replica target is a 90 cm long cylinder of 2.6 cm diameter with a density of 1.83 g/cm^3 (approximately 1.9 interaction length).

Currently, a preliminary result of the $\pi^{\pm}$ production for the thin target data [209] is available for T2K. It is shown in Fig. 8.6 and 8.7. The σ_{prod} was measured by NA61 as $\sigma_{prod} = 225.0$ mb. This distribution covers approximately 92% and 98% of the T2K phase space for π^+ and π^-, respectively. An overall 20% systematic error is assigned to this distribution. The σ_{prod} has 10% uncertainty.

8.3 Tuning of the hadron production

8.3.1 Overview of the tuning

Since the pion and kaon productions are most important for the prediction of the neutrino flux, they are tuned in JNUBEAM so as to reproduce the existing hadron production data. The tuning is done by reweighting the number of produced particles per interaction (multiplicity) and the particle-producing interaction rate (production cross-section σ_{prod}); the multiplicity and σ_{prod} used in the MC simulation are compared to the data, and are reweighted by the data/MC ratio. Therefore, this data/MC ratio for the multiplicity and σ_{prod} are presented in this section.

In FLUKA 2008, which is utilized to simulate interactions in the target, the quasi-elastic interaction is categorized into the elastic interaction. Therefore, σ_{prod} is equal to σ_{inel}, with

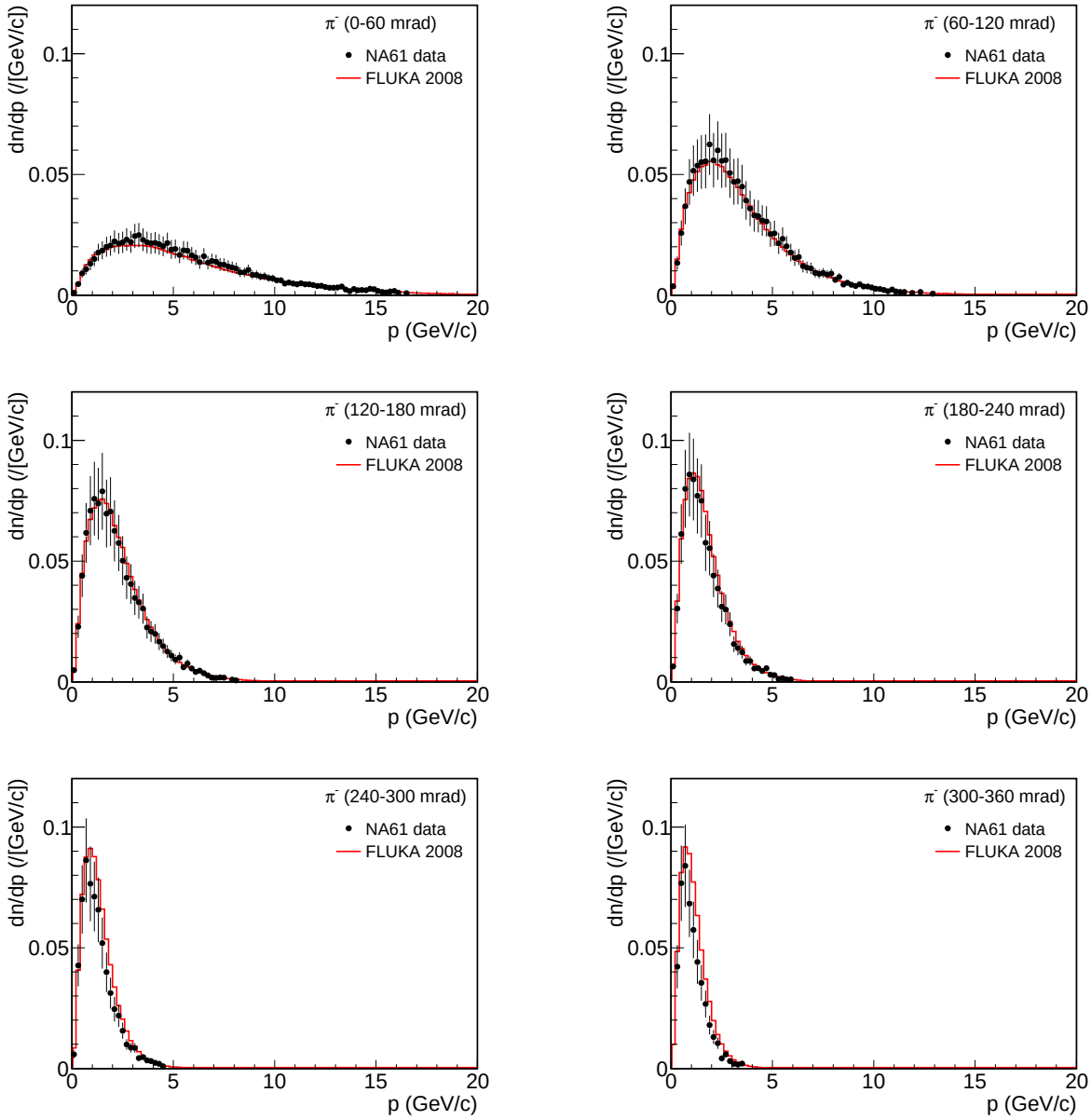

Figure 8.7: $\mathrm{d}n/\mathrm{d}p(p)$ distribution of π^- in different θ angle intervals in 30 GeV proton and C interactions measured by NA61 [209]. The FLUKA prediction (solid line) is also drawn. The error bar shows the 20% overall error.

Table 8.6: Summary of the hadron production tuning.

	Used data/model for the tuning
Multiplicity	
Secondary $\pi^{\pm}$	NA61 thin target data
Tertiary $\pi^{\pm}$ from secondary protons	NA61 thin target data and Feynman scaling
Secondary and tertiary $K^{\pm}$	FLUKA 2008 (not tuned; cf. Appendix E)
The other hadrons	FLUKA 2008 (not tuned)
Production cross-section	
$\pi^{\pm}$, $K^{\pm}$ and protons inside the target	FLUKA 2008 (not tuned)
$\pi^{\pm}$, $K^{\pm}$ and protons outside the target	Data in Table 8.7
The other hadrons inside the target	FLUKA 2008 (not tuned)
The other hadrons outside the target	GCALOR (not tuned)

which the multiplicity is normalized. In this analysis, the multiplicities of secondary pions and tertiary pions from secondary proton interactions are tuned to the NA61 thin target data. That is described in Sec. 8.3.2 and 8.3.3. For the kaon multiplicity, the FLUKA prediction is used because there are a few kaon production data available for T2K. A possible method for the kaon tuning with the past data is discussed in Appendix E. The multiplicities of the other secondary and tertiary hadrons, like tertiary pions from secondary pion interactions, are not tuned since their contributions to the neutrino flux are small as shown in Table 8.5.

In Sec. 8.3.4, the σ_{prod} tuning is applied to the proton, $\pi^{\pm}$ and $K^{\pm}$ interactions (see Ref. [211] for detail). Some models are compared to various cross-section measurements for these hadrons with a momentum less than 30 GeV/c. When σ_{inel} is measured, σ_{quel} is subtracted from it to obtain σ_{prod}. Basically, one of the models which agrees best with the σ_{prod} data is adopted. If necessary, the model is reweighted to agree with the σ_{prod} data.

These hadron production tunings are summarized in Table 8.6.

8.3.2 Secondary $\pi^{\pm}$ multiplicities

The multiplicity (dn/dp) distribution of the secondary pions in FLUKA is calculated under the same condition as in the NA61 thin target data [209]. It is normalized by $\sigma_{prod} = 231.3$ mb calculated in the simulation. The ratio of NA61 to FLUKA is shown in Fig. 8.8 (see also Fig. 8.6 and 8.7). The data shows slightly higher multiplicity than the FLUKA prediction for the forward $\pi^{\pm}$ and slightly lower multiplicity for the $\pi^{\pm}$ with the larger θ angle. The number of secondary pions in each p-θ bin (Fig. 8.5) is reweighted with this ratio to tune the FLUKA primary interactions to the NA61 data. For pions outside the phase space covered by NA61, the FLUKA prediction is used without any correction.

8.3.3 Tertiary $\pi^{\pm}$ multiplicities

The multiplicity of tertiary pions from the secondary proton interactions depends on the secondary proton momentum. The momentum distribution of the secondary protons which contribute to the neutrino flux at Super-K is shown in Fig. 8.9. There are two peaks: one for inelastically scattered protons around 30 GeV/c and the other for secondary produced protons around 15 GeV/c. The multiplicity distribution of the tertiary pions for each proton momentum is estimated by using the NA61 data and the Feynman scaling [212]; the dn/dp distribution of $\pi^{\pm}$ for the 30 GeV incident proton from the NA61 thin target data is scaled to one for any

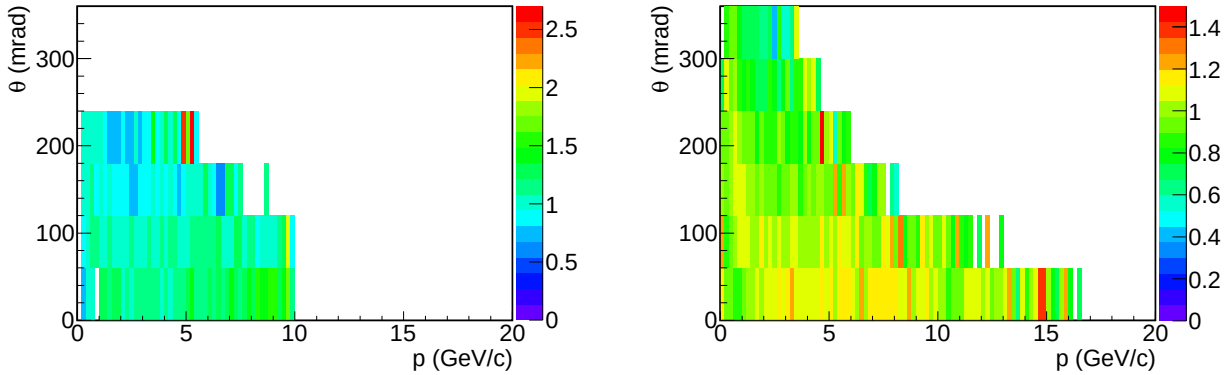

Figure 8.8: $\mathrm{d}n/\mathrm{d}p(p,\theta)$ ratio of NA61 to FLUKA for π^+ (left) and π^- (right).

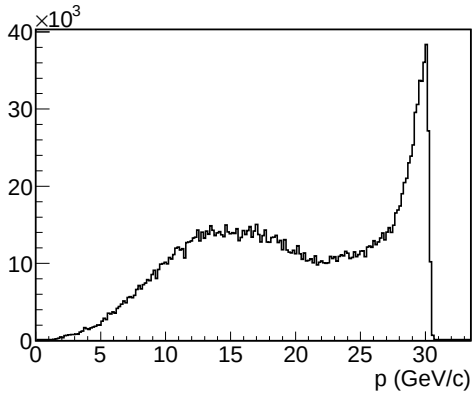

Figure 8.9: Momentum distribution of the secondary protons whose descendant neutrinos go to Super-K. Only secondary protons from inelastic interactions are plotted. It is estimated with the pre-tuned JNUBEAM.

proton momentum with the Feynman scaling. The multiplicity of the secondary protons from the primary interaction is not tuned in this analysis.

Feynman scaling

R.P. Feynman argued that in the interaction of two oncoming particles at the center-of-mass energy $\sqrt{s}$, the probability of finding a produced particle of kind i with mass m, transverse and longitudinal momentum p_T and p_L and the energy $E = \sqrt{m^2 + p_T^2 + p_L^2}$ is of the form:

$$f_i(p_T, x_F)\frac{\mathrm{d}p_L}{E}\mathrm{d}^2p_T, \tag{8.7}$$

where f_i is called Feynman function and denotes the particle distribution, and $x_F \equiv 2p_L/\sqrt{s}$ is called Feynman x. The f_i is independent of $\sqrt{s}$ when expressed in terms of p_T and x_F. That suggests an approximate scaling of the single-particle inclusive invariant cross-section. Integration of the expression 8.7 results in Feynman's conclusion that for asymptotically large energies, the mean total number of any kind of particles $\langle N \rangle$ rises logarithmically with $\sqrt{s}$:

$$\langle N \rangle \propto \ln \sqrt{s}. \tag{8.8}$$

Feynman x is not very convenient for the scaling to different $\sqrt{s}$ near kinematical limits of the particle production (i.e. at incident momenta in the range 5–30 GeV/c). Instead, the parameter

$$x_F^{cm} \equiv \frac{p_L^{cm}}{p_{max}^{cm}} \tag{8.9}$$

was found to be more suitable [213], where "cm" denotes the variable in the center-of-mass system. x_F^{cm} is equal to x_F at very high energies. p_{max}^{cm} is the maximum momentum kinematically available to the produced particle i. In the calculation of x_F^{cm}, it is assumed that the target is a proton at rest, or an inclusive interaction of p + p $\rightarrow i + X$:

$$p_{max}^{cm} = \frac{1}{2}\sqrt{s - 2(m^2 + M_{min}^2) + \frac{(m^2 - M_{min}^2)^2}{s}}, \tag{8.10}$$

with M_{min} being the minimum total mass of X allowed by the conservation laws of charge, baryon number and strangeness. When the particle i is a π^+, π^-, K^+, K^- or K^0, M_{min} is the mass of p + n, 2p + π^+, p + Λ, 2p + K^+ or p + Σ, respectively.

Multiplicity ratio in the x_F-p_T phase space

In order to apply the Feynman scaling, p and θ of each tertiary pion are converted to x_F and p_T according to Eq. 8.9 and 8.10, where the $\sqrt{s}$ is calculated from the secondary proton momentum. Figure 8.10 shows the x_F-p_T distribution of the tertiary pions which contribute the neutrino flux at Super-K. Each tertiary pion is reweighted with the dn/dp ratio of NA61 to FLUKA shown in Fig. 8.11, which is converted from the one in p-θ for the 30 GeV incident proton shown in Fig. 8.8.

8.3.4 Interaction rate

Comparison between data and models

The cross-section data listed in Table 8.7 are compared with the hadron interaction models, FLUKA 2008 and GCALOR. In our neutrino flux simulation, FLUKA is used for the interactions inside the target (predominantly p, $\pi^\pm$ and $K^\pm$ interactions with C), while GCALOR is used for the ones outside the target (predominantly p, $\pi^\pm$ and $K^\pm$ interactions with Al of the horn conductor).

The production cross-sections are plotted in Fig. 8.12. For the cross-sections measured by S.P. Denisov *et al.*, it is ambiguous whether the quasi-elastic cross-section has been subtracted; for this study, it is assumed that the quasi-elastic cross-section has been subtracted. There is a good agreement between the data and FLUKA. On the other hand, there are disagreements between the data and GCALOR. Therefore, the σ_{prod} tuning is necessary only for the GCALOR part.

Tuning of the interaction rate

The probability $P_{\rm int}$ that a particle with a momentum p travels a distance x in a material and then interacts with the material in Δx is calculated as

$$P_{\rm int} = e^{-n\sigma(p)x} \cdot n\sigma(p)\Delta x, \tag{8.11}$$

where n is the atomic number density of the material and σ is the cross-section for the particle in the material. Therefore, the σ_{prod} in GCALOR can be tuned by reweighting the probability with a factor:

$$w = \frac{\sigma_{prod}^{\rm data}(p)}{\sigma_{prod}^{\rm MC}(p)} \cdot \exp\left[-n\left\{\sigma_{prod}^{\rm data}(p) - \sigma_{prod}^{\rm MC}(p)\right\}x\right]. \tag{8.12}$$

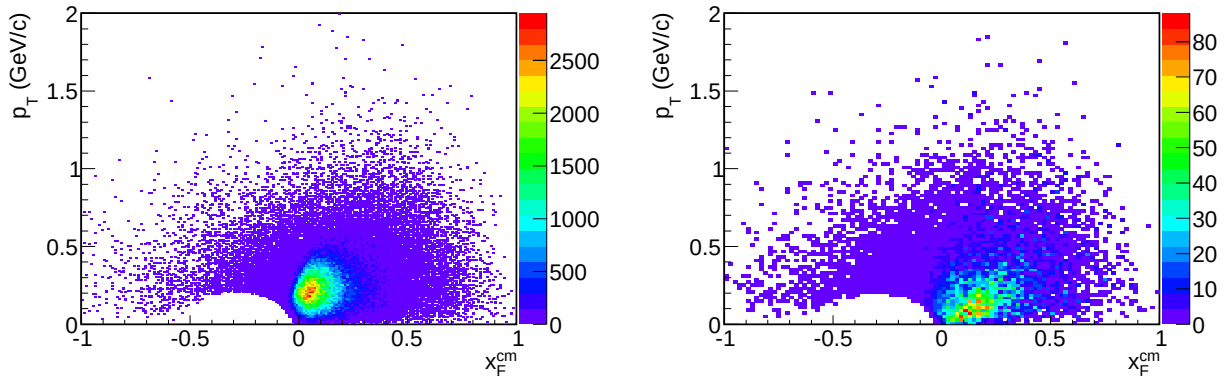

Figure 8.10: x_F^{cm}-p_T distribution of tertiary π^+ (left) and π^- (right) whose descendant neutrinos go to Super-K. It is estimated with the pre-tuned JNUBEAM.

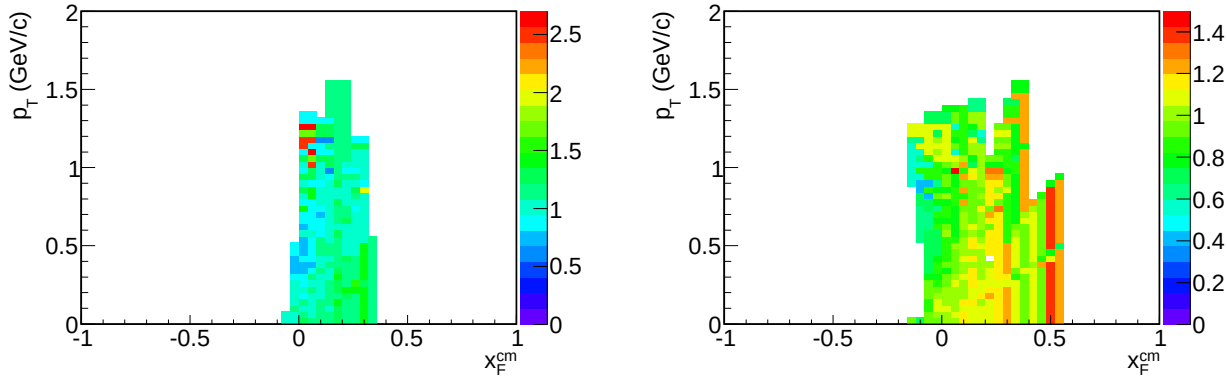

Figure 8.11: $\mathrm{d}n/\mathrm{d}p$ ratio of NA61 to FLUKA in x_F^{cm}-p_T for π^+ (left) and π^- (right).

Table 8.7: Cross-section data used for the tuning of the interaction rate. The last column specifies whether the inelastic or production cross-section is measured.

Data	Beam	Target	p_{beam} (GeV/c)	Measured cross-section
NA61 [157]	p	C	30.9238	σ_{prod}
Belletini [210]	p	C, Al, etc.	19.3, 21.5	σ_{inel}
Chen [214]	p	C, Al, etc.	1.53	σ_{inel}
Denisov [215]	$\pi^\pm$, $K^\pm$, p, etc.	C, Al, etc.	6.65–60	either σ_{inel} or σ_{prod}
Allaby [216]	π^-, K^-, etc.	C, Al, etc.	20–65	σ_{inel}
Longo [217]	π^+, p	C, Al, etc.	3	σ_{inel}
Bobchenko [218]	π^-, p	C, Al, etc.	1.75–9	σ_{inel}
Allardyce [219]	$\pi^\pm$	C, Al, etc.	0.71–2	σ_{inel}
Vlasov [220]	π^-	C, Al	2–6.7	σ_{inel}
Cronin [221]	π^-	C, Al, etc.	0.73–1.33	σ_{inel}
Abrams [222]	$K^\pm$ etc.	C etc.	1.0–3.3	σ_{inel}

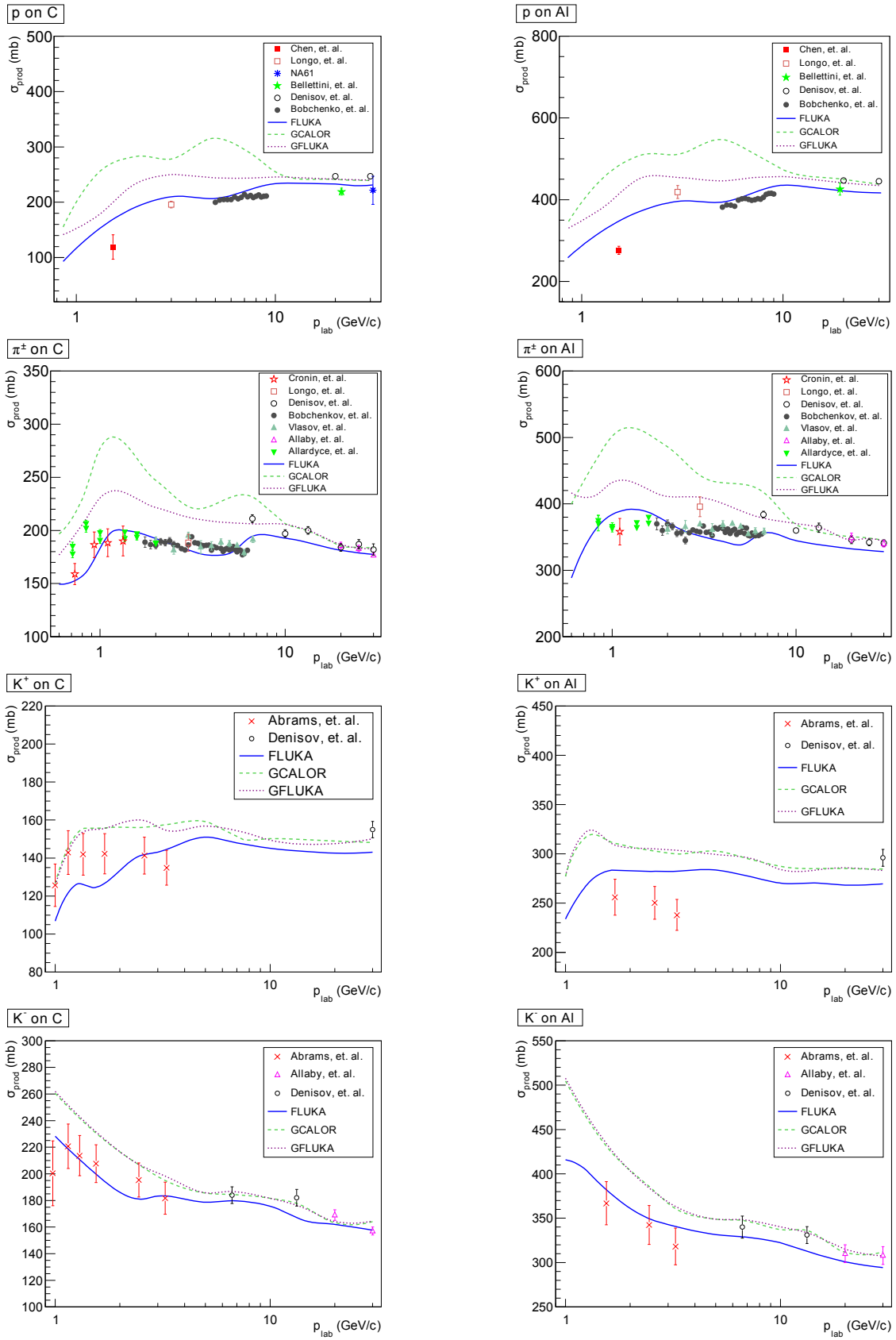

Figure 8.12: Production cross-sections of proton, $\pi^{\pm}$ and $K^{\pm}$ interactions with carbon and aluminum. These plots come from Ref. [211].

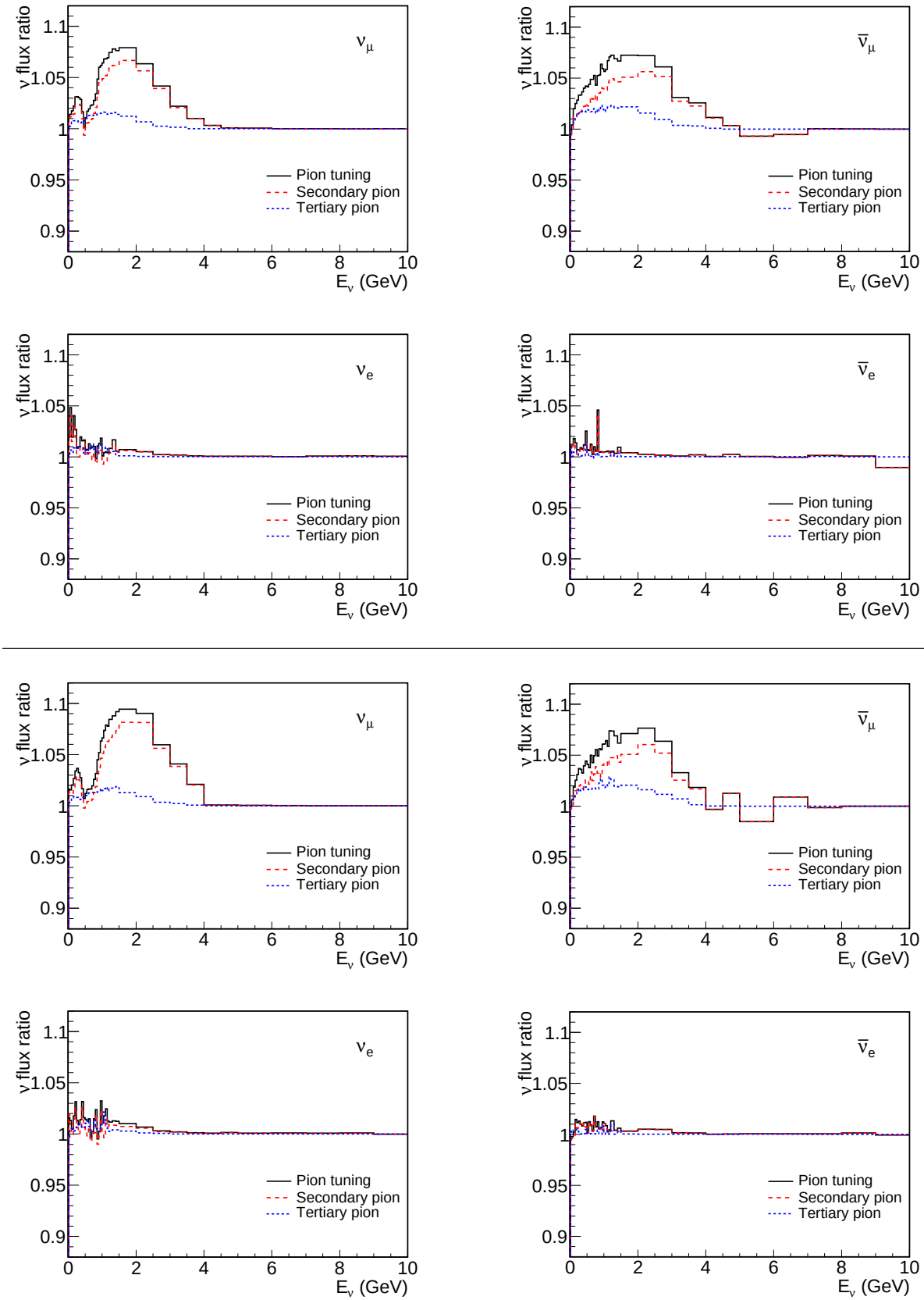

Figure 8.13: Ratio of the neutrino flux of each flavor at Super-K (upper) and the ND280 off-axis detector (lower) before and after the tuning of the pion multiplicities. The solid line represents the total flux change by tuning both the secondary and tertiary pion multiplicities.

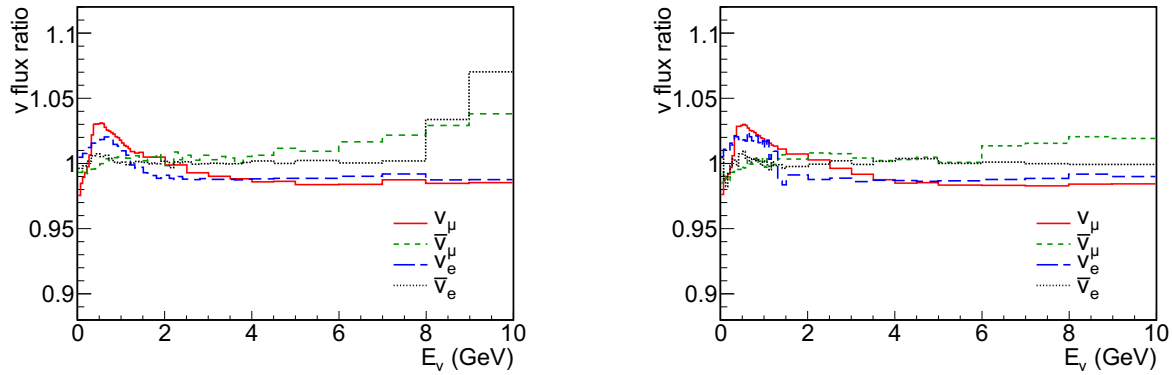

Figure 8.14: Ratio of the neutrino flux at Super-K (left) and the ND280 off-axis detector (right) before and after the tuning of the production cross-sections.

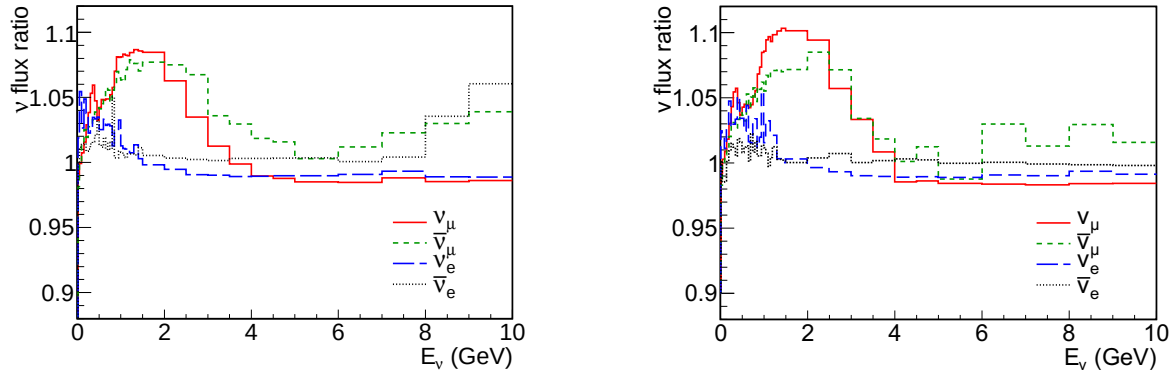

Figure 8.15: Total change of the neutrino flux at Super-K (left) and the ND280 off-axis detector (right) by the all hadron production tunings.

8.4 Expected neutrino flux

As a result of the hadron tunings described above, the neutrino flux changes by a factor shown in Fig. 8.13 (for the multiplicity tuning) and 8.14 (for the σ_{prod} tuning). The total change is shown in Fig. 8.15. The tuning of the secondary pion multiplicity is significant for the ν_μ and $\bar{\nu}_\mu$ flux predictions; the ν_μ and $\bar{\nu}_\mu$ flux around a few GeV increases by several %. On the other hand, for the ν_e and $\bar{\nu}_e$ flux predictions, the hadron tunings have less significance.

The expected neutrino flux after those hadron tunings is shown in Fig. 8.16. In this figure, the flux is normalized to the number of protons used for the analysis, 3.23×10^{19} protons (for Super-K) and 2.88×10^{19} protons (for the ND280 off-axis detector). For the ND280 off-axis detector, it is also normalized to the FGD fiducial area ($|x| < 80$ cm and $-74.5 < y < 85.5$ cm). The $\bar{\nu}_e$ flux is much less than the flux of the other flavor. Therefore, it is omitted in the following sections.

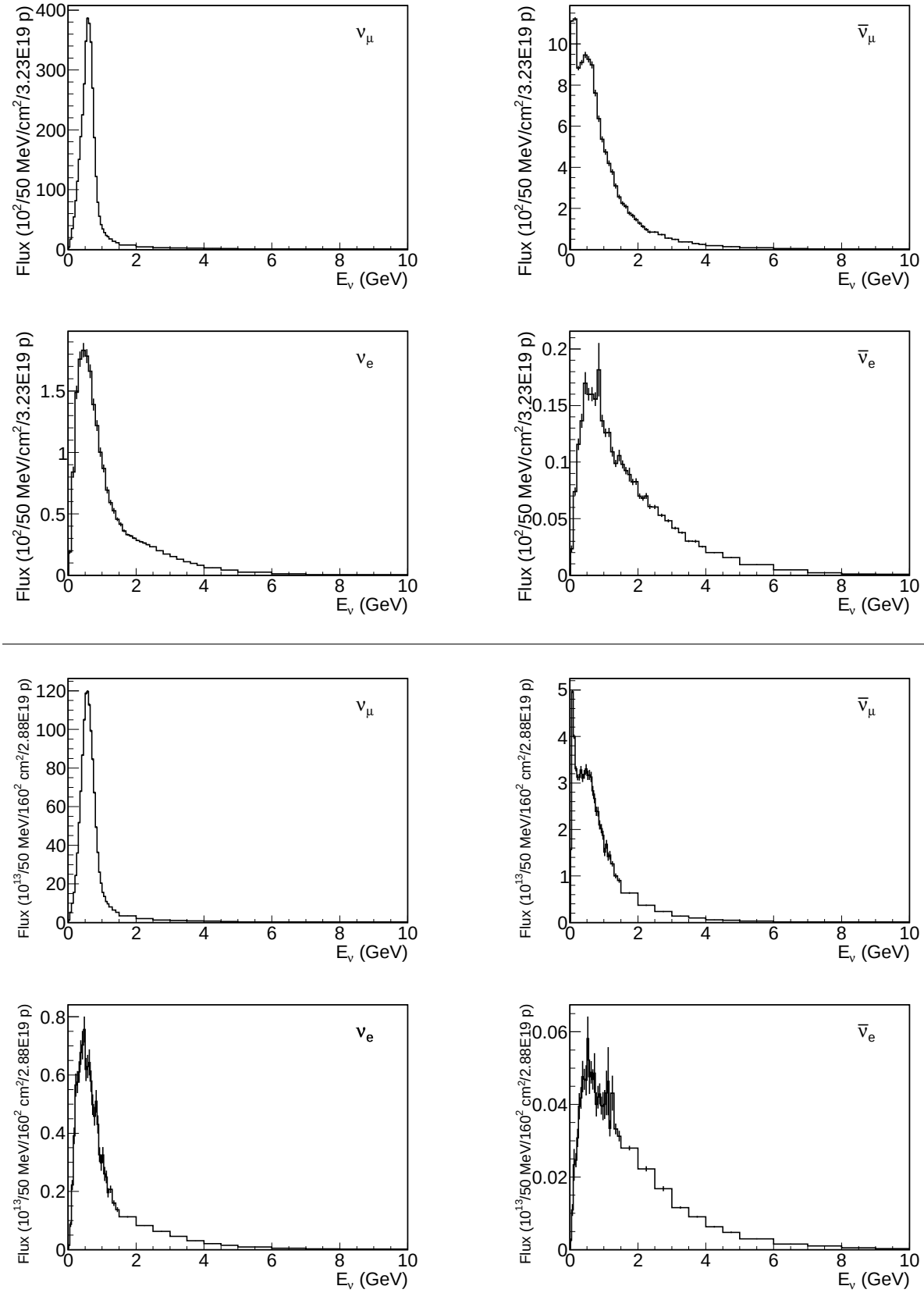

Figure 8.16: Neutrino flux of each flavor at Super-K (upper) and the ND280 off-axis detector (lower) estimated by the tuned JNUBEAM. The error bar is the MC statistical error. The flux in this figure is normalized to the accumulated number of protons used for the analysis: 3.23×10^{19} protons for Super-K and 2.88×10^{19} protons for the ND280 off-axis detector.

8.5 Systematic error of the neutrino flux from the hadron production uncertainties

This section describes the systematic error of the neutrino flux arising from the hadron production uncertainties. The uncertainties of the $\pi^{\pm}$, $K^{\pm}$ and K^0_L multiplicities and production cross-sections are evaluated in Sec. 8.5.1, 8.5.2, 8.5.3 and 8.5.4, respectively. The resultant systematic error of the neutrino flux at Super-K and the ND280 off-axis detector is summarized in Sec. 8.5.5.

8.5.1 Uncertainty of the pion multiplicity

The uncertainty of the secondary and tertiary pion multiplicities comes from the 20% systematic error of the $dn/dp(p,\theta)$ distribution measured by NA61. For the region not covered by NA61, 50% is assigned to the error. The uncertainty of the Feynman scaling for the tertiary pion multiplicity is neglected, because the fraction of the contribution of the tertiary pions to the neutrino flux is as small as ∼20% and the 20% error on the secondary pion multiplicity is dominant to the neutrino flux error. However, it should be evaluated in the future analysis.

8.5.2 Uncertainty of the charged kaon multiplicity

The uncertainty of the charged kaon multiplicity is evaluated by using the experimental data by T. Eichten *et al.* [223]. They measured particle productions in the 24 GeV/c proton interactions in a thin Be target, or the Lorentz invariant single particle production densities per interacting proton:

$$\omega(p,\theta) = 2\frac{E}{p^2}\frac{d^2N}{d\Omega dp} = 2\frac{E}{p^2}\cdot\frac{1}{\sigma_{inel}}\frac{d^2\sigma}{d\Omega dp}, \tag{8.13}$$

where E and p are the energy and momentum of the produced particle, θ is the production angle of the particle and Ω is the solid angle in the laboratory system. The integration of d^2N gives the mean multiplicity of the produced particle. They used $\sigma_{inel} = 227 \pm 12$ mb[§] measured by G. Bellettini *et al.* [210] in 19.3 GeV/c proton interactions in a thin Be target. In our analysis, the ω is renormalized by $\sigma_{prod} = \sigma_{inel} - \sigma_{quel} = 195$ mb, where $\sigma_{quel} = 32.0$ mb is obtained by using the Bellettini model. The ω distribution is shown in Fig. 8.17. T. Eichten *et al.* assigned a 15% systematic error of the overall scale and 5% and 2–5% (depending on the momentum) systematic errors for individual data points. Adding the error on σ_{abs}, the total systematic error of the overall scale is 16%. The total of the overall and individual systematic errors is 18%. The statistical error is negligibly small compared to the systematic errors.

The difference between the Eichten data in Fig. 8.17 and the FLUKA prediction in Fig. 8.18 under the same condition (24 GeV/c proton and Be interaction) is assigned to the uncertainty of the kaon multiplicity in FLUKA for the 30 GeV proton and C interaction. Since the data and FLUKA are compared at 24 GeV/c, the difference or the ratio of the data to FLUKA is scaled to one at 30 GeV according to the Feynman scaling; the ratio is considered to be the same for kaons with the same x_F and p_T. The ratio in x_F-p_T is shown in Fig. 8.19. The kaons which contribute to the neutrino flux at Super-K distribute in the x_F-p_T phase space as shown in Fig. 8.20. About a half of them is covered by the Eichten data. This ratio is the data/FLUKA difference not for C but for Be. The difference of ω between Be and C is estimated to be approximately 10% according to the A-scaling (see Appendix E.1.2 for details). Therefore, conservatively, this 10% is assigned to the uncertainty arising from the target difference.

In total, both for the secondary and tertiary productions in the 30 GeV proton and C interaction in FLUKA, the uncertainty of the charged kaon multiplicity in each x_F-p_T bin is

[§]In their paper, they call it absorption cross-section (σ_{abs}) instead of σ_{inel}.

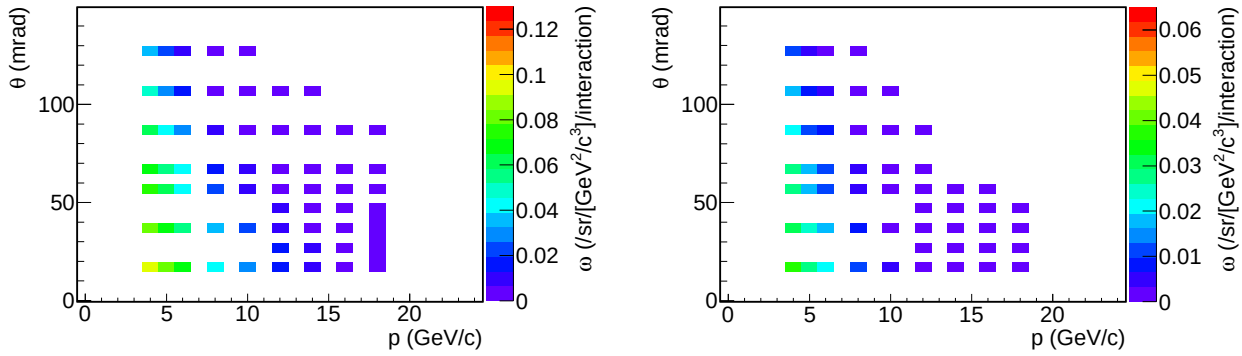

Figure 8.17: $\omega(p, \theta)$ distribution of K^+ (left) and K^- (right) in 24 GeV/c proton and Be interactions measured by T. Eichten *et al.* It is renormalized by $\sigma_{prod} = 195$ mb. The binning is arbitrary.

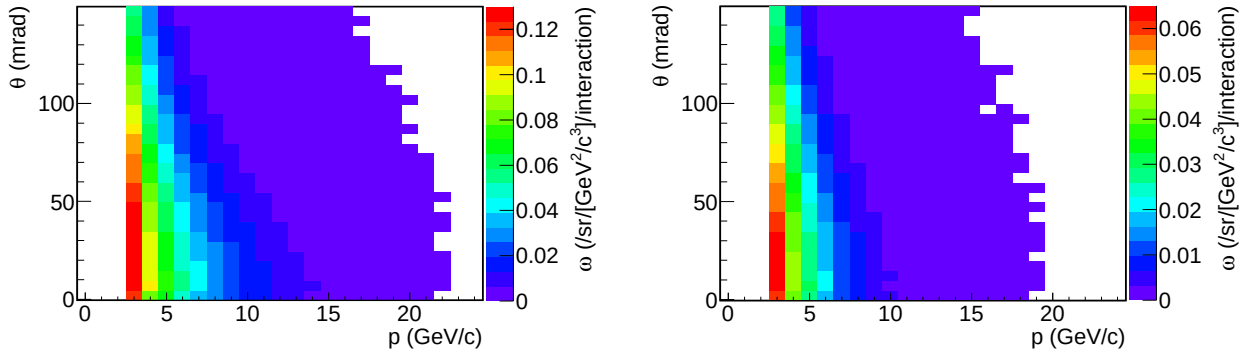

Figure 8.18: $\omega(p, \theta)$ distribution of K^+ (left) and K^- (right) in 24 GeV/c proton and Be interactions in FLUKA. Kaons with a momentum below 2 GeV/c are cut in this histogram.

obtained by quadratically adding the followings: the difference of ω between the Eichten data and FLUKA shown in Fig. 8.19, the 18% systematic error on the Eichten data and the 10% difference of ω between Be and C, and hence ∼30% in total. For kaons out of the region covered by the Eichten data, the multiplicity uncertainty is assumed to be 50%.

8.5.3 Uncertainty of the K^0_L multiplicity

The K^0_L multiplicity is estimated from the Eichten $K^\pm$ multiplicities by using the simple quark parton model [224, 225] (QPM) because there is no K^0_L production data available for T2K. In the simple QPM with an assumption of the isospin symmetry, $n \equiv u_v/d_v = 2$, $u_s = \bar{u}_s = d_s = \bar{d}_s$ and $s_s = \bar{s}_s$ where q_v and q_s are the number densities of valence and sea quarks, respectively, inside the proton. That leads to the relation among the numbers of K^0_L, K^+ and K^- productions, $N(K^0_L)$, $N(K^+)$ and $N(K^-)$:

$$N(K^0_L) = N(K^0_S) = \frac{N(K^+) + (2n-1)N(K^-)}{2n} = \frac{N(K^+) + 3N(K^-)}{4}. \tag{8.14}$$

The derivation of this equation can be found in Appendix E.3. Figure 8.21 shows the $\omega(p, \theta)$ distribution of K^0_L derived from ω of $K^\pm$ by means of this equation. Figure 8.22 shows one in FLUKA simulated under the same condition as the Eichten data. In order to scale 24 GeV/c to 30 GeV, the ω ratio of the QPM to FLUKA predictions is plotted in x_F-p_T as shown in Fig. 8.23. The coverage of the T2K phase space (Fig. 8.24) is approximately 40%.

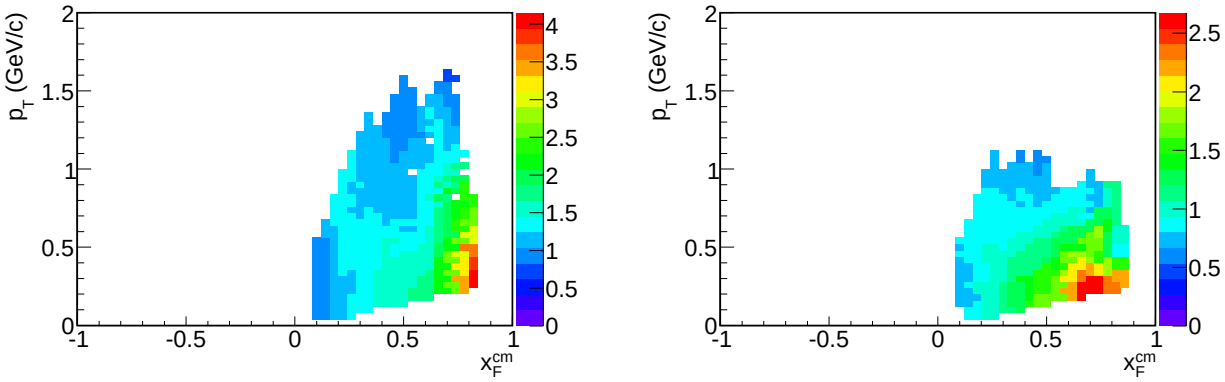

Figure 8.19: $\omega(x_F, p_T)$ ratio of the Eichten data to FLUKA for K^+ (left) and K^- (right).

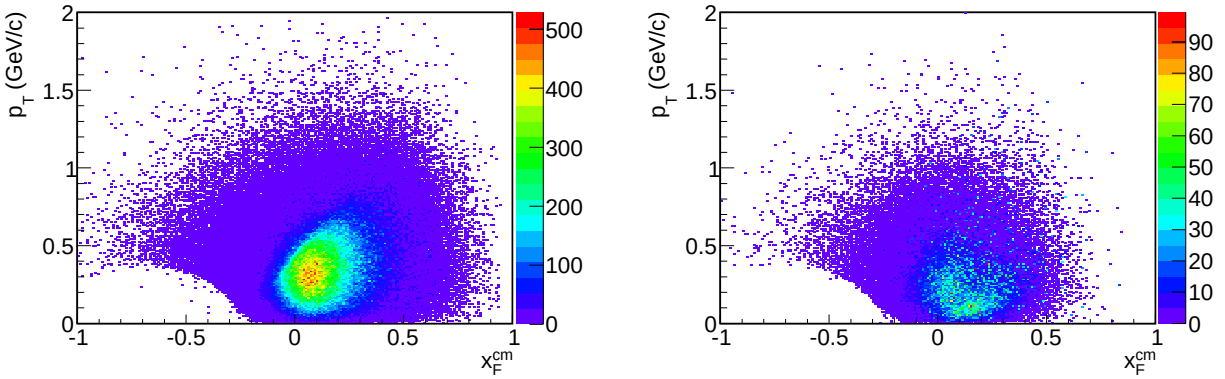

Figure 8.20: x_F^{cm}-p_T distribution of secondary K^+ (left) and K^- (right) whose descendant neutrinos go to Super-K. It is estimated with the pre-tuned JNUBEAM.

It was verified that the QPM agrees within 15% with direct measurements of the K^0_S production up to around $x_F = 0.5$ [226]. At large values of x_F, i.e. in the fragmentation region of the incident proton, the x_F dependence of $n(= u_v/d_v)$ becomes important. However, in this thesis, that dependence is disregarded because almost all the K^0_L which contribute to the neutrino flux at Super-K distribute in $x_F < 0.5$ as shown in Fig. 8.24.

The QPM/FLUKA difference in Fig. 8.23, the 18% systematic error on the Eichten data, the 10% uncertainty of ω due to the target difference and the 15% uncertainty of the QPM are considered to be the uncertainty of the K^0_L multiplicity in FLUKA both for the secondary and tertiary productions. For K^0_L out of the region covered by the QPM prediction, the uncertainty is assumed to be 50%.

8.5.4 Uncertainty of the production cross-section

The uncertainty in the σ_{prod} tuning is summarized here. The detail of this uncertainty is described elsewhere [227].

The uncertainty of the σ_{prod} tuning is estimated by studying the systematic and statistical uncertainties of the experimental data used in the tuning, as well as the consistency between the experiments. The magnitude of the discrepancy between the experiments (see Fig. 8.12) was found to be nearly equal to the quasi-elastic cross-section σ_{quel}. Therefore, the amount of σ_{quel} is applied to the uncertainty of the σ_{prod} tuning, i.e. $\Delta\sigma_{prod} = \sigma_{quel}$ ($\approx$ a few tens %).

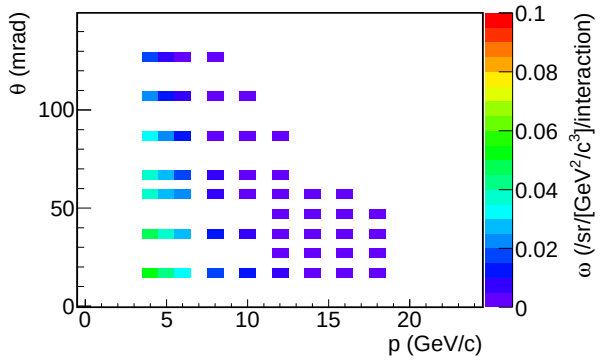

Figure 8.21: $\omega(p, \theta)$ distribution of K^0_L from the simple QPM.

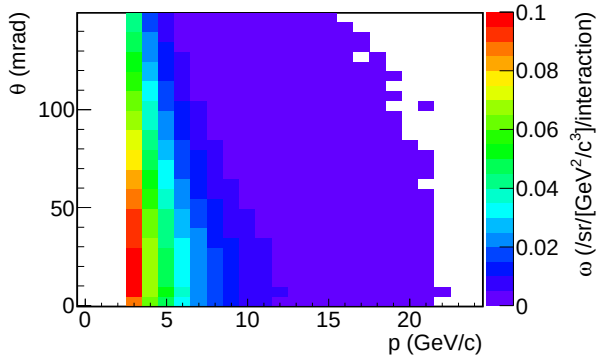

Figure 8.22: $\omega(p, \theta)$ distribution of K^0_L in FLUKA. Kaons with a momentum below 2 GeV/c are cut.

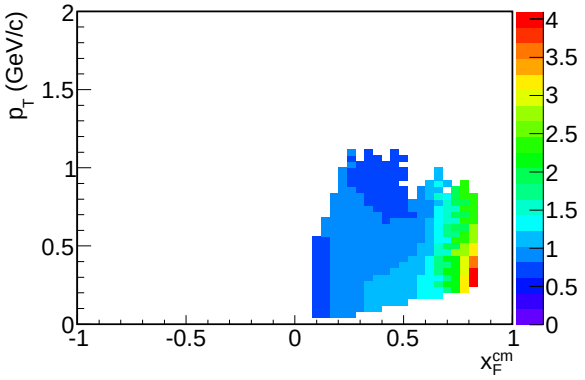

Figure 8.23: $\omega(x_F, p_T)$ ratio of the QPM to FLUKA for K^0_L.

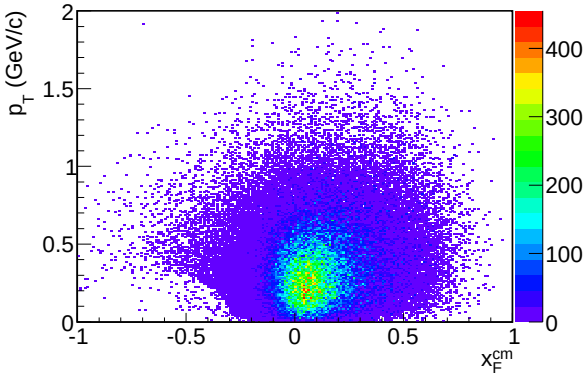

Figure 8.24: x_F^{cm}-p_T distribution of secondary K^0_L whose descendant neutrinos go to Super-K. It is estimated with the pre-tuned JNUBEAM.

8.5.5 Systematic error of the neutrino flux

The systematic error of the neutrino flux due to the multiplicity uncertainty is estimated as the increase of the neutrino flux when the secondary or tertiary particles in every p-θ or x_F-p_T bin are increased by the amount of the multiplicity uncertainty. In this estimation, since bin-to-bin correlations are not specified at this moment, they are assumed to have a positive correlation to give a reasonably conservative estimate of the flux uncertainty. The systematic error of the neutrino flux due to the σ_{prod} uncertainty is estimated as the variation of the neutrino flux when σ_{prod} is changed by the amount of its uncertainty.

The resultant systematic error of the neutrino flux is shown in Fig. 8.25 and 8.26. It is also summarized in Table 8.8. For the flux of every flavor, the error is dominated by the uncertainty of the secondary $\pi^{\pm}$ multiplicities at the lower energies and by the secondary $K^{\pm}$ multiplicities at the higher energies. This is because the proportion of the secondary $\pi^{\pm}$ and $K^{\pm}$ contributions to the neutrino flux is largest at the lower and higher energies, respectively. For the flux error from the uncertainty of the secondary $\pi^{\pm}$ multiplicities, the shape (energy spectrum) of the flux error basically represents the proportion of the secondary $\pi^{\pm}$ contribution since the uncertainty of the secondary $\pi^{\pm}$ multiplicity is constant (20%). The large flux error below 0.5 GeV originates

from the uncertainty of the pion multiplicity for $\theta > 240$ mrad (50%), which was not measured by NA61. For the flux error from the uncertainty of the $K^{\pm}$ and K^0_L multiplicities, the large difference of ω between the Eichten data and FLUKA at large x_F causes the large systematic error of the neutrino flux at the high energies. In order to reduce this error, tuning of the kaon multiplicity is necessary. For approximately a half of the kaons in the T2K phase space, 50% uncertainty on the multiplicity is assigned at this moment since there is no relevant data. To further reduce the flux error, the multiplicity data around $x_F = 0$ is necessary.

The systematic error of the neutrino flux from the hadron production uncertainties amounts to ∼20%. However, it is expected that a large amount of these flux errors cancel out in terms of the near-to-far extrapolation because there is a correlation between the flux variations at Super-K and the ND280 off-axis detector. In the future analysis, NA61 will update the pion multiplicity with less uncertainty [228] and also provide the kaon multiplicity for 30 GeV proton and carbon interactions, which will significantly reduce the flux error.

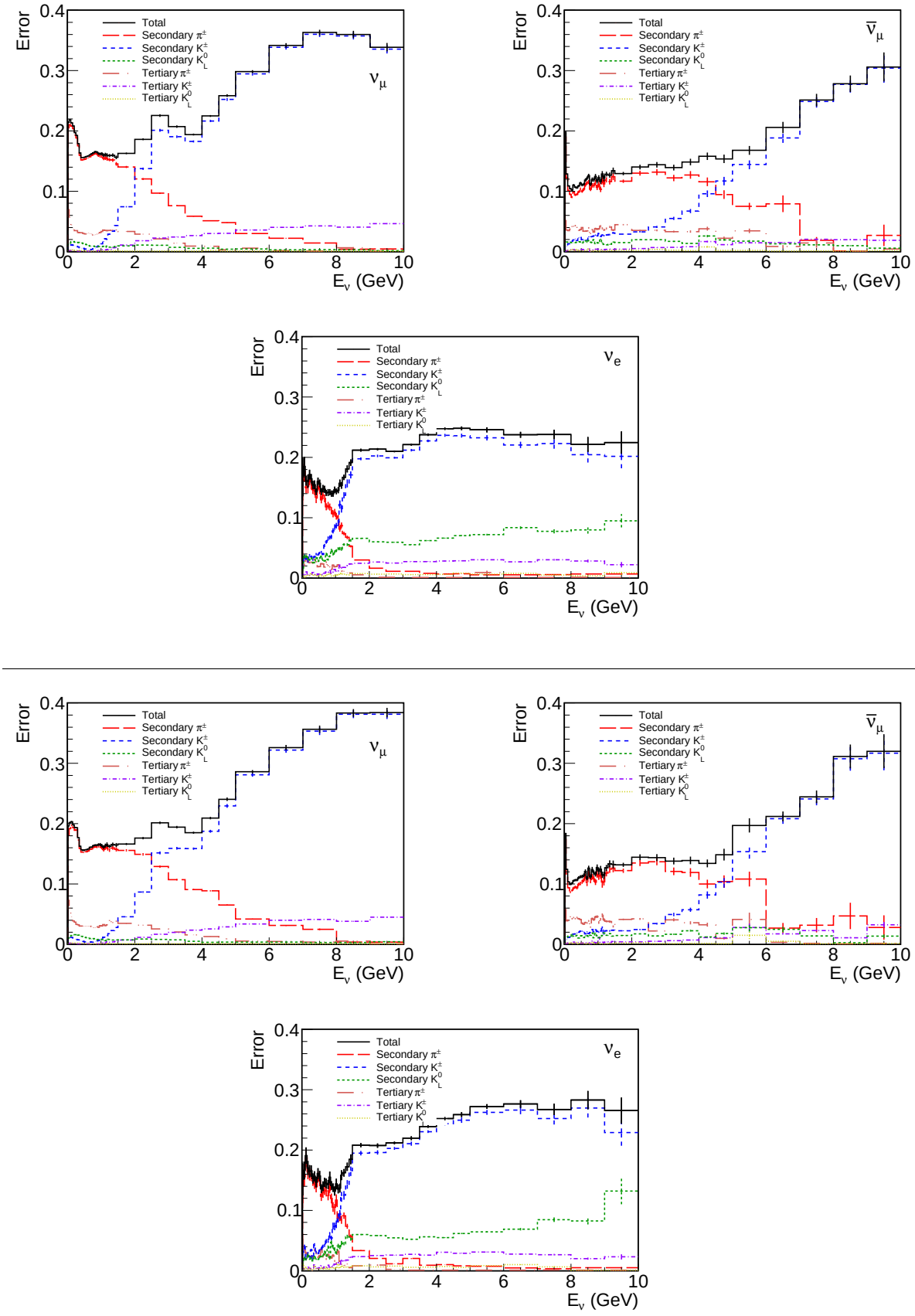

Figure 8.25: Systematic error of the neutrino flux at Super-K (upper) and the ND280 off-axis detector (lower) from the uncertainty of the hadron multiplicities. This is a fractional error of the neutrino flux of each flavor. The error bar is the MC statistical error.

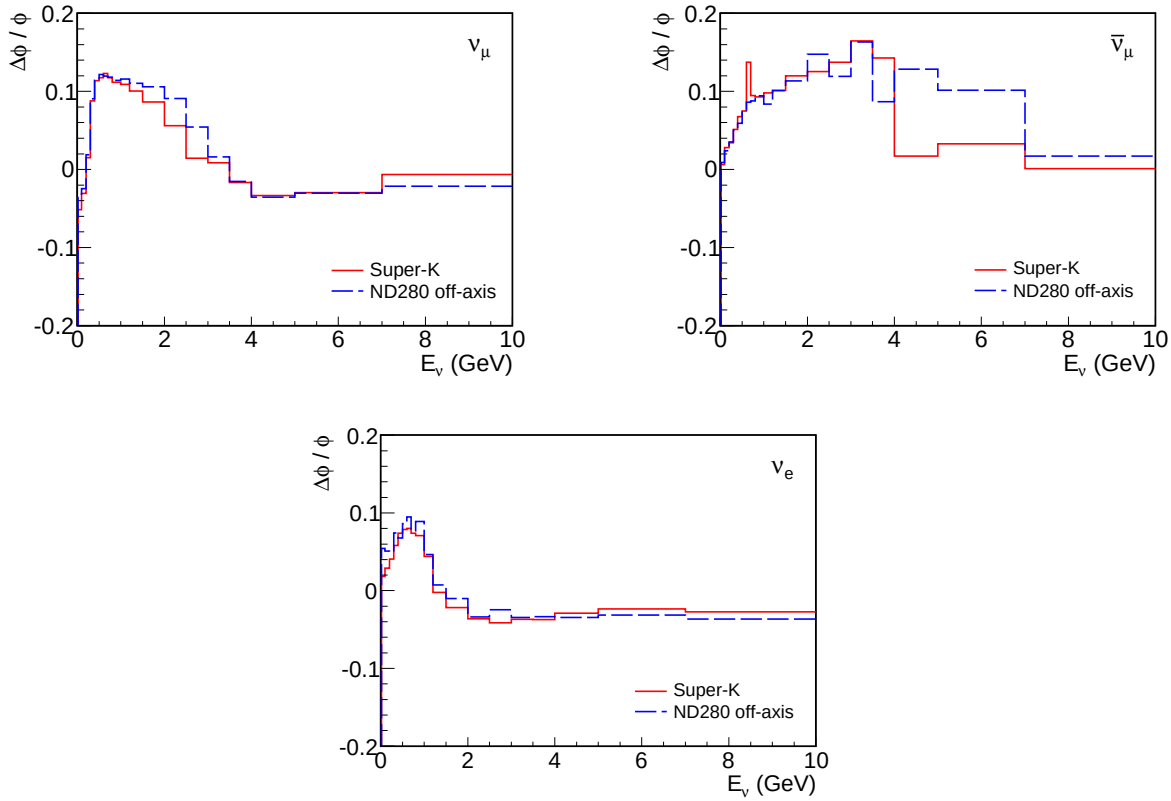

Figure 8.26: Variation of the ν_μ (upper left), $\bar{\nu}_\mu$ (upper right) and ν_e (lower) flux ϕ at Super-K and the ND280 off-axis detector due to the σ_{prod} uncertainty. This is a fractional variation of the neutrino flux of each flavor.

Table 8.8: Summary of the hadron production uncertainty and the systematic error of the Super-K ν_μ flux at 0.6 GeV. Outside the data region, 50% is assigned for the hadron production uncertainty.

	Hadron production uncertainty	ν_μ flux error
Multiplicity		
Secondary $\pi^\pm$	20% (NA61)	15.6%
Tertiary $\pi^\pm$	20% (NA61); Feynman scaling error is neglected	3.1%
Secondary $K^\pm$	∼20% (Eichten/FLUKA diff.), 18% (Eichten), 10% (Be/C diff.)	0.4%
Tertiary $K^\pm$	∼20% (Eichten/FLUKA diff.), 18% (Eichten), 10% (Be/C diff.)	0.1%
Secondary K^0_L	∼25% (QPM/FLUKA diff.), 18% (Eichten), 10% (Be/C diff.), 15% (QPM)	1.0%
Tertiary K^0_L	∼25% (QPM/FLUKA diff.), 18% (Eichten), 10% (Be/C diff.), 15% (QPM)	0.1%
Secondary proton	Not evaluated	–
Production cross-section	Amount of σ_{quel}	12.3%
Total		20.1%

Chapter 9

Expected Number of Neutrino Events at Super-K

In this chapter, the expected number of neutrino events at Super-K is predicted by using the neutrino flux obtained in the previous chapter. The expected number of neutrino events is presented in Sec. 9.1. The systematic error of the expected number arising from the neutrino flux uncertainty is discussed in Sec. 9.2, and summarized with the other systematic error sources in Sec. 9.3.

9.1 Prediction of the number of neutrino events

As discussed in Sec. 7.3, the expected number of neutrino events at Super-K ($N_{\rm SK}^{exp}$) is estimated by normalizing the MC prediction at Super-K ($N_{\rm SK}^{\rm MC}$) with the ratio of the observation to the MC prediction at ND280 ($N_{\rm ND}/N_{\rm ND}^{\rm MC}$). Using the tuned neutrino flux obtained in the previous chapter, $N_{\rm SK}^{\rm MC}$ and $N_{\rm ND}^{\rm MC}$ are estimated according to Eq. 7.4. $N_{\rm ND}^{\rm MC}$ is given in Sec. 9.1.1. Then, $N_{\rm SK}^{exp}$ is estimated in Sec. 9.1.2. In this chapter, the neutrino oscillation probability is calculated by using the world's best-fit values of the neutrino oscillation parameters [194, 229, 230].

9.1.1 Normalization by the ND280 off-axis detector

By using the tuned neutrino flux shown in Fig. 8.16, the number of neutrino interactions is estimated in the ND280 off-axis detector. The same criteria as for the data described in Appendix D.2 are applied to the MC neutrino events. The MC selected events are classified into ν_μ, $\bar{\nu}_\mu$ and ν_e CC/NC interactions using the MC true information. The true neutrino energy spectrum of the selected events for each interaction is shown in Fig. 9.1, and the number of each interaction is summarized in Table 9.1. The total number of the MC selected events is 1372.0, while the one in the data is 1456 (see Appendix D.2). Thus, the ratio of the measured to the estimated number of neutrino events is $1.061 \pm 0.028\ ^{+0.044}_{-0.038} \pm 0.039$, where the first, second and third errors are the statistical error, systematic error due to the detector systematical uncertainty and systematic error due to the neutrino interaction model uncertainty, respectively. This ratio is used for the neutrino flux normalization to estimate the number of neutrino events at Super-K. Though it deviates from one by 6%, this deviation is within the ∼20% systematic error of the neutrino flux.

9.1.2 Expected number of neutrino events at Super-K

By using the tuned neutrino flux at Super-K shown in Fig. 8.16 with the flux normalization by the ND280 off-axis detector, neutrino events in Super-K are estimated. From the MC neutrino

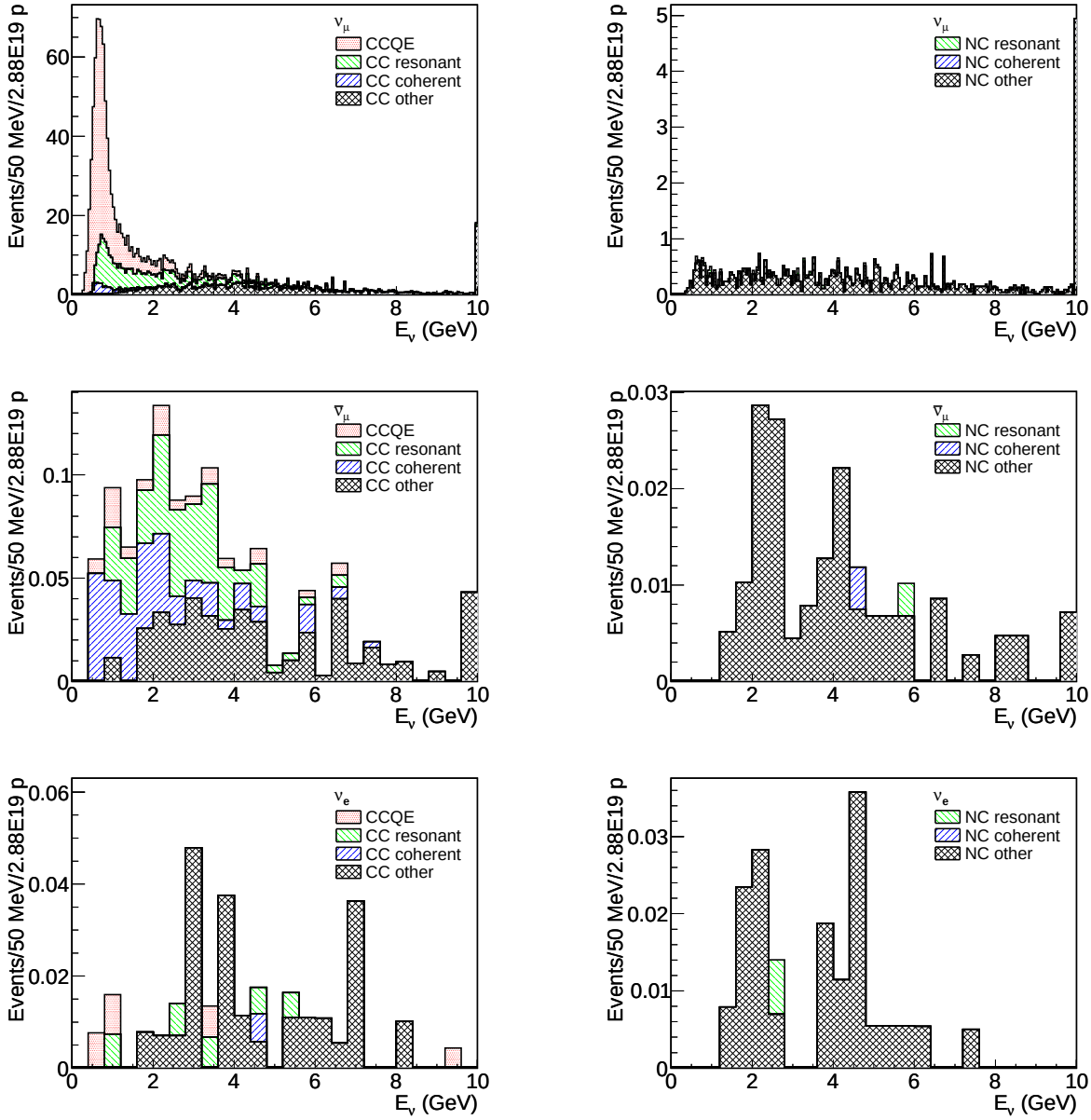

Figure 9.1: Stacked histograms of the expected neutrino events at the ND280 off-axis detector as a function of the true neutrino energy. They are selected as ν_μ CC interactions, but are classified using the MC true information as followings: ν_μ (upper), $\bar{\nu}_\mu$ (middle), ν_e (lower), CC (left) and NC (right) interactions. Events with $E_\nu > 10$ GeV are added to the last bin of the histogram.

Table 9.1: Expected number of neutrino events at the ND280 off-axis detector. The observed number of events is listed in the last column.

	MC breakdown			MC total	Data	Data/MC ratio
	CCQE	CC non-QE	NC			
ν_μ interaction	696.1	609.4	52.5	1358.0		
$\bar{\nu}_\mu$ interaction	0.7	8.3	1.5	10.5		
ν_e interaction	0.2	2.0	1.3	3.5		
Total				1372.0	1456	1.061

events, fully-contained fiducial volume (FCFV) events are selected and classified as single-ring μ-like, single-ring e-like and multi-ring events according to the same selection criteria as for the data described in Sec. 7.2.1 and 7.2.2.

Expected number of ν_μ events for the disappearance analysis

The ν_μ events used for the ν_μ disappearance analysis are selected from the MC single-ring μ-like events according to the same selection criteria as for the data described in Sec. 7.2.3. The expected spectrum of these events, $N_{\rm SK}^{\rm MC}(E_\nu^{rec})$, is shown in Fig. 9.2, where the neutrino energy is reconstructed as E_ν^{rec} according to Eq. 2.3 assuming the CCQE interaction. $N_{\rm SK}^{\rm MC}(E_\nu^{rec})$ in two cases are plotted in this figure: null oscillation and $\nu_\mu \leftrightarrow \nu_\tau$ oscillation at $|\Delta m^2_{32}| = 2.4\times10^{-3}$ eV^2 and $\sin^2 2\theta_{23} = 1.0$. The expected number of the ν_μ events is summarized in Table 9.2 (null oscillation case) and Table 9.3 (oscillation case).

Expected number of ν_e appearance signals

From the MC FCFV events, ν_e signal events are selected according to the same criteria for the data described in Sec. 7.2.4. The expected spectra of the ν_e signal and background events are shown in Fig. 9.3, and the expected number of the ν_e events is summarized in Table 9.4. Here, the probability of the three flavor neutrino oscillation including the matter effect is calculated by using a software package called Prob3++ [231, 232] assuming $\Delta m^2_{21} = 7.6 \times 10^{-5}$ eV^2, $|\Delta m^2_{32}| = 2.4 \times 10^{-3}$ eV^2, $\sin^2 2\theta_{12} = 0.8704$, $\sin^2 2\theta_{23} = 1.0$, $\sin^2 2\theta_{13} = 0.1$, $\delta_{\rm CP} = 0$ and the earth density $\rho = 3.2$ g/cm^3. Only $\nu_\mu \to \nu_e$, $\nu_e \to \nu_e$, $\nu_\mu \to \nu_\mu$ and $\bar{\nu}_\mu \to \bar{\nu}_\mu$ oscillations are taken into account; the other oscillations are disregarded since their contributions are negligible.

9.1.3 Systematic error of the expected number of neutrino events at Super-K

In the calculation of $N_{\rm SK}^{exp}$ (Eq. 7.3 and 7.4), each term in these equations can vary by a factor of f, where f represents the systematic uncertainty, called systematic parameter. The systematic parameter is defined as a relative value to the MC prediction and can vary within its error δf, i.e. $f = 1 \pm \delta f$. Therefore, the $N_{\rm SK}^{exp}$ distribution with the systematic parameters is calculated as follows:

$$N_{\rm SK}^{exp}(\vec{f};\Delta m^2,\theta) = f^{norm}\cdot N_{\rm ND}\cdot\frac{N_{\rm SK}^{\rm MC}(f_{\rm SK}^{\phi},f^{\sigma},f^{\rm FSI},f^{\varepsilon_{\rm SK}};\Delta m^2,\theta)}{N_{\rm ND}^{\rm MC}(f_{\rm ND}^{\phi},f^{\sigma},f^{\varepsilon_{\rm ND}})} \tag{9.1}$$

$$= f^{norm}\cdot N_{\rm ND}\cdot f_{\rm SK/ND}^{\phi}(\Delta m^2,\theta)\cdot\frac{N_{\rm SK}^{\rm MC}(f^{\sigma},f^{\rm FSI},f^{\varepsilon_{\rm SK}};\Delta m^2,\theta)}{N_{\rm ND}^{\rm MC}(f^{\sigma},f^{\varepsilon_{\rm ND}})}, \tag{9.2}$$

where each systematic parameter f represents the systematic uncertainty related to the following term:

- f^{norm}: the normalization of $N_{\rm ND}$ (statistical error of $N_{\rm ND}$).
- $f_{\rm SK}^{\phi}(E_\nu)$, $f_{\rm ND}^{\phi}(E_\nu)$: the neutrino flux at Super-K and ND280, respectively.
- $f_{\rm SK/ND}^{\phi}(\Delta m^2,\theta)$: the normalization of $N_{\rm SK}^{\rm MC}/N_{\rm ND}^{\rm MC}$ related to the neutrino flux.
- $f^{\sigma}(E_\nu)$: the neutrino cross-sections.
- $f^{\rm FSI}(E_\nu^{rec})$: the nuclear effects at the neutrino interaction (Final State Interaction; FSI).
- $f^{\varepsilon_{\rm SK}}(E_\nu^{rec})$, $f^{\varepsilon_{\rm ND}}(E_\nu)$: the Super-K and ND280 detector efficiencies, respectively.

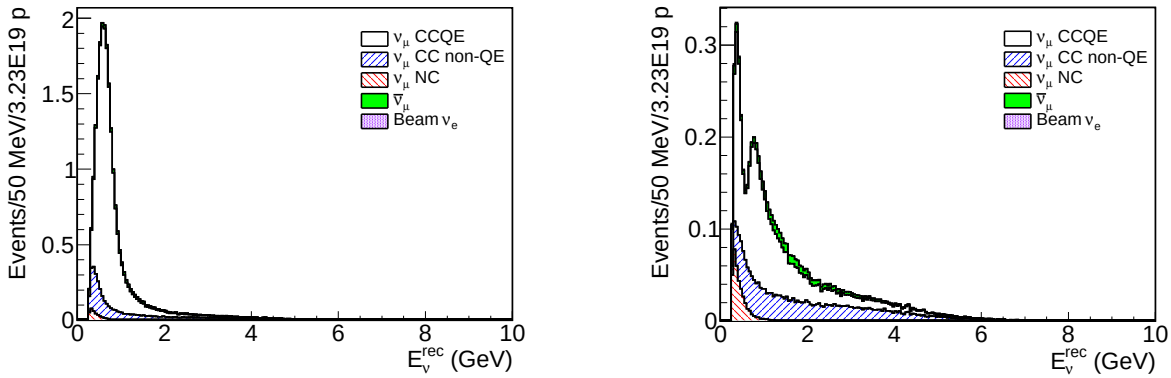

Figure 9.2: Stacked histograms of the expected ν_μ events for the ν_μ disappearance analysis at Super-K as a function of the reconstructed neutrino energy (after the ND280 normalization). They are normalized to the same number of the accumulated protons in the data, 3.23×10^{19} protons. Left: null oscillation case. Right: $\nu_\mu \leftrightarrow \nu_\tau$ oscillation case at $|\Delta m^2_{32}| = 2.4 \times 10^{-3}$ eV^2 and $\sin^2 2\theta_{23} = 1.0$.

Table 9.2: Expected number of FCFV events at Super-K and ν_μ events for the ν_μ disappearance analysis with 3.23×10^{19} protons in case of null oscillation (after the ND280 normalization).

	MC breakdown					
	ν_μ			$\bar{\nu}_\mu$	Beam ν_e	MC total
Event category	CCQE	CC non-QE	NC			
FCFV	19.01	12.01	3.87	1.18	0.81	36.88
Single-ring μ-like	18.21	5.26	0.40	0.76	0.02	24.65
Single-ring e-like	0.23	0.41	0.79	0.06	0.46	1.95
Multi-ring	0.57	6.34	2.68	0.36	0.33	10.28
ν_μ events	18.07	3.61	0.38	0.74	0.02	22.82

Table 9.3: Expected number of FCFV events at Super-K and ν_μ events for the ν_μ disappearance analysis with 3.23×10^{19} protons in case of $\nu_\mu \leftrightarrow \nu_\tau$ oscillation at $|\Delta m^2_{32}| = 2.4 \times 10^{-3}$ eV and $\sin^2 2\theta_{23} = 1.0$ (after the ND280 normalization).

	MC breakdown					
	ν_μ			$\bar{\nu}_\mu$	Beam ν_e	MC total
Event category	CCQE	CC non-QE	NC			
FCFV	3.96	7.35	3.87	0.81	0.81	16.80
Single-ring μ-like	3.67	2.64	0.40	0.45	0.02	7.18
Single-ring e-like	0.07	0.16	0.79	0.05	0.46	1.53
Multi-ring	0.22	4.55	2.68	0.31	0.33	8.09
ν_μ events	3.60	1.92	0.38	0.43	0.02	6.35

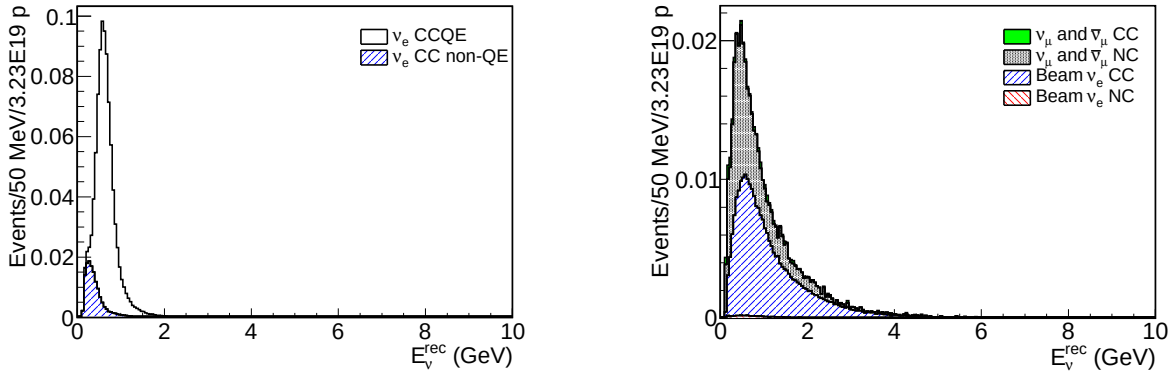

Figure 9.3: Stacked histograms of the expected ν_e appearance signal (left) and background (right) events at Super-K as a function of the reconstructed neutrino energy (after the ND280 normalization). They are normalized to the same number of the accumulated protons in the data, 3.23×10^{19} protons. The three flavor neutrino oscillation probability is calculated on an assumption that $\Delta m^2_{21} = 7.6 \times 10^{-5}$ eV^2, $|\Delta m^2_{32}| = 2.4 \times 10^{-3}$ eV^2, $\sin^2 2\theta_{12} = 0.8704$, $\sin^2 2\theta_{23} = 1.0$, $\sin^2 2\theta_{13} = 0.1$, $\delta_{\rm CP} = 0$ and $\rho = 3.2$ g/cm^3. The $E^{\rm rec}_\nu < 1250$ MeV selection is not applied in this figure.

Table 9.4: Expected number of ν_e appearance events at Super-K with 3.23×10^{19} protons. The three flavor neutrino oscillation probability is calculated on an assumption that $\Delta m^2_{21} = 7.6 \times 10^{-5}$ eV^2, $|\Delta m^2_{32}| = 2.4 \times 10^{-3}$ eV^2, $\sin^2 2\theta_{12} = 0.8704$, $\sin^2 2\theta_{23} = 1.0$, $\sin^2 2\theta_{13} = 0.1$, $\delta_{\rm CP} = 0$ and $\rho = 3.2$ g/cm^3 (after the ND280 normalization).

		MC breakdown			MC total
		CCQE	CC non-QE	NC	
ν_e appearance signal		0.77	0.13	–	0.90
Background	ν_μ	0.00	0.00	0.13	0.13
	$\bar{\nu}_\mu$	0.00	0.00	0.01	0.01
	Beam ν_e	0.12	0.04	0.00	0.16
Total					1.20

The systematic parameters related to the neutrino flux ($f^\phi_{\rm SK}$ and $f^\phi_{\rm ND}$ in Eq. 9.1) are factored out, and the flux related error on $N^{\rm MC}_{\rm SK}/N^{\rm MC}_{\rm ND}$ ($f^\phi_{\rm SK/ND}$ in Eq. 9.2) is estimated in this thesis. By treating the beam related uncertainty as the term of the ratio $N^{\rm MC}_{\rm SK}/N^{\rm MC}_{\rm ND}$, a large amount of the uncertainty can cancel out. $f^\phi_{\rm SK/ND}$ has to be evaluated for given neutrino oscillation parameters. It is studied in the following section. The other systematic parameters are studied elsewhere [201, 202, 233–235] and are just summarized in Sec. 9.3.

9.2 Systematic error of the flux normalization

The following uncertainties are considered for the estimation of the systematic error of the flux normalization, $\delta f^\phi_{\rm SK/ND}$: the hadron production multiplicities and cross-sections, the proton beam parameters, the horn focusing, the neutrino beam direction, and the target and horn alignment. They are summarized in Table 9.5, assuming $|\Delta m^2_{32}| = 2.4 \times 10^{-3}$ eV^2, $\sin^2 2\theta_{23} = 1.0$ and $\sin^2 2\theta_{13} = 0.1$. Currently, the uncertainties of the hadron production are the dominant

Table 9.5: Systematic error of the flux normalization $\delta f^{\phi}_{\mathrm{SK/ND}}$ for $|\Delta m^2_{32}| = 2.4 \times 10^{-3}$ eV^2, $\sin^2 2\theta_{23} = 1.0$ and $\sin^2 2\theta_{13} = 0.1$.

	$\delta f^{\phi}_{\mathrm{SK/ND}}$ (%)			
	ν_μ events for the	ν_e appearance		
Systematic error source	ν_μ disappearance	Signal	Background	Total
Hadron production				
$\pi^{\pm}$ multiplicity	4.41	10.70	5.55	9.10
$\mathrm{K}^{\pm}$ and $\mathrm{K}^0_{\mathrm{L}}$ multiplicity	4.90	9.64	7.17	7.88
Production cross-section	0.16	4.03	0.67	2.84
Beam operation				
Proton beam parameter	0.39	1.11	2.06	1.35
Horn current	0.38	0.77	0.24	0.64
Neutrino beam direction	0.53	0.61	0.58	0.60
Beamline alignment				
Target alignment	0.07	0.34	0.21	0.31
Horn alignment	0.05	0.17	0.10	0.15
Total	6.64	15.03	9.35	12.48

sources of $\delta f^{\phi}_{\mathrm{SK/ND}}$. They are discussed in Sec. 9.2.1. The uncertainties related to the beam operation are sufficiently small by virtue of our stable beam operation and precise measurement of the beam. They are discussed in Sec. 9.2.2. The uncertainties related to the beamline alignment are discussed in Appendix F.2.

9.2.1 Uncertainty of the hadron production

The systematic error of the neutrino flux itself arising from the hadron production uncertainties is discussed in Sec. 8.5 and is summarized in Table 8.8. The systematic errors of the flux normalization from the multiplicity and production cross-section uncertainties are evaluated in different ways.

Multiplicity uncertainty

$\delta f^{\phi}_{\mathrm{SK/ND}}$ is obtained by accumulating the $N^{\mathrm{MC}}_{\mathrm{SK}}/N^{\mathrm{MC}}_{\mathrm{ND}}$ uncertainties arising from the multiplicity uncertainty in ith bin of p–θ or x_F–p_T. Suppose $(\Delta N^{\mathrm{MC}}_{det})_i$ (det = SK or ND) is the uncertainty of N^{MC}_{det} arising from the ith bin uncertainty of the multiplicity distribution. When $(\Delta N^{\mathrm{MC}}_{det})_i$ is small,

$$\frac{N^{\mathrm{MC}}_{\mathrm{SK}} + (\Delta N^{\mathrm{MC}}_{\mathrm{SK}})_i}{N^{\mathrm{MC}}_{\mathrm{ND}} + (\Delta N^{\mathrm{MC}}_{\mathrm{ND}})_i} \approx \frac{N^{\mathrm{MC}}_{\mathrm{SK}}}{N^{\mathrm{MC}}_{\mathrm{ND}}} \left\{ 1 + \frac{(\Delta N^{\mathrm{MC}}_{\mathrm{SK}})_i}{N^{\mathrm{MC}}_{\mathrm{SK}}} - \frac{(\Delta N^{\mathrm{MC}}_{\mathrm{ND}})_i}{N^{\mathrm{MC}}_{\mathrm{ND}}} \right\}. \tag{9.3}$$

Therefore,

$$\delta f^{\phi}_{\mathrm{SK/ND}}(\Delta m^2, \theta) = \sum_i \left| \frac{N^{\mathrm{MC}}_{\mathrm{SK}} + (\Delta N^{\mathrm{MC}}_{\mathrm{SK}})_i}{N^{\mathrm{MC}}_{\mathrm{ND}} + (\Delta N^{\mathrm{MC}}_{\mathrm{ND}})_i} \Big/ \frac{N^{\mathrm{MC}}_{\mathrm{SK}}}{N^{\mathrm{MC}}_{\mathrm{ND}}} - 1 \right| \approx \sum_i \left| \frac{(\Delta N^{\mathrm{MC}}_{\mathrm{SK}})_i}{N^{\mathrm{MC}}_{\mathrm{SK}}} - \frac{(\Delta N^{\mathrm{MC}}_{\mathrm{ND}})_i}{N^{\mathrm{MC}}_{\mathrm{ND}}} \right|. \tag{9.4}$$

In this analysis, the $(N^{\mathrm{MC}}_{\mathrm{SK}}/N^{\mathrm{MC}}_{\mathrm{ND}})_i$ uncertainties are linearly added in the most conservative manner since the bin-to-bin correlation of the multiplicity uncertainties is not known at this

time. $\Delta(N_{det}^{\rm MC})_i$ is calculated as

$$\Delta(N_{\rm SK}^{\rm MC})_i = \sum_{E_\nu} N_{\rm SK}^{\rm MC}(E_\nu;\Delta m^2,\theta)\cdot\left(\frac{\Delta\phi_{\rm SK}}{\phi_{\rm SK}}\right)_i, \tag{9.5}$$

$$\Delta(N_{\rm ND}^{\rm MC})_i = \sum_{E_\nu} N_{\rm ND}^{\rm MC}(E_\nu)\cdot\left(\frac{\Delta\phi_{\rm ND}}{\phi_{\rm ND}}\right)_i, \tag{9.6}$$

where $(\Delta\phi_{\rm det}/\phi_{\rm det})_i$ is the systematic error of the neutrino flux due to the ith bin uncertainty of the multiplicity distribution.

The obtained systematic error $\delta f^{\phi}_{\rm SK/ND}$ shown in Table 9.5 is smaller than the systematic error of the neutrino flux shown in Fig. 8.25. This is because the correlation between $(\phi_{\rm SK})_i$ and $(\phi_{\rm ND})_i$ makes a cancelation of $\Delta(N_{\rm SK}^{\rm MC})_i$ and $\Delta(N_{\rm ND}^{\rm MC})_i$ in Eq. 9.4. When the bin-to-bin correlation of the multiplicity uncertainties is known and it is properly taken into account in Eq. 9.4, this systematic error is sure to get smaller.

Production cross-section uncertainty

For the production cross-section uncertainty, $\delta f^{\phi}_{\rm SK/ND}$ is estimated as a variation of $N_{\rm SK}^{\rm MC}/N_{\rm ND}^{\rm MC}$ when the production cross-section varies by the amount of its uncertainty in JNUBEAM:

$$\delta f^{\phi}_{\rm SK/ND}(\Delta m^2,\theta) = \frac{N_{\rm SK}^{\rm MC}(\Delta m^2,\theta)+\delta N_{\rm SK}^{\rm MC}}{N_{\rm ND}^{\rm MC}+\delta N_{\rm ND}^{\rm MC}}\Big/\frac{N_{\rm SK}^{\rm MC}(\Delta m^2,\theta)}{N_{\rm ND}^{\rm MC}} - 1. \tag{9.7}$$

In this equation, $\delta N_{\rm SK}^{\rm MC}$ and $\delta N_{\rm ND}^{\rm MC}$ are obtained from the systematic error of the neutrino flux $\Delta\phi/\phi$ due to the production cross-section uncertainty shown in Fig. 8.26:

$$\delta N_{\rm SK}^{\rm MC} = \sum_{E_\nu} N_{\rm SK}^{\rm MC}(E_\nu;\Delta m^2,\theta)\cdot\frac{\Delta\phi_{\rm SK}}{\phi_{\rm SK}}, \tag{9.8}$$

$$\delta N_{\rm ND}^{\rm MC} = \sum_{E_\nu} N_{\rm ND}^{\rm MC}(E_\nu)\cdot\frac{\Delta\phi_{\rm ND}}{\phi_{\rm ND}}. \tag{9.9}$$

Since there is a correlation between $\Delta\phi_{\rm SK}/\phi_{\rm SK}$ and $\Delta\phi_{\rm ND}/\phi_{\rm ND}$, the resultant systematic error $\delta f^{\phi}_{\rm SK/ND}$ shown in Table 9.5 is smaller than the systematic error of the neutrino flux.

9.2.2 Uncertainties related to the neutrino beam operation

The systematic errors of the flux normalization from the uncertainties related to the neutrino beam operation are evaluated in the same way as the one from the production cross-section uncertainty, according to Eq. 9.7, 9.8 and 9.9. The systematic errors of the neutrino flux $\Delta\phi/\phi$ arising from the beam-related uncertainties are studied below.

$\Delta\phi/\phi$ from the uncertainties of the proton beam parameters

The systematic errors of the proton beam parameters are summarized in Table 6.5. The variation of the neutrino flux was studied for every parameter, and it was found to be negligibly small for the parameters other than for the beam center and angle in y. Therefore, the beam center ($y_0 = 0.84 \pm 0.58$ cm) and the beam angle ($\mathrm{d}y/\mathrm{d}s = 0.004 \pm 0.286$ mrad) are varied in a correlated way ($\rho_y = 0.3918$) in accordance with Eq. C.1; i.e. the following four cases were studied: (y_0 [cm], $\mathrm{d}y/\mathrm{d}s$ [mrad]) = (1.42, 0.116), (1.07, 0.290), (0.26, −0.108) and (0.61, 0.282). Figure 9.4 shows the flux variation $\Delta\phi/\phi$ at Super-K and the ND280 off-axis detector for the case which gives the maximum variation for each neutrino flavor and detector. This flux error is large (∼10%) around 1 GeV, but correlates between Super-K and the ND280 off-axis detector.

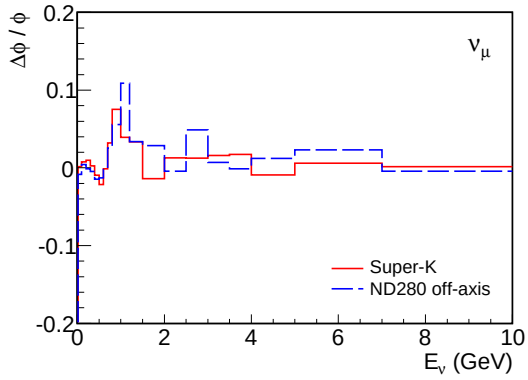

Figure 9.4: Variation of the ν_μ flux ϕ at Super-K and the ND280 off-axis detector due to the uncertainty of the proton beam parameters y_0 and $\mathrm{d}y/\mathrm{d}s$. This is a fractional variation of the neutrino flux of each flavor. For the $\bar{\nu}_\mu$ and ν_e flux, see Fig. F.1.

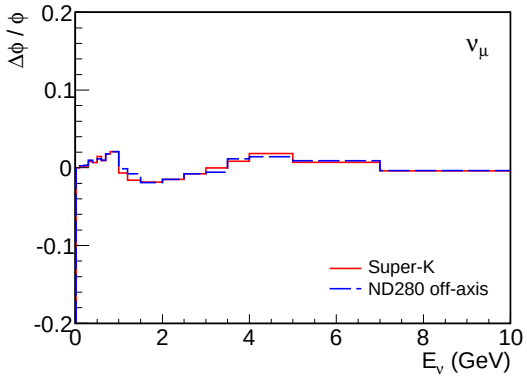

Figure 9.5: Variation of the ν_μ flux ϕ at Super-K and the ND280 off-axis detector due to the horn current uncertainty. This is a fractional variation of the neutrino flux of each flavor. For the $\bar{\nu}_\mu$ and ν_e flux, see Fig. F.2.

$\Delta\phi/\phi$ from the uncertainty of the horn currents

The systematic error of the horn magnetic field was discussed in Sec. 3.2.2 (see Table 3.3). It is less than 2%. The horn current variation during the physics run can be disregarded because it is negligibly small as shown in Table 6.6. Figure 9.5 shows the neutrino flux variation due to the horn current change by 2% (5 kA). The flux error is a few %, and correlates between Super-K and the ND280 off-axis detector.

The effect of the magnetic field in the horn inner conductor was also studied (see Appendix F.1). It can be disregarded in this analysis.

$\Delta\phi/\phi$ from the uncertainty of the neutrino beam direction (off-axis angle)

As shown in Sec. 6.3.2 and 7.1.2 (see also Appendix D.1.2), the neutrino beam direction was measured by the muon monitor and INGRID. The measurements by the two detectors are compared in Fig. 9.6. For the muon monitor, the mean beam direction during each period is plotted with an error bar representing the spill-by-spill fluctuation of the beam direction in RMS. The y direction by the muon monitor in this figure is corrected for the tilted beamline effect discussed in Sec. 6.4.5. For INGRID, the beam direction estimated from the accumulated neutrino event profile during each period is plotted with the statistical error. The two measurements agree with each other within the error.

The following errors are assigned as the systematic error of the neutrino beam direction: the systematic error of the INGRID measurement (0.34 mrad in x and 0.38 mrad in y including the INGRID alignment error), the deviation of the beam direction measured by INGRID from the beam axis (0.008 mrad in x and 0.24 mrad in y) and the alignment error (0.0024 mrad both in x and y for Super-K, and 0.026 mrad in x and 0.038 mrad in y for the ND280 off-axis detector). In total, the systematic error of the neutrino beam direction relative to the Super-K or the ND280 off-axis detector direction is 0.34 mrad in x and 0.45 mrad in y. It corresponds to 0.44 mrad (0.104 mrad in the direction angle θ_x and 0.427 mrad in the depression angle θ_y) for the uncertainty of the off-axis angle. Here, the off-axis angle θ_{OA} is calculated from the beam

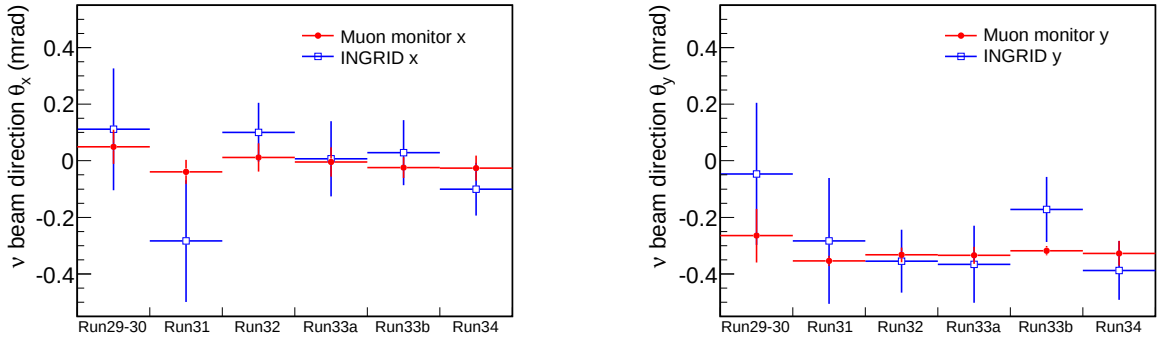

Figure 9.6: Neutrino beam direction measured by the muon monitor and INGRID. The error bar represents the RMS of the spill-by-spill fluctuation of the beam direction for the muon monitor and the statistical error for INGRID.

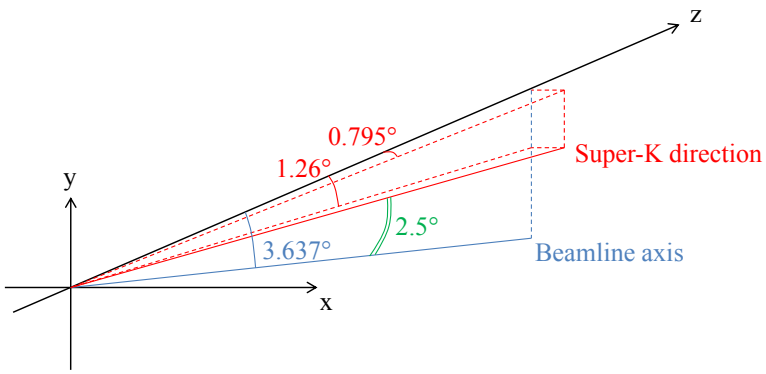

Figure 9.7: Schematic view of the beamline axis and the Super-K direction. x and z are the horizontal axes and y is the vertical one. The z axis is defined so that the beamline axis lies on the y-z plane.

direction $\vec{n}_{\rm beam}$ and the Super-K (or ND280) one $\vec{n}_{\rm SK}$ according to the following equation:

$$\cos\theta_{\rm OA} = \vec{n}_{\rm SK} \cdot \vec{n}_{\rm beam}, \tag{9.10}$$

$$\begin{cases} n_x = n_z \tan\theta_x, \\ n_y = n_z \tan\theta_y, \\ n_z = 1/\sqrt{1+\tan^2\theta_x + \tan^2\theta_y}, \end{cases}$$

where $\vec{n}_{\rm beam,SK} = (n_x, n_y, n_z)$ and $|\vec{n}| = 1$. $\theta_x = 0.795^\circ$ and $\theta_y = 1.26^\circ$ for $\vec{n}_{\rm SK}$, and $\theta_x = 0^\circ$ and $\theta_y = 3.637^\circ$ for $\vec{n}_{\rm beam}$ on the beamline axis as shown in Fig. 9.7. Therefore, the $\theta_{\rm OA}$ uncertainty is calculated as

$$\Delta(\theta_{\rm OA})_x \simeq |0^\circ - 0.795^\circ| / \sin\theta_{\rm OA} \times 0.34 \text{ mrad}, \tag{9.11}$$

$$\Delta(\theta_{\rm OA})_y \simeq |3.637^\circ - 1.26^\circ| / \sin\theta_{\rm OA} \times 0.45 \text{ mrad}. \tag{9.12}$$

The neutrino flux uncertainty due to the uncertainty of the off-axis angle is evaluated by looking at a variation of the neutrino flux when Super-K and the ND280 off-axis detector in JNUBEAM are moved by the amount corresponding to the off-axis angle uncertainty. Figure 9.8

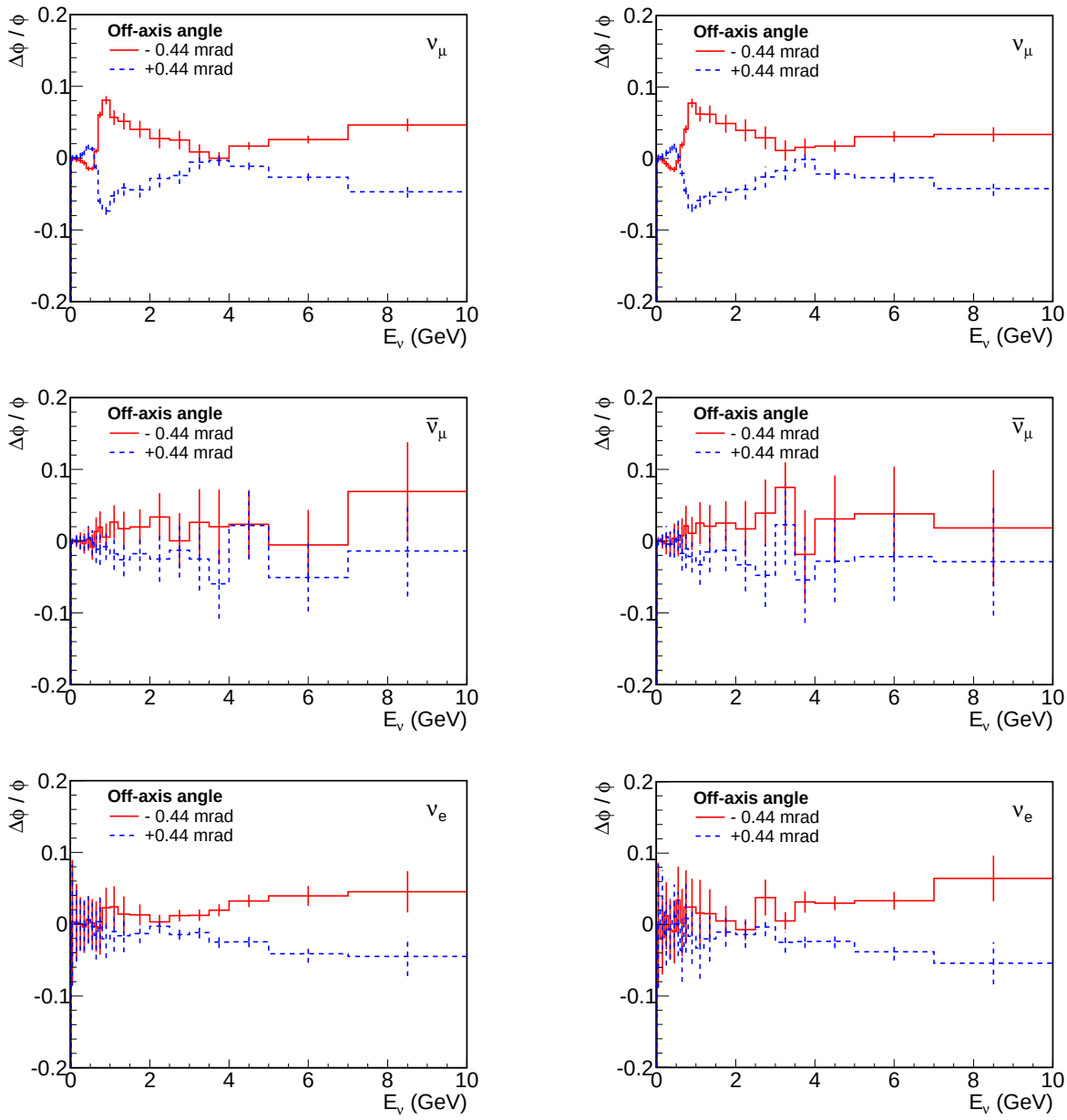

Figure 9.8: Variation of the ν_μ (upper), $\bar{\nu}_\mu$ (middle) and ν_e (lower) flux ϕ at Super-K (left) and the ND280 off-axis detector (right) due to the uncertainty of the off-axis angle. This is a fractional variation of the neutrino flux of each flavor. The error bar is the MC statistical error.

shows the variation of the neutrino flux. The flux variations at Super-K and the ND280 off-axis detector are similar to each other. Therefore, the resultant $\delta f^{\phi}_{\mathrm{SK/ND}}$ is small.

9.3 Summary of the expected number of neutrino events

Table 9.6 shows the systematic error of the expected number of ν_μ events for the ν_μ disappearance analysis [236], $N_{\rm SK}^{exp}(\nu_\mu)$, in case of the two-flavor $\nu_\mu \leftrightarrow \nu_\tau$ oscillation at $|\Delta m^2_{32}| = 2.4\times10^{-3}$ eV^2 and $\sin^2 2\theta_{23} = 1.0$. In this case, the total systematic error on $N_{\rm SK}^{exp}(\nu_\mu)$ is estimated to be $^{+17.1}_{-16.9}$%. Hence,

$$N_{\rm SK}^{exp}(\nu_\mu) = 6.35^{+1.09}_{-1.08}, \tag{9.13}$$

for the 3.23×10^{19} POT data.

Table 9.7 shows the systematic error of the expected number of background events for the ν_e appearance [237], $N_{\rm SK}^{exp}(\nu_e$ background). It is the case of the null $\nu_\mu \rightarrow \nu_e$ oscillation and the two-flavor $\nu_\mu \leftrightarrow \nu_\tau$ oscillation at $|\Delta m^2_{32}| = 2.4\times10^{-3}$ eV^2 and $\sin^2 2\theta_{23} = 1.0$. The total systematic error on $N_{\rm SK}^{exp}(\nu_e$ background) is estimated to be $^{+24.1}_{-24.0}$%. In the case of the three-flavor oscillation at $\Delta m^2_{21} = 7.6\times10^{-5}$ eV^2, $|\Delta m^2_{32}| = 2.4\times10^{-3}$ eV^2, $\sin^2 2\theta_{12} = 0.8704$, $\sin^2 2\theta_{23} = 1.0$, $\sin^2 2\theta_{13} = 0.1$, $\delta_{\rm CP} = 0$ and $\rho = 3.2$ g/cm^3, the systematic error on the expected number of ν_e appearance signal plus background events, $N_{\rm SK}^{exp}(\nu_e$ total), is estimated to be $^{+20.0}_{-19.8}$%. Hence,

$$N_{\rm SK}^{exp}(\nu_e \text{ background}) = 0.30 \pm 0.08, \tag{9.14}$$

$$N_{\rm SK}^{exp}(\nu_e \text{ total}) = 1.20 \pm 0.24, \tag{9.15}$$

for the 3.23×10^{19} POT data.

Table 9.6: List of the systematic parameters, their 1σ uncertainties, and the effect of 1σ systematic parameter variation on the expected number of ν_μ events for the ν_μ disappearance analysis [236]. The two-flavor $\nu_\mu \leftrightarrow \nu_\tau$ oscillation at $|\Delta m^2_{32}| = 2.4\times10^{-3}$ eV^2 and $\sin^2 2\theta_{23} = 1.0$ is assumed in this table.

Systematics	Error source	1σ uncertainty of f	$\Delta N_{\rm SK}^{exp}/N_{\rm SK}^{exp}$ (%)
$f^{\phi}_{\rm SK/ND}$	Beam, hadron production	6.64%	±6.64
$f^{\varepsilon_{\rm SK}}$ [201]	Efficiency of ν_μ CCQE	7.8%	±4.73
	Efficiency of ν_μ non-CCQE	25.5%	±8.36
	Efficiency of NC	115.1%	±7.47
	Efficiency of ν_e CC	100%	±0.05
	Reconstructed energy scale	1%	±0.00
$f^{\varepsilon_{\rm ND}}$ [235]	Detector, physics model	+5.60/−5.17%	+5.60/−5.17
$f^{\rm FSI}$ [234]	Final state interactions	E_ν^{rec} dependent	±5.99
f^{σ} [233]	CCQE cross-section (shape)	E_ν dependent (5% at 0.6 GeV)	±2.53
	CC1π cross-section	30% (<2), 20% (>2 GeV)	+0.44/−0.49
	Cross-section of CC others	30% (<2), 25% (>2 GeV)	+4.13/−3.69
	NC cross-section	36%	+0.87/−0.90
	ν_e/ν_μ CC cross-section ratio	6%	±0.00
f^{norm} [235]	Statistics of $N_{\rm ND}$	2.7%	±2.70
		Total	+17.1/−16.9

The flux normalization error is one of the dominant errors. As described in the previous sections, it mainly comes from the hadron production uncertainties, which will be reduced with an update of the NA61 measurement.

With these expected number of events, the statistical error of the observed number of events is dominant; we succeeded in estimating the systematic error on $N_{\rm SK}^{exp}$ to be less than the statistical error at this moment. The statistical error will be comparable to the systematic error around 1.7×10^{20} POT (5.3 times larger than the current POT), when the analysis has to be updated.

Table 9.7: List of the systematic parameters, their 1σ uncertainties, and the effect of 1σ systematic parameter variation on the expected number of ν_e background events [237]. The three-flavor oscillation at $\Delta m^2_{21} = 7.6 \times 10^{-5}$ eV^2, $|\Delta m^2_{32}| = 2.4 \times 10^{-3}$ eV^2, $\sin^2 2\theta_{12} = 0.8704$, $\sin^2 2\theta_{23} = 1.0$, $\sin^2 2\theta_{13} = 0.1$, $\delta_{\rm CP} = 0$ and $\rho = 3.2$ g/cm^3 is assumed in this table.

Systematics	Error source	1σ uncertainty of f	$\Delta N_{\rm SK}^{exp}/N_{\rm SK}^{exp}$ (%)
$f^{\phi}_{\rm SK/ND}$	Beam, hadron production	9.35%	±9.35
$f^{\varepsilon_{\rm SK}}$ [202]	Normalization	1.42%	±1.42
	Energy scale	1%	±0.50
	Ring counting	1.9%/1.6% (beam/signal ν_e)	±8.40
	Muon PID	0.3%	±1.00
	Electron PID	1.1%/1.4% (beam/signal ν_e)	±8.10
	POLfit mass cut	6.1%/4.1% (beam/signal ν_e)	±7.70
	Decay electron finding	0.8%	±0.30
	π^0 rejection	18.0%	±5.90
$f^{\varepsilon_{\rm ND}}$ [235]	Detector, physics model	+5.60/−5.17%	+5.60/−5.17
$f^{\rm FSI}$ [234]	Final state interactions	E_ν^{rec} dependent	±10.32
f^{σ} [233]	CCQE cross-section (shape)	E_ν dependent (5% at 0.6 GeV)	±2.72
	CC1π cross-section	30% (<2), 20% (>2 GeV)	±2.10
	CC coherent cross-section	100%	±3.06
	Cross-section of CC others	30% (<2), 25% (>2 GeV)	±4.43
	NC1π^0 cross-section	30% (<1), 20% (>1 GeV)	±5.56
	NC coherent cross-section	30%	±2.37
	Cross-section of NC others	30%	±2.53
	ν_e/ν_μ CC cross-section ratio	6%	±3.28
f^{norm} [235]	Statistics of $N_{\rm ND}$	2.7%	±2.7
		Total	+24.1/−24.0

Chapter 10

Observed Number of Neutrino Events at Super-K

10.1 Neutrino events at Super-K

Every our effort on the stable beam operation bore the memorial first T2K neutrino event at Super-K on February 24, 2010 (see Fig. 10.1). Since then, Super-K has successfully accumulated T2K neutrino events. This section summarizes the events observed in Super-K with the 3.23×10^{19} protons on target. The detail of the Super-K analysis is described elsewhere [200–202].

10.1.1 Fully-contained fiducial volume (FCFV) event

The on-timing FC and FCFV events are selected according to the criteria described in Sec. 7.2.1, and the number of those events is listed in Table 10.1. The definition of on-timing is -2 to $+10$ μsec from the arrival time of the leading edge of each spill. With the 3.23×10^{19} protons, 33 FC events and 23 FCFV events were observed.

Figure 10.2 shows the distribution of the time interval from the spill leading edge to the event (ΔT_0) for all the Super-K neutrino events in the T2K 1 msec beam-time window. (In the ΔT_0 calculation, time of the neutrino flight for 295 km and hardware offsets at Tokai and Super-K are considered.) No off-timing FC events were observed. That indicates successful event synchronization between J-PARC and Super-K with our GPS systems and the low background rate as explained later. The flat distribution of the low energy (LE) and OD events in the off-timing indicates that there is no time dependent bias for the data acquisition or the event selection. Figure 10.3 shows the ΔT_0 distribution of all the FC events. Here, ΔT_0 is corrected for the event-by-event difference in the neutrino flight distance and photon propagation length by using the reconstructed vertex position. All the FC events cluster with nearly 581 nsec bunch intervals. That is a more confident evidence for the event synchronization.

Backgrounds to the FC events are caused dominantly by low energy activities. The number of backgrounds is estimated by using dummy spill data. In 2823506 dummy spills with 900 μsec time window each, two FC events were observed. Both these events were low energy ($\sim$10 MeV/c) activities near the inner detector wall. Therefore, the number of FC background events is estimated to be 999070×12 μsec $\times 2$ events / $(2823506 \times 900$ μsec$) = 0.0094 \pm 0.0067$(sta.), where 999070 is the number of spills used in this analysis and 12 μsec is the width of the on-timing window.

Backgrounds to the FCFV events are caused dominantly by atmospheric neutrinos. The number of FCFV background events is calculated using the atmospheric neutrino event rate in SK-IV (8.06 ± 0.17 events/day) as 999070×12 μsec $\times 8.06$ events /day $= 0.00112 \pm 0.00002$(sta.). Thus, the amount of background events in the FC and FCFV event samples is negligibly small.

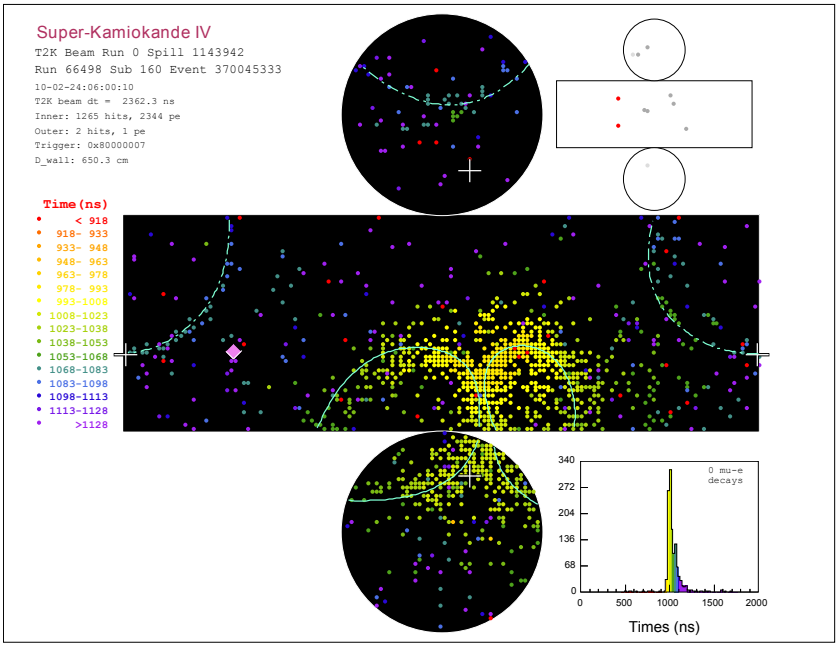

Figure 10.1: Super-K event display showing the first T2K neutrino event. The cylindrical inner and outer detectors are expanded in the center and the top right corner of this figure, respectively. The four white crosses represent the reconstructed vertex position (the height by the left-right pair and the horizontal position by the top-bottom pair). The direction from the reconstructed vertex to the pink diamond shows the beam direction. The dots represent PMT hits. In this event, there are three Cherenkov rings, which are fitted with circles. All of these rings are fully contained in the inner detector. Two of them are showering and their invariant mass is reconstructed to be 133.8 MeV/c^2; they are most likely photons from a π^0. The bottom right plot is a distribution of the PMT hit timing. No hits by Michel electrons from muon decays are found in this event.

Table 10.1: The number of on-timing FC and FCFV events observed at Super-K with the 3.23×10^{19} protons. The expected number of background events is listed in the last column with the statistical error.

	Observed					Background
Run	29–31	32	33	34	Total	
Num. of protons ($\times 10^{19}$)	0.34	0.76	1.21	0.93	3.23	
FC	2	15	9	7	33	0.0094 ± 0.0067(sta.)
FCFV	2	11	8	2	23	0.00112 ± 0.00002(sta.)

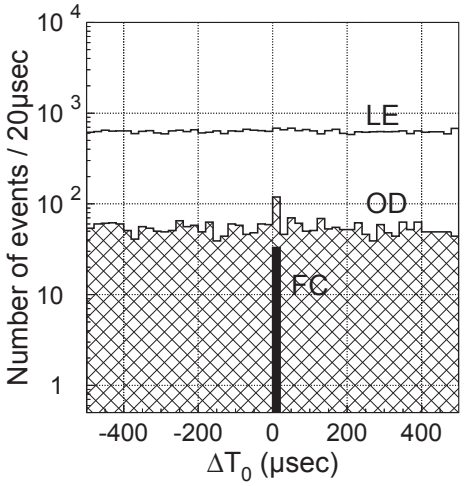

Figure 10.2: Stacked histogram of the time interval from the spill leading edge to the event (ΔT_0) for all the Super-K neutrino events in the T2K 1 msec beam-time window. The low energy (LE), outer detector (OD) and FC events are shown in this figure.

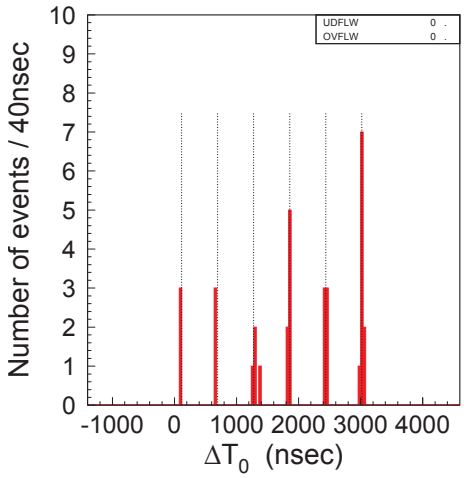

Figure 10.3: Distribution of the time interval from the spill leading edge to the event (ΔT_0) for all the FC events. No FC event lies outside the range of this figure. The six dotted vertical lines represent bunch center positions with 581 nsec intervals fitted to the observed FC event times.

Among the 23 FCFV events, eight single-ring μ-like, two single-ring e-like, thirteen multi-ring events were observed. A sample event display of one of the single/multi-ring μ-like event is shown in Fig. 10.4 and 10.5.

10.1.2 ν_μ events for the ν_μ disappearance analysis

The cuts for the ν_μ disappearance analysis described in Sec. 7.2.3 are applied to the single-ring μ-like events, and all of the eight events pass the cuts. This observed number of ν_μ events for the ν_μ disappearance analysis is consistent with the expectation in case of the two-flavor $\nu_\mu \leftrightarrow \nu_\tau$ oscillation at $|\Delta m^2_{32}| = 2.4 \times 10^{-3}$ eV^2 and $\sin^2 2\theta_{23} = 1.0$ (6.35 events), while the expectation in case of null oscillation is 22.82 events (see Table 10.2). We succeeded to see the deficit of the neutrino events in T2K due to the neutrino oscillation.

10.1.3 Candidate for the ν_e appearance signal

To search for the ν_e appearance, the cuts described in Sec. 7.2.4 are applied to the 23 FCFV events. The number of events after each cut is summarized in Table 10.3. Two events survive as single-ring e-like events. The reconstructed information on these events is listed in Table 10.4. One of them is rejected because a decay electron was found 3.5 μsec after the primary event as shown in Fig. 10.6. The other event passes all the cuts, and it is the first candidate of the ν_e appearance signal. The event display of this ν_e candidate is shown in Fig. 10.7.

This observed number of the ν_e candidate is consistent with the expectation in case of the three-flavor oscillation (1.20 events) and also with the one in case of null oscillation (0.30 events). The sensitivity to θ_{13} is poor with this only one event. We continue to accumulate neutrino events to search for the ν_e appearance signal and to measure θ_{13}.

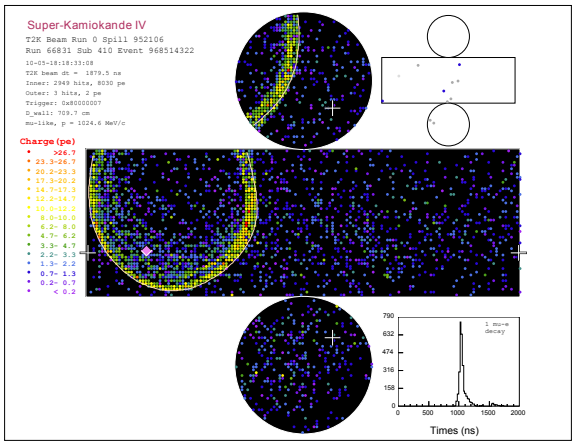

Figure 10.4: Super-K event display of the single-ring μ-like event. The reconstructed muon momentum is 1025 MeV/c. A Michel electron from the muon decay was found approximately 500 nsec after the muon signal.

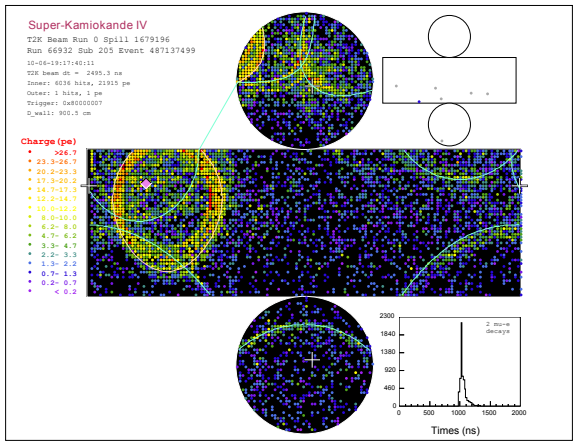

Figure 10.5: Super-K event display of the multi-ring μ-like event. Four Cherenkov rings are reasonably identified. The largest visible energy Cherenkov ring is μ-like and the reconstructed muon momentum is 1438 MeV/c. Two Michel electrons from the muon decays were found.

Table 10.2: The number of ν_μ events for the ν_μ disappearance analysis with the 3.23×10^{19} protons. For the expectation with the oscillation, the two-flavor $\nu_\mu \leftrightarrow \nu_\tau$ oscillation is assumed at $|\Delta m^2_{32}| = 2.4 \times 10^{-3}$ eV^2 and $\sin^2 2\theta_{23} = 1.0$.

	Observation	Expectation	
		Oscillation	Null oscillation
ν_μ events	8	6.35	22.82

Table 10.3: Event summary of the T2K ν_e appearance search with the 3.23×10^{19} protons. For the expectation, the three-flavor oscillation is assumed at $\Delta m^2_{21} = 7.6 \times 10^{-5}$ eV^2, $|\Delta m^2_{32}| = 2.4 \times 10^{-3}$ eV^2, $\sin^2 2\theta_{12} = 0.8704$, $\sin^2 2\theta_{23} = 1.0$, $\sin^2 2\theta_{13} = 0.1$, $\delta_{\rm CP} = 0$ and $\rho = 3.2$ g/cm^3.

Selections	Number of events	Expectation	
		Signal	Background
FCFV	23		
$E_{\rm vis} > 100$ MeV	20		
Single-ring	8		
e-like ring	2		
No decay electrons	1		
POLfit mass < 105 MeV/c^2	1		
$E^{\rm rec}_\nu < 1250$ MeV	1		
Candidate of the ν_e appearance signal	1	0.90	0.30

Table 10.4: Reconstructed information on the single-ring e-like events. θ_e is the scattering angle of the reconstructed Cherenkov ring relative to the beam direction.

	Event 1	Event 2	T2K cut
Date (JST)	May 1, 2010, 04:50:58	May 12, 2010, 21:03:22	
Ring, PID	1-ring e-like	1-ring e-like	1-ring e-like
Momentum	181 MeV/c	378 MeV/c	> 100 MeV/c
Number of decay electrons	1	0	0
$\cos\theta_e$	0.026 (89 degrees)	0.55 (57 degrees)	N/A
POLfit mass	46.6 MeV/c^2	0.13 MeV/c^2	< 105 MeV/c^2
$E_{\rm rec}$	257 MeV	496 MeV	< 1250 MeV

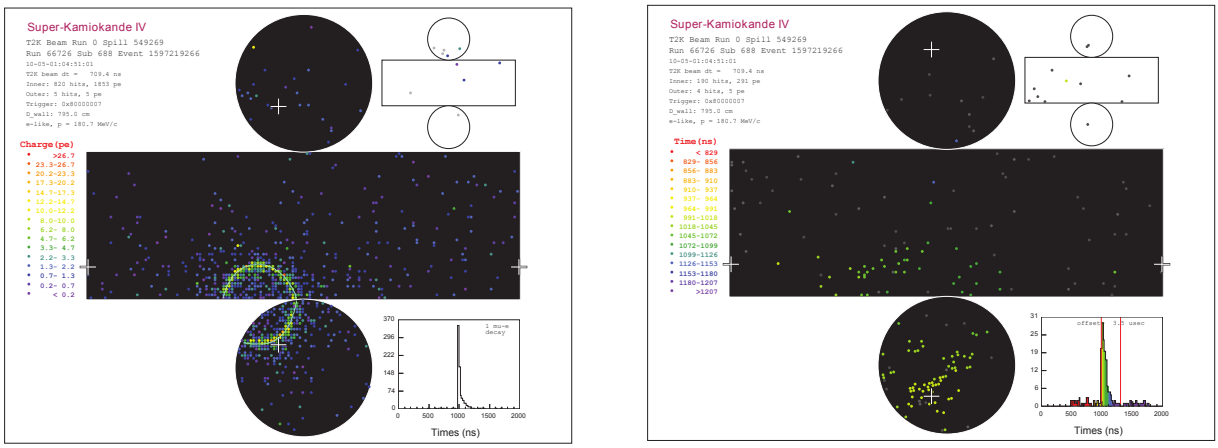

Figure 10.6: Super-K event display of the rejected single-ring e-like event (left). A subsequent event was observed (right) 3.5 μsec after the primary event.

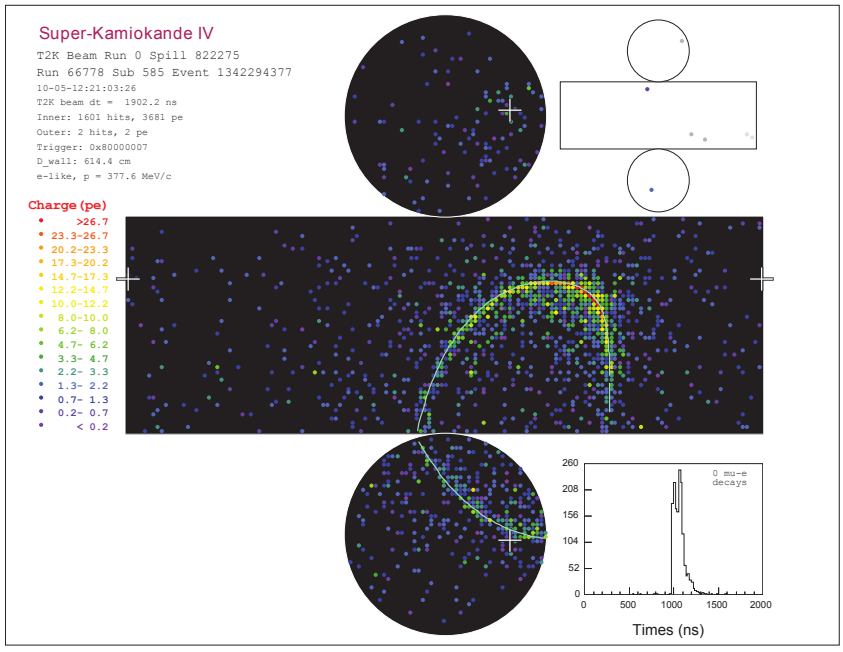

Figure 10.7: Super-K event display of the T2K first candidate of the ν_e appearance signal.

10.2 Summary of the analysis

In this thesis, the way to estimate the neutrino flux at Super-K was established for the first time in T2K. The neutrino flux was estimated using the Monte Carlo simulation, JNUBEAM, tuned with the external hadron production data. In addition, the systematic error of the neutrino flux was evaluated. It was found to be sufficiently small to meet the T2K requirement, except the systematic error from the hadron production uncertainties. That is the fruits of the stable beam operation and precise measurement of the beam, and gives us the confidence to continue the beam operation in this way.

We confirmed that the number of the observed neutrino events at Super-K for the ν_μ disappearance analysis is consistent with the expected number with the neutrino oscillation. To measure θ_{23} precisely and to search for the ν_e appearance signal, more events are necessary, and we continue our efforts to increase the beam power and to produce the neutrino beam with this high quality.

Chapter 11

Conclusions

Nature has longed for us finding the ν_e appearance to reveal the size of the neutrino generation mixing angle θ_{13}, and finding whether θ_{23} is exactly 45 degrees or not. The T2K experiment started the beam operation in April of 2009 and started taking the physics data to study the neutrino oscillation in January of 2010. T2K is a long-baseline neutrino oscillation experiment, utilizing the J-PARC high intensity proton beam to generate the muon neutrino beam. In T2K, where the neutrino event statistics is essential to find the ν_e appearance, the precise tuning of the proton beam orbit is the most urgent issue to increase the beam power. In addition, the precise estimation of the neutrino flux is required, and it is impossible without the stable beam operation and the precise measurement of the neutrino beam generated, particularly the neutrino beam direction. Since T2K adopts the off-axis beam configuration, in which the neutrino energy spectrum is sensitive to the neutrino beam direction, the neutrino beam direction has to be tuned within 1 mrad and be measured with a precision better than 0.25 mrad. Therefore, the muon monitor, which monitors the neutrino beam direction by measuring the muon beam, is one of the most important components in T2K.

One of the purposes of the studies presented in this thesis is to realize the precise tuning and stable beam operation by using the muon monitor. We designed and constructed the muon monitor to measure the world's most intense muon beam stably with high precision and to be tolerant of radiation. In the T2K beam operation, we proved the muon monitor to have the capability to monitor the targeting position of the proton beam, the horn focusing, and the neutrino beam direction with a precision better than 0.2 mrad. Using the muon monitor, we succeeded in the stable beam monitoring and in the precise tuning and the stable beam operation.

Another main subject of this thesis is the estimation of the neutrino flux, which is necessary to predict the expected number of neutrino events in Super-K. To estimate the neutrino flux, we developed the Monte Carlo simulation (JNUBEAM) and established the method to tune the hadron production in JNUBEAM with the external hadron production data. In this thesis, we performed the tuning of JNUBEAM to the NA61 preliminary $\pi^{\pm}$ production data. We also evaluated the systematic error of the neutrino flux and the flux normalization error for the expectation of the number of neutrino events at Super-K. The systematic error of the neutrino flux normalization ($\delta f^{\phi}_{\mathrm{SK/ND}}$) is estimated to be 6.64% for the expected number of ν_μ events for the ν_μ disappearance analysis and 9.35% (12.48%) for the expected number of background (signal plus background) events for the ν_e appearance, while the total systematic error is $^{+17.1}_{-16.9}$% for the former and $^{+24.1}_{-24.0}$% ($^{+20.0}_{-19.8}$%) for the latter. Hence, the expected number is $6.35^{+1.09}_{-1.08}$ for the ν_μ events and 0.30 ± 0.08 (1.20 ± 0.24) for the ν_e background (signal plus background) events. They are estimated on an assumption of the two-flavor $\nu_\mu \leftrightarrow \nu_\tau$ oscillation at $|\Delta m^2_{32}| = 2.4 \times 10^{-3}$ eV^2 and $\sin^2 2\theta_{23} = 1.0$ for the ν_μ events and the three-flavor oscillation at $\Delta m^2_{21} = 7.6 \times 10^{-5}$ eV^2, $|\Delta m^2_{32}| = 2.4 \times 10^{-3}$ eV^2, $\sin^2 2\theta_{12} = 0.8704$, $\sin^2 2\theta_{23} = 1.0$, $\sin^2 2\theta_{13} = 0.1$, $\delta_{\mathrm{CP}} = 0$ and

$\rho = 3.2$ g/cm^3 for the ν_e events. We confirmed that the observed number of the ν_μ events is consistent with the expectation with the $\nu_\mu \leftrightarrow \nu_\tau$ oscillation and that the observed number of the ν_e candidates is consistent both with the expectations with and without the $\nu_\mu \rightarrow \nu_e$ oscillation; eight ν_μ events and one candidate of the ν_e appearance signal were observed in Super-K with the 3.23×10^{19} protons accumulated during the physics run from January to June of 2010. The dominant source of $\delta f^{\phi}_{\mathrm{SK/ND}}$ is the uncertainty of the $\pi^{\pm}$ and $\mathrm{K}^{\pm}$ multiplicities, which can be reduced with an update of the NA61 measurement in future. Other than the multiplicity uncertainties, $\delta f^{\phi}_{\mathrm{SK/ND}}$ is much smaller than the T2K requirement. That represents the success of the stable beam operation and precise measurement of the beam, to which the muon monitor contributed.

In conclusion, we succeeded in launching the T2K experiment under guarantee of the well-tuned, stable and precisely measured beam and in suppressing the systematic uncertainty on the neutrino flux arising from the beam-related uncertainties much below the T2K requirement. Therefore, with increment of the beam power of J-PARC, it will not be long before T2K takes initiative to explore or measure θ_{13} among the world's competitive experiments.

Appendix A

Near-to-Far Extrapolation

In T2K, the precise prediction of the neutrino flux is realized with the near-to-far extrapolation. The near-to-far extrapolation is a method in which the neutrino flux at the J-PARC site before oscillation is measured by a near detector and is extrapolated to the far detector (Super-K). The near detector is placed on the direction to Super-K so that it can measure almost the same neutrino energy spectrum as Super-K. The near-to-far extrapolation is expressed as follows:

$$\begin{aligned}\phi_{\mathrm{SK}}(E_{\mathrm{SK}}) &= R_{\mathrm{F/N}}(E_{\mathrm{SK}}, E_{\mathrm{ND}}) \cdot \phi_{\mathrm{ND}}(E_{\mathrm{ND}}) \\ &= R_{\mathrm{F/N}}(E_{\mathrm{SK}}, E_{\mathrm{ND}}) \cdot \frac{N^{obs}_{\mathrm{ND}}(E_{\mathrm{ND}})}{\sigma_{\mathrm{ND}}(E_{\mathrm{ND}}) \cdot \epsilon_{\mathrm{ND}}(E_{\mathrm{ND}})},\end{aligned} \tag{A.1}$$

where $R_{\mathrm{F/N}}(E_{\mathrm{SK}}, E_{\mathrm{ND}})$ is a matrix, called the transfer matrix, which relates the neutrino energy spectra $\phi_{\mathrm{ND}}(E_{\mathrm{ND}})$ at the near detector and $\phi_{\mathrm{SK}}(E_{\mathrm{SK}})$ at Super-K. $R_{\mathrm{F/N}}(E_{\mathrm{SK}}, E_{\mathrm{ND}})$ is obtained by estimating $\phi^{\mathrm{MC}}_{\mathrm{SK}}(E_{\mathrm{SK}})$ and $\phi^{\mathrm{MC}}_{\mathrm{ND}}(E_{\mathrm{ND}})$ with a MC simulation. $\phi^{\mathrm{MC}}_{\mathrm{ND}}(E_\nu)$ is shown in Fig. A.1 with the scaled $\phi^{\mathrm{MC}}_{\mathrm{SK}}(E_\nu)$, and the ratio $R_{\mathrm{F/N}}(E_\nu) \equiv \phi^{\mathrm{MC}}_{\mathrm{SK}}(E_\nu)/\phi^{\mathrm{MC}}_{\mathrm{ND}}(E_\nu)$ is shown in Fig. A.2. $R_{\mathrm{F/N}}(E_\nu)$ is a simple expression of the matrix $R_{\mathrm{F/N}}(E_{\mathrm{SK}}, E_{\mathrm{ND}})$ and is called the far-near ratio. The shape of $\phi_{\mathrm{ND}}(E_\nu)$ is almost the same as one of $\phi_{\mathrm{SK}}(E_\nu)$. The difference of the shape is due to the geometrical acceptance difference between the near and far detectors.

The effect of the acceptance difference is explained as the difference of the allowed θ_ν in Eq. 2.5 between the near and far detectors (see Fig. A.3). For a given pion decaying into a neutrino and a muon, only the neutrino produced with a certain angle ($\theta_\nu = \theta_{\mathrm{SK}}$), or a certain neutrino energy according to Eq. 2.5, can leave for Super-K. On the other hand, to leave for the near detector, the neutrino can have a certain range of the angle around θ_{SK} ($\theta_{\mathrm{SK}} - \Delta\theta < \theta_\nu < \theta_{\mathrm{SK}} + \Delta\theta$), or a certain range of the energy. That is why the $\phi_{\mathrm{ND}}(E_\nu)$ shape is not the same as the $\phi_{\mathrm{SK}}(E_\nu)$ one.

Equation 2.5 tells that the energy of neutrinos detected in Super-K (E_{SK}) depends only on their parent pion kinematics at the decay point, and that E_{ND} depends on the pion kinematics, pion decay position and the neutrino detection position in the near detector. The pion kinematics at the decay is mainly determined by the proton beam parameters at the target, the pion kinematics at the production in the target and the bending of the pion by the horns. Therefore, these pieces of information on the beamline (the proton beam, pion kinematics and horn magnetic field) are necessary to predict the neutrino flux $\phi^{\mathrm{MC}}_{\mathrm{SK}}$ and $\phi^{\mathrm{MC}}_{\mathrm{ND}}$. The uncertainties on the beamline information nearly scale to the uncertainties of $\phi^{\mathrm{MC}}_{\mathrm{SK}}$ and $\phi^{\mathrm{MC}}_{\mathrm{ND}}$. However, since ϕ_{SK} and ϕ_{ND} originate from pions with almost the same kinematics, the beamline uncertainties cancel out in terms of $R_{\mathrm{F/N}} = \phi^{\mathrm{MC}}_{\mathrm{SK}}/\phi^{\mathrm{MC}}_{\mathrm{ND}}$. Thus, as for the uncertainty of ϕ_{SK} arising from the beamline uncertainties, the uncertainty estimated according to Eq. A.1 is much less than the one estimated only with the MC simulation. This kind of cancellation of uncertainties between the near and far detectors is the advantage of the near-to-far extrapolation.

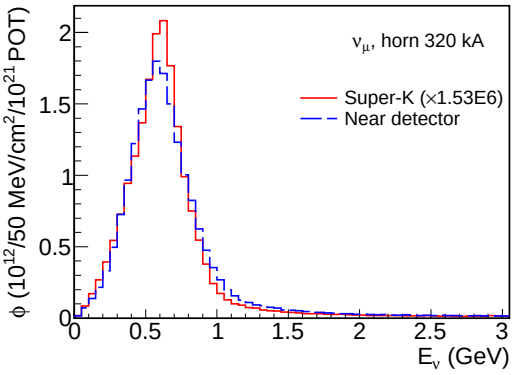

Figure A.1: ν_μ energy spectrum at the near detector estimated with a Monte Carlo simulation. The spectrum at Super-K is scaled so that the total flux is the same as the one at the near detector.

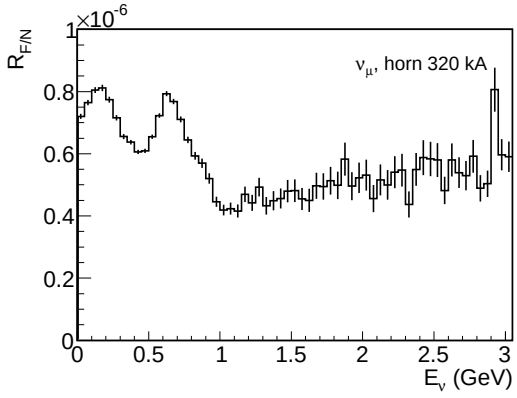

Figure A.2: Far-near ratio of the ν_μ flux. The error bar is the MC statistical error.

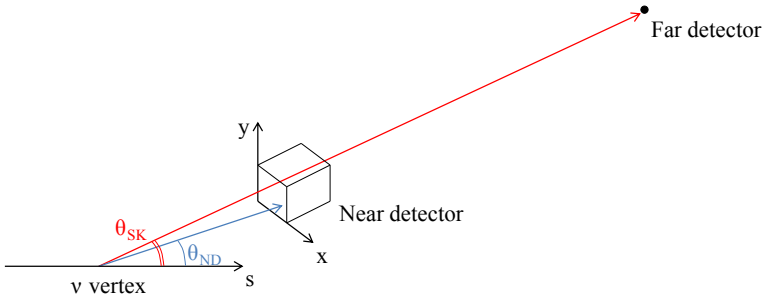

Figure A.3: Illustration of the near and far (Super-K) detectors showing their acceptance difference from a viewpoint of the J-PARC site. θ_{ND} and θ_{SK} are the directions from a given neutrino vertex to the near and far detectors, respectively, relative to a given axis s. θ_{SK} is always the same independent from the neutrino vertex position. On the other hand, θ_{ND} varies depending on the detection position (x, y) at the near detector and the neutrino vertex position.

Another cancellation arises in the uncertainty of the neutrino cross-section. For the T2K neutrino beam energies, the neutrino cross-section has not been well measured, and its uncertainty is as large as about 20%. However, one can find the $\sigma_{\mathrm{SK}}/\sigma_{\mathrm{ND}}$ term when Eq. A.1 is substituted for Eq. 2.4. Many correlating uncertainties on σ_{SK} and σ_{ND} cancel out in this ratio term.

Appendix B

Monte Carlo Simulations for Super-K

To estimate the number of neutrino events in Super-K, two MC simulation programs are utilized: NEUT for a simulation of the neutrino interactions and SKDETSIM for a simulation of the detector response. These simulation programs are briefly described in this appendix.

B.1 Neutrino interaction simulation (NEUT)

Neutrino interactions with nuclear targets are simulated with NEUT [238,239] (a neutrino interaction simulation library). NEUT is also used in the Kamiokande, Super-Kamiokande, K2K and SciBooNE experiments. NEUT simulates neutrino interactions with the hydrogen and oxygen nuclei, which are constituents of water. It also simulates interactions with the carbon, argon and iron nuclei. It covers a wide energy range of neutrinos from several tens of MeV to hundreds of TeV.

In NEUT, the following neutrino interactions in both charged current (CC) via W boson exchange ($\nu_\ell + N \to \ell + X$) and neutral current (NC) via Z boson exchange ($\nu_\ell + N \to \nu_\ell + X$) are considered:

- quasi-elastic scattering (QE), $\nu_\ell + N \to \ell(\nu_\ell) + N'$;
- resonant single meson production, $\nu_\ell + N \to \ell(\nu_\ell) + N'+$ meson;
- resonant single γ production, $\nu_\ell + N \to \ell(\nu_\ell) + N' + \gamma$;
- coherent π production, $\nu_\ell + {}^{16}\mathrm{O} \to \ell(\nu_\ell) + \pi + X$;
- deep inelastic scattering (DIS), $\nu_\ell + N \to \ell(\nu_\ell) + N'+$ hadrons,

where N and N' are nucleons (proton or neutron, or Λ for N' in the single K production) and ℓ is a charged lepton. CCQE is the major interaction in T2K, and it is the signal for both the ν_μ disappearance and the ν_e appearance. CC and NC single pion productions (CC1π and NC1π^0) are the significant backgrounds for the ν_μ disappearance and the ν_e appearance, respectively. The neutrino-nucleus cross-section in NEUT for each interaction is shown in Fig. B.1. The neutrino interaction models applied to NEUT are explained below.

B.1.1 Quasi-elastic scattering (QE)

CCQE is a two-body scattering between a neutrino and a nucleon via $\mathrm{W}^\pm$ exchange. In NEUT, the CCQE cross-section is evaluated based on the model of Llewellyn-Smith [243]. The amplitude

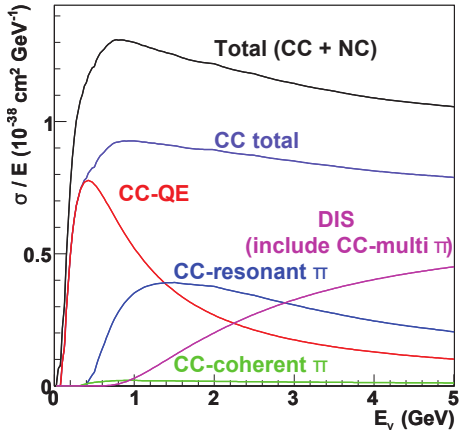

Figure B.1: Neutrino-nucleus cross-sections per nucleon divided by the neutrino energy in NEUT.

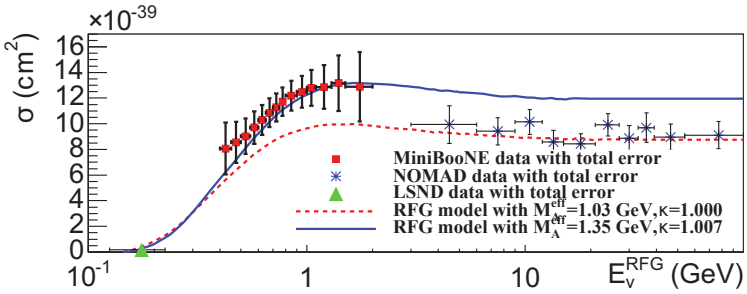

Figure B.2: Total cross-section of the ν_μ CCQE interaction as a function of the neutrino energy E_ν from the MiniBooNE experiment, quoted from [240]. Results from the NOMAD [241] and LSND [242] experiments are also plotted. Predictions with the NUANCE simulation with two different RFG parameter variations ($M_A = 1.03$ and 1.35 GeV/c^2) are superimposed.

of this process is described by the product of the leptonic and hadronic weak currents. To calculate the cross-section off nucleons in a nucleus, the relativistic Fermi gas (RFG) model by R.A. Smith and E.J. Moniz [244] is used. Both Llewellyn-Smith and RFG models use the vector and axial-vector form factors of the nucleon. The vector coupling constant, or the vector mass M_V, is set at $0.84(\pm0.1)$ GeV/c^2. The axial-vector mass M_A is set at $1.21(\pm0.2)$ GeV/c^2 to have good agreements with the recent neutrino experiments, K2K [92] and MiniBooNE [245], whose neutrino beam energy is nearly equal to the one in T2K. It should be noted that the previous world average of M_A was 1.026 ± 0.021 [246] and there exists an inconsistency on M_A as shown in Fig. B.2, which has been left to be solved.

The nucleons are treated as quasi-free particles, and the Fermi motion of the nucleons along with the Pauli exclusion principle is taken into account; the momentum distribution of the target nucleon is assumed to be flat up to the Fermi surface momentum of 225 ± 25 MeV/c, and the binding energy is set at 27 MeV ($\pm100\%$). The Fermi motion affects the reconstruction of the neutrino energy E_ν, since E_ν is reconstructed as Eq. 2.3 assuming the target nucleon is at rest. In Super-K, the difference between the true and reconstructed E_νs mainly arises from the Fermi motion.

The NCQE cross-sections are calculated by using the following relations [247, 248]:

$$\sigma(\nu p \to \nu p) = 0.153 \times \sigma(\nu n \to \mu^- p), \tag{B.1}$$
$$\sigma(\bar{\nu} p \to \bar{\nu} p) = 0.218 \times \sigma(\bar{\nu} n \to \mu^+ n), \tag{B.2}$$
$$\sigma(\nu n \to \nu n) = 1.5 \times \sigma(\nu p \to \nu p), \tag{B.3}$$
$$\sigma(\bar{\nu} n \to \bar{\nu} n) = 1.0 \times \sigma(\bar{\nu} p \to \bar{\nu} p). \tag{B.4}$$

B.1.2 Resonant single meson production

The neutrino induced single meson production is dominated by a baryonic resonance excitation off a single nucleon bound in a nucleus. The resonance state N^* promptly decays into a nucleon and a meson in the final state:

$$\nu + N \to \ell + N^*, \quad N^* \to N' + \text{meson}. \tag{B.5}$$

For this interaction, the model of D. Rein and L.M. Sehgal [249, 250] is adopted. NEUT also treats the Pauli blocking effect in the decay of the resonance, which suppresses the cross-section by a few percent; and the pion-less delta decay, which does not produce the pion with a 20% probability in all the resonant delta decays.

The inclusive CC1π^+ cross-section for $E_\nu < 2$ GeV has been measured by ANL [251], K2K [252] and MiniBooNE [253], and the prediction by NEUT agrees within 23% with those data. Above 2 GeV, there is no cross-section data available. For the $\nu p \to \mu^- p \pi^+$ mode, the angular distribution of the π^+ has been measured [254], with which NEUT agrees well.

For the NC1π^0 production, the momentum spectrum of the outgoing π^0 has been measured by K2K [255], MiniBooNE [256] and SciBooNE [257]. The discrepancy between those data and NEUT is approximately 20%.

B.1.3 Coherent pion production

Neutrinos can interact coherently with nucleons in the target nucleus, and produce a pion. In the coherent process, the four-momentum transfer to the target nucleus is generally small so that the effective dimensions of space involved in the interactions are large compared to the dimensions of the target. Due to the small momentum transfer, the outgoing lepton and pion are produced forward in the lab frame, and no nuclear breakup occurs. For the coherent pion production, large discrepancies exist among models as shown in Fig. B.3. NEUT adopts the model of D. Rein and L.M. Sehgal [258, 259]. K2K [260] and SciBooNE [261] reported the upper limit on the CC coherent pion production cross-section, which is smaller than the prediction by NEUT. Therefore, a large systematic error (100%) is assigned on the NEUT prediction for this mode.

B.1.4 Deep inelastic scattering (DIS)

DIS is the dominant interaction in the high energy region. It is understood as the neutrino-quark interaction. For the CC DIS, the GRV98 parton distribution functions [267] are used to calculate the cross-section. Additionally, corrections developed by A. Bodek and U.K. Yang [268] are adopted to improve the agreement with the experiments in the low q^2 region. K2K [269] and MiniBooNE [270] observed the higher cross-section by nearly 30% than the NEUT prediction.

B.1.5 Nuclear effects

Hadrons generated in the neutrino interaction in a nucleus can interact within the nucleus with a large probability. Therefore, particles or their momenta observed in the detector can be different

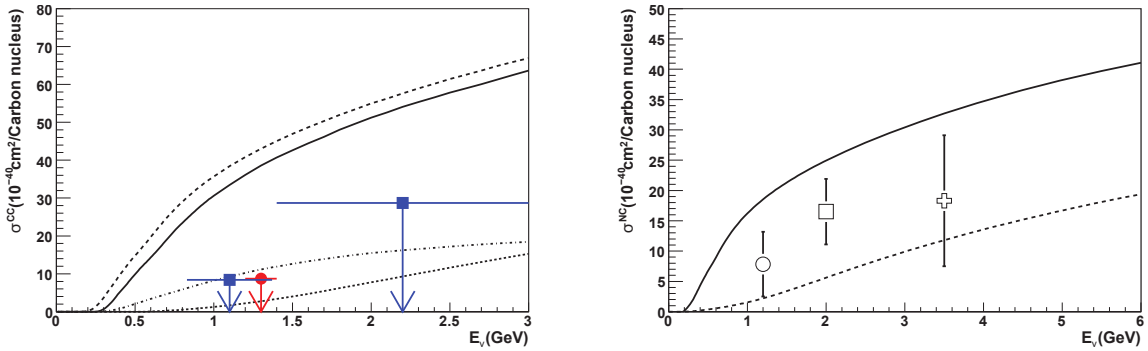

Figure B.3: Cross-sections of the coherent pion production off a carbon nucleus for CC (left) and NC (right), quoted from [239]. The lines are model predictions: D. Rein and L.M. Sehgal [258, 259] (solid line), A. Kartavtsev *et al.* [262] (dotted line) and L. Alvarez-Russo *et al.* [263] (dash-dotted line). The filled boxes and filled circle show the upper limits measured by K2K [260] and SciBooNE [261], respectively. The open circle, open box and open cross are the measurements by MiniBooNE [264], Aachen-Padova [265] and Gargamelle [266], respectively.

from those at the primary neutrino interaction. These effects are also simulated in NEUT. The interactions in the target nucleus are treated by using a cascade model inside NEUT.

Pion interactions in nucleus

The neutrino-induced pion production is one of the dominant interactions in T2K, and the interaction rate of the pion in the nucleus is quite large. The following pion interactions are treated in NEUT: the inelastic scattering, charge exchange and absorption reaction. In addition, the production of particles is taken into account for the high energy pions. The interaction cross-section of the pion (< 500 MeV/c) in the nucleus is calculated with the model of L.L. Salcedo *et al.* [271], which agrees well with the past experimental data [272].

B.2 Super-K detector simulation (SKDETSIM)

The Super-K detector response to the particle generated in the neutrino interaction by NEUT is handled by SKDETSIM, a program library based on GEANT3. SKDETSIM simulates the particle propagation across the detector; Cherenkov photon propagation; reflection, refraction and absorption of the Cherenkov light on materials; photo-electron production; and response of the electronics.

For the hadronic interaction in water, GCALOR is used because of its success at reproducing pion interactions around 1 GeV [273]. For pions with momentum below 500 MeV, however, custom routines have been written. For the propagation of the Cherenkov photon in water, SKDETSIM considers the absorption, Rayleigh scattering and Mie scattering.

B.2.1 Cherenkov photon propagation

Scattering and absorption coefficients of the photon in water have been tuned to a number of laser calibration sources. Position dependence of the water quality has been tuned to measurements with a γ-ray source, called Ni source.* The refractive index of water is set at a value from the experimental data [274].

A lump of Ni wires is contained in a polyethylene tank with purified water, and a Cf radioactive source is set in its center. Neutrons from this Cf source are used to induce Ni(n,γ)Ni reactions.

Those tunings of the water interaction parameters bring the agreement between data and the SKDETSIM prediction for various data sample metrics to a few percent level.

B.2.2 Reflection, refraction and absorption of light on materials

The Cherenkov light propagating in the Super-K water can be reflected, refracted or absorbed by the acrylic cover on the PMT face, the PMT surface, the black PET sheet on the inner detector surface and the Tyvek® sheet on the outer detector surface.

The transparency and refractive index of the acrylic cover were measured before the installation. The reflection, refraction and absorption on the PMT surface and the black sheet have been tuned to laser injection data. Those on the Tyvek sheet has been tuned to cosmic ray muon data.

B.2.3 Photoelectron production and response of the electronics

For the absolute quantum efficiency of the PMTs, the measurement by Hamamatsu Photonics K.K. is referred to. The relative differences of the quantum efficiencies of the PMTs are measured by the Ni source. Based on the measurements in Super-K, the one photo-electron distribution, the ADC threshold effect, the PMT and ADC saturation and the timing resolution are tuned. The efficiency of the ADC charge integration is calculated by simulating the waveform.

A yield of the Cherenkov photons is compared between data and the SKDETSIM prediction by using cosmic ray muons passing vertically through the detector. The photoelectron distributions agree well within 1–2%.

Appendix C

Neutrino Beamline Operation

This appendix describes the detail of the good beam spill selection and the proton beam measurement.

C.1 Detail of the good beam spill selection

The criteria described in Sec. 7.1.1 are applied to the beam data taken from January to June of 2010 to select good beam spills. Details of the selections are described below.

Good GPS status

The time difference between the two GPSs at the J-PARC site during the physics run is shown in Fig. C.1. On March 3rd and 29th, the GPS hardware was restarted, which caused the time offset of GPS1. However, the GPS system was stable over the physics run, and every spill passes the good GPS status selection.

Normal beam condition

By the normal beam condition selection, 6385 spills are cut due to the following reasons:

- The current of the second vertical steering magnet in the preparation section (PV2) became unstable during February 26–28th, 2010 (139 spills are cut).
- Because the HV monitor of the muon monitor froze, the HV of the muon monitor was artificially turned off by mistake for seven minutes on March 20th, 2010 (119 spills are cut).
- The PV2 current became unstable for 7.5 hours on March 21st, 2010 (6093 spills are cut).
- A spike current was observed in PV2 on March 21st, 2010 (34 spills are cut).

The unstable PV2 current caused a shift of the proton beam center at the target by about ± 1 mm in y and a shift of the muon profile center by about ± 3 cm in y.

Horn current cut

In this analysis, the threshold of the horn current cut is set at ± 5 kA from the mean value of each horn current. The measurement of the horn currents was discussed in Sec. 6.3.1. One spill is lost by this cut.

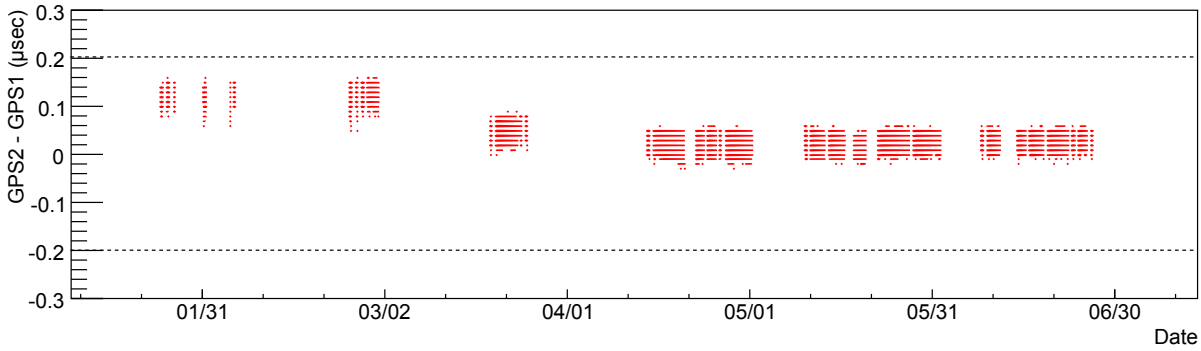

Figure C.1: Stability of the GPS system at the J-PARC site during the physics run. The vertical axis is the time difference between the two GPSs. The dotted lines show the threshold of the good GPS status selection.

Muon profile center cut

As shown in Fig. 6.23, the muon profile center was stable during the physics run. No spill is lost by this cut.

Muon yield cut

As shown in Fig. 6.24, the muon yield was stable during the physics run. The mean of the yield was 33.53 nC/(10^{12} proton)/spill for the silicon array. The threshold of the muon yield cut is set at the mean ± 5%. From May 8th to June 1st, when the attenuation level of the CT readout system was increased, the muon yield cut is set at the mean ± (10×RMS). By this cut, 0.04% of the spills are lost. This spill loss is caused by a shift of the FADC gate timing of the muon monitor.*

C.2 Proton beam measurement

C.2.1 Performance of the proton beam monitors

Basic performances of the proton beam monitors are summarized here. Their systematic errors and shot-by-shot fluctuations are listed in Table C.1. They were estimated in the beam operation.

CT

CT measures the proton beam intensity with an absolute scale precision of 2%, which arises from the precision of the calibration. The difference of the measured beam intensity among the five CTs was 1.6% at the maximum, and the difference between the average of the five CTs and the CT in the MR was 1.2%. These differences originate not from the beam loss but from the measurement uncertainty. The beam loss was measured by the beam loss monitors to be less than 0.01% in the neutrino beamline and at the extraction from the MR.

The shot-by-shot fluctuation is estimated at 0.5% by looking at the correlation among the five CTs. It agrees with an expectation from the FADC sampling timing and the electrical noise.

*The gate timing shift was caused by a trouble with a transceiver module which received the beam timing signal. The timing shift occurred only in January and February before the transceiver was replaced with new one.

Table C.1: Systematic errors and shot-by-shot fluctuations of the proton beam monitors for the measurement of the profile center x_0 and y_0, width σ_x and σ_y and the absolute number of protons N. The x_0 and y_0 systematic errors of the SSEM, ESM and OTR monitor in this table include the alignment precisions.

	Δx_0 (mm)	Δy_0 (mm)	$\Delta\sigma_x$ (mm)	$\Delta\sigma_y$ (mm)	$\Delta N/N$ (%)
Systematic error					
CT	–	–	–	–	2
SSEM	< 0.45	< 0.45	0.2	0.2	–
ESM	< 0.45	< 0.45	–	–	–
OTR monitor	0.40	0.43	0.30	0.27	–
Shot-by-shot fluctuation					
CT	–	–	–	–	0.5
SSEM	0.01–0.02	0.01–0.02	0.05	0.05	–
ESM	0.02–0.04	0.02–0.04	–	–	–
OTR monitor	0.15	0.10	0.15	0.07	–

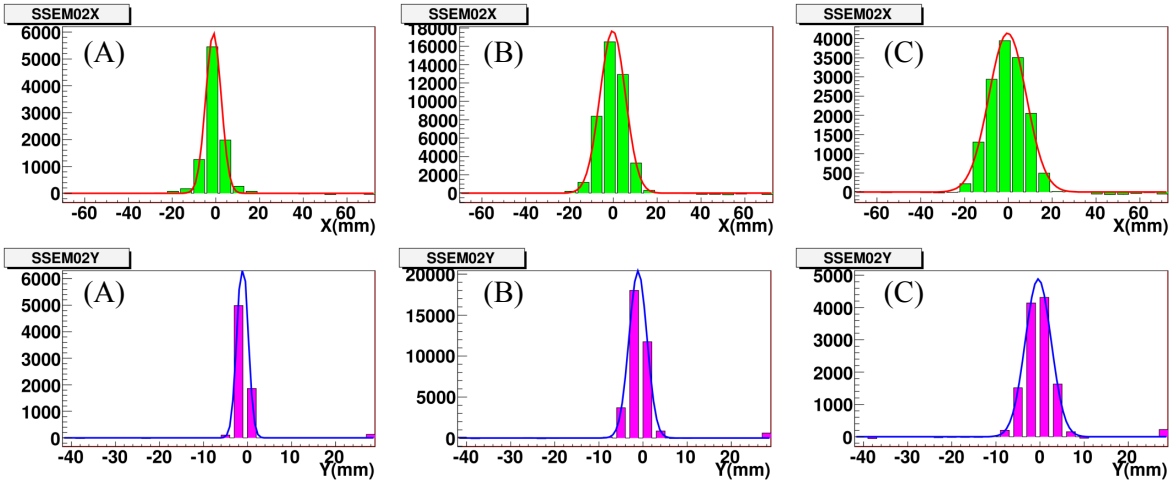

Table C.2: Horizontal (upper) and vertical (lower) proton beam profile measured by the SSEM just after the extraction from the MR. The solid line shows a Gaussian fitted to the SSEM measurement. (A) 2.6×10^{12} protons/spill. (B) 1.2×10^{13} protons/spill. (C) 3.5×10^{13} protons/spill. Because the attenuation level of the SSEM attenuator was changed, the vertical scale in these plots does not scale to the proton beam intensity.

The CTs also measure the beam timing by looking at the timing of the first bunch peak. The fluctuation of the timing was 5 nsec in RMS.

SSEM

Examples of the proton beam profile measured by the SSEM just after the extraction from the MR are shown in Fig. C.2. The beam center and width (1σ) are derived by fitting a Gaussian distribution to the profile. The measurement precision of the beam position is estimated to be less than 450 μm: 10–20 μm for the measurement fluctuation, 100–400 μm for the alignment

precision and 200 μm for the systematic uncertainty other than the alignment. The systematic uncertainty of the beam width measurement is 200 μm. These systematic uncertainties of the beam position and width were estimated using a toy Monte Carlo simulation, in which the effect of the following systematic uncertainty sources was studied: the electrical noise, beam shape, relative positions of the strips, gain differences among the strips and cross-talks.

ESM

The measurement precision of the beam position is estimated to be less than 450 μm: 20–40 μm for the measurement fluctuation, 100–400 μm for the alignment precision and 200 μm for the systematic uncertainty other than the alignment. The systematic uncertainty is the same as the one for the SSEM because the ESM is calibrated with the SSEMs.

OTR monitor

A sample event display of the OTR monitor is shown in Fig. C.2. It was taken with the titanium alloy foil at 5.1×10^{13} protons/spill. The proton beam profile is reconstructed by fitting a Gaussian distribution to the data. For the beam position (x_0, y_0), the measurement precision is estimated to be (431, 434) μm: (150, 100) μm for the measurement fluctuation, (300, 300) μm for the alignment precision and (270, 297) μm for the systematic uncertainty other than the alignment. For the beam width (σ_x, σ_y), it is estimated to be (329, 272) μm: (150, 70) μm for the measurement fluctuation and (292, 262) μm for the systematic uncertainty. These systematic uncertainties were studied using simulated OTR images.

Beam loss monitor

By comparing the beam loss with and without the SSEMs in the beamline, the beam loss monitor (BLM) is calibrated because the titanium foils of each SSEM cause 0.005% beam loss. The beam loss along the primary beamline at the 50 kW operation is shown in Fig. C.3. It is estimated that the BLM has a sensitivity down to 16 mW beam loss. No significant beam loss was found when the SSEMs were out of the beamline.

C.2.2 Extrapolation of the proton beam orbit and optics

The proton beam center and angle at the entrance of the baffle or on the target upstream surface are estimated by fitting the beam center measured by ESM19, SSEM18 (or ESM20), SSEM19 and the OTR monitor for x, and SSEM18 (or ESM20), SSEM19 and the OTR monitor for y. The more upstream ESMs or SSEMs cannot be used for the extrapolation because there is a quadrupole magnet (FQ4) at the upstream of ESM19 and a vertical dipole magnet (FVD2) at the upstream of ESM20 and SSEM18.

The proton beam width, emittance and Twiss parameters at the entrance of the baffle or on the target upstream surface are estimated by fitting the beam width measured by SSEM14–19 and the OTR monitor. This fit includes a model to describe the effects of the three quadrupole magnets (FQ2–4). The position-angle profile of the proton beam is reconstructed for each spill assuming a Gaussian distribution:

$$n_p(x,x') = \frac{n_p(\mathrm{CT05})}{2\pi\sigma_x\sigma_{x'}\sqrt{1-\rho^2}} \exp\left[-\frac{1}{2(1-\rho^2)}\left\{\frac{(x-x_0)^2}{\sigma_x^2} - 2\rho\frac{(x-x_0)(x'-x'_0)}{\sigma_x\sigma_{x'}} + \frac{(x'-x'_0)^2}{\sigma_{x'}^2}\right\}\right], \tag{C.1}$$

where $n_p(x,x')$ is the number of protons at a position x and angle x', $n_p(\mathrm{CT05})$ is the number of protons measured by the most downstream CT, σ_x is the positional profile width, $\sigma_{x'}$ is the

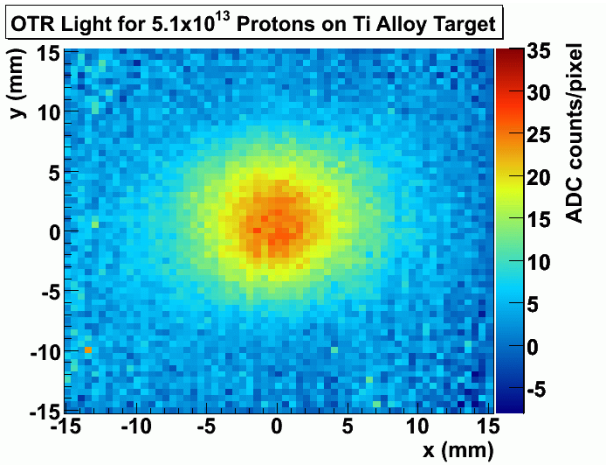

Figure C.2: Proton beam profile measured by the OTR monitor (Ti alloy foil) at 5.1×10^{13} protons/spill.

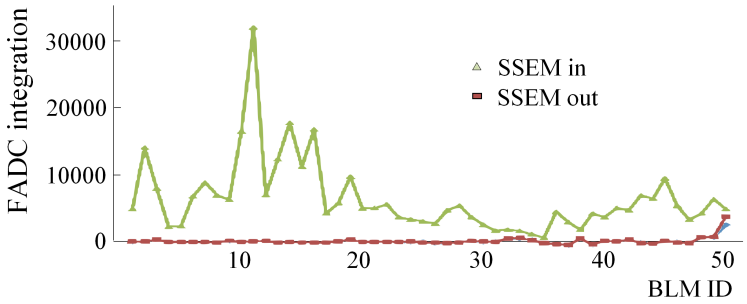

Figure C.3: Beam loss along the primary beamline at the 50 kW operation. BLM1 is placed at the extraction, and BLM50 at the end of the primary beamline. The loss at BLM50 without the SSEMs indicates a beam loss by the beam window.

angular profile width, and x_0 and x'_0 are the profile centers. The Twiss parameters (α, β and γ) and the beam emittance ϵ are obtained from the following equations:

$$\beta\gamma - \alpha^2 = 1, \tag{C.2}$$

$$\sigma_x = \frac{\sqrt{\beta\epsilon}}{2}, \tag{C.3}$$

$$\sigma_{x'} = \frac{\sqrt{\epsilon\gamma}}{2} = \frac{\epsilon\sqrt{1+\alpha^2}}{4\sigma_x}, \tag{C.4}$$

$$\gamma x^2 + 2\alpha x x' + \beta x'^2 = \epsilon, \tag{C.5}$$

and ρ is written as

$$\rho = -\frac{(\sqrt{\epsilon\alpha}/2)^2}{\sigma_x \sigma_{x'}} = -\frac{\alpha}{\sqrt{1+\alpha^2}}. \tag{C.6}$$

Appendix D

Measurement of Neutrino Beam Events at ND280

This appendix presents the neutrino beam events measured by the ND280 detectors during the physics run. The measurement by INGRID and the off-axis near detector is described in Sec. D.1 and D.2, respectively. Only the spills after the good beam spill selections are used in those analyses.

D.1 Measurement of the neutrino beam by INGRID

A typical neutrino event in an INGRID module is shown in Fig. D.1. INGRID accumulated neutrino events during the physics run and monitored the neutrino beam. Only the results of the INGRID analysis on the neutrino beam stability are shown in this section. Details of this analysis can be found elsewhere [199].

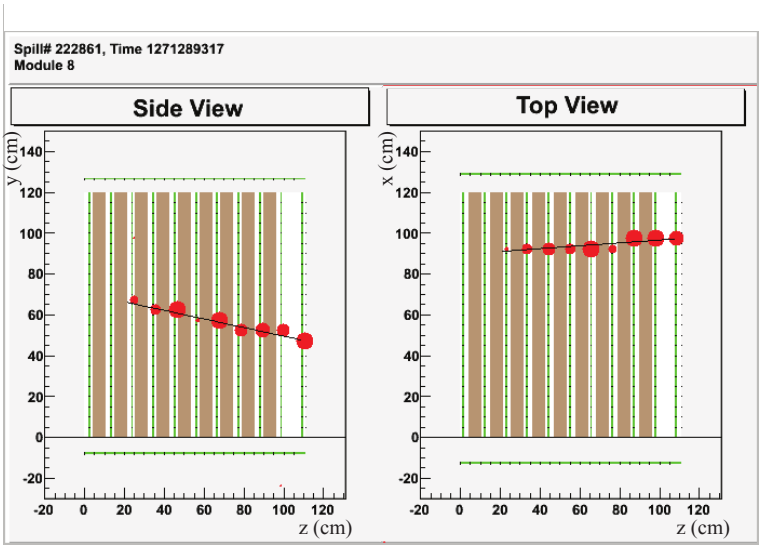

Figure D.1: A typical neutrino event in an INGRID module. Green cells in this figure show the scintillator bars, and the size of the red circle represents the size of the observed signal in each cell. The neutrino beam enters from the left side. This figure indicates that a neutrino interaction occurred in this module and a charged particle was produced.

D.1.1 Neutrino event selections

To select neutrino CC events whose vertices are contained in each INGRID module, the following selection criteria are applied:

1. "Time clustering": more than three hits within ±50 nsec are required to reject hits due to random MPPC noise, where a "hit" is defined as an ADC signal larger than 2.5 p.e. (photoelectrons). These clustering hits are classified as an event.

2. "Number of active planes selection": events in which the number of active planes is more than two are selected to reject MPPC noise hits further. The active plane is a scintillator plane with at least one coincidence hit both in x and y layers. Each of the x and y layers in the active plane is called the active layer.

3. "p.e./(number of active layers)": events with average p.e. per active layer (total p.e. of all hits in the active planes divided by the number of all active layers) > 6.5 are selected.

4. "Tracking": hits in the active planes are tracked from the downstream and are fitted to a straight line.

5. "Track matching": z position difference of the longest track between the x-z and y-z views is required to be less than two planes. Badly fitted tracks are rejected by this track matching.

6. "Beam timing cut": evens within ±100 nsec from the expected bunch timing are selected. This cut rejects background events such as cosmic muons off beam timing.

7. "Upstream VETO cut": When the upstream end of the track is on one of the VETO planes, this event is cut as a background in which neutrino vertex is outside the INGRID module.

8. "Fiducial volume cut": the volume with $10 \leq x \leq 110$ cm, $10 \leq y \leq 110$ cm and z from the first (most upstream) iron plane to the ninth scintillator plane (see Fig. D.1) is defined as the fiducial volume of each INGRID module. When the upstream end of the track is inside the fiducial volume, this event is selected as a neutrino event.

D.1.2 Neutrino beam direction measured by INGRID

The neutrino beam profile is reconstructed from the number of neutrino events at each INGRID module. Figure D.2 shows the reconstructed profile during the physics run. The profile is fitted to a Gaussian distribution to get its center, or the neutrino beam direction, which is the direction from the target to the INGRID profile center. Note that INGRID uses the different coordinate definition from the beamline coordinate in x: $x_{\mathrm{INGRID}} = -x_{beam}$. The INGRID vertical modules are misaligned by -1.9 cm, which has to be subtracted from the profile y center in Fig. D.2 to get the actual profile center.

The history of the profile center is shown in Fig. D.3. In this figure, the x center is plotted in the INGRID coordinate system, and the y center is corrected for the misalignment. The shifted profile y center from the beamline axis can be also seen in INGRID as in the muon monitor. The profile center and width for each run are summarized in Table D.1. The mean of the profile center, or the mean neutrino beam direction, during the physics run is summarized in Table D.2. INGRID confirmed that the neutrino beam was produced in the direction between ±1 mrad from the beamline axis, which is required for T2K.

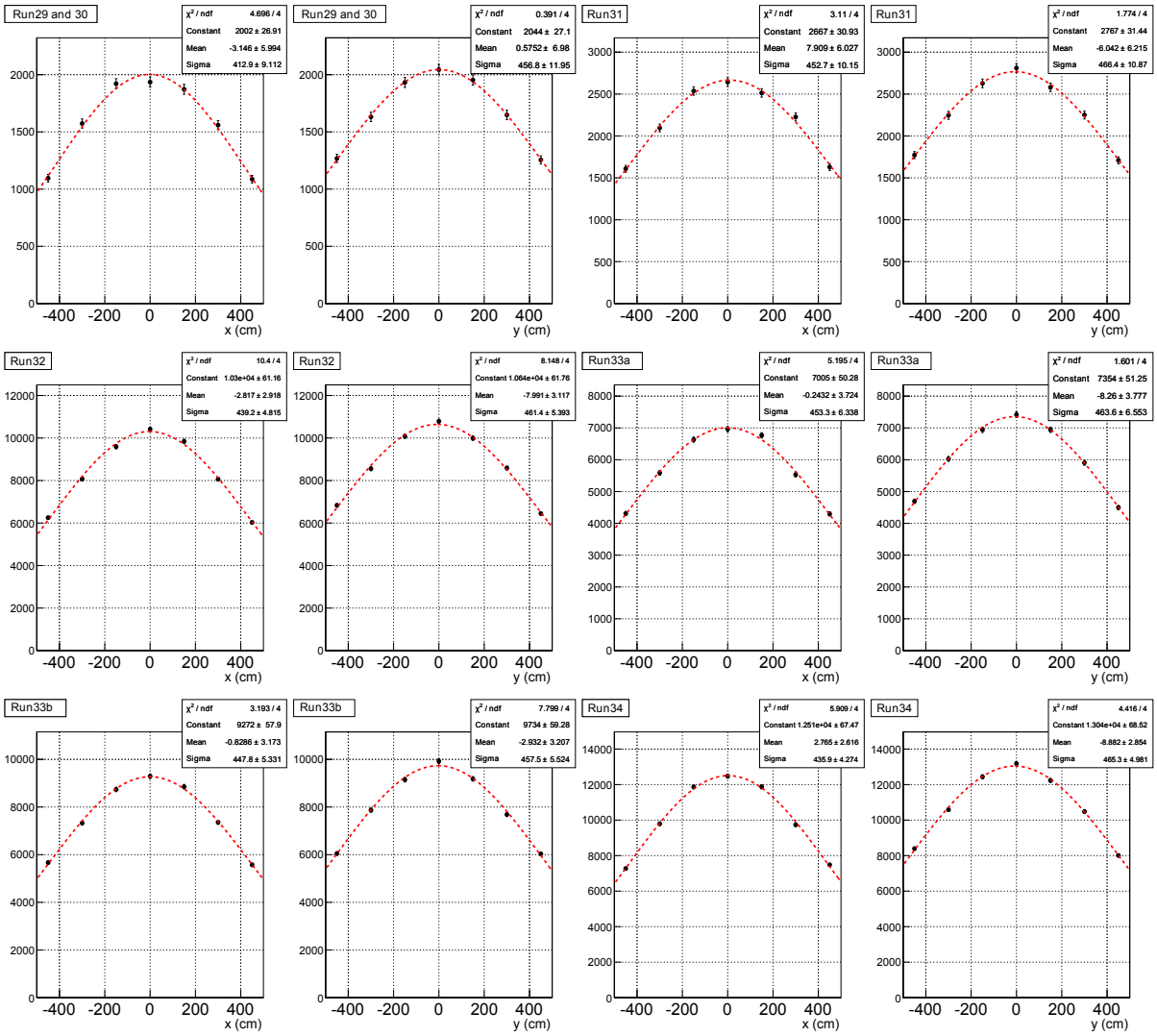

Figure D.2: Neutrino beam profile measured by INGRID. The number of neutrino events is accumulated run-by-run. The fitting result with a Gaussian distribution is superimposed. INGRID uses the different coordinate from the beamline coordinate in x: $x_{\mathrm{INGRID}} = -x_{beam}$. The misalignment in y is not corrected in these figures.

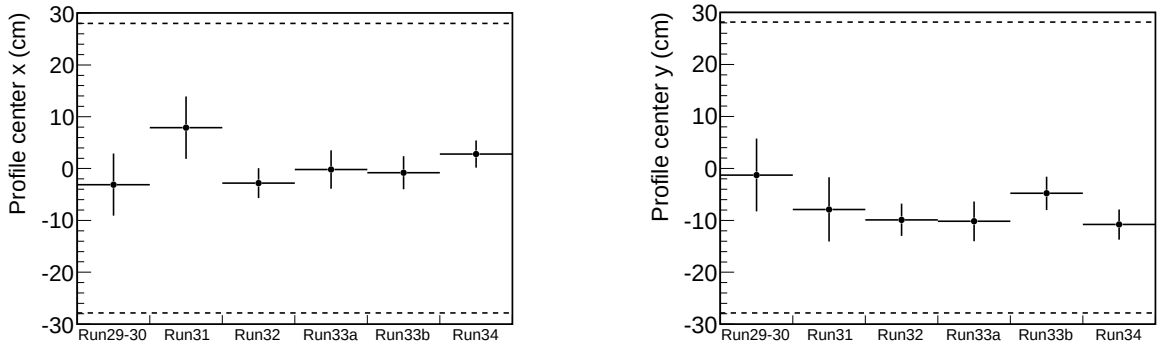

Figure D.3: INGRID profile center during the physics run. Only the statistical error is shown. INGRID uses the different coordinate from the beamline coordinate in x: $x_{\mathrm{INGRID}} = -x_{beam}$. The correction for the misalignment in y is applied in this figure. The dotted lines indicate the positions which correspond to the ± 1 mrad beam direction.

Table D.1: Profile center and width of the neutrino beam measured by INGRID during each physics run. INGRID uses the different coordinate from the beamline coordinate in x: $x_{\mathrm{INGRID}} = -x_{beam}$. The correction for the misalignment in y is applied in this table. Only the statistical error is given in this table.

Run	x center (cm)	y center (cm)	x width (cm)	y width (cm)
29, 30	-3.1 ± 6.0	0.6 ± 7.0	413 ± 9	457 ± 12
31	7.9 ± 6.0	-6.0 ± 6.2	453 ± 10	466 ± 11
32	-2.8 ± 2.9	-8.0 ± 3.1	439 ± 5	461 ± 5
33a	-0.2 ± 3.7	-8.3 ± 3.8	453 ± 6	464 ± 7
33b	-0.8 ± 3.2	-2.9 ± 3.2	448 ± 5	458 ± 6
34	2.8 ± 2.6	-8.9 ± 2.9	436 ± 4	465 ± 5

Table D.2: Mean neutrino beam direction measured by INGRID during the physics run (in the INGRID coordinate system).

	x	y
Profile center (cm)	0.2 ± 1.4(sta.) ± 9.2(sys.)	-6.6 ± 1.5(sta.) ± 10.4(sys.)
Beam direction (mrad)	0.01 ± 0.05(sta.) ± 0.33(sys.)	-0.24 ± 0.05(sta.) ± 0.37(sys.)

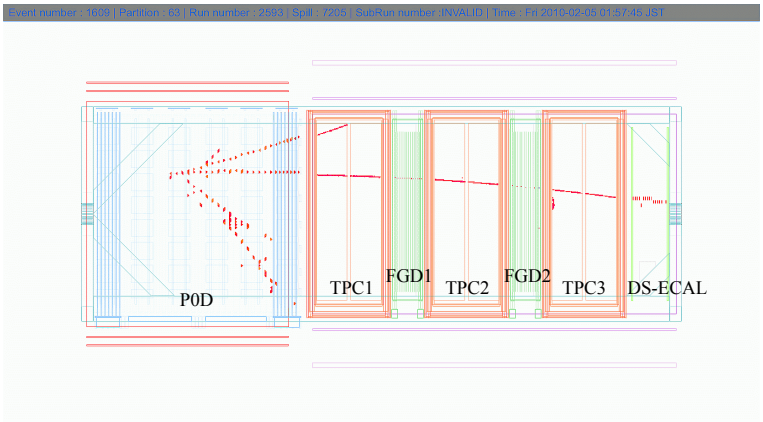

Figure D.4: Event display of the ND280 off-axis detector showing the first neutrino event candidate with the magnet on. The magnetic field was 0.188 T at this time. The neutrino beam enters from the left side.

D.2 Neutrino events at the ND280 off-axis detector

The ND280 off-axis detector has successfully accumulated neutrino events since it observed the first neutrino event on on February 5th, 2010 (Fig. D.4). The magnet operated at 0.18 T during the physics run till June of 2010.

In the first analysis of the neutrino events in the ND280 off-axis detector, only the FGDs and TPCs were used to obtain the normalization factor against the MC prediction. Inclusive samples of (mainly) CC interactions which occur in the FGDs are selected in this analysis. Details of this analysis can be found elsewhere [158, 235]. Here, the FGDs and TPCs are called, from the upstream, FGD1, 2 and TPC1, 2 and 3, respectively, as shown in Fig. D.4.

D.2.1 Neutrino event selections

Firstly, FGD hits are associated with TPC tracks with a simple algorithm: TPC2 (TPC3) tracks are extrapolated back to FGD1 (FGD2), using a linear extrapolation in the x-z plane and a circle in the y-z plane. When the distance between the extrapolated track and each FGD hit is less than 3 cm, the hit is considered to be associated with the track.

Then, the following selection criteria are applied to select CC interactions in the FGDs:

1. Use only events associated with the beam trigger.
2. Require no track in TPC1 to veto through-going muons or high energy upstream interactions.
3. Require that there is at least one track in TPC2, the associated hits in FGD1 start in the FGD1 fiducial volume, and the momentum of the track is larger than 50 MeV/c.
4. Select the track with the highest momentum among the negative tracks in TPC2 as a lepton track.
5. Apply to this track a PID cut based on the TPC information about the energy deposit versus momentum, to select a muon and to reject a low energy electron/positron.
6. Repeat the steps 3–5 for TPC3 and FGD2 when there is no track in TPC2.

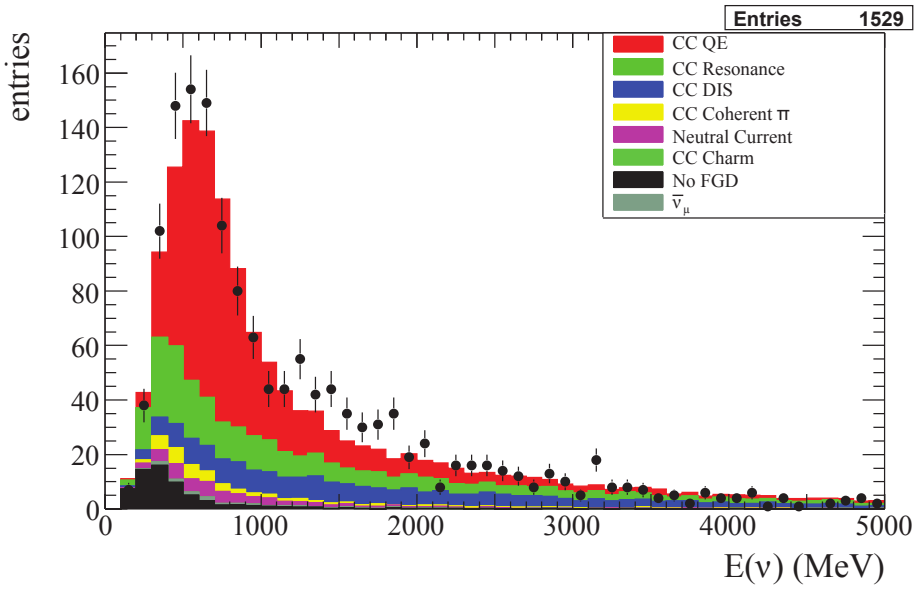

Figure D.5: Distribution of the reconstructed neutrino energy (calculated under the CCQE assumption) for the selected events in the ND280 tracker. The dots are the data, and the histograms are the MC predictions (NEUT). This figure comes from Ref. [235].

The fiducial volume of each FGD is defined as $|x| < 80$ cm, $-74.5 < y < 85.5$ cm and the layers except the most upstream x and y layers. Therefore, the fiducial volume is $1.6 \times 1.6 \times 0.31 = 0.79$ m^3 for each FGD.

Finally, a specific selection is applied to suppress backgrounds by single "entering" tracks; a track produced outside the FGD and entering the inner part of the tracker can be a background when it enters from the side of the FGD with a large angle and a small momentum. Therefore, events are rejected when they have a single entering track with an angle $\cos\theta < 0.9$ and a momentum $p < 500$ MeV/c. Here, the entering track is flagged when a TPC extrapolated track is close to FGD hits lying outside the fiducial volume, or the distance is less than 15 cm.

Consequently, 1529 events are selected in the data. Figure D.5 shows the reconstructed neutrino energy distribution for the selected events. These events include background interactions outside the FGDs (labeled as "No FGD" in this figure), which are expected to be 4.8%. The number of selected events in the FGDs ($N^{\mathrm{FGD}}_{\mathrm{data}}$) is obtained by subtracting this background:

$$N^{\mathrm{FGD}}_{\mathrm{data}} = 1456, \tag{D.1}$$

with a $\pm 2.7\%$ statistical error, $(-3.6, +4.2)\%$ systematic error due to detector systematical uncertainties and $\pm 3.7\%$ systematic error due to physics model uncertainties (efficiency variation of the detector due to the neutrino interaction uncertainties).

Appendix E

Tuning of the Kaon Production in JNUBEAM

For the kaon multiplicities in the neutrino flux estimation, the FLUKA prediction was used and its uncertainty was evaluated by using the Eichten data in Chap. 8. In this appendix, a method to tune the kaon multiplicities is described. In addition, the systematic error of the neutrino flux arising from the uncertainty of the tuned kaon multiplicities is reevaluated.

E.1 Tuning of the kaon multiplicities and its uncertainty

The Eichten data (see Sec. 8.5.2) is fitted with the BMPT parametrization proposed by M. Bonesini *et al.* [226] in order to estimate the kaon multiplicity also in the phase space not covered by this data. The fitted BMPT function is used to tune the FLUKA prediction. In addition, this function is used to compare the Eichten data with the other kaon production data at different incident proton energies for the evaluation of the uncertainty of the BMPT parametrization.

E.1.1 Kaon production data around 30 GeV

The kaon production data for around 30 GeV incident proton energy are summarized in Table E.1. The Eichten Be data is used for the BMPT parametrization, and the Allaby Be data [275] and the Fitch Al data [276] are used for validation of the BMPT parametrization. J.V. Allaby *et al.* measured $\mathrm{d}^2\sigma/\mathrm{d}\Omega\mathrm{d}p$ (b/sr/[GeV/c]) in 19.2 GeV/c proton and Be interactions, and V.L. Fitch *et al.* measured $\mathrm{d}^2N/\mathrm{d}\Omega\mathrm{d}p$ (particles /sr/[GeV/c]/circulating-proton) in 30 GeV proton and Al interactions. In this analysis, these cross-sections are normalized to $\omega \equiv (2E/p^2) \cdot (\mathrm{d}^2N/\mathrm{d}\Omega\mathrm{d}p)$ and the units are converted as follows:

$$\begin{aligned} &\frac{\mathrm{d}^2N}{\mathrm{d}\Omega\mathrm{d}p} \ \text{(particles/sr/[GeV/c]/interacting-proton)} \\ =&\frac{1}{\eta}\left(\frac{\mathrm{d}^2N}{\mathrm{d}\Omega\mathrm{d}p}\right)_{\text{Fitch}} = \frac{1}{\sigma_{inel}}\left(\frac{\mathrm{d}^2\sigma}{\mathrm{d}\Omega\mathrm{d}p}\right)_{\text{Allaby}} \end{aligned} \tag{E.1}$$

where η is the targeting efficiency estimated at $36.7 \pm 7.0\%$* from the effective target thickness (37 ± 7 g/cm^2) in the Fitch measurement and from σ_{inel} for Al (445 ± 6.7 mb [215]). For the normalization of the Allaby data, $\sigma_{inel} = 227 \pm 12$ mb [210] is used. The other data listed in Table E.1 are used only for confirmation because they are not reliable.

*V.L. Fitch *et al.* quoted in their paper approximately 50% targeting efficiency from private communication.

Table E.1: $K^{\pm}$ production data around 30 GeV.

	Beam energy or momentum	Target	Available data
Allaby [275]	19.2 GeV/c	Be, B_4C, Al, Cu, Pb	$\frac{d^2\sigma}{d\Omega dp}$
Eichten [223]	24.0 GeV/c	Be, B_4C, Al, Cu, Pb	ω
Becker [277]	28.5 GeV/c	Be, Ti, W	$E\frac{d^3\sigma}{dp^3}$ extrapolated to $A = 1$
Schwarzschild [278]	29.5 GeV/c	Be, Al, Fe	Large normalization error (100%)
Baker [279]	29.5 GeV	Be, Al	$\frac{d^2N}{d\Omega dp}$ for $\pi^{\pm}$ and its K/π ratio
Fitch [276]	30.0 GeV	Be, Al	Only Al data for $K^{\pm}$
NA61 [154, 155]	30.0 GeV	C	$K^{\pm}$ data is not available yet.

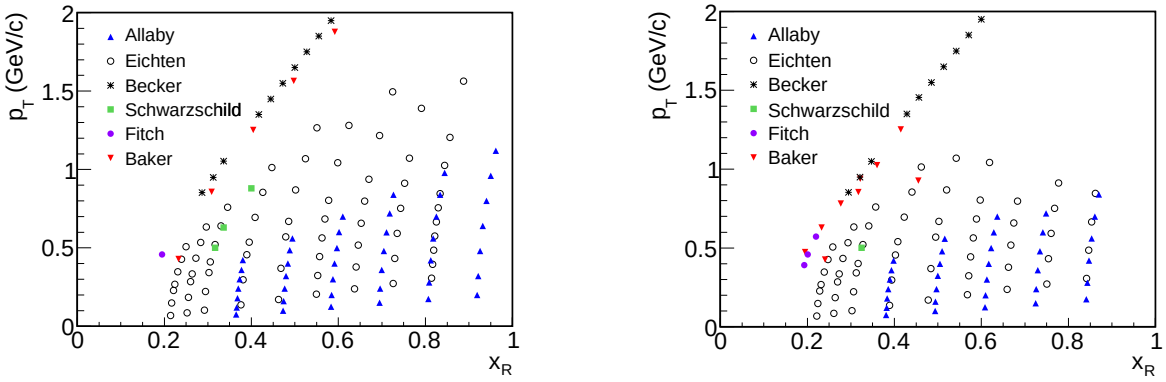

Figure E.1: K^+ (left) and K^- (right) production data around 30 GeV plotted in x_R-p_T. Only Be (Allaby, Eichten, Becker, Schwarzschild and Baker) and Al (Fitch) data are shown in this figure.

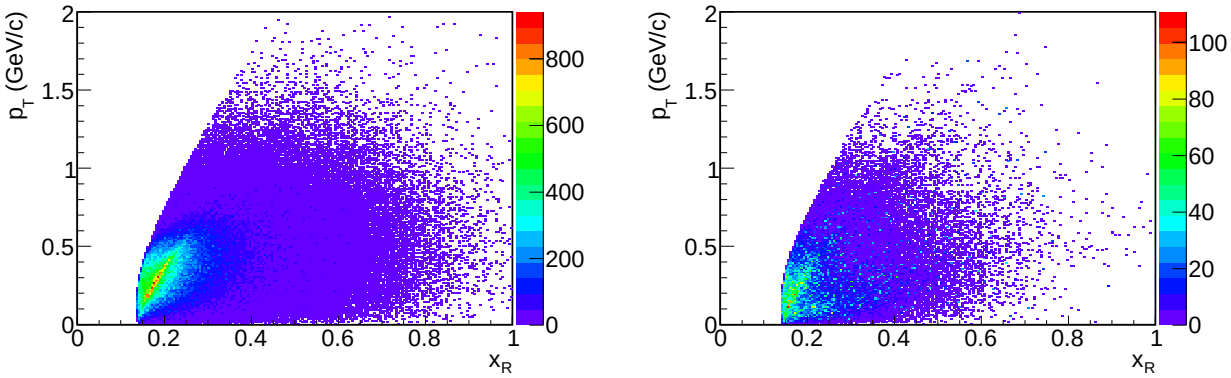

Figure E.2: x_R-p_T distribution of secondary K^+ (left) and K^- (right) whose descendant neutrinos go to Super-K. It is estimated with the pre-tuned JNUBEAM.

In the BMPT parametrization, the radial scaling variable x_R [280–282] is used instead of x_F. It is defined as

$$x_R \equiv \frac{E^{cm}}{E^{cm}_{max}}, \tag{E.2}$$

and is always positive, where E^{cm} is the energy of the produced particle in the center-of-mass system. E^{cm}_{max} is equal to $\sqrt{p^{cm2}_{max} + m^2}$, i.e. from Eq. 8.10,

$$E^{cm}_{max} = \frac{1}{2}\left(\sqrt{s} + \frac{m^2 - M^2_{min}}{\sqrt{s}}\right). \tag{E.3}$$

Figure E.1 shows the x_R-p_T phase space covered by those kaon production data. According to the Feynman scaling, the kaon multiplicities for different incident proton energies should be the same at the same x_R and p_T. The T2K phase space in x_R-p_T is shown in Fig. E.2 for the secondary $K^{\pm}$ which contribute to the neutrino flux at Super-K. One can see that there are few data which cover the T2K phase space in $x_R < 0.2$. The Allaby and Fitch data cover different phase spaces, in each of which the uncertainty of the BMPT parametrization is evaluated.

E.1.2 Parametrization of the kaon multiplicity

BMPT parametrization

The BMPT parametrization is an empirical parameterization of the inclusive invariant cross-sections for positive sign secondary meson (π^+, K^+) production in proton and Be interactions[†] based on general physical arguments. The cross-section is parametrized as [226]:

$$E\frac{d^3\sigma}{dp^3} = A(1-x_R)^{\alpha}(1+Bx_R)x_R^{-\beta}\{1 + a'(x_R)p_T + b'(x_R)p_T^2\}e^{-a'(x_R)p_T}, \tag{E.4}$$

where $a'(x_R) = a/x_R^{\gamma}$ and $b'(x_R) = a^2/2x_R^{\delta}$, and A, B, α, β, a, b, γ and δ are constants to be found by fitting. For the use of this analysis, the following formula is adopted:

$$E\frac{d^3\sigma}{dp^3} = A(1-x_R)^{\alpha}(1+Bx_R)x_R^{-\beta}\{1 + a'(x_R)p_T\}e^{-a'(x_R)p_T}, \tag{E.5}$$

which can provide a better fit to the kaon data around 30 GeV than the original BMPT formula. The Eichten Be data is fitted to this formula. The obtained parameters are listed in Table E.2, and the fitting results are shown in Fig. E.3.

In Fig. E.4, the BMPT function fitted with the Eichten Be data is compared with the Allaby Be data to estimate the uncertainty of the BMPT parametrization at $x_R > 0.35$. For the Allaby data, the error for the individual data points is typically 3–5% including the statistical error, and the overall error is 16% (15% from their measurement and 5.3% from σ_{inel}). The difference between the Allaby data and the fitted BMPT function ranges −40–20% for K^+, and −11–19% ($\leq$ 12 GeV/c) and −81–66% (at 14 GeV) for K^-. The maximum difference between the data and BMPT and 16% of the Eichten overall error are assigned to the uncertainty of the $K^{\pm}$ multiplicity in the x_R-p_T region covered by the Allaby data.

In order to compare the fitted BMPT function with the Fitch Al data, this Al data has to be scaled to Be one and has to be corrected for the kaon absorption because they used a long target. Firstly, for the correction of the kaon absorption, the Fitch data ($d^2N/d\Omega dp$) is divided by $1 - R_{abs}(p)/2$ (= 0.86 for K^+ and 0.81–0.84 for K^-), where $R_{abs}(p)$ is the kaon absorption rate as a function of the kaon momentum p for the Al target calculated by using the $K^{\pm}$ total

[†]The BMPT parametrization was invented to simulate the CNGS neutrino beam [31, 32], whose proton beam energy is 400 GeV.

Table E.2: BMPT parameters obtained by the fitting of the Eichten Be data.

	A (mb/GeV^2)	B	α	β	a (GeV^{-1})	γ	χ^2/ndf
K^+	3.04	1.77	1.65	0.774	5.91	−0.399	54.9/62
K^-	6.20	2.64	5.16	0.203	5.08	−0.164	61.0/49

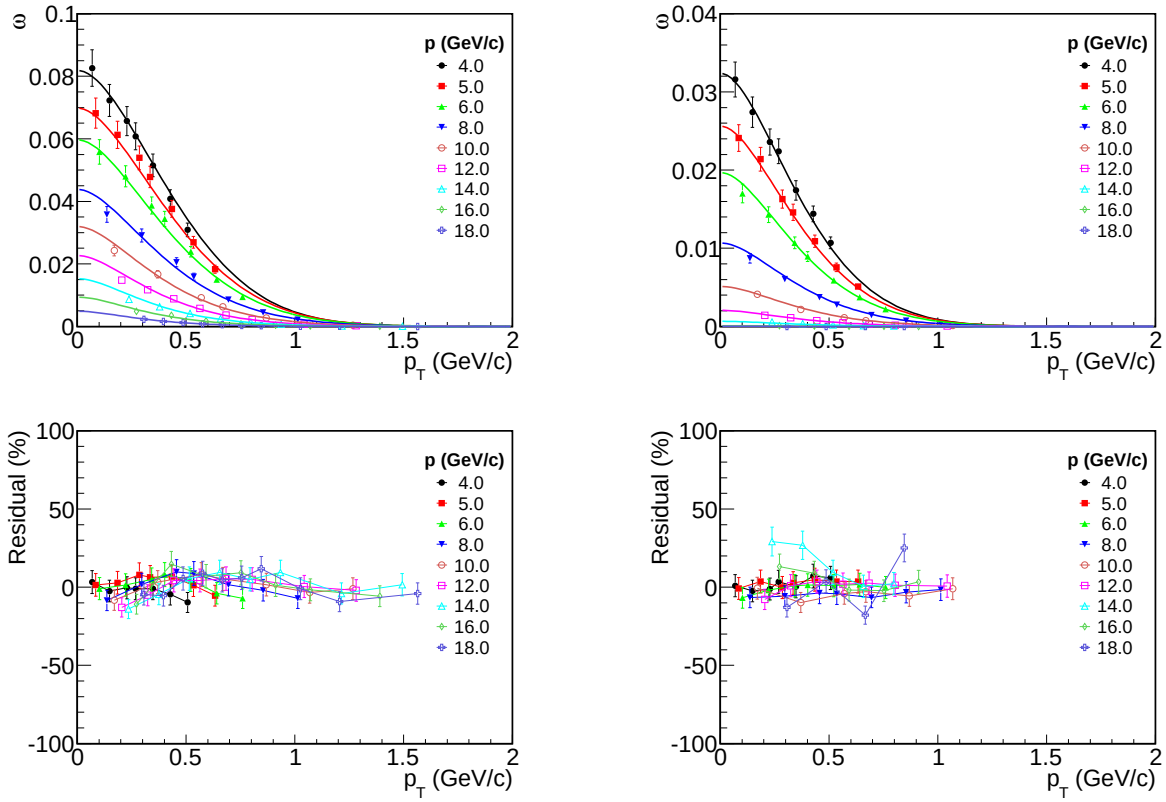

Figure E.3: Upper: ω of K^+ (left) and K^- (right) for Be as a function of p_T measured by T. Eichten *et al.* Data collected at the same kaon momenta p in the laboratory system are displayed with the same symbol. The fitted BMPT function is superimposed. Lower: Residual of the data from the fit for K^+ (left) and K^- (right).

absorption cross-section $\sigma_{abs}(p)$ on Al. This $\sigma_{abs}(p)$ on Al is obtained by scaling $\sigma_{abs}(p)$ on Be [215] and C [283] in accordance with $\sigma_{abs} = \sigma_0 A^\alpha$, where A is the atomic mass number and $\alpha = 0.80 \pm 0.01$ for K^+ and 0.76 ± 0.01 for K^- [283]. Secondary, the corrected Fitch data is scaled from Al to Be in the same way described below (Eq. E.6). In Fig. E.5, the BMPT function fitted with the Eichten Be data is compared with the corrected and A-scaled Fitch data. For the Fitch data, the error for the individual data points is 14–25% including the error of the absorption correction, and the overall error is 33% (25% from the number of circulating protons, 19% from the targeting efficiency and 10% from the A-scaling as explained later). The difference between the data and BMPT function is 1% for K^+ and −6–27% for K^-. For the K^+ multiplicity in the x_R-p_T region covered by the Fitch data, the same amount of uncertainty in the Allaby region

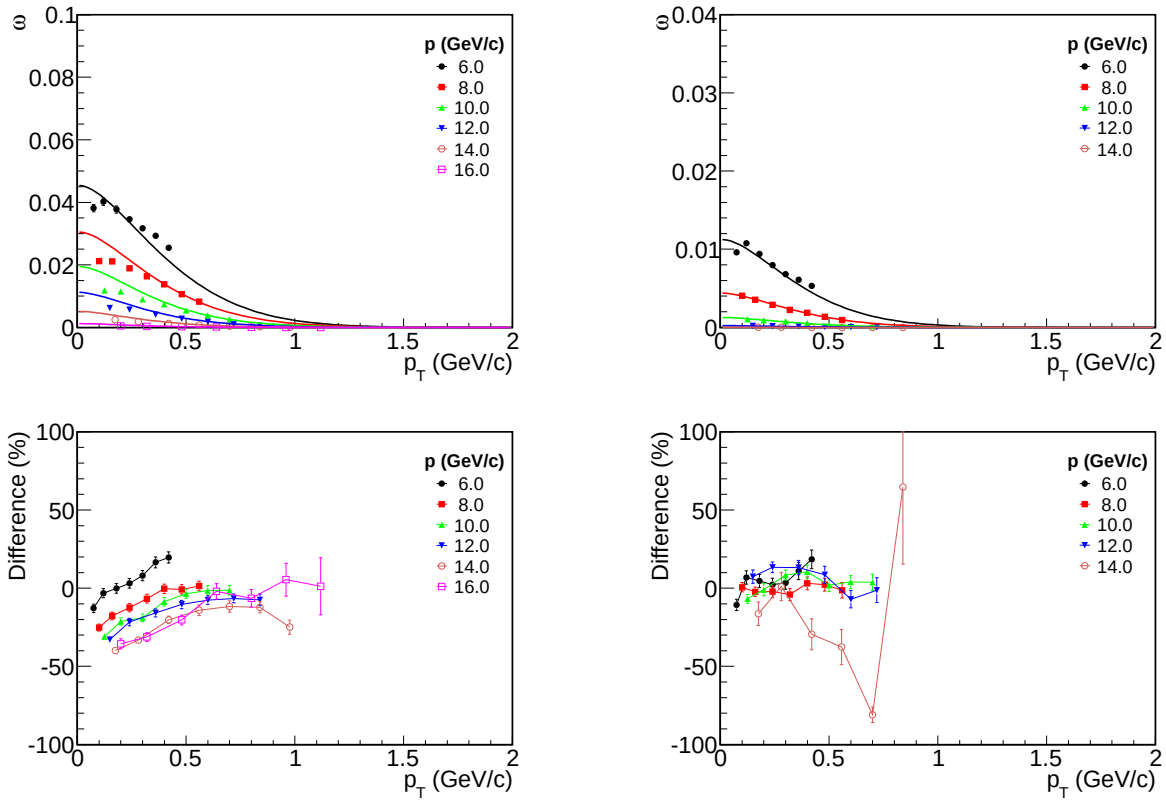

Figure E.4: Upper: ω of K^+ (left) and K^- (right) for Be as a function of p_T measured by J.V. Allaby *et al.* Data collected at the same kaon momenta p in the laboratory system are displayed with the same symbol. The BMPT function fitted with the Eichten Be data is superimposed. Lower: Residual of the data from the fitted BMPT function for K^+ (left) and K^- (right).

is conservatively assigned. For the K^- multiplicity, the 27% difference between the data and BMPT and 33% of the Fitch overall error are assigned to the uncertainty.

A-scaling

The kaon multiplicity for the graphite target is estimated by scaling the fitted BMPT function for the proton Be interactions utilizing the atomic mass number (A) dependence of inclusive hadron productions, which was studied by D.S. Barton *et al* [284]. They fitted experimental data at 24 GeV/c ($\pi^\pm$, $K^\pm$, p and $\bar{p}$ production by T. Eichten *et al.*), 300 GeV (Λ^0, $\bar{\Lambda}^0$ and K^0_S) [285] and 400 GeV (Ξ^0 and neutron) [286,287] in addition to their measurement at 100 GeV ($\pi^\pm$, $K^\pm$, p and $\bar{p}$) to the empirical form:

$$E\frac{d^3\sigma}{dp^3} = \sigma_0 A^\alpha, \tag{E.6}$$

where α is a function of Feynman x. By fitting α to a polynomial function, they obtained $\alpha(x_F^{cm}) = 0.74 - 0.55x_F^{cm} + 0.26x_F^{cm2}$.

When the Eichten Be data for $K^\pm$ is scaled to Al according to Eq. E.6 with their fit parameters, there is found a systematical discrepancy by approximately 10% between the A-scaled data and the Eichten Al data. Therefore, to obtain new parameters for α, the Eichten Be and Al data for $K^\pm$ are fitted to Eq. E.6. At this time, x_R is used instead of x_F^{cm} since the BMPT function, which is a function of x_R, has to be scaled from Be to C. The obtained parameters are listed in

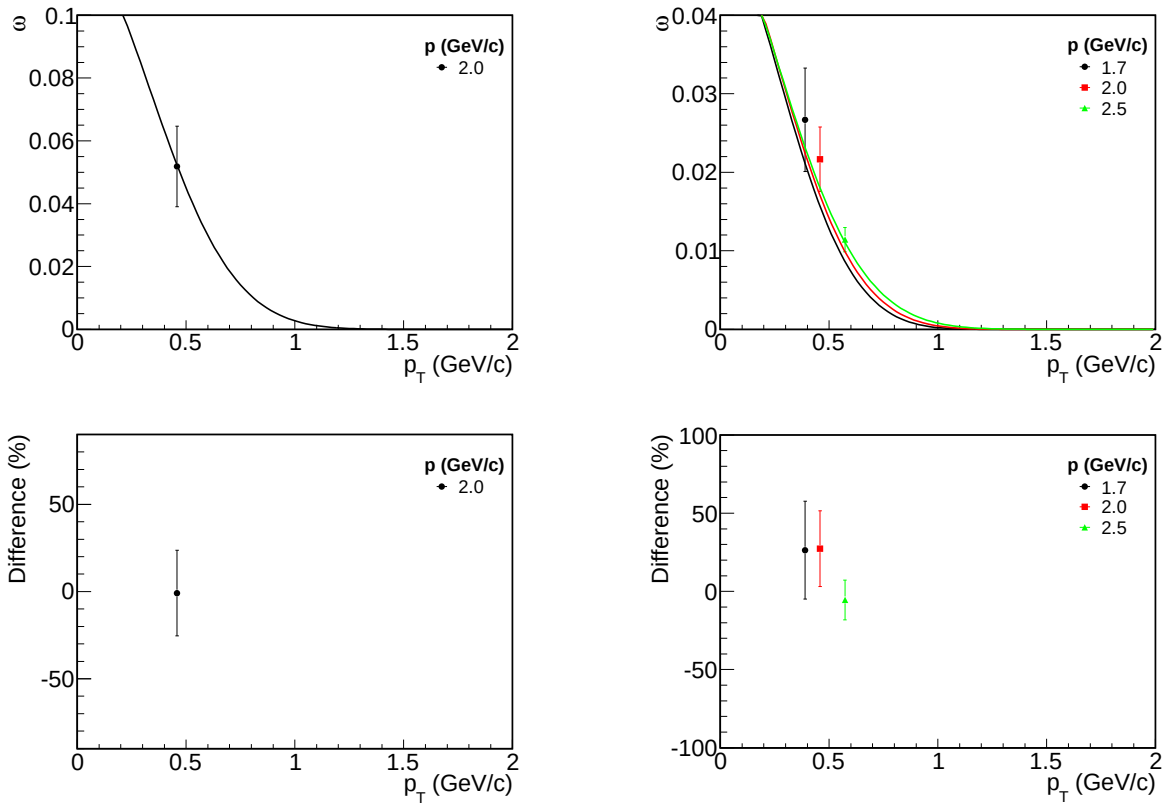

Figure E.5: Upper: ω of K^+ (left) and K^- (right) for Be as a function of p_T measured by V.L. Fitch *et al.* after the correction of the absorption and the A-scaling from Al to Be. Data collected at the same kaon momenta p in the laboratory system are displayed with the same symbol. The BMPT function fitted with the Eichten Be data is superimposed. Lower: Residual of the data from the fitted BMPT function for K^+ (left) and K^- (right).

Table E.3. They are found to be almost the same as those obtained with x_F^{cm}, and are consistent within the error with those by D.S. Barton *et al.* other than the constant term. That means the refitting does not change the p_T dependence, but eliminates the 10% discrepancy. The Eichten Be data is scaled to Al with those new parameters, and is compared with the Eichten Al data as shown in Fig E.6. The difference between the A-scaled data and the Eichten Al data is almost within 10%, independent of the kaon momentum p and p_T. Because the difference of ω between Be and C should be smaller than the difference between Be and Al, the error of the A-scaling from Be to C is expected to be less than 10%.

With the A-scaling, the fitted BMPT function is scaled from Be to C. The obtained ω distribution for $K^\pm$ is shown in Fig. E.7. The uncertainties of the $K^\pm$ multiplicities are summarized in Table E.4.

E.1.3 Reweighting of the secondary $K^\pm$ multiplicities

The ω distribution of the secondary $K^\pm$ in FLUKA (Fig. E.8) is calculated under the same condition as T2K other than the target thickness: interactions of 30 GeV protons and a 1 cm thick C target. It is normalized by $\sigma_{inel} = 231.3$ mb calculated in the simulation. The ω ratio of the A-scaled and fitted BMPT function to the FLUKA prediction is shown in Fig. E.9. The number of secondary $K^\pm$ in each x_R-p_T bin is reweighted with this ratio. The BMPT function covers all the phase space and every $K^\pm$ is reweighted.

Table E.3: Parameters for the A-scaling α obtained by the fitting of the Eichten Be and Al data with $\alpha(x_R) = a + bx_R + cx_R^2$. The best fit values by D.S. Barton *et al.* [284] are also listed for comparison.

	a	b	c	χ^2/ndf
K^+	0.855 ± 0.054	-0.37 ± 0.28	0.05 ± 0.40	52.5/62
K^-	0.852 ± 0.055	-0.77 ± 0.30	0.43 ± 0.32	28.8/49
Barton	0.74	-0.55	0.26	0.7

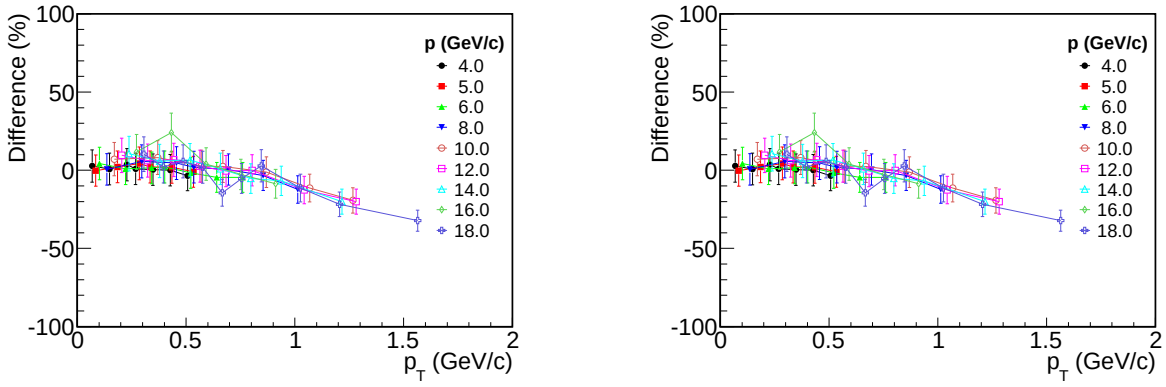

Figure E.6: Difference between the scaled ω from Be to Al and ω of Al for K^+ (left) and K^- (right) as a function of p_T. Data collected at the same kaon momenta p in the laboratory system are displayed with the same symbol. The Be and Al data measured by T. Eichten *et al.* are used.

Table E.4: Uncertainty of the $K^\pm$ multiplicity parameterized with the BMPT function using the Eichten Be data and scaled from Be to C. The uncertainty is evaluated in different x_R-p_T regions covered by the Allaby and Fitch data. For the K^+ multiplicity in the Fitch region, the same amount of uncertainty in the Allaby region is conservatively assigned.

	K^+		K^-		
	Fitch	Allaby	Fitch	Allaby region	
Source of the uncertainty	region	region	region	$p < 13$	$p > 13$ (GeV/c)
Data overall error	16%	16%	33%	16%	16%
BMPT-data difference	40%	40%	27%	19%	81%
A-scaling error	10%	10%	10%	10%	10%
Total	45%	45%	44%	27%	84%

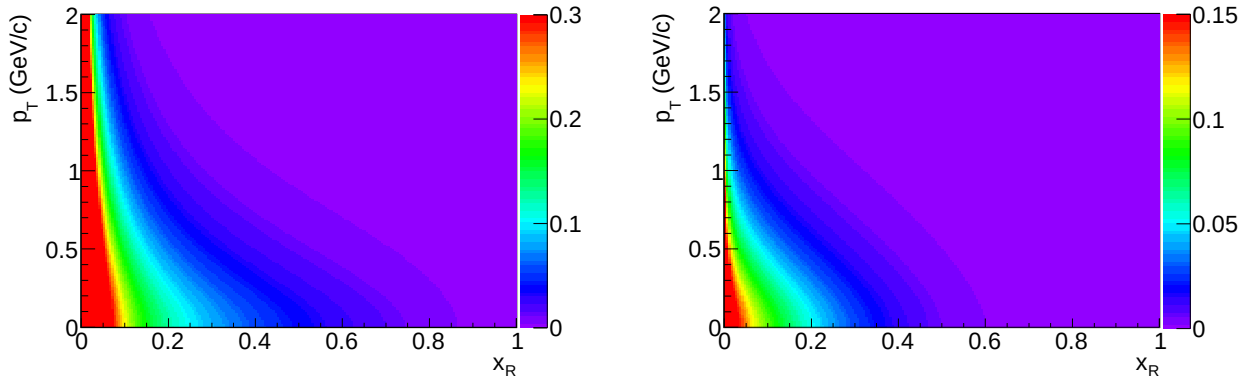

Figure E.7: $\omega(x_R, p_T)$ distribution of K^+ (left) and K^- (right) in proton and C interactions with the BMPT parametrization. The parametrization is done for the Eichten data (24 GeV/c proton and Be interactions).

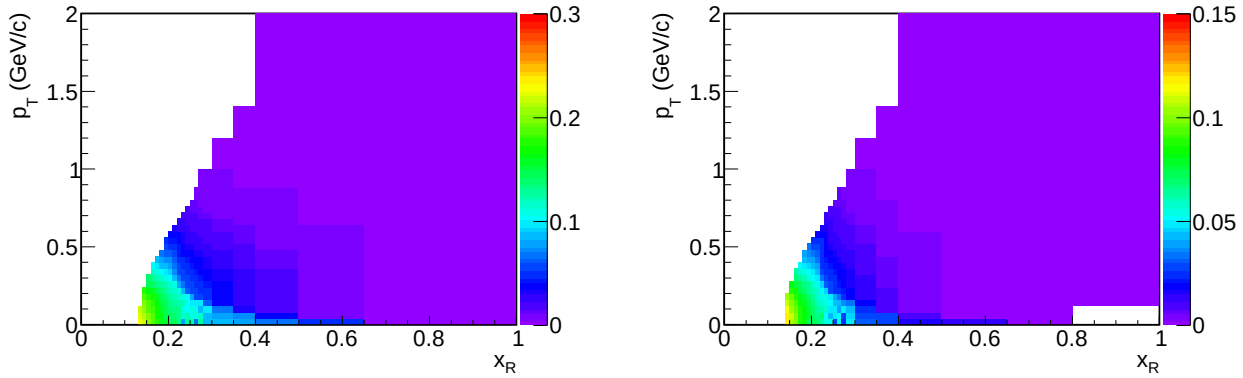

Figure E.8: $\omega(x_R, p_T)$ distribution of K^+ (left) and K^- (right) in proton and C interactions in FLUKA.

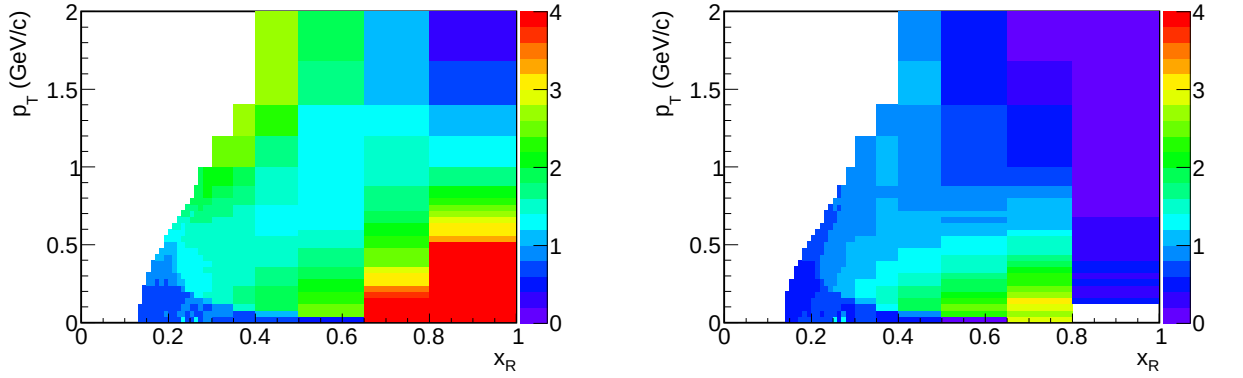

Figure E.9: $\omega(x_R, p_T)$ ratio of the A-scaled and fitted BMPT function to the FLUKA prediction for K^+ (left) and K^- (right).

E.1.4 Reweighting of the secondary K^0_L multiplicities

The K^0_L multiplicity is calculated according to Eq. 8.14 (the simple quark parton model; QPM). Figure E.10 shows the $\omega(x_R, p_T)$ distribution of K^0_L derived from the A-scaled and fitted BMPT functions for $K^{\pm}$. Figure E.11 shows one in FLUKA obtained in the same way as for $K^{\pm}$. The ω ratio of the QPM to FLUKA predictions is shown in Fig. E.12. By using this ratio, the number of secondary K^0_L, which distribute as shown in Fig. E.13, is reweighted in the same way as for $K^{\pm}$.

The uncertainty of the K^0_L multiplicity is also calculated according to Eq. 8.14 with the uncertainty of the $K^{\pm}$ multiplicities listed in Table E.4. In addition, the uncertainty of the QPM (15%, based on the comparison with a measurement [226]) is taken into account. The uncertainty of the K^0_L multiplicity is summarized in Table E.5.

E.1.5 Reweighting of the tertiary $K^{\pm}$ and K^0_L multiplicities

The tertiary $K^{\pm}$ and K^0_L multiplicities are also reweighted in the same way as described above. In JNUBEAM, x_R and p_T are calculated for each kaon, which is then reweighted by the data/FLUKA ratio shown in Fig. E.9 (for $K^{\pm}$) and Fig. E.12 (for K^0_L). At this time, the validity of the BMPT parametrization is not evaluated below the incident proton momentum of 19.2 GeV/c (the Allaby data). It is assumed that the fitted BMPT function can be applied for any secondary proton momenta shown in Fig. 8.9.

E.1.6 Effect of the kaon multiplicity tuning on the neutrino flux

As a result of the kaon multiplicity tuning described above, the neutrino flux changes by a factor shown in Fig. E.14. The tuning is significant for the neutrino flux of every flavor, at the high energies in particular (see Fig. 8.13 for comparison with the pion tuning).

E.2 Reevaluation of the systematic error of the neutrino flux from the hadron production uncertainty

The systematic error of the neutrino flux is reevaluated based on the uncertainty of the kaon multiplicities discussed in Appendix E.1 (listed in Table E.4 and E.5). It is estimated in the same way as described in Sec. 8.5. Figure E.15 shows the systematic error of the neutrino flux from the uncertainty of the secondary and tertiary kaon multiplicities. In this figure, the error for the pion multiplicities estimated in Sec. 8.5 is also plotted. Since the uncertainty of the Feynman scaling is added, the error for the kaon multiplicities becomes large compared to the one in Fig. 8.25.

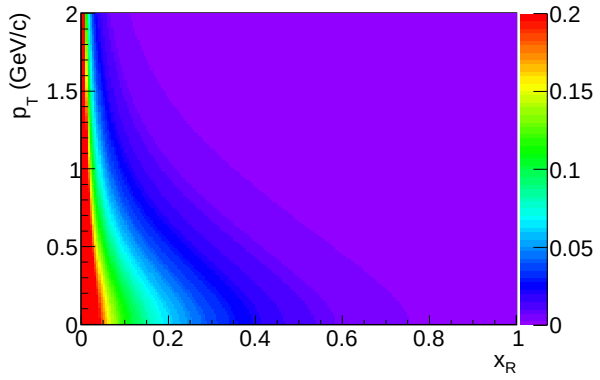

Figure E.10: $\omega(x_R, p_T)$ distribution of K^0_L from the simple QPM.

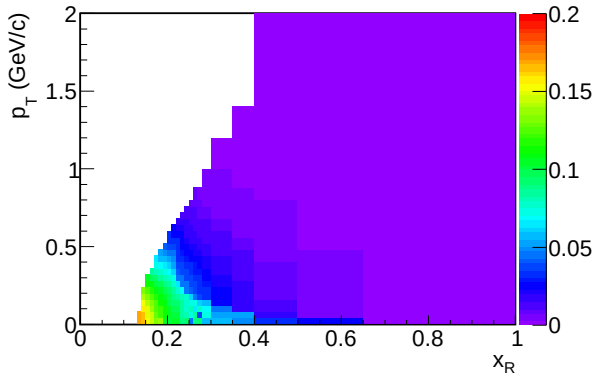

Figure E.11: $\omega(x_R, p_T)$ distribution of K^0_L in FLUKA.

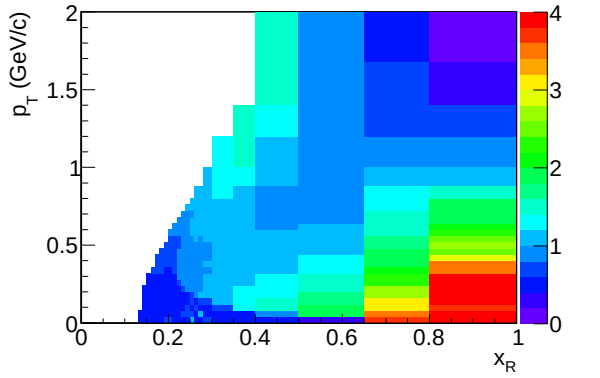

Figure E.12: $\omega(x_R, p_T)$ ratio of the QPM to FLUKA predictions for K^0_L.

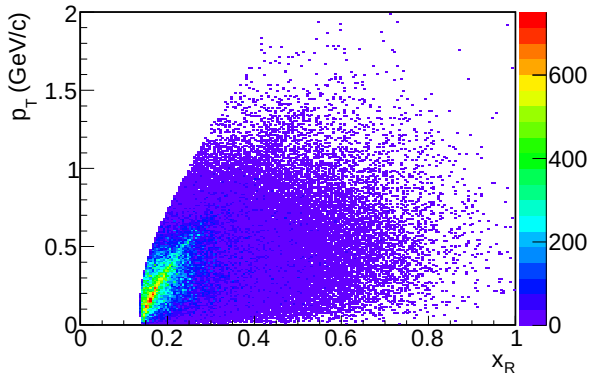

Figure E.13: x_R-p_T distribution of secondary K^0_L whose descendant neutrinos go to Super-K. It is estimated with the pre-tuned JNUBEAM.

Table E.5: Uncertainty of the K^0_L multiplicity estimated by using the QPM. The uncertainty is evaluated in different x_R-p_T regions covered by the Allaby and Fitch data.

	K^0_L		
	Fitch	Allaby region	
Source of the uncertainty	region	$p < 13$	$p > 13$ (GeV/c)
Uncertainty of the K^+ multiplicity	45%	45%	45%
Uncertainty of the K^- multiplicity	44%	27%	84%
Uncertainty of the QPM	15%	15%	15%
Total	38%	28%	66%

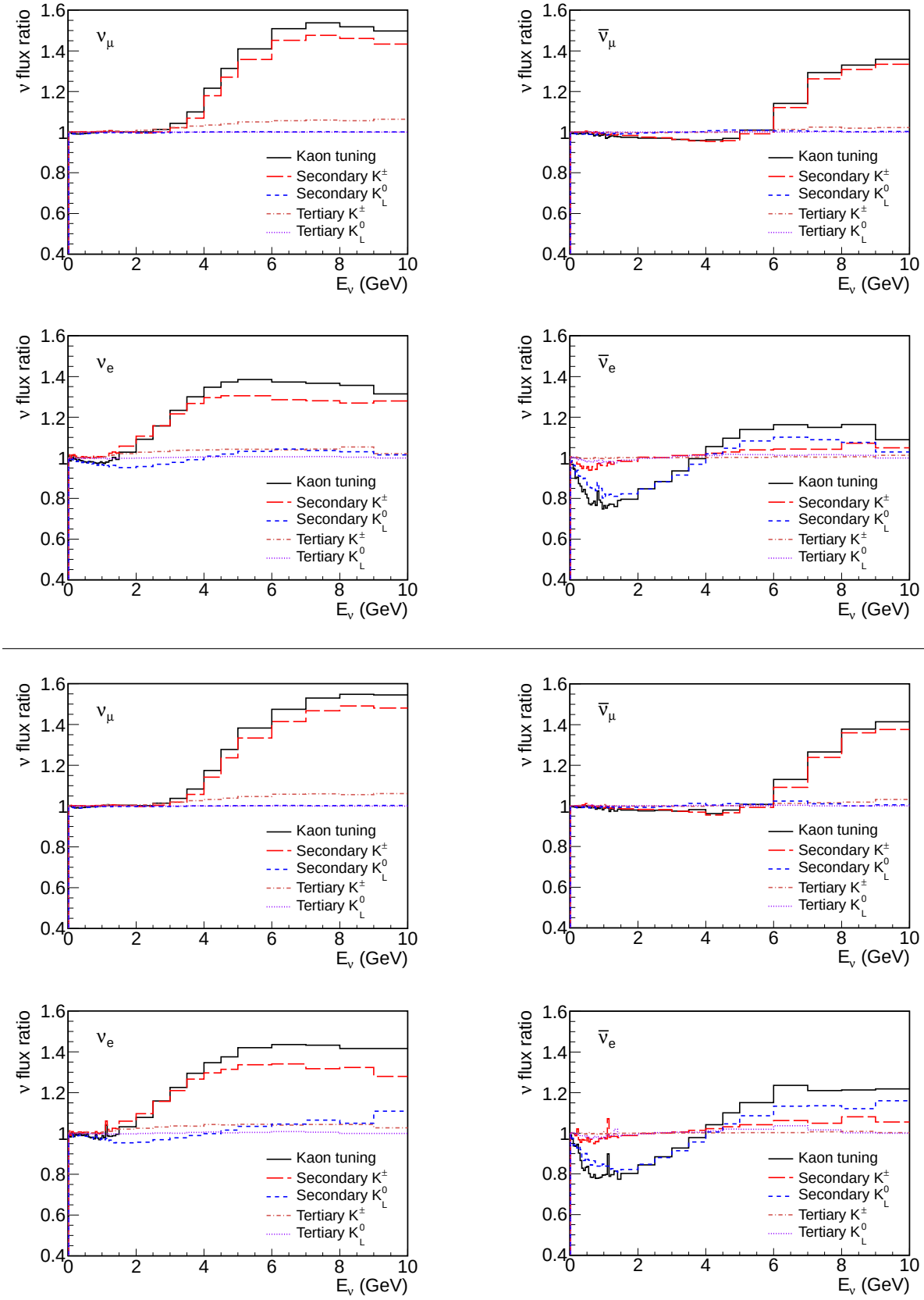

Figure E.14: Ratio of the neutrino flux of each flavor at Super-K (upper) and the ND280 off-axis detector (lower) before and after the tuning of the kaon multiplicities. The solid line represents the total flux change by tuning both the secondary and tertiary kaon multiplicities.

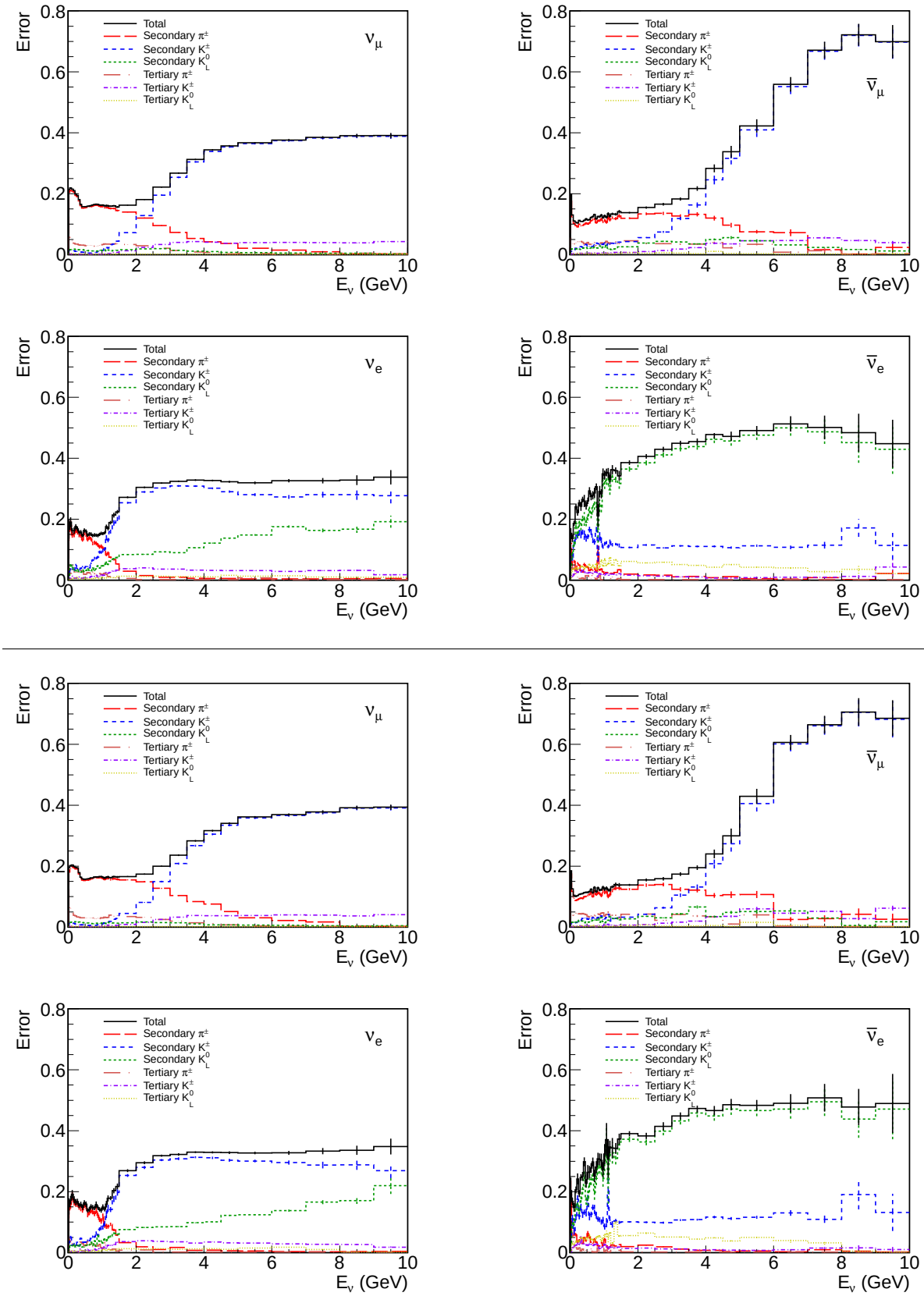

Figure E.15: Systematic error of the neutrino flux at Super-K (upper) and the ND280 off-axis detector (lower) from the uncertainty of the tuned $\pi^{\pm}$, $K^{\pm}$ and K^0_L multiplicities. This is a fractional error of the neutrino flux of each flavor. The error bar is the MC statistical error.

E.3 Simple quark parton model for the K^0_L production

The derivation of Eq. 8.14 from the simple quark parton model is given here. In this model, $n \equiv u_v/d_v = 2$, $u_s = \bar{u}_s = d_s = \bar{d}_s$ and $s_s = \bar{s}_s$ where q_v and q_s are the number densities of valence and sea quarks, respectively, inside a proton. Suppose that the relative numbers of K^+, K^-, K^0 and $\overline{K}^0$ produced in a proton-proton interaction are $N(K^+)$, $N(K^-)$, $N(K^0)$ and $N(\overline{K}^0)$, respectively. Because one sea s- or $\bar{s}$-quark is necessary to produce one K^+ ($u\bar{s}$), K^- ($\bar{u}s$), K^0 ($d\bar{s}$) or $\overline{K}^0$ ($\bar{d}s$) in this interaction (uud-uud), $N(K^+)$, $N(K^-)$, $N(K^0)$ and $N(\overline{K}^0)$ depend on the number of u-, $\bar{u}$-, d- and $\bar{d}$-quarks, respectively. Therefore,

$$N(K^+) \propto 2u_v + u_s, \tag{E.7}$$
$$N(K^-) \propto \bar{u}_s = u_s, \tag{E.8}$$
$$N(K^0) \propto d_v + d_s, \tag{E.9}$$
$$N(\overline{K}^0) \propto \bar{d}_s = d_s. \tag{E.10}$$

From Eq. E.7 and E.8,

$$d_v = \frac{u_v}{n} \propto \frac{N(K^+) - N(K^-)}{2n}, \tag{E.11}$$
$$d_s = u_s \propto N(K^-). \tag{E.12}$$

Thus, the relative numbers of K^0_L and K^0_S productions, or $N(K^0_L)$ and $N(K^0_S)$, are calculated as

$$\begin{aligned} N(K^0_L) = N(K^0_S) &= \frac{N(K^0_L) + N(K^0_S)}{2} = N(K^0) \\ &= \frac{N(K^+) - N(K^-)}{2n} + N(K^-) \\ &= \frac{N(K^+) + (2n-1)N(K^-)}{2n}. \end{aligned} \tag{E.13}$$

Appendix F

Systematic Error of the Neutrino Flux (Supplement)

This appendix describes the systematic errors of the neutrino flux $\Delta\phi/\phi$ which are omitted in Sec. 9.2 since they are negligibly small compared to the other systematic errors. The systematic error of the flux normalization $\delta f^{\phi}_{\mathrm{SK/ND}}$ due to $\Delta\phi/\phi$ described in this appendix is evaluated according to Eq. 9.7, 9.8 and 9.9. It is included in Table 9.5.

F.1 Uncertainties related to the neutrino beam operation

$\Delta\phi/\phi$ from the uncertainties of the proton beam parameters and horn currents

The systematic errors of the $\bar{\nu}_\mu$ and ν_e flux $\Delta\phi/\phi$ due to the uncertainties of the proton beam parameters and horn currents are shown in Fig. F.1 and F.2, respectively.

Effect of the magnetic field in the inner conductor

To evaluate the effect of the horn magnetic field in the inner conductor (B_{inner}), two MC samples with different B_{inner} models were generated with JNUBEAM: one without B_{inner} ($B_{inner} = 0$) and the other in the maximum B_{inner} case ($B_{inner} \propto 1/r$). These samples are compared to the nominal neutrino flux with B_{inner} according to Eq. 8.1. The variation from the nominal

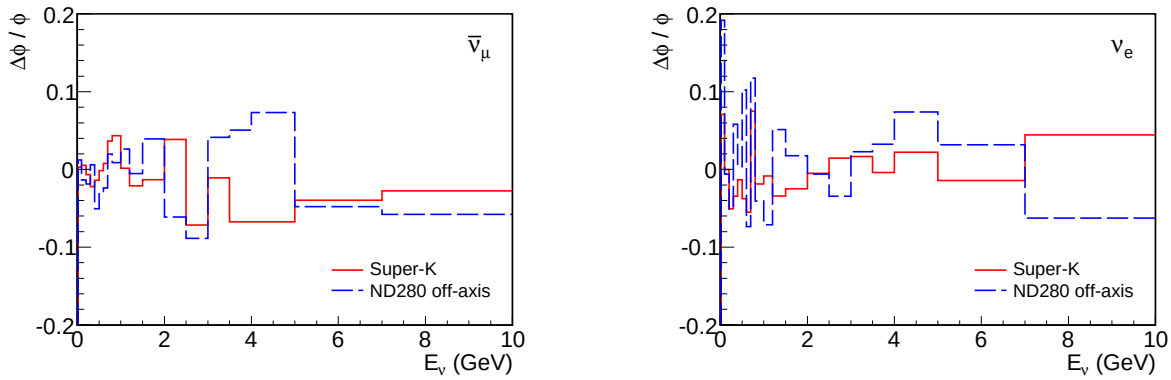

Figure F.1: Variation of the $\bar{\nu}_\mu$ (left) and ν_e (right) flux ϕ at Super-K and the ND280 off-axis detector due to the uncertainty of the proton beam parameters y_0 and $\mathrm{d}y/\mathrm{d}s$. This is a fractional variation of the neutrino flux of each flavor. For the ν_μ flux, see Fig. 9.4.

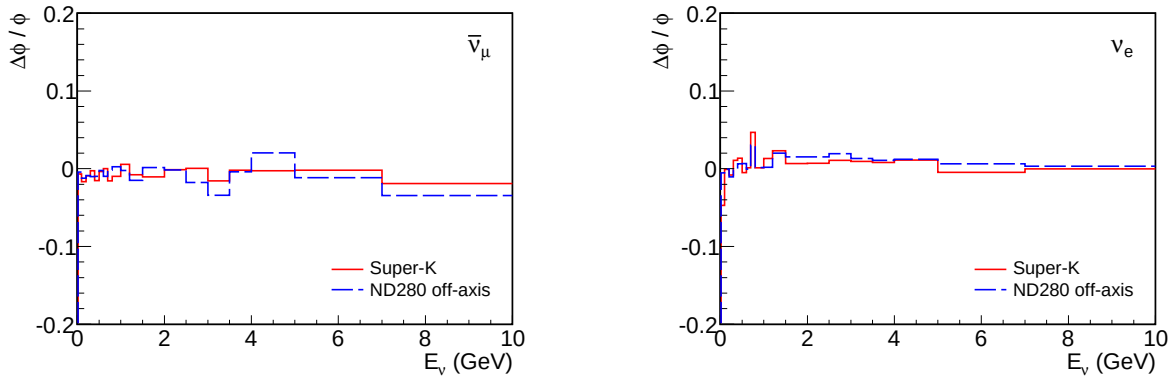

Figure F.2: Variation of the $\bar{\nu}_\mu$ (left) and ν_e (right) flux ϕ at Super-K and the ND280 off-axis detector due to the horn current uncertainty. This is a fractional variation of the neutrino flux of each flavor. For the ν_μ flux, see Fig. 9.5.

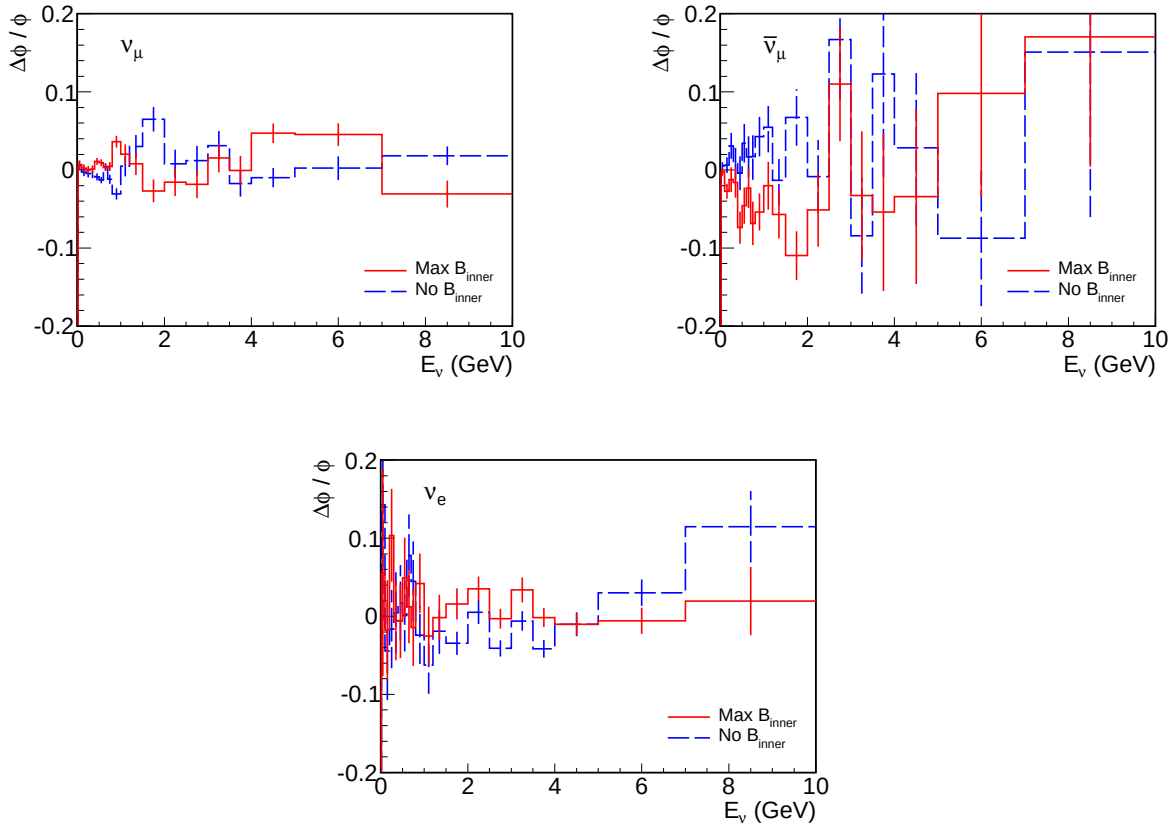

Figure F.3: Variation of the ν_μ (upper left), $\bar{\nu}_\mu$ (upper right) and ν_e (lower) flux ϕ at Super-K for the different models of the horn magnetic field in the inner conductor (B_{inner}): $B_{inner} \propto 1/r$ as "Max B_{inner}" and $B_{inner} = 0$ as "No B_{inner}". This is a fractional variation of the neutrino flux of each flavor. The error bar is the MC statistical error.

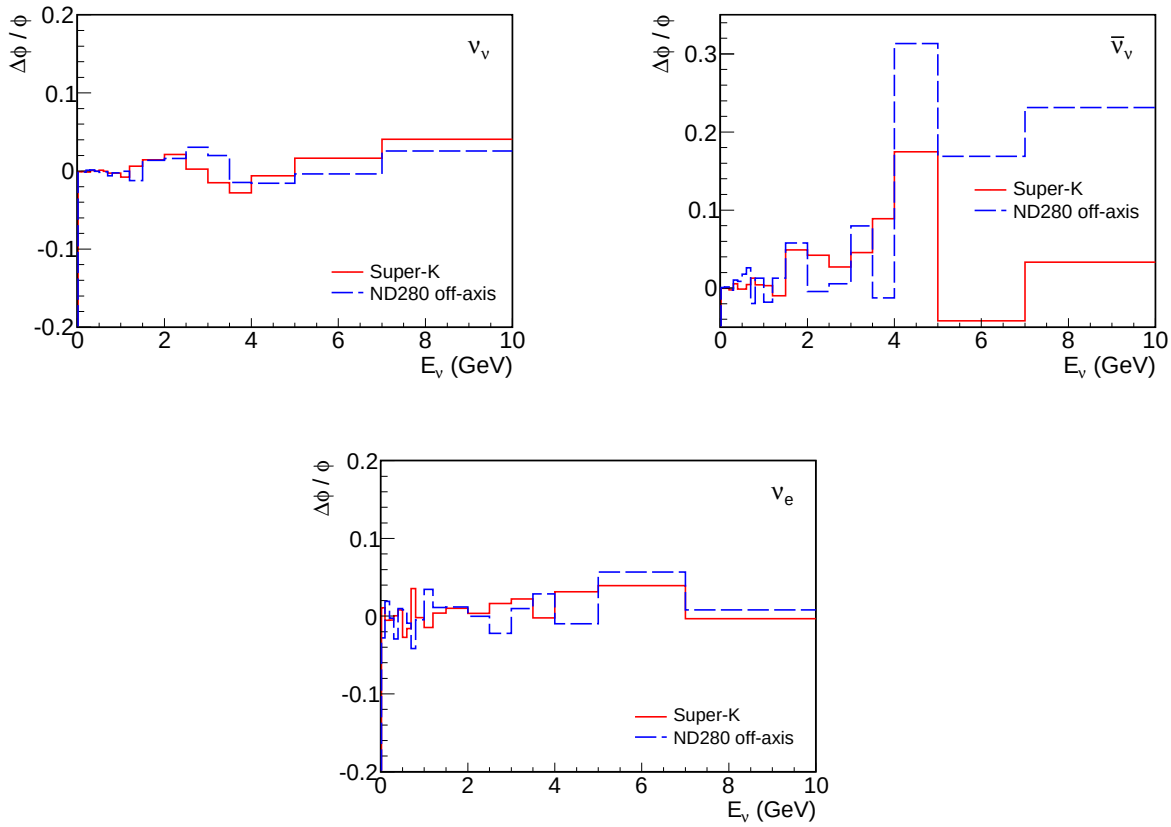

Figure F.4: Variation of the ν_μ (upper left), $\bar{\nu}_\mu$ (upper right) and ν_e (lower) flux ϕ at Super-K and the ND280 off-axis detector due to the target alignment. This is a fractional variation of the neutrino flux of each flavor.

flux is shown in Fig. F.3. These B_{inner} models are extreme examples, but the variation of the neutrino flux is less than 10%. (For high energy $\bar{\nu}_\mu$, the MC statistical error is too large to evaluate the variation.) Practically, the uncertainty of B_{inner} is considered to be much smaller than the difference between the extreme and nominal cases. Therefore, the effect of the B_{inner} uncertainty on the neutrino flux prediction is disregarded in this analysis.

F.2 Uncertainties related to the alignment

$\Delta\phi/\phi$ from the target misalignment

The target is aligned relative to the first horn inner conductor. It is fixed at the upstream part onto the upstream surface of the first horn with a precision of 0.1 mm. This alignment uncertainty can be disregarded in the neutrino flux prediction. Though the target head was fixed on the horn axis, the target end was found to be off the axis. The target is tilted by 1.3 mrad in horizontal and 0.1 mrad in vertical. This tilt of the target relative to the horn axis cannot be neglected.

To estimate the effect of this tilt on the neutrino flux prediction, a MC sample was generated with the tilted target. The neutrino flux variation of this sample from the nominal one, in which the target is perfectly aligned, is shown in Fig. F.4.

$\Delta\phi/\phi$ from the uncertainty of the horn alignment

The horns are well aligned with a precision of 0.3 mm in the horizontal and 1.0 mm both in the vertical and beam axis directions. The uncertainty of the first horn alignment is not evaluated here either, because it is included in the uncertainties of the proton beam center and angle measured by the OTR monitor; the OTR monitor is aligned relative to the first horn axis and the uncertainty of the first horn alignment correlates with those proton beam uncertainties. Therefore, only the effects of the alignment uncertainties for the second and third horns are evaluated.

After some tests with JNUBEAM in which all three horns were misaligned in a correlated way by the amount of the alignment uncertainty in a given direction, it was found that the misalignment in the vertical direction has the largest effect on the ν_μ flux prediction. The effect of the misalignment in the other directions is small and dominated by the MC statistical error. Therefore, only the alignment uncertainty in the vertical direction is considered below.

To estimate the neutrino flux uncertainty due to the horn alignment uncertainty, four MC samples were generated in which the second or third horn was moved by 5 or -5 mm in vertical. The 5 mm correspond to the 5σ of the alignment uncertainty. The generated neutrino flux is denoted as ϕ^+_{H2}, ϕ^-_{H2}, ϕ^+_{H3} or ϕ^-_{H3}. Then, the variation of the neutrino flux due to the 1σ uncertainty is estimated according to

$$\Delta\phi_i = \frac{1}{5}\left(\frac{\phi^+_{H2(i)} - \phi^-_{H2(i)}}{\phi^+_{H2(i)} + \phi^-_{H2(i)}} + \frac{\phi^+_{H3(i)} - \phi^-_{H3(i)}}{\phi^+_{H3(i)} + \phi^-_{H3(i)}}\right), \tag{F.1}$$

where ϕ_i stands for the flux in the ith neutrino energy bin. In a conservative manner, the second and third horn effects are linearly added assuming the full correlation between them. The resultant variation of the neutrino flux is shown in Fig. F.5.

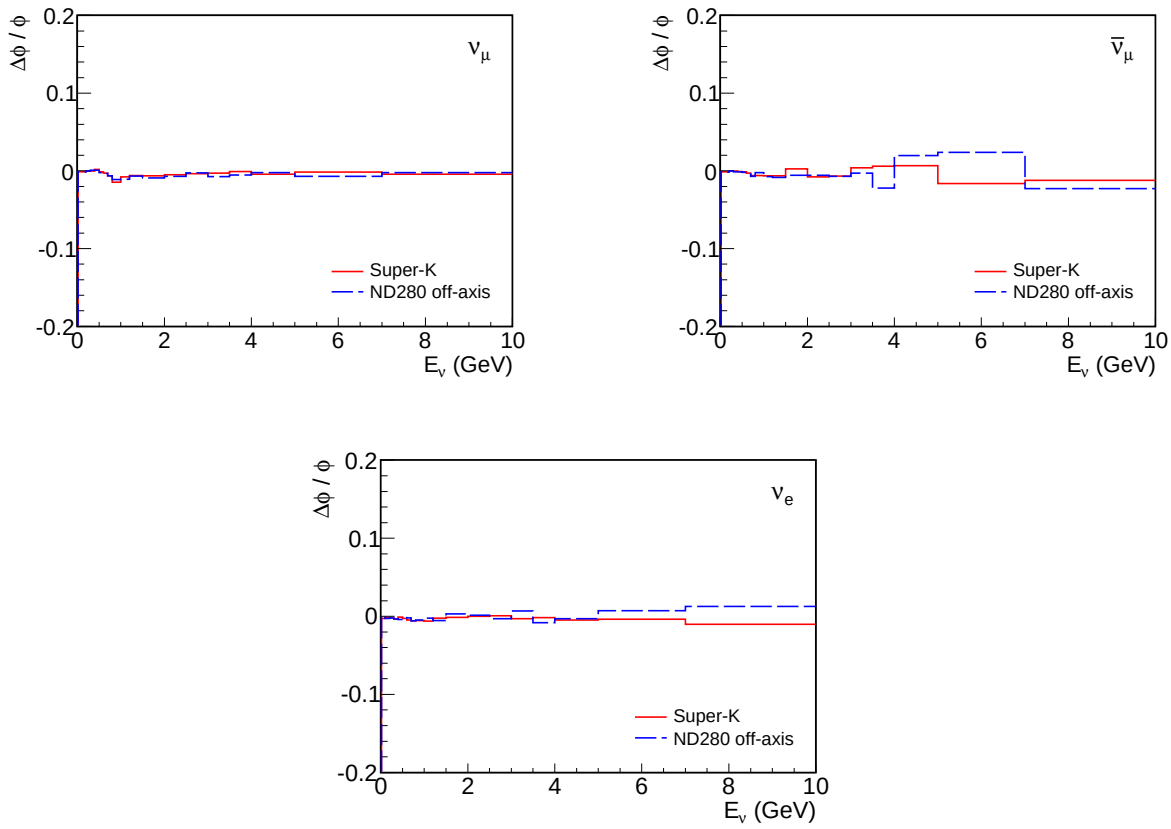

Figure F.5: Variation of the ν_μ (upper left), $\bar{\nu}_\mu$ (upper right) and ν_e (lower) flux ϕ at Super-K and the ND280 off-axis detector due to the alignment uncertainties of the second and third horns. This is a fractional variation of the neutrino flux of each flavor.

List of Tables

1.1 Sensitivity of different oscillation experiments to Δm^2. 10
1.2 The best-fit values of $\Delta m^2_{\odot}$ and $\tan^2\theta_{\odot}$ from two-flavor oscillation analyses. . . . 11
1.3 The best-fit values of $|\Delta m^2_{atm}|$ at $\sin^2 2\theta_{atm} = 1$ and the allowed regions from two-flavor oscillation analyses. 12
1.4 Upper limit of θ_{13}. 13

3.1 Design parameters of the LINAC, RCS and MR in J-PARC. 30
3.2 Design parameters of the fast extracted proton beam. 30
3.3 Systematic error on the horn magnetic field. 36

4.1 Characteristics of the muon beam at the muon monitor. 43

5.1 Estimated collected charge for the T2K muon beam. 52
5.2 Characteristics of the electron beam and the NuMI muon beam at the muon alcove 2. 53
5.3 Specification of the muon monitor detectors and their performances measured in the beam tests. 59

6.1 Dependence of the muon beam on the horn currents. 67
6.2 Result of the fitting to the correlation between the muon profile and proton beam centers. 70
6.3 Result of the fitting to the correlation between the muon profile width and the proton beam center. 72
6.4 Stability of the proton beam on the target surface during the physics run. 74
6.5 Parameters of the accumulated proton beam profile at the baffle and their systematic errors. 75
6.6 Stability of the horn currents during the physics run. 76
6.7 Stability of the muon beam during the physics run. 78
6.8 Alignment error of the muon monitor detectors relative to the target. 79
6.9 Density and thickness of the dump graphite core, Fe plates and concrete wall. . . 81
6.10 Summary of the systematic error of the muon monitor. 84

7.1 Summary of the physics run in the first half of 2010. 85
7.2 Number of spills after each good beam spill selection. 87
7.3 Number of spills after each good spill selection at Super-K. 89

8.1 Neutrino-producing decay modes considered in JNUBEAM. 95
8.2 Proportion of particles which are parents of neutrinos at Super-K. 96
8.3 Proportion of secondary particles which contribute to neutrinos at Super-K. . . . 99
8.4 Proportion of tertiary particles which are produced by the secondary protons and contribute to neutrinos at Super-K. 99

8.5 Proportion of secondary particles which contribute to neutrinos at Super-K after undergoing reinteractions (secondary interactions). 99
8.6 Summary of the hadron production tuning. 102
8.7 Cross-section data used for the tuning of the interaction rate. 105
8.8 Summary of the hadron production uncertainty and the systematic error of the ν_μ flux. 116

9.1 Expected number of neutrino events at the ND280 off-axis detector. 118
9.2 Expected number of FCFV events at Super-K and ν_μ events for the ν_μ disappearance analysis with 3.23×10^{19} protons with null oscillation. 120
9.3 Expected number of FCFV events at Super-K and ν_μ events for the ν_μ disappearance analysis with 3.23×10^{19} protons with oscillation. 120
9.4 Expected number of ν_e appearance events at Super-K with 3.23×10^{19} protons. . 121
9.5 Systematic error of the flux normalization. 122
9.6 List of the systematic parameters and the systematic error of the expected number of ν_μ events for the ν_μ disappearance analysis. 128
9.7 List of the systematic parameters and the systematic error of the expected number of ν_e background events. 129

10.1 The number of on-timing FC and FCFV events observed at Super-K with the 3.23×10^{19} protons. 131
10.2 The number of ν_μ events for the ν_μ disappearance analysis with the 3.23×10^{19} protons. 133
10.3 Event summary of the T2K ν_e appearance search with the 3.23×10^{19} protons. . 133
10.4 Reconstructed information on the single-ring e-like events. 134

C.1 Systematic errors and shot-by-shot fluctuations of the proton monitors. 147
C.2 Proton beam profile measured by the SSEM. 147

D.1 Profile center and width of the neutrino beam measured by INGRID during each physics run. 153
D.2 Mean neutrino beam direction measured by INGRID during the physics run. . . 153

E.1 $K^\pm$ production data around 30 GeV. 157
E.2 BMPT parameters obtained by the fitting of the Eichten Be data. 159
E.3 Parameters for the A-scaling obtained by the fitting of the Eichten Be and Al data. 162
E.4 Uncertainty of the $K^\pm$ multiplicity parameterized with the BMPT function using the Eichten Be data and scaled from Be to C. 162
E.5 Uncertainty of the K^0_L multiplicity estimated by using the QPM. 165

List of Figures

1.1 Regions of the neutrino squared-mass difference and mixing angle favored or excluded by various experiments. . . . 10
1.2 Contours of the solar neutrino oscillation parameters. . . . 11
1.3 Contours of the atmospheric neutrino oscillation parameters. . . . 12
1.4 Ranges of $\sin^2\theta_{13}$ preferred by different data sets and combinations. . . . 13
1.5 Two possible types of the neutrino mass spectrum. . . . 15
1.6 Relation between $P(\nu_\mu \to \nu_e)$ measured in long-baseline accelerator experiments and $\sin^2 2\theta_{13}$ directory measured by reactor experiments. . . . 16

2.1 Overview of the T2K experiment. . . . 17
2.2 T2K sensitivity to θ_{13} as a function of $|\Delta m^2_{32}|$. . . . 18
2.3 Neutrino energy spectrum at Super-K estimated with a Monte Carlo simulation. 19
2.4 Neutrino oscillation probability as a function of the neutrino energy. . . . 19
2.5 Expected number of ν_e events as a function of the reconstructed neutrino energy. 21
2.6 Expected energy spectrum of ν_μ CCQE events at Super-K. . . . 21
2.7 Features of T2K. . . . 22
2.8 Illustration of an example of the pion decay chain producing a muon neutrino. . 23
2.9 Neutrino energy as a function of the pion momentum when the neutrino is produced in a certain direction. . . . 24
2.10 ν_μ energy spectra at Super-K in the off- and on-axis beam configurations. . . . 24
2.11 T2K sensitivity to θ_{13} as a function of the integrated beam power. . . . 25

3.1 Bird eye's view of the J-PARC site. . . . 29
3.2 Injection scheme from the RCS to the MR. . . . 29
3.3 Overview of the T2K neutrino beamline. . . . 31
3.4 Photographs of the primary beamline monitors. . . . 32
3.5 Location of the primary beamline monitors. . . . 32
3.6 Side view of the secondary beamline. . . . 34
3.7 Photograph of the OTR monitor carousel. . . . 35
3.8 Cross section view of the target. . . . 35
3.9 Cross section view of the first horn. . . . 35
3.10 ND280 detectors. . . . 38
3.11 Exploded view of the ND280 off-axis detector. . . . 38
3.12 INGRID detector. . . . 39
3.13 Schematic overview of Super-K. . . . 41
3.14 Illustration of the T2K beam data acquisition at Super-K. . . . 41

4.1 Profile of charged particles at the muon monitor in JNUBEAM. . . . 43
4.2 Momentum distribution of muons at the muon monitor. . . . 43

4.3 p-θ distribution of secondary pions whose descendant muons reach the muon monitor. . . . 43
4.4 Schematic view of the muon monitor. . . . 45
4.5 Photograph of the silicon PIN photodiodes and the ionization chambers in the support enclosure. . . . 46
4.6 Drawing of the bottom end of the ionization chamber. . . . 47
4.7 Drawing of a sensor of the ionization chamber. . . . 47
4.8 Diagram of the gas system for the ionization chambers. . . . 49
4.9 Moving stage for the silicon PIN photodiode and for the ionization chamber. . . . 50

5.1 Pulse shapes of the ionization chamber with the Ar-N_2 and with the He-N_2 mixtures. 54
5.2 Pulse shapes of the silicon PIN photodiode. . . . 54
5.3 Collected charge as a function of the applied voltage for the ionization chamber with the Ar-N_2 and with the He-N_2 mixtures. . . . 55
5.4 Collected charge versus the beam intensity for the ionization chamber with the Ar-N_2 and with He-N_2 mixtures at several applied voltages. . . . 56
5.5 Collected charge versus the beam intensity for the silicon PIN photodiode. . . . 56
5.6 Stability of the signal of the miniature ionization chamber with the pure He gas and the silicon PIN photodiodes measured in the NuMI beamline. . . . 58
5.7 Collected charge versus the proton beam intensity for the miniature ionization chamber with the pure He gas and the silicon PIN photodiode measured in the NuMI beamline. . . . 58
5.8 Typical waveform of the signal from the ionization chamber and silicon PIN photodiode. . . . 61
5.9 Charge distributions of the chamber and silicon arrays. . . . 61
5.10 Total charge of the chamber and silicon arrays as a function of the proton beam intensity. . . . 62
5.11 Intrinsic resolution for the total charge measurement as a function of the proton beam intensity. . . . 63
5.12 Intrinsic resolution for the profile center measurement as a function of the proton beam intensity. . . . 63

6.1 First neutrino beam signal taken by the muon monitor. . . . 64
6.2 Projection distributions of the silicon array for different horn currents. . . . 66
6.3 Total charge of the silicon array as a function of the first horn current and the second and third horn current. . . . 66
6.4 Total charge of the silicon array as a function of the all horn currents. . . . 66
6.5 Total charge of the silicon array as a function of the first horn current around 250 kA. . . . 66
6.6 Total charge of the silicon array as a function of the second and third horn current around 250 kA. . . . 66
6.7 Muon profile width (σ_x) as a function of the first horn current and the second and third horn current. . . . 67
6.8 Muon profile width (σ_x) as a function of the horn current. . . . 67
6.9 Variation of the muon profile width as a function of the first horn current around 250 kA. . . . 67
6.10 Variation of the muon profile width as a function of the second and third horn current around 250 kA. . . . 67
6.11 Projection distributions of the silicon array for shifted beams. . . . 69
6.12 Correlation between the muon profile and proton beam centers in the horizontal direction with the horn focusing. . . . 70

6.13 Correlation between the muon profile and proton beam centers with different proton beam angles. . . . 70
6.14 Correlation between the muon profile and proton beam centers in the vertical direction with the horn focusing. . . . 70
6.15 Correlation between the muon profile and proton beam centers in the horizontal direction without the horn focusing. . . . 70
6.16 Correlation between the muon yield and the proton beam center. . . . 71
6.17 Correlation between the muon profile width and the proton beam center. . . . 72
6.18 Proton beam center at the target during the physics run. . . . 73
6.19 Proton beam angle at the target during the physics run. . . . 73
6.20 Proton beam width at the target during the physics run. . . . 73
6.21 Accumulated proton beam profile at the baffle over the physics run. . . . 75
6.22 Horn currents during the physics run. . . . 76
6.23 Muon profile center during the physics run. . . . 76
6.24 Muon yield during the physics run. . . . 77
6.25 Muon profile width during the physics run. . . . 78
6.26 Variation of the muon profile center measured by the chamber array at different positions. . . . 80
6.27 Top view of the beam dump. . . . 81
6.28 Muon profile at the silicon array when the beam dump Fe is thicker by ±1 cm. . . . 81
6.29 Shift of the muon profile center as a function of the effective thickness of the dump. 81
6.30 Illustration of muon paths to the muon monitor across the beam dump. . . . 82
6.31 Variation of the muon profile center measured by the chamber array during the calibration of the silicon PIN photodiode. . . . 83

7.1 Number of protons delivered to the neutrino beamline during the physics run. . . 86
7.2 Daily number of neutrino events measured by INGRID. . . . 87
7.3 History of the accumulated number of protons for the good beam spills with the Super-K good spill selections. . . . 89

8.1 Geometrical setup in the FLUKA simulation. . . . 94
8.2 Geometrical setup in JNUBEAM. . . . 94
8.3 Contribution of each parent particle to the neutrino flux at Super-K. . . . 96
8.4 Contribution of each secondary particle to the neutrino flux at Super-K. . . . 97
8.5 p-θ distribution of secondary pions and kaons whose descendant neutrinos go to Super-K. . . . 98
8.6 $\mathrm{d}n/\mathrm{d}p(p)$ distribution of π^+ in different θ angle intervals in 30 GeV proton and C interactions measured by NA61. . . . 100
8.7 $\mathrm{d}n/\mathrm{d}p(p)$ distribution of π^- in different θ angle intervals in 30 GeV proton and C interactions measured by NA61. . . . 101
8.8 $\mathrm{d}n/\mathrm{d}p(p,\theta)$ ratio of NA61 to FLUKA for $\pi^\pm$. . . . 103
8.9 Momentum distribution of the secondary protons whose descendant neutrinos go to Super-K. . . . 103
8.10 x_F^{cm}-p_T distribution of tertiary $\pi^\pm$ whose descendant neutrinos go to Super-K. . . . 105
8.11 $\mathrm{d}n/\mathrm{d}p$ ratio of NA61 to FLUKA in x_F^{cm}-p_T for $\pi^\pm$. . . . 105
8.12 Production cross-sections of proton, $\pi^\pm$ and $\mathrm{K}^\pm$ interactions with carbon and aluminum. . . . 106
8.13 Ratio of the neutrino flux before and after the tuning of the pion multiplicities. . . . 107
8.14 Ratio of the neutrino flux before and after the tuning of the production cross-sections. . . . 108

8.15 Total change of the neutrino flux at Super-K and the ND280 off-axis detector by the all hadron production tunings. . . . 108
8.16 Neutrino flux estimated by the tuned JNUBEAM. . . . 109
8.17 $\omega(p,\theta)$ distribution of $K^{\pm}$ in 24 GeV/c proton and Be interactions measured by T. Eichten *et al.* . . . 111
8.18 $\omega(p,\theta)$ distribution of $K^{\pm}$ in 24 GeV/c proton and Be interactions in FLUKA. . . 111
8.19 $\omega(x_F,p_T)$ ratio of the Eichten data to FLUKA for $K^{\pm}$. . . . 112
8.20 x_F^{cm}-p_T distribution of $K^{\pm}$ whose descendant neutrinos go to Super-K. . . . 112
8.21 $\omega(p,\theta)$ distribution of K^0_L from the simple QPM. . . . 113
8.22 $\omega(p,\theta)$ distribution of K^0_L in FLUKA. . . . 113
8.23 $\omega(x_F,p_T)$ ratio of the QPM to FLUKA for K^0_L. . . . 113
8.24 x_F^{cm}-p_T distribution of K^0_L whose descendant neutrinos go to Super-K. . . . 113
8.25 Systematic error of the neutrino flux from the uncertainty of the hadron multiplicities. . . . 115
8.26 Variation of the neutrino flux due to the production cross-section uncertainty. . . 116

9.1 Stacked histogram of the expected neutrino events at the ND280 off-axis detector as a function of the true neutrino energy. . . . 118
9.2 Stacked histogram of the expected ν_μ events for the ν_μ disappearance analysis at Super-K as a function of the reconstructed neutrino energy. . . . 120
9.3 Stacked histogram of the expected ν_e appearance events at Super-K as a function of the reconstructed neutrino energy. . . . 121
9.4 Variation of the ν_μ flux due to the uncertainty of the proton beam parameters. . 124
9.5 Variation of the ν_μ flux due to the horn current uncertainty. . . . 124
9.6 Neutrino beam direction measured by the muon monitor and INGRID. . . . 125
9.7 Schematic view of the beamline axis and the Super-K direction. . . . 125
9.8 Variation of the neutrino flux due to the uncertainty of the neutrino beam direction. 126

10.1 Super-K event display showing the first T2K neutrino event. . . . 131
10.2 Stacked histogram of ΔT_0 for all the Super-K neutrino events in the T2K 1 msec beam-time window. . . . 132
10.3 Distribution of ΔT_0 for all the FC events. . . . 132
10.4 Super-K event display of the single-ring μ-like event. . . . 133
10.5 Super-K event display of the multi-ring μ-like event. . . . 133
10.6 Super-K event display of the rejected single-ring e-like event. . . . 134
10.7 Super-K event display of the T2K first candidate of the ν_e appearance signal. . . 134

A.1 Neutrino energy spectrum at the near detector estimated with a Monte Carlo simulation. . . . 139
A.2 Far-near ratio of the ν_μ flux. . . . 139
A.3 Illustration of the near and far detectors showing their acceptance difference from a viewpoint of the J-PARC site. . . . 139

B.1 Neutrino-nucleus cross-sections per nucleon divided by the neutrino energy in NEUT. . . . 141
B.2 Total cross-section of the ν_μ CCQE interaction as a function of the neutrino energy. 141
B.3 Cross-sections of the coherent pion production off a carbon nucleus. . . . 143

C.1 Stability of the GPS system at the J-PARC site during the physics run. . . . 146
C.2 Proton beam profile measured by the OTR monitor. . . . 149
C.3 Beam loss in the primary beamline at the 50 kW operation. . . . 149

D.1 A typical neutrino event in an INGRID module. 150
D.2 Profile of the neutrino events measured by INGRID. 152
D.3 INGRID profile center during the physics run. 153
D.4 Event display of the ND280 off-axis detector showing the first neutrino event candidate with the magnet on at 0.188 T. 154
D.5 Distribution of the neutrino energy (calculated under the CCQE assumption) for the selected events in the ND280 tracker. 155

E.1 $K^{\pm}$ production data around 30 GeV plotted in x_R-p_T. 157
E.2 x_R-p_T distribution of $K^{\pm}$ whose descendant neutrinos go to Super-K. 157
E.3 ω of $K^{\pm}$ for Be as a function of p_T measured by T. Eichten *et al.* 159
E.4 ω of $K^{\pm}$ for Be as a function of p_T measured by J.V. Allaby *et al.* 160
E.5 ω of $K^{\pm}$ for Be as a function of p_T measured by V.L. Fitch *et al.* after the correction of the absorption and the A-scaling. 161
E.6 Difference of the scaled ω from Be to Al and one of Al for $K^{\pm}$ as a function of p_T. 162
E.7 $\omega(x_R, p_T)$ distribution of $K^{\pm}$ in proton and C interactions with the BMPT parametrization. 163
E.8 $\omega(x_R, p_T)$ distribution of $K^{\pm}$ in proton and C interactions in FLUKA. 163
E.9 $\omega(x_R, p_T)$ ratio of the A-scaled and fitted BMPT function to the FLUKA prediction for $K^{\pm}$. 163
E.10 $\omega(x_R, p_T)$ distribution of K^0_L from the simple QPM. 165
E.11 $\omega(x_R, p_T)$ distribution of K^0_L in FLUKA. 165
E.12 $\omega(x_R, p_T)$ ratio of the QPM to FLUKA predictions for K^0_L. 165
E.13 x_R-p_T distribution of K^0_L whose descendant neutrinos go to Super-K. 165
E.14 Ratio of the neutrino flux of each flavor before and after the tuning of the kaon multiplicities. 166
E.15 Systematic error of the neutrino flux from the uncertainty of the tuned $\pi^{\pm}$, $K^{\pm}$ and K^0_L multiplicities. 167

F.1 Variation of the $\bar{\nu}_\mu$ and ν_e flux due to the uncertainty of the proton beam parameters. 169
F.2 Variation of the $\bar{\nu}_\mu$ and ν_e flux due to the horn current uncertainty. 170
F.3 Variation of the neutrino flux for the different models of the horn magnetic field in the inner conductor. 170
F.4 Variation of the neutrino flux due to the target alignment. 171
F.5 Variation of the neutrino flux due to the alignment uncertainty of the second and third horns. 173

Bibliography

[1] W. Pauli, Letter to L. Meitner and her colleagues dated 4 December 1930 (letter open to the participants of the conference in Tübingen) (1930), recorded in W. Pauli, *Wissenschaftlicher Briefwechsel mit Bohr, Einstein, Heisenberg u.a.*, Band II (Springer, Berlin, 1985) p. 39.

[2] C.L. Cowan, Jr., F. Reines, F.B. Harrison, H.W. Kruse, and A.D. McGuire, Science **124**, 103 (1956).

[3] G. Danby et al., Phys. Rev. Lett. **9**, 36 (1962).

[4] The ALEPH Collaboration, the DELPHI Collaboration, the L3 Collaboration, the OPAL Collaboration, the SLD Collaboration, the LEP Electroweak Working Group and the SLD Electroweak and Heavy Flavour Groups, Phys. Rept. **427**, 257 (2006).

[5] K. Kodama et al. (DONUT Collaboration), Phys. Lett. B **504**, 218 (2001).

[6] C.F. von Weizsäcker, Physikalische Zeitschrift **39**, 633 (1938).

[7] H.A. Bethe, Phys. Rev. **55**, 434 (1939).

[8] R. Davis, Jr., D.S. Harmer, and K.C. Hoffman, Phys. Rev. Lett. **20**, 1205 (1968).

[9] B. Pontecorvo, Chalk River Lab. report PD-205, 1946.

[10] J.N. Bahcall, W.A. Fowler, I. Iben, Jr., and R.L. Sears, Astrophys. J. **137**, 344 (1963).

[11] R.L. Sears, Astrophys. J. **140**, 477 (1964).

[12] H. R. P. Pochoda, Planet. Space Sci. **12**, 119 (1964).

[13] K.S. Hirata et al., Phys. Rev. Lett. **63**, 16 (1989).

[14] P. Anselmann et al. (GALLEX Collaboration), Phys. Lett. B **285**, 376 (1992).

[15] W. Hampel et al. (GALLEX Collaboration), Phys. Lett. B **447**, 127 (1999).

[16] M. Altmann et al. (GNO Collaboration), Phys. Lett. B **616**, 174 (2005).

[17] J.N. Abdurashitov et al. (SAGE Collaboration), Phys. Rev. C **80**, 015807 (2009).

[18] Y. Fukuda et al., Phys. Rev. Lett. **81**, 1158 (1998).

[19] K.S. Hirata et al., Phys. Lett. B **205**, 416 (1988).

[20] Y. Fukuda et al. (Super-Kamiokande Collaboration), Phys. Rev. Lett. **81**, 1562 (1998).

[21] Y. Ashie et al. (The Super-Kamiokande Collaboration), Phys. Rev. Lett. **93**, 101801 (2004).

[22] V. Barger, J.G. Learned, S. Pakvasa, and T.J. Weiler, Phys. Rev. Lett. **82**, 2640 (1999).

[23] E. Lisi, A. Marrone, and D. Montanino, Phys. Rev. Lett. **85**, 1166 (2000).

[24] M.H. Ahn et al., Phys. Rev. Lett. **90**, 041801 (2003).

[25] E. Aliu et al. (The K2K Collaboration), Phys. Rev. Lett. **94**, 081802 (2005).

[26] Q.R. Ahmad et al. (SNO Collaboration), Phys. Rev. Lett. **87**, 071301 (2001).

[27] S. Fukuda et al. (Super-Kamiokande Collaboration), Phys. Rev. Lett. **86**, 5651 (2001).

[28] B. Aharmim et al. (SNO Collaboration), Phys. Rev. C **72**, 055502 (2005).

[29] B. Aharmim et al. (SNO Collaboration), Phys. Rev. Lett. **101**, 111301 (2008).

[30] M. Guler et al. (OPERA Collaboration), CERN/SPSC 2000-028, 2000.

[31] Ed. K. Elsener, CERN 98-02, INFN/AE-98/05, 1998.

[32] R. Bailey et al., CERN-SL/99-034(DI), INFN/AE-99/05, 1999.

[33] N. Agafonova et al., Phys. Lett. B **691**, 138 (2010).

[34] B. Touschek, Z. Phys. **125**, 108 (1949).

[35] J. Tiomno, Nuovo. Cim. Serie X **1**, 226 (1955).

[36] B. Stech and J.H.D. Jensen, Z. Phys. **141**, 175 (1955).

[37] B. Pontecorvo, Zh. Eksp. Teor. Fiz. **33**, 549 (1957), and **34**, 247 (1958).

[38] Z. Maki, M. Nakagawa, and S. Sakata, Prog. Theor. Phys. **28**, 870 (1962).

[39] B. Pontecorvo, Zh. Eksp. Teor. Fiz. **53**, 1717 (1967), Sov. Phys. JETP **26**, 984 (1968).

[40] E. Majorana, Nuovo Cim. **14**, 171 (1937).

[41] N. Cabibbo, Phys. Rev. Lett. **10**, 531 (1963).

[42] M. Kobayashi and T. Maskawa, Prog. Theor. Phys. **49**, 652 (1973).

[43] V. Gribov and B. Pontecorvo, Phys. Lett. B **28**, 493 (1969).

[44] S.M. Bilenky and B. Pontecorvo, Phys. Rept. **41**, 225 (1978).

[45] M. Goeppert-Mayer, Phys. Rev. **48**, 512 (1935).

[46] W.H. Furry, Phys. Rev. **56**, 1184 (1939).

[47] L. Wolfenstein, Phys. Rev. D **17**, 2369 (1978).

[48] S.P. Mikheyev and A.Yu. Smirnov, Yad. Fiz. **42**, 1441 (1985), Sov. J. Nucl. Phys. **42**, 913–917 (1985), Nuovo Cim. C **9**, 17–26 (1986).

[49] Georg G. Raffelt, hep-ph/0208024, 2002.

[50] M.M. Guzzoa, A. Masierob, and S.T. Petcov, Phys. Lett. B **260**, 154 (1991).

[51] E. Roulet, Phys. Rev. D **44**, R935 (1991).

[52] R.N. Mohapatra et al., Rept. Prog. Phys. **70**, 1757 (2007).

[53] V. Barger, K. Whisnant, S. Pakvasa, and R.J.N. Phillips, Phys. Rev. D **22**, 2718 (1980).

[54] F.D. Stacey, *Physics of the Earth*, John Wiley & Sons Inc, New York, 1969.

[55] A.M. Dziewonski and F. Gilbert, Quart. J. R. Astr. Soc. **35**, 401 (1973).

[56] K.E. Bullen, *The Earth's Density*, Chapman and Hall, London, 1975.

[57] A.M. Dziewonski and D.L. Anderson, Phys. Earth Planet. Interiors **25**, 297 (1981).

[58] N. Cabibbo, Phys. Lett. B **72**, 333 (1978).

[59] S. Pakvasa, AIP Conf. Proc. **68**, 1164 (1980).

[60] V. Barger, K. Whisnant, and R.J.N. Phillips, Phys. Rev. Lett. **45**, 2084 (1980).

[61] S.M. Bilenky and F. Niedermayer, Yad. Fiz. **34**, 1091 (1981), Sov. J. Nucl. Phys. **34**, 606 (1981).

[62] C. Jarlskog, Phys. Rev. Lett. **55**, 1039 (1985).

[63] I. Dunietz, O.W. Greenberg, and Dan-di Wu, Phys. Rev. Lett. **55**, 2935 (1985).

[64] M. Tanimoto, Phys. Rev. D **55**, 322 (1997).

[65] J. Arafune and J. Sato, Phys. Rev. D **55**, 1653 (1997).

[66] J. Arafune, M. Koike, and J. Sato, Phys. Rev. D **56**, 3093 (1997), Erratum-ibid. D **60**, 119905 (1999).

[67] H. Minakata and H. Nunokawa, Phys. Rev. D **57**, 4403 (1998).

[68] T.K. Kuo and J. Pantaleone, Phys. Lett. B **198**, 406 (1987).

[69] M. Fukugita and M. Tanimoto, Phys. Lett. B **515**, 30 (2001).

[70] L. Borodovsky et al., Phys. Rev. Lett. **68**, 274 (1992).

[71] B. Achkar et al., Nucl. Phys. B **434**, 503 (1995).

[72] F. Dydak et al., Phys. Lett. B **134**, 281 (1984).

[73] M. Apollonio et al., Eur. Phys. J. C **27**, 331 (2003).

[74] E. Eskut et al. (The CHORUS Collaboration), Phys. Lett. B **497**, 8 (2001).

[75] M.B. Smy (for the Super-Kamiokande Collaboration), Nucl. Phys. Proc. Suppl. **118**, 25 (2003).

[76] G.L. Fogli, E. Lisi, A. Marrone, and A. Palazzo, Prog. Part. Nucl. Phys. **57**, 742 (2006).

[77] S. Abe et al. (The KamLAND Collaboration), Phys. Rev. Lett. **100**, 221803 (2008).

[78] B. Armbruster et al. (KARMEN Collaboration), Phys. Rev. D **65**, 112001 (2002).

[79] S. Yamamoto et al. (K2K Collaboration), Phys. Rev. Lett. **96**, 181801 (2006).

[80] A. Aguilar et al. (LSND Collaboration), Phys. Rev. D **64**, 112007 (2001).

[81] A.A. Aguilar-Arevalo et al. (MiniBooNE Collaboration), Phys. Rev. Lett. **98**, 231801 (2007).

[82] P. Adamson et al. (MINOS Collaboration), Phys. Rev. Lett. **101**, 131802 (2008).

[83] P. Astier et al. (NOMAD Collaboration), Nucl. Phys. B **611**, 3 (2001).

[84] P. Astier et al. (NOMAD Collaboration), Phys. Lett. B **570**, 19 (2003).

[85] J.P. Cravens et al. (The Super-Kamiokande Collaboration), Phys. Rev. D **78**, 032002 (2008).

[86] M. Shiozawa, talk at International School of Nuclear Physics, 27th Course, "Neutrinos in Cosmology, in Astro, Particle, and Nuclear Physics," Erice, Sicily, 2005.

[87] B. Aharmim et al. (SNO Collaboration), Phys. Rev. C **81**, 055504 (2010).

[88] B.T. Cleveland et al., Astrophys. J. **496**, 505 (1998).

[89] C. Arpesella and others (Borexino Collaboration), Phys. Rev. Lett. **101**, 091302 (2008).

[90] J. Hosaka et al. (Super-Kamiokande Collaboration), Phys. Rev. D **73**, 112001 (2006).

[91] Y. Ashie et al. (Super-Kamiokande Collaboration), Phys. Rev. D **71**, 112005 (2005).

[92] M.H. Ahn et al. (K2K Collaboration), Phys. Rev. D **74**, 072003 (2006).

[93] The MINOS Collaboration, Fermilab NuMI-L-337, 1998.

[94] J. Hylen et al., FERMILAB-TM-2018, 1997.

[95] D.G. Michael et al. (MINOS Collaboration), Phys. Rev. Lett. **97**, 191801 (2006).

[96] P. Adamson et al. (MINOS Collaboration), Phys. Rev. D **77**, 072002 (2008).

[97] M. Apollonio et al., Phys. Lett. B **466**, 415 (1999).

[98] F. Boehm et al., Phys. Rev. D **64**, 112001 (2001).

[99] P. Adamson et al. (The MINOS Collaboration), Phys. Rev. D **82**, 051102(R) (2010).

[100] J. Hosaka et al. (Super-Kamiokande Collaboration), Phys. Rev. D **74**, 032002 (2006).

[101] G.L. Fogli, E. Lisi, A. Marrone, A. Palazzo, and A.M. Rotunno, Phys. Rev. Lett. **101**, 141801 (2008).

[102] G.L. Fogli, E. Lisi, A. Marrone, A. Palazzo, and A.M. Rotunno, J. Phys. Conf. Ser. **203**, 012103 (2010).

[103] M. Sanchez, FNAL Wine and Chees Seminar, February 27, 2009.

[104] T. Yanagida and M. Yoshimura, Prog. Theor. Phys. **64**, 1870 (1980).

[105] V. Barger, P. Langacker, J.P. Leveille, and S. Pakvasa, Phys. Rev. Lett. **45**, 692 (1980).

[106] E. Ma and P. Roy, Phys. Rev. D **52**, R4780 (1995).

[107] R. Foot and R.R. Volkas, Phys. Rev. D **52**, 6595 (1995).

[108] E.J. Chuna, A.S. Joshipura, and A.Yu. Smirnov, Phys. Lett. B **357**, 608 (1995).

[109] A.A. Aguilar-Arevalo et al. (The MiniBooNE Collaboration), arXiv:1007.1150, 2010.

[110] N. Okada and O. Yasuda, Int. J. Mod. Phys. A **12**, 3669 (1997).

[111] V. Barger, B. Kayser, J. Learned, T. Weiler, and K. Whisnant, Phys. Lett. B **489**, 345 (2000).

[112] O.L.G. Peres and A.Yu. Smirnov, Nucl. Phys. B **599**, 3 (2001).

[113] R.N. Mohapatra et al., Rept. Prog. Phys. **70**, 1757 (2007).

[114] L. Wolfenstein, Phys. Rev. D **18**, 958 (1978).

[115] P.F. Harrison, D.H. Perkins, and W.G. Scott, Phys. Lett. B **458**, 79 (1999).

[116] P.F. Harrison, D.H. Perkins, and W.G. Scott, Phys. Lett. B **530**, 167 (2002).

[117] P.F. Harrison and W.G. Scott, Phys. Lett. B **535**, 163 (2002).

[118] P.F. Harrison and W.G. Scott, Phys. Lett. B **557**, 76 (2003).

[119] Z.Z. Xing, Phys. Lett. B **533**, 85 (2002).

[120] X.G. He and A. Zee, Phys. Lett. B **560**, 87 (2003).

[121] E. Ma, Phys. Rev. Lett. **90**, 221802 (2003).

[122] E. Ma, Phys. Lett. B **583**, 157 (2004).

[123] C.I. Low and R.R. Volkas, Phys. Rev. D **68**, 033007 (2003).

[124] S. Chang, S.K. Kang, and K. Siyeon, Phys. Lett. B **597**, 78 (2004).

[125] E. Ma, Phys. Rev. D **70**, 031901(R) (2004).

[126] F. Plentinger and W. Rodejohann, Phys. Lett. B **625**, 264 (2005).

[127] P.F. Harrison and W.G. Scott, Phys. Lett. B **628**, 93 (2005).

[128] S. Luo and Z.Z. Xing, Phys. Lett. B **632**, 341 (2006).

[129] W. Grimus and L. Lavoura, JHEP **01**, 018 (2006).

[130] M. Koike and J. Sato, Phys. Rev. D **61**, 073012 (2000), Erratum-ibid. D **62**, 079903 (2000).

[131] V. Barger, S. Geer, R. Raja, and K. Whisnant, Phys. Rev. D **62**, 073002 (2000).

[132] B. Richter, hep-ph/0008222, 2000.

[133] V. Barger et al., hep-ph/0103052, 2001.

[134] M. Freund, P. Huber, and M. Lindner, Nucl. Phys. B **615**, 331 (2001).

[135] J.H. Christenson, J.W. Cronin, V.L. Fitch, and R. Turlay, Phys. Rev. Lett **13**, 138 (1964).

[136] M. Fukugita and T. Yanagida, Phys. Lett. B **174**, 45 (1986).

[137] V.A. Kuzmin, V.A. Rubakov, and M.E. Shaposhnikov, Phys. Lett. B **155**, 36 (1985).

[138] S. Dimopoulos and L. Susskind, Phys. Rev. D **18**, 4500 (1978).

[139] F. Ardellier et al., hep-ex/0405032, 2004.

[140] X. Guo et al. (Daya Bay Collaboration), hep-ex/0701029, 2007.

[141] J.K. Ahn et al. (RENO Collaboration), hep-ex/10031391, 2010.

[142] V. Barger, D. Marfatia, and K. Whisnant, Phys. Rev. D **65**, 073023 (2002).

[143] H. Minakata and H. Nunokawa, JHEP **0110**, 001 (2001).

[144] J.B. Castell, M.B. Gavela, J.J.G. Cadenas, P. Hernándezc, and O. Mena, Nucl. Phys. B **608**, 301 (2001).

[145] G.L. Fogli and E. Lisi, Phys. Rev. D **54**, 3667 (1996).

[146] P. Huber, M. Lindner, M. Rolinec, T. Schwetz, and W. Winter, Nucl. Phys. Proc. Suppl. **145**, 190 (2005).

[147] H. Minakata, H. Sugiyama, O. Yasuda, K. Inoue, and F. Suekane, Phys. Rev. D **68**, 033017 (2003).

[148] D.S. Ayres et al. (The NOνA Collaboration), hep-ex/0503053, 2005.

[149] Y. Itow et al., hep-ex/0106019, KEK-REPORT-2001-4, 2001.

[150] M. Aoki et al., hep-ex/0607013, 2006.

[151] Accelerator Technical Design Report for J-PARC, KEK-Report 2002-13 and JAERI-Tech 2003-044.

[152] S. Fukuda et al. (Super-Kamiokande Collaboration), Nucl. Instr. and Meth. A **501**, 418 (2003).

[153] D. Beavis et al., Proposal of BNL AGS E-889, 1995.

[154] N. Antoniou et al. (the NA61/SHINE Collaboration), CERN-SPSC-2006-034, 2006.

[155] N. Antoniou et al. (the NA61/SHINE Collaboration), CERN-SPSC-2007-004, 2007.

[156] N. Abgrall et al. (the NA61/SHINE Collaboration), CERN-SPSC-2007-033, 2007.

[157] N. Abgrall et al. (the NA61/SHINE Collaboration), CERN-SPSC-2008-018, 2008.

[158] C. Giganti, *Particle Identification in the T2K TPCs and study of the electron neutrino component in the T2K neutrino beam*, PhD thesis, L'Université Paris-Sud 11, 2010.

[159] T. Nakamoto et al., IEEE Trans. on Appl. Superconductivity **14**, 616 (2004).

[160] T. Nakamoto et al., Development of superconducting combined function magnets for the proton transport line for the j-parc neutrino experiment, in *Proc. of 2005 Particle Acc. Conf.*, pages 495–499, 2005.

[161] T. Ogitsu et al., IEEE Trans. on Appl. Superconductivity **15**, 1175 (2005).

[162] S. van der Meer, CERN-61-07, 1961.

[163] R.B. Palmer, CERN-65-32, 1965.

[164] K. Matsuoka et al., Nucl. Instr. and Meth. A **623**, 385 (2010), doi:10.1016/j.nima.2010.03.010.

[165] K. Matsuoka et al., Nucl. Instr. and Meth. A (2010), doi:10.1016/j.nima.2010.09.074.

[166] T. Higuchi et al., CHEP-2003-TUGT004, 2003.

[167] The maximum integrated acquisition system (midas), developed at psi and triumph, `https://midas.psi.ch/`.

[168] Root – a data analysis framework, `http://root.cern.ch/`.

[169] Experimental physics and industrial control system (epics), `http://www.aps.anl.gov/epics/`.

[170] Strategic accelerator design, developed in kek, `http://acc-physics.kek.jp/SAD/`.

[171] M.B. Luque et al. (UA1 Collaboration), Nucl. Instr. and Meth. **176**, 175 (1980).

[172] L. Trung, *Event reconstruction and energy calibration using cosmic muons for the T2K pizero detector*, PhD thesis, Stony Brook University, 2009.

[173] N. Abgrall et al., Nucl. Instr. and Meth. A (to be published), arXiv:1012.0865.

[174] T. Lindner and the T2K-FGD group, J. Phys. Conf. Ser. **136**, 042035 (2008).

[175] Y. Giomataris, P. Rebourgeard, J.P. Robert, and G. Charpak, Nucl. Instr. and Meth. A **376**, 29 (1996).

[176] M. Ziembicki et al., Acta Phys. Polon. B **41**, 1579 (2010).

[177] M.B. Smy et al. (Super-Kamiokande Collaboration), Phys. Rev. D **69**, 011104 (2004).

[178] M. Malek et al. (Super-Kamiokande Collaboration), Phys. Rev. Lett. **90**, 061101 (2003).

[179] M. Shiozawa et al. (Super-Kamiokande Collaboration), Phys. Rev. Lett. **81**, 3319 (1998).

[180] Y. Hayato et al. (The Super-Kamiokande Collaboration), Phys. Rev. Lett. **83**, 1529 (1999).

[181] J.B.M. Pattison, "The CERN neutrino beam", in *Proceedings of the CERN Neutrino Meeting*, pages 13–31, 1969, CERN Yellow Report 69-28.

[182] P. Astier et al. (NOMAD Collaboration), Nucl. Instr. and Meth. A **515**, 800 (2003).

[183] A.P. Bugorsky et al., Nucl. Instr. and Meth. **146**, 367 (1977).

[184] C.Y. Chi et al., Nucl. Instr. and Meth. A **281**, 448 (1989).

[185] A. Marsili et al., CERN-AB-Note-2008-044 BI, 2008.

[186] S. Kopp et al., Nucl. Instr. and Meth. A **568**, 503 (2006).

[187] P. Beynel, P. Maier, and H. Schonbacher, Compilation of radiation damage test data – part III: Materials used around high-energy accelerators, CERN 82-10, European Organization for Nuclear Research, Geneva, 1982.

[188] Average energy required to produce an ion pair, ICRU Report 31, Washington, DC, 1979.

[189] S.J. Harris and C.E. Doust, Radiation Research **66**, 11 (1976).

[190] D.H. Wilkinson, *IONIZATION CHAMBERS AND COUNTERS*, Cambridge Univ. Press, 1950.

[191] R. Zwaska, *Accelerator systems and instrumentation for the NuMI neutrino beam*, PhD thesis, the University of Texas at Austin, 2005.

[192] H.J. Ziock et al., IEEE Trans. Nucl. Sci. **40**, 344 (1993).

[193] A. Van Ginneken, FERMILAB-FN-0522, 1989.

[194] K. Nakamura et al. (Particle Data Group), J. Phys. G **37**, 075021 (2010).

[195] Stopping-power and range tables for electrons, National Institute of Standards and Technology, Physics Laboratory, 2005, `http://physics.nist.gov/PhysRefData/Star/Text/ESTAR.html`.

[196] L.B. Loeb, *Basic Processes of Gaseous Electronics*, University of California Press, Berkeley, 1955.

[197] J.A. Hornbeck, Phys. Rev. **83**, 374 (1951).

[198] J.M. Kirshner and D.S. Toffolo, J. Appl. Phys. **23**, 594 (1952).

[199] M. Otani et al., T2K technical note T2K-TN-041, 2011.

[200] K. Iyogi, S. Nakayama, and Y. Obayashi for the SK-LB group and the T2K-SK group, T2K technical note T2K-TN-027, 2010.

[201] J. Kameda and R. W. for the SK-LB and T2K-SK working groups, T2K technical note T2K-TN-034, 2010.

[202] J. Albert, H. Kaji, S. Nakayama, S. Mine, and K. O. for the SKLB and T2KSK groups, T2K technical note T2K-TN-028, 2010.

[203] T. Barszczak, *The Efficient Discrimination of Electron and Pi-Zero Events in a Water Cherenkov Detector and the Application to Neutrino Oscillation Experiments*, PhD thesis, University of California, Irvine, 2005.

[204] S. Mine, T2K technical note T2K-TN-005, 2009.

[205] Geant – detector description and simulation tool, Application Software Group, Computing and Networks Division, CERN, Geneva (1993).

[206] G. Battistoni et al., "the fluka code: Description and benchmarking", in *Proceedings of the Hadronic Shower Simulation Workshop 2006*, edited by R. R. M. Albrow, Fermilab 6–8 September 2006, 2007, AIP Conference Proceeding 896, 31–49.

[207] A. Fasso', A. Ferrari, J. Ranft, and P.R. Sala, "fluka: a multi-particle transport code", CERN-2005-10 (2005), INFN/TC_05/11, SLAC-R-773.

[208] C. Zeitnitz and T. Gabriel, in *Proc. of International Conference on Calorimetry in High Energy Physics*, Tallahasse, FL, USA, February, 1993.

[209] N. Abgrall et al. (the NA61 Collaboration), CERN-SPSC-2010-025; SPSC-SR-066, 2010.

[210] G. Bellettini et al., Nucl. Phys. **79**, 609 (1966).

[211] N. Abgrall et al. (beam working group), T2K technical note T2K-TN-038, 2011.

[212] R.P. Feynman, Phys. Rev. Lett. **23**, 1415 (1969).

[213] U. Amaldi et al., Nucl. Phys. B **86**, 403 (1975).

[214] F.F. Chen, C.P. Leavitt, and A.M. Shapiro, Phys. Rev. **99**, 857 (1955).

[215] S.P. Denisov, Yu.D. Prokoshkin, and D.A. Stoyanova, Nucl. Phys. B **61**, 62 (1973).

[216] J.V. Allaby et al., Yad. Fiz. **12**, 538 (1970).

[217] M.J. Longo and B.J. Moyer, Phys. Rev. **125**, 701 (1962).

[218] B.M. Bobchenko et al., Sov. J. Nucl. Phys. **30**, 805 (1979), Yad. Fiz. **30**, 1553 (1979).

[219] B.W. Allardyce et al., Nucl. Phys. A **209**, 1 (1973).

[220] A.V. Vlasov et al., Sov. J. Nucl. Phys. **27**, 222 (1978), Yad. Fiz. **27**, 413 (1978).

[221] J.W. Cronin, R. Cool, and A. Abashian, Phys. Rev. **107**, 1121 (1957).

[222] R.J. Abrams et al., Phys. Rev. D **1**, 1917 (1970).

[223] T. Eichten et al., Nucl. Phys. B **44**, 333 (1972).

[224] R.P. Feynman, *Photon-Hadron Interactions*, Benjamin, New York, 1972.

[225] J.D. Bjorken and E.A. Paschos, Phys. Rev. **185**, 1975 (1969).

[226] M. Bonesini et al., Eur. Phys. J. C **20**, 13 (2001).

[227] V. Galymov et al. (beam working group), T2K technical note T2K-TN-039, 2011.

[228] N. Abgrall et al. (the NA61/SHINE Collaboration), CERN-PH-EP-2011-005, 2011.

[229] G.L. Fogli et al., Phys. Rev. D **78**, 033010 (2008).

[230] T. Schwetz, M. Tórtola, and José W.F. Valle, New J. Phys. **10**, 113011 (2008), arXiv:0808.2016v3.

[231] Prob3++, `http://www.phy.duke.edu/ raw22/public/Prob3++/`.

[232] V. Barger, K. Whisnant, and R.J.N. Phillips, Phys. Rev. D **22**, 1636 (1980).

[233] P. de Perio et al., T2K technical note T2K-TN-030, 2011.

[234] P. de Perio et al., T2K technical note T2K-TN-032, 2011.

[235] C. Giganti, F. Blaszczyk, A. Longhin, and M. Zito, T2K technical note T2K-TN-015-V3, 2011.

[236] J. Kameda for the SK-LB and T.-S. working groups, T2K technical note T2K-TN-045, 2011.

[237] J. Albert and K. O. for the T2K oscillation analysis working group, T2K technical note T2K-TN-042, 2011.

[238] Y. Hayato, Nucl. Phys. Proc. Suppl. **112**, 171 (2002).

[239] Y. Hayato, Acta Phys. Polon. B **40**, 2477 (2009).

[240] T. Katori (for the MiniBooNE Collaboration), AIP Conf. Proc. **1222**, 471 (2010).

[241] K.S. Kuzmin, V.V. Lyubushkin, and V.A. Naumov, Eur. Phys. J. C **54**, 517 (2008).

[242] L.B. Auerbach et al. (LSND Collaboration), Phys. Rev. C **66**, 015501 (2002).

[243] C.H. Llewellyn Smith, Phys. Rept. **3**, 261 (1972).

[244] R.A. Smith and E.J. Moniz, Nucl. Phys. B **43**, 605, Erratum-ibid. B **101**, 547 (1975).

[245] A.A. Aguilar-Arevalo et al. (The MiniBooNE Collaboration), Phys. Rev. Lett. **100**, 032301 (2008).

[246] V. Bernard, L. Elouadrhiri, and Ulf.G. Meissner, J. Phys. G **28**, R1 (2002).

[247] K. Abe et al., Phys. Rev. Lett. **56**, 1107 (1986), Erratum-ibid. **56**, 1883 (1986).

[248] Carl H. Albright, C. Quigg, R.E. Shrock, and J. Smith, Phys. Rev. D **14**, 1780 (1976).

[249] D. Rein and L.M. Sehgal, Ann. Phys. **133**, 79 (1981).

[250] D. Rein, Z. Phys. C **35**, 43 (1987).

[251] G.M. Radecky et al., Phys. Rev. D **25**, 1161 (1982), Erratum-ibid. D **26**, 3297 (1982).

[252] A. Rodriguez et al. (K2K Collaboration), Phys. Rev. D **78**, 032003 (2008).

[253] A.A. Aguilar-Arevalo et al. (The MiniBooNE Collaboration), Phys. Rev. Lett. **103**, 081801 (2009).

[254] T. Kitagaki et al., Phys. Rev. D **34**, 2554 (1986).

[255] S. Nakayama et al. (The K2K Collaboration), Phys. Lett. B **619**, 255 (2005).

[256] A.A. Aguilar-Arevalo et al. (The MiniBooNE Collaboration), Phys. Rev. D **81**, 013005 (2010).

[257] Y. Kurimoto et al. (The SciBooNE Collaboration), Phys. Rev. D **81**, 033004 (2010).

[258] D. Rein and L.M. Sehgal, Nucl. Phys. B **223**, 29 (1983).

[259] D. Rein and L.M. Sehgal, Phys. Lett. B **657**, 207 (2007).

[260] M. Hasegawa et al. (K2K Collaboration), Phys. Rev. Lett. **95**, 252301 (2005).

[261] K. Hiraide et al. (The SciBooNE Collaboration), Phys. Rev. D **78**, 112004 (2008).

[262] A. Kartavtsev, E.A. Paschos, and G.J. Gounaris, Phys. Rev. D **74**, 054007 (2006).

[263] L. Alvarez-Ruso, L.S. Geng, S. Hirenzaki, and M.J. Vicente Vacas, Phys. Rev. C **75**, 055501 (2007), Erratum-ibid. C **80**, 019906 (2009).

[264] J.L. Raaf, *A Measurement of the Neutrino Neutral Current π^0 Cross-Section at MiniBooNE*, PhD thesis, University of Cincinnati, 2005.

[265] H. Faissner et al., Phys. Lett. B **125**, 230 (1983).

[266] E. Isiksal, D. Rein, and J.G. Morfin, Phys. Rev. Lett. **52**, 1096 (1984).

[267] M. Gluck, E. Reya, and A. Vogt, Eur. Phys. J. C **5**, 461 (1998).

[268] A. Bodek and U.K. Yang, AIP Conf. Proc. **670**, 110 (2003).

[269] C. Mariani (for the K2K Collaboration), AIP Conf. Proc. **1189**, 339 (2009).

[270] A.A. Aguilar-Arevalo et al. (MiniBooNE Collaboration), FERMILAB-PUB-10-426-e, 2010.

[271] L.L. Salcedo, E. Oset, M.J. Vicente-Vacas, and C. Garcia-Recio, Nucl. Phys. A **484**, 557 (1988).

[272] D. Ashery et al., Phys. Rev. C **23**, 2173 (1981).

[273] C. Zeitnitz and T.A. Gabriel, Nucl. Instr. and Meth. A **349**, 106 (1994).

[274] I. Thormahlen, J. Straub, and U. Grigull, J. Phys. Chem. Ref. Data **14**, 933 (1985).

[275] J.V. Allaby et al., CERN 70-12, 1970.

[276] V.L. Fitch, S.L. Meyer, and P.A. Piroué, Phys. Rev. **126**, 1849 (1962).

[277] U. Becker et al., Phys. Rev. Lett. **37**, 1731 (1976).

[278] A. Schwarzschild and Č. Zupančič, Phys. Rev. **129**, 854 (1963).

[279] W.F. Baker et al., Phys. Rev. Lett. **7**, 101 (1961).

[280] K. Kinoshita and H. Noda, Prog. Theor. Phys. **46**, 1639 (1971).

[281] E. Yen, Phys. Rev. D **10**, 836 (1974).

[282] F.E. Taylor et al., Phys. Rev. D **14**, 1217 (1976).

[283] R.J. Abrams et al., Phys. Rev. D **4**, 3235 (1971).

[284] D.S. Barton et al., Phys. Rev. D **27**, 2580 (1983).

[285] P. Skubic et al., Phys. Rev. D **18**, 3115 (1978).

[286] L. Pondrom, private communication.

[287] M.R. Whalley et al., University of Michigan Report UM-HE-79-14, 1979.